Investigation of Elastic Anisotropy and Texture of Austenitic Stainless Steel Weld Metal Using Diffraction and Self-Consistent Modelling

Thesis

UNRESTRICTED

Investigation of Elastic Anisotropy and Texture of Austenitic Stainless Steel Weld Metal Using Diffraction and Self-Consistent Modelling.

Shiv Sharma

Thesis submitted to the Department of Design, Development, Environment and Materials of The Open University, Milton Keynes, UK for the degree of Doctor of Philosophy

November 2009

DATE of SUBMISSION: 5 NOV 2009
DATE of AWARD: 24 MAY 2010

Contents

Abstract

Welding of austenitic stainless steels is a prominent process in several industrial sectors including nuclear, aerospace, chemical and process. During finite element modelling of weld properties, it is assumed that the weld metal is homogeneous. During the modelling process weld metal is assigned the same elastic constants as that of parent metal. This can introduce erroneous results during the calculation of strains. Weld metal is usually highly anisotropic due to directional solidification. Weld metal also possesses typical fibre texture as the grains grow along the maximum thermal gradient when cooling and the result is long, columnar grains. These grains usually have a particular crystallographic direction along the solidification direction. Weld metals usually have [001] crystallographic planes along the solidification direction, and it has been termed as [001] fibre texture. The resulting fibre texture due to solidification has an important consequence on weld metal properties. Depending on the grain orientations, different mechanical properties are observed as compared with an ideal homogeneous and isotropic material. Different types of austenitic weld metals have been investigated in this work. The mechanical response of different types of weld metal, in different directions has been analysed using in-situ tension/compression and neutron diffraction. It has been observed that the Young's modulus for the weld metal is direction dependent. These variations have been explained on the basis of texture investigation using the electron backscatter diffraction (EBSD) technique. The texture results have been correlated with the material response and it has been observed that the more pronounced the crystallographic texture, the more anisotropic is the material response under applied loading. Finally, the directional Young's modulus has also been calculated from elasto–plastic self-consistent modelling using Hutchinson's formalism (using the FORTRAN sub-routine written by Carlos Tome).

Acknowledgements

I would like to express my sincere thanks to my supervisors Prof. Lyndon Edwards (Now at ANSTO, Australia), Prof. Michael Fitzpatrick, Dr. Martin Rist and external co-supervisor Dr. Mark Turski (Magnesium Elektron, Manchester) for providing me with valuable guidance and support for the duration of my study at The Open University.

I also want to thank Prof. John Bouchard for his helpful advice and Dr. Richard Haigh for reading the thesis chapters. I am also thankful to Dr. Mark Daymond for his valuable comments on the results of neutron diffraction experiments, texture and EPSC modelling. I am also thankful to Dr. Mike Spindler (British Energy) and Dr. John Francis for providing useful comments about welding metallurgy.

I would also like to thank Dr. Ed Oliver (ISIS), Dr A Pardowska (ISIS), Dr. D. J. Hughes (ILL), Dr. M. Hoffmann (FRM II), Dr. Peter Spalthoff (GKSS), Christian Randau (FRM II) for their help and cooperation during experiments at the respective institutes. I am also grateful to the Research School for the generous funding and for providing me with an opportunity to study at The Open University.

I would like to say thanks to the secretarial staff of the research school and DDEM for help with clerical matters. In particular I want to thank Paula Piggott, Sarah Wood, Kathryn Reeves from the research school and Rehana Malik, Debby Derbyshire and Courtney Courtnage from the DDEM. I am also thankful to the technical staff of the DDEM. In particular I want to thank Stan Hiller, Pete Ledgard and Gordon Imlach.

I would also like to thank Olivier Zanellato for helping me with EPSC modelling and Ashwin Rao for help with neutron diffraction experiments. I am also thankful to Kashif and Himanshu for useful discussions. I am also thankful to Nicky Clarkson for helping with the styles and formatting.

List of Figures

List of Tables

Introduction

Austenitic stainless steels are alloys which have excellent resistance to corrosion and very good mechanical properties [1]. These alloys exhibit high toughness at cryogenic temperatures and good resistance to oxidation at elevated temperatures to ~875 K [2]. They are widely used in power plants, chemical process industries and reactors. To make iron alloys stainless, addition of at least 10.5% chromium is required. However, all austenitic stainless steels contain at least 15% chromium and smaller quantities of nickel, manganese, carbon and nitrogen to stabilise the f.c.c. austenitic structure [3]. Austenitic stainless steels are classified as readily weldable materials; however, the weld metals of fully austenitic stainless steels are susceptible to hot cracking. By adding small amounts of δ-ferrite in the electrodes the susceptibility to hot cracking can be avoided [4]. Depending on the composition and cooling rate the weld metal microstructure of austenitic stainless steels exhibits various ferrite morphologies. The composition and the cooling rate influence the solidification mode which in turn influences the texture in the weld metal. The grain growth is easy in the [001] direction in the austenitic stainless steels. Therefore when the randomly oriented grains in the base metal begin to grow into the weld metal, crystals oriented with a [001] direction parallel to the solidification direction is favoured by competitive growth processes [5].

The preferred orientations in the austenitic stainless steel weld metal causes mechanical anisotropy which has implications for diffraction based strain measurement and in-situ deformation behaviour of weld metal. The elastic modulus for the weld metal becomes orientation dependent and very low values can be observed in certain orientations.

In-situ neutron diffraction techniques [6] are widely used to study the inter-granular stresses in polycrystalline materials. These techniques have also been used to

calculate the bulk diffraction elastic constants and hkl dependent diffraction elastic constants [7]. EPSC (Elasto-plastic self-consistent) modelling techniques have also been widely used to predict the inter-granular stresses and to calculate the diffraction elastic constants [8]. These techniques have also been used to model the angular variation of the Young's modulus in polycrystalline materials.

In the present study several austenitic stainless steel welds have been investigated. These include 316 and 308 austenitic weld metals. These weld specimens were produced by British Energy for the Young's modulus measurement and fatigue testing. It was decided by The Open University to use these specimens for in-situ neutron diffraction for measuring the diffraction Young's modulus of the weld metal. This type of experiment also provided information about the anisotropic behaviour of the weld metal as the weld metal was deformed in-situ in different orientations in the neutron beam. This type of experiment for the weld metal has not been reported previously. This is the first attempt to study the deformation behaviour of the weld metal using in-situ neutron diffraction.

The experimental work included characterisation of microstructure using optical microscopy and EBSD. Texture investigation using EBSD and neutron diffraction has been carried out.

In 316 austenitic stainless steel welds very intense recrystallization cube texture has been observed as compared with a nearly random texture in 308 austenitic stainless steel welds. The highly textured nature of the weld metal results in correspondingly anisotropic mechanical properties.

In-situ neutron diffraction techniques have been used to calculate the Young's modulus for various types of welds. EPSC techniques have also been used to calculate the Young's modulus based on the EBSD texture data. Angular variation of the elastic modulus has also been carried out.

Because of the anisotropy of the weld metal the Young's modulus in the weld metal becomes orientation dependent and it may attain values well below that being used in current literature for the design of weld structures. This is particularly important in the case of conversion of strains to the stresses in the diffraction experiments or the finite element calculations. An incorrect value of the Young's modulus may introduce erroneous results.

Chapter Synopses

Chapter 1 is mainly a literature review chapter related to residual stresses, their measurement by diffraction, texture in materials, in-situ deformation of materials and modelling of materials using various techniques such as the Kroner and the EPSC models.

Chapter 2 provides details about various specimens and their manufacturing details which have been used in various experiments e.g metallography, EBSD and neutron texture and in-situ diffraction. Fundamentals of weld solidification and metallurgy have also been reviewed. Various solidification modes of austenitic stainless steels have been reviewed. Optical microstructure results from present experiments have been presented and discussed.

Chapter 3 provides details about the texture results from present work on various types of welds using EBSD and neutron diffraction. The results have been presented in the form of pole figures and orientation distribution function sections.

Chapter 4 provides details about the in-situ neutron diffraction technique used to measure the inter-granular stresses and the diffraction elastic constants. Results from present work using in-situ tension and compression have been presented and discussed.

Chapter 5 is a discussion chapter about the texture development in the welds and its implications for Young's modulus measurement. It also provides details about the

EPSC modelling results from present work and their comparison with the neutron diffraction results.

Chapter 6 is a concluding chapter.

Nomenclature

σ_{ij}	second rank stress tensor
ε_{ij}	second rank strain tensor
γ_{ij}	second rank shear strain tensor
C_{ijkl}	fourth rank stiffness tensor
S_{ijkl}	fourth rank compliance tensor
E	Young's modulus
G	Shear modulus
K	Bulk modulus
ν	Poisson's ratio
λ	wavelength
k_i	incident radiation wave-vector
k_f	scattered radiation wave-vector
Q	diffraction vector in the direction of measurement of strain
d_{hkl}	interplanar spacing
θ	Bragg angle for diffraction
h, k, l	Miller indices for a plane
l_1, l_2, l_3	direction cosines
d_0	stress free reference spacing
φ, ψ	azimuthal and polar angles in the $\sin^2\psi$ geometry
$d_{\varphi\psi}$	interplanar spacing in the $\sin^2\psi$ geometry
$L_{\varphi\psi}$	diffraction vector in the $\sin^2\psi$ geometry
S_1, S_2, S_3	axes of the specimen coordinate system in the $\sin^2\psi$ geometry
y_i	measured Bragg profile of a diffraction peak
K_A, K_B	sample and crystal coordinate systems for the definition of an orientation

$\varphi_1, \varphi, \varphi_2$	Euler angles
α, β	polar and azimuthal angles of a pole
χ, φ, ω	angles in the Eulerian cradle

Chapter 1 Inter-granular Stresses and Texture in Materials: Measurement and Modelling

1.1 Introduction

This chapter provides details about stress, strain and measuring inter-granular stresses in engineering materials using neutron diffraction. The experimental work related to strain measurement by neutron diffraction techniques has been reviewed. Modelling of inter-granular stresses using various techniques has been described.

1.2 Introduction to Tensors

A single number unrelated to any axes of reference is defined as a tensor of zero rank (e.g. a scalar quantity such as density) [9]. Three numbers or components, each of which is associated with one of the axes of reference are required to specify a tensor of the first rank (e.g. a vector quantity such as force). Nine numbers or components, each of which is associated with a pair of axes (taken in a particular order) are required to specify a tensor of the second rank. Stress and strain are tensors of the second rank and the components of stress and strain therefore are written with two subscripts e.g. σ_{11} or ε_{11}.

The rank of a tensor quantity is equal to the number of the subscripts. A second rank tensor quantity T_{kl} can be transformed in the following way:

$$T'_{ij} = a_{ik} a_{jl} T_{kl} \qquad (1.1)$$

where $a_{ik} a_{jl}$ are the direction cosines.

The elastic constants which relate the stress to the strain or vice versa are tensors of the fourth rank and these require 81 numbers. Physical quantities such as the elastic constants represented by 81 numbers T_{mnop} are transformed in the following way:

$$T'_{ijkl} = a_{im} a_{jn} a_{ko} a_{lp} T_{mnop} \qquad (1.2)$$

where $a_{im}a_{jn}a_{ko}a_{lp}$ are the direction cosines.

1.3 The concept of stress

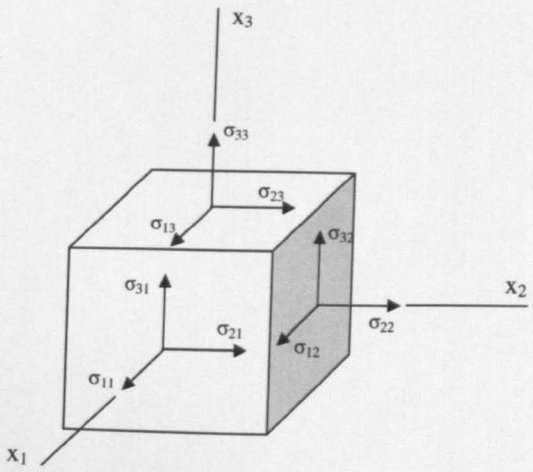

Fig. 1.1 The forces on the face of a unit cube in a homogeneous stressed body [9].

A body is said to be in a state of stress if it is acted on by external forces or one part of the body exerts a force on the neighbouring parts [9]. There are two kinds of external forces which act on a volume element situated within a stressed body, the body forces and the surface forces. The body forces such as gravitational forces, magnetic forces or in the case of a body in motion, inertia forces, act throughout the body on all its elements and their magnitudes are proportional to the volume of the element. The surface forces such as the pressure of one body on another or hydrostatic pressure are distributed over the surface of the body [10]. These forces are proportional to the area of the surface of the element. The force per unit area is called a stress.

If the forces acting on the surface of an element of fixed shape and orientation are independent of the position of the element in the body, the stress is said to be homogeneous.

Consider a unit cube within the body (Fig. 1.1) with edges parallel to the axes Ox_1, Ox_2, Ox_3. Any force exerted by the material outside the cube upon the material inside

the cube will be transmitted across each face of the cube. The force transmitted across each face may be resolved into three components. The component of the force in the $+Ox_i$ direction transmitted across that face of the cube which is perpendicular to Ox_j is denoted by σ_{ij}. σ_{11}, σ_{22}, σ_{33} are the normal components of stress and σ_{12}, σ_{21}, σ_{23} etc. are the shear components. The σ_{ij} thus defined form a second rank tensor and also $\sigma_{ij} = \sigma_{ji}$.

1.4 The concept of Strain

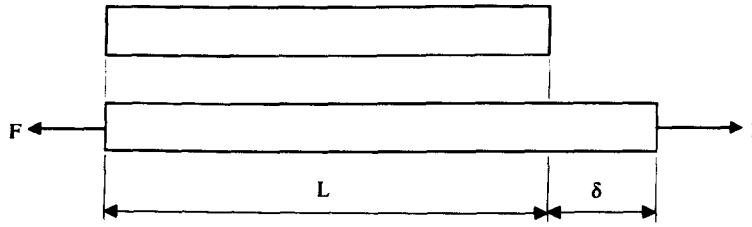

Fig. 1.2 Direct or normal strain

Strain has been defined as the non-dimensional expression of deformation [11].

1.4.1 Direct or normal strain

Direct strain is defined as the change in length per unit original length. Consider the uniform bar shown in Fig. 1.2 subjected to an axial tensile load F. If the resulting extension of the bar is δ and its unloaded length is L, then the direct tensile strain is

$$\varepsilon = \delta/L \qquad (1.3)$$

1.4.2 Shear Strain

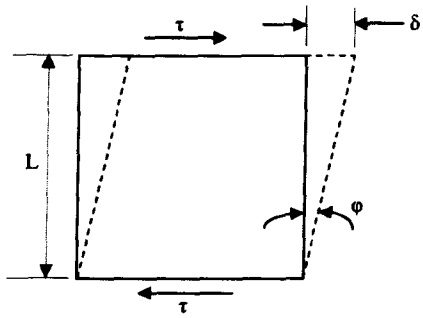

Fig. 1.3 shear strain

The distortion produced in the block shown in Fig. 1.3 under the influence of shear stresses, τ, is δ. Shear strain [12] γ is defined as

$\gamma = \delta/L = tan\ \varphi$ ($\approx \varphi$ for small distortions). (1.4)

1.5 Basic Continuum Relation between Strain and Stress

The most general anisotropic form of linear elastic stress-strain relations (Hooke's law) may be expressed as [13, 14]

$$\varepsilon_{ij} = S_{ijkl}\sigma_{kl} \tag{1.5}$$

and

$$\sigma_{ij} = C_{ijkl}\varepsilon_{kl} \tag{1.6}$$

where S_{ijkl} is the compliance tensor and C_{ijkl} is the elastic stiffness tensor (often called just the elastic constants). Both S_{ijkl} and C_{ijkl} are fourth rank tensor quantities. If we expanded eq. 1.5 or 1.6, we would get nine equations, each with nine terms, 81 constants in all. However because of symmetry of ε_{ij} and σ_{ij} (that is $\sigma_{ij} = \sigma_{ji}$) only 36 of the components of the compliance tensor are independent and distinct terms. The same is true of the elastic stiffness tensor.

For an isotropic elastic solid, the stress-strain relations are expressed by

$$\sigma_x = \frac{E}{1+\nu}\varepsilon_{ij} + \frac{\nu E}{(1+\nu)(1-2\nu)(\varepsilon_x + \varepsilon_y + \varepsilon_z)} \quad (1.7)$$

These relations contain the normal strains only, no shear strains.

However for an anisotropic solid, we have the following relations (expanding eq. 1.6)

$$\sigma_{11} = C_{1111}\varepsilon_{11} + C_{1122}\varepsilon_{22} + C_{1133}\varepsilon_{33} + C_{1123}(2\varepsilon_{23}) + C_{1113}(2\varepsilon_{13}) + C_{1112}(2\varepsilon_{12}) \quad (1.8)$$

For anisotropic elastic solids both normal strains and shear strains are capable of contributing to a normal stress.

The elastic constants are defined by the equations

$$C_{11} = \frac{\Delta\sigma_{11}}{\Delta\varepsilon_{11}} \text{ all } \varepsilon_{ij} \text{ constant except } \varepsilon_{11}. \quad (1.9)$$

It is difficult to perform the measurement of C_{11} experimentally since the specimen must be constrained mechanically to prevent strains such as ε_{23}.

However, the coefficients of elastic compliance can be determined by using equations

$$S_{11} = \frac{\Delta\varepsilon_{11}}{\Delta\sigma_{11}} \text{ all } \sigma_{ij} \text{ constant except } \sigma_{11}. \quad (1.10)$$

The components of C_{ij} can be determined by matrix inversion after experimentally determining the components of S_{ij}.

Due to symmetry of the elastic constants ($C_{ij} = C_{ji}$), the number of independent constants is further reduced. Out of 36 constants C_{ij} there are six constants where $i = j$. This leaves 30 constants where $i \neq j$, but only half of these are independent constants since $C_{ij} = C_{ji}$. Therefore, for a general anisotropic linear elastic solid there are (30/2) + 6 = 21 elastic constants.

Due to symmetry of the crystal structure, the number of independent constants can be reduced further. For example for a cubic crystal structure, the number of independent elastic constants is just 3.

For a cubic crystal structure the following relation exists between the moduli of stiffness and compliance:

$$\left.\begin{aligned} C_{11} &= \frac{(S_{11}+S_{12})}{(S_{11}-S_{12})(S_{11}+2S_{12})} \\ C_{12} &= \frac{-S_{12}}{(S_{11}-S_{12})(S_{11}+2S_{12})} \\ C_{44} &= \frac{1}{S_{44}} \end{aligned}\right\} \tag{1.11}$$

The moduli of compliances can be determined from the measured moduli of stiffness by using the relation [15]:

$$\left.\begin{aligned} S_{11} &= \frac{(C_{11}^2-C_{12}^2)}{(C_{11}^3+2C_{12}^3-3C_{11}C_{12}^2)} \\ S_{12} &= \frac{-C_{12}(C_{11}-C_{12})}{(S_{11}-S_{12})(S_{11}+2S_{12})} \\ S_{44} &= \frac{1}{C_{44}} \end{aligned}\right\} \tag{1.12}$$

1.6 Residual Stresses

Residual stresses are self-equilibrating stresses existing in materials under uniform temperature conditions when the material is not subjected to any externally applied loading [16]. Strain incompatibilities due to inhomogeneous elastic or plastic deformation of materials give rise to residual stresses. If any material containing residual stresses is loaded externally the real stress state will comprise loading stresses and residual stresses. Therefore from a structural integrity point of view it is very important to evaluate the residual stresses. Residual stresses can be introduced into structural components both during manufacturing and as a result of deformation during use [17]. Depending upon the type of loading experienced by a structural member the presence of residual stresses can be beneficial or detrimental to its strength. In general a residual stress distribution which increases the applied stress will be detrimental and the one which reduces the applied stress by acting in the opposite direction to the applied stresses will be beneficial. Tensile surface residual stresses in the case of cyclic loading in tension can be particularly harmful since these may aid crack initiation and growth by fatigue. For components experiencing this type of loading, those manufacturing processes are preferred which leave compressive, crack inhibiting, residual surface stresses.

Residual stresses originate from misfits between different regions e.g. those caused by the non-uniform plastic deformation of a bent bar; from sharp thermal gradients e.g. those caused during welding or heat treatment operations [18].

1.6.1 Residual Stress Length Scales

Residual stresses can be classified over three length scales as shown in Fig. 1.4 for a two phase material containing the phases α and β.

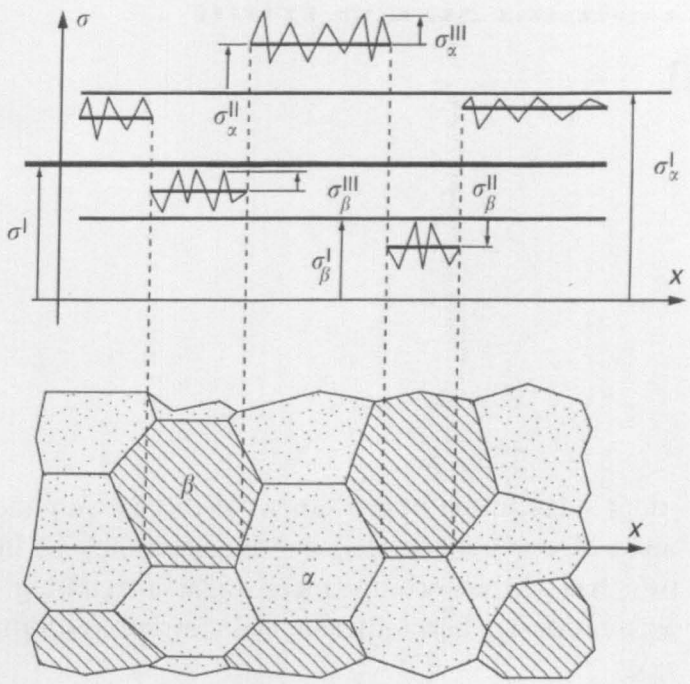

Fig. 1.4 The three types of stresses in a two phase material [19].

Type I residual stresses (σ_R^I): These types of residual stresses are homogeneous over a very large number of grains of the material [16]. These are also homogeneous over a specific phase of the material as shown in Fig. 1.4.An example of type I residual stresses is shown in Fig. 1.5. These are also classified as macro-stresses. The internal forces related to these stresses are balanced on all planes. The moments related to these forces are equal to zero around all axes.

Type II residual stresses (σ_R^{II}): These types of residual stresses are homogeneous within a single grain or phase of the material [16]. In polycrystalline materials low level type II stresses nearly always exist because of the fact that the elastic and thermal properties of differently oriented neighbouring grains are different [18]. When the microstructure contains several phases or phase transformations take place, more significant grain scale stresses occur. The internal forces related to these stresses are in balance between the different grains or phases.

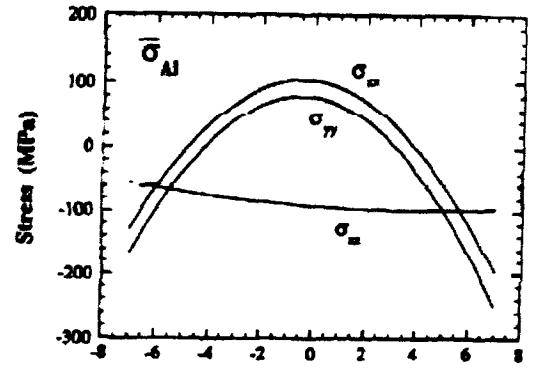

(a) Distance from center of plate (cm).

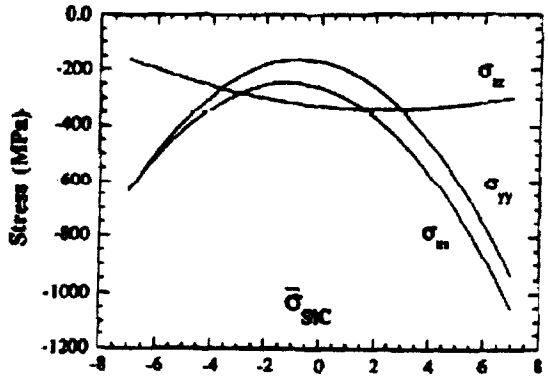

(b) Distance from center of plate (cm).

Fig. 1.5 Example of type 1 residual stresses: (a) The through thickness variation of the calculated total stress in Al matrix of the Al/20% SiC Plate (b) The through thickness variation of the calculated total stress in SiC reinforcement of the Al/20% SiC plate [20].

Type III residual stresses (σ_R^{III}): These types of residual stresses are homogeneous over a few inter-atomic distances [16]. The internal forces related to these stresses are in balance around dislocations or point defects.

Type II and III residual stresses are classified together as micro-stresses.

1.7 The Theory of Stress/Strain Analysis with Diffraction

In a structural member of interest it is not possible to measure the strain at a single point [21]. The strain averaged over a sampled gauge volume which is defined by the apertures or collimators, is measured by diffraction techniques.

The distance between atomic planes of a crystalline specimen is utilised as an internal strain gauge in all diffraction based stress analysis techniques [22]. The lattice plane spacing d_{hkl} can be determined for any reflection *hkl* from the angular position θ of the appropriate diffraction peak by utilising Bragg's law; $\lambda = 2d_{hkl}\, sin\theta$, where λ is the wavelength of the radiation used [23]. The diffraction vector $L_{\varphi\psi}$ (Fig. 1.6) which bisects the angle between the incident and diffracted beams is normal to this plane spacing.

The strain, ε, along the diffraction vector $L_{\varphi\psi}$ can be defined as:

$$\varepsilon = \frac{d_{\phi\psi} - d_0}{d_0} \tag{1.13}$$

The d_0 is the unstressed plane spacing corresponding to the *hkl* planes. The strains in the specimen coordinate system (S_i) can be expressed in terms of the measured strains

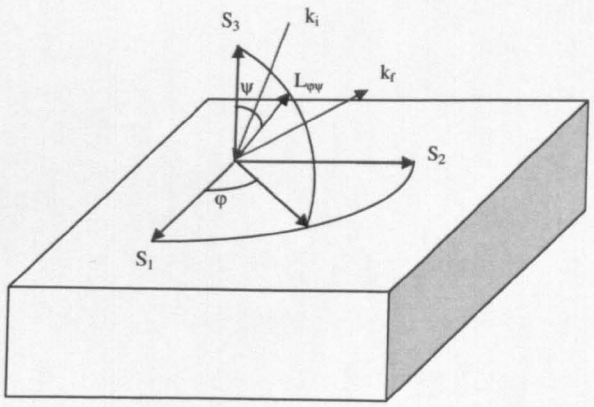

Fig. 1.6 Definition of the sample coordinate system Si and the measurement direction $L_{\varphi\psi}$. Different grains diffract at different ψ tilts in polycrystalline samples.

through a second rank tensor transformation after defining the diffraction coordinate system with $L_{\varphi\psi}$ as one of the axes using:

$$\varepsilon'_{ii} = a_{ik}\, a_{il}\, \varepsilon_{kl}. \tag{1.14}$$

The index "*i*" is usually chosen as 3 and ε'_{ii} is defined along $L_{\varphi\psi}$. The advantage of this convention is that the strain measured along $L_{\varphi\psi}$ can be transformed to the sample coordinate system. After substituting the appropriate direction cosines for a_{ik}, a_{il}, in terms of the angles φ, ψ, the following relation is obtained:

$$\begin{aligned}\frac{d_{\varphi\psi} - d_0}{d_0} = {} & \varepsilon_{11}\cos^2\phi\sin^2\psi + \varepsilon_{12}\sin 2\phi\sin^2\psi + \varepsilon_{22}\sin^2\phi\sin^2\psi \\ & + \varepsilon_{33}\sin^2\psi - \varepsilon_{33} + \varepsilon_{13}\cos\phi\sin 2\psi + \varepsilon_{23}\sin\phi\sin 2\psi\end{aligned} \tag{1.15}$$

Equation (1.15) is the fundamental equation of diffraction based stress/strain analysis and it contains six unknowns. The strains ε_{ij} in the specimen coordinate system, S_i, can be calculated after determining d_{hkl} along six or more independent directions. The strain and stress are tri-axial in most cases and can be represented by a strain tensor ε and stress tensor σ. An elastically isotropic model with macroscopic Young's modulus E and Poisson's ratio ν can be assumed for calculating the principal internal stresses along these axes using [24]:

$$\begin{aligned}\sigma_x &= \frac{E}{(1+\nu)(1-2\nu)}[(1-\nu)\varepsilon_x + \nu(\varepsilon_y + \varepsilon_z)] \\ \sigma_y &= \frac{E}{(1+\nu)(1-2\nu)}[(1-\nu)\varepsilon_y + \nu(\varepsilon_x + \varepsilon_z)] \\ \sigma_z &= \frac{E}{(1+\nu)(1-2\nu)}[(1-\nu)\varepsilon_z + \nu(\varepsilon_x + \varepsilon_y)]\end{aligned} \tag{1.16}$$

The values of the elastic constants appropriate to the specific (*h k l*) crystallographic plane on which the strain is being measured, are used in the case of a single peak analysis. Bulk values are used in the case of a multi-peak Rietveld/Pawley refinement.

The variation of $d_{\varphi\psi}$ with φ and ψ is predicted by the equation (1.15) for all material classes that yield diffraction peaks. The variation of $d_{\varphi\psi}$ with $sin^2\psi$ is linear (Fig. 1.7a)

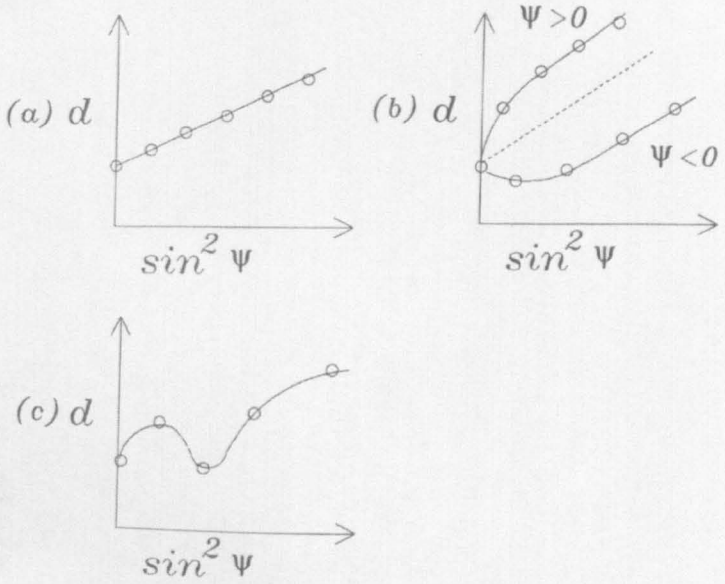

Fig. 1.7 Types of $d_{\varphi\psi}$ vs $\sin^2\psi$ plots: Figures a, b depict regular behaviour. Figure (c) depicts oscillatory behaviour [22].

if the shear terms ε_{31}, ε_{32} are zero. The variation of $d_{\varphi\psi}$ with $sin^2\psi$ will exhibit curvature and ψ-splitting (Fig. 1.7b) if the shear terms are finite. In the case of a textured material the variation of $d_{\varphi\psi}$ with $sin^2\psi$ exhibits oscillatory behaviour (Fig. 1.7c).

1.8 Strain Measurement Using Neutron Diffraction

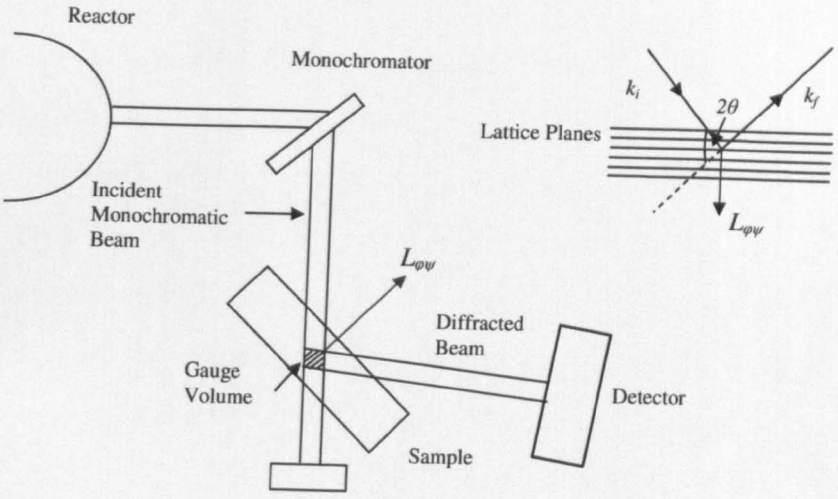

Fig. 1.8 The principles of strain measurement at a typical reactor source

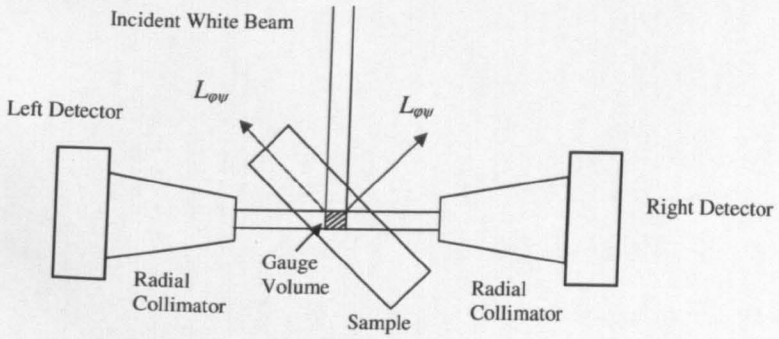

Fig. 1.9 The principles of strain measurement at a time of flight source, showing the definition of gauge volume sampled and the direction of strain measured.

As neutrons can penetrate into many materials to a large distance (>3-4 cm) unimpeded, they make a suitable choice for strain measurement within the bulk of the materials. Using neutron diffraction the residual strain within the engineering materials of interest can be measured in two ways:

(a) at a nuclear reactor source (Fig. 1.8)

(b) at a time of flight source (Fig. 1.9)

At a nuclear reactor source, the white beam from the reactor is first monochromated to a desired wavelength λ utilising the Bragg reflection from a large single crystal monochromator [25]. A Soller slit collimator is used to define the direction of the monochromated beam. A Soller slit assembly is again used to define the direction of the scattered beam. The neutrons scattered through an angle 2θ are counted by the detector. The area of the beam incident on the sample and entering the detector is defined by horizontal and vertical apertures in a neutron absorbing cadmium mask. However at a time of flight source a white beam of neutrons is directly incident on the sample. Therefore neutrons of different energies (and hence wavelengths) are incident on the sample and a complete diffraction spectrum can be recorded.

The intersection of the incident and scattered beam defines the gauge volume or the volume sampled by the diffractometer.

Cones of diffracted neutrons at angles $\varphi_{hkl} = 2\,\theta_{hkl}$ about the incident beam are generated by polycrystalline materials. Bragg's law provides these angles:

$$2d_{hkl}\sin\theta_{hkl} = \lambda \qquad (1.17)$$

where d_{hkl} is the lattice spacing of planes with Miller indices *hkl*. Only those crystallites or grains in the sample which satisfy Bragg's law and which are oriented so that the planes are at an angle θ to the incident beam generate the cones of scattering. A scattering vector $L_{\varphi\psi} = k_i - k_f$ can be defined where k_i and k_f are the incident and scattered neutron wavevectors, of magnitude

$$|k| = 2\pi/\lambda \qquad (1.18)$$

If λ is held constant, differentiating Bragg's law gives for a given reflection,

$$\Delta d/d_0 = -\cot\theta\Delta\theta \qquad (1.19)$$

which means that a small lattice strain $\varepsilon = (d - d_0)/d_0 = \Delta d/d_0$ will give rise to a change (shift) in scattering angle for diffraction [26]. From the measured change in the scattering angle $\Delta\theta = -\varepsilon \tan\theta$ the strain ε can be determined.

An extremely good instrumental resolution is required for measurement as the strains due to the internal stresses are small, typically $\Delta d/d \approx 10^{-3} - 10^{-4}$ [27]. The instrumental resolution ($\Delta d/d$) which is defined by the full width at half maximum (*FWHM*) at a conventional angle dispersive diffractometer is given by the sum of two contributions:

- From the uncertainty in wavelength ($\Delta\lambda$) which arises from the collimation angle ($\Delta\theta$) of the beam from the neutron monochromator.
- The accuracy with which the diffracting angle may be measured ($\Delta\theta$).

$$[\Delta d/d]^2 = [\Delta\lambda/\lambda]^2 + [\cot\theta\,\Delta\theta]^2. \qquad (1.20)$$

It is highly desirable that the sensitivity, defined as an appropriate fraction of ($\Delta d/d$) be of the same order or less than the minimum strain to be measured.

To calculate the absolute strain it is essential to know the lattice spacing d_0 of the unstrained material. The lattice strain has been defined as the relative difference between two lattice spacings. Therefore it becomes necessary to make two sets of measurements; one on the stressed sample and another on the stress-free reference sample of the same material [28]. Special care must be taken when choosing the stress-free reference sample in order to avoid the systematic errors which may be caused by an incomplete stress relief within the reference sample, by changing the chemical or structural composition or by changes in the ambient temperature during measurement.

Annealing can be used to make a reference sample stress free and this is the most widely used solution to the d_0 problem [29]. However this simple solution doesn't work in all cases. Multiphase materials usually retain considerable phase specific

stresses after the annealing procedure due to differences in the thermal expansion. Also the sample may contain chemical gradients so that the d_0 varies accordingly. In this case, before the annealing process, it may be necessary to sample the reference section and then determine d_0 at various parts of the sample. In those cases where the chemical gradient is produced by rapid quenching even the section and anneal procedure fails as the chemical composition is altered by the annealing process. As an example martensite will be converted to a mixture of ferrite and cementite. In such a case the d_0 has to be estimated from an analysis of the microstructure or other quantities such as micro-hardness.

The direction of the scattering vector $L_{\phi\psi}$ is that of the strain being measured. For diffraction peak to be observed there must be a sufficient number of crystallites present in the sample with (*hkl*) planes perpendicular to the direction in which the strain is to be measured.

At a time of flight source [30] a white beam of neutrons containing a range of wavelengths is incident upon the sample and the strain can be determined by using the following relations,

$$\varepsilon = \Delta\lambda / \lambda = \Delta t / t \qquad (1.21)$$

where $t = L/v = (\lambda m/h)L$ is the time taken for the neutron with mass m and velocity v to traverse a path length L and h is Planck's constant. A complete diffraction spectrum (Fig. 1.10) can be recorded.

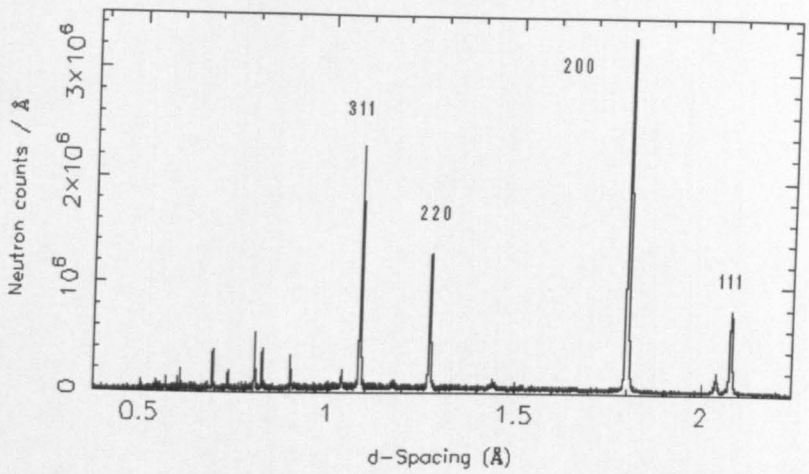

Fig. 1.10 An example diffraction spectrum obtained from stainless steel weld metal at a time of flight source. Major austenite peaks are labelled.

Using neutron diffraction, measurements in six orientations are required to define the strain tensor at a point completely inside the structural member. If the principal stress directions are known, measurement of the strain in these three orientations is sufficient to determine the stress state of the material at a given location in the material [31]. Measurement time can be reduced by assuming principal stress directions as neutron stress measurements are usually time consuming. If the principal strain axes are known, the sample coordinate system can be attached to the sample so as to coincide with them. The shear strain components ε_{12}, ε_{13} and ε_{23} will then be zero and the principal strains ε_1, ε_2 and ε_3 will correspond to strains ε_{11}, ε_{22} and ε_{33} respectively and can be determined by measuring $\varepsilon_{\varphi\psi}$ at (φ, ψ) equal to (0, 90), (90, 90) and (0, 0) [32].

There might be a possibility that the principal strain (stress) directions are not in the directions assumed so that the shear strain components in the sample coordinate system have non-zero values. The shear strain components make no contribution to the measured strain $\varepsilon_{\varphi\psi}$ at the tilts (0, 90), (90, 90) and (0, 0). Thus, in measuring strains in these directions one correctly measures these strain components no matter

what the values of the shear strains. However a possible error arises in assuming these components as principal strains, ε_i, rather than the components ε_{ii}. If the shear stresses are not zero the principal stresses will not be along three sample coordinate system axes but will instead be in some other direction depending upon the values of the shear strain components.

1.9 Structure Refinement using the Rietveld Method

The Rietveld method [33, 34] of profile analysis is a crystal structure refinement technique which utilises least-squares fitting of the diffraction profile. Several factors such as neutron spectral distribution, the monochromator mosaic distribution, the transmission functions of the Soller slits, and the sample shape and crystallinity affect the measured profile of a single powder diffraction peak. An almost exactly Guassian peak shape is produced by the convolution of these factors.

The contribution of a Bragg peak to the measured profile y_i at position $2\theta_i$ can be written as:

$$y_i = tS_k^2 j_k L_k \frac{2\sqrt{\ln 2}}{H_k\sqrt{\pi}} \exp[-4\ln 2\{(2\theta_i - 2\theta_k)/H_k\}^2] \qquad (1.22)$$

where

t = step width of the counter

$S_k^2 = F_k^2 + J_k^2$, the sum of the nuclear and magnetic contributions respectively

j_k = the multiplicity of the reflection

L_k = the Lorentz factor

$2\theta_k$ = the calculated position of the Bragg peak corrected for the zero point shift of the counter.

H_k = full width at half height

Putting $I_k = tS_k^2 j_k L_k \frac{2\sqrt{\ln 2}}{H_k\sqrt{\pi}}$ and $b_k = 4\ln 2 / H_k^2$, equation (1.22) can be simplified to

$$y_i = I_k \exp[-b_k\{(2\theta_i - 2\theta_k)^2 \tag{1.23}$$

Introducing peak asymmetry parameter P

$$y_i = I_k \exp[-b_k\{(2\theta_i - 2\theta_k)^2][1 - P(2\theta_i - 2\theta_k)^2 s/\tan\theta_k\} \tag{1.24}$$

where s = +1, 0, -1 depending on the difference $2\theta_i - 2\theta_k$ being positive, zero or negative respectively.

The intensity correction for preferred orientation can be written as

$$I_{corr} = I_{obs} \exp(-G\alpha^2) \tag{1.25}$$

where α is the acute angle between the scattering vector and the normal to the crystallites. G is the preferred orientation parameter and is a measure for the half width of the assumed Gaussian distribution of the normals about the preferred orientation direction.

Equation (1.24) can also be written as

$$y_i = w_{i,k} S_k^2 \tag{1.26}$$

where

$$w_{i,k} = tj_k L_k \frac{2\sqrt{\ln 2}}{H_k\sqrt{\pi}} \exp[-b_k\{(2\theta_i - 2\theta_k)^2][1 - P(2\theta_i - 2\theta_k)^2 s/\tan\theta_k\}$$

$w_{i,k}$ is a measure of the contribution of the Bragg peak at position $2\theta_k$ to the diffraction profile y_i at position $2\theta_i$.

In the case of peak overlap

$$y_i = \sum_k w_{i,k} S_k^2 \tag{1.27}$$

where the summation is over all reflections which can theoretically contribute to y_i on the basis of their position $2\theta_k$ and their halfwidth H_k.

By writing

$$S_k^2 = (F_k^2 + J_k^2)\exp[-2Q\sin^2\theta_k / \lambda^2 + G\alpha_k^2] \qquad (1.28)$$

Q is here the overall isotropic temperature factor.

The least squares parameters can be divided into two groups. The first group, the profile parameters define the positions, the halfwidths, and the possible asymmetry of the diffraction peaks in addition to a property of the powder sample i.e. preferred orientation.

The second group, the structure parameters, define the contents of the asymmetric unit cell.

In the least squares refinement the function *M* has to be minimised with respect to the parameters and in the case of profile refinement

$$M = \sum_i W_i \left\{ y_i(obs) - \frac{1}{c} y_i(calc) \right\}^2 \qquad (1.29)$$

where

$\sum_i$ = the sum over the independent observations.

1.10 Examples: (Residual Stress Measurement Using Neutron Diffraction)

It is the residual stress which is important from the structural integrity point of view. Diffraction based techniques are very effective for measuring residual stresses within engineering components. However, the diffraction based stress measurement techniques measure the strain and the stress has to be calculated from the measured strain by using appropriate value of the Young's modulus. Therefore, it is very important that the texture and anisotropy of the material must be considered in order to have an accurate value of the Young's modulus. Some of the materials of the

engineering interest such as the welds can be highly anisotropic and one must be very careful while converting the measured strains to stresses.

Spooner [35] investigated the residual stresses in two multi-pass welds (14 weld passes) in type 304 stainless steel plates using neutron diffraction. The plates were 25 mm thick. Type 308 stainless steel was used as a filler metal. The welding process used was semiautomatic hot-wire gas tungsten arc welding process. One of the welds was made by depositing weld metal while the weld assembly was vibrated at a frequency below the resonant frequency. This was done in order to evaluate the effect of vibratory stress relieving. The (111) and (200) reflections from the austenitic weld were measured.

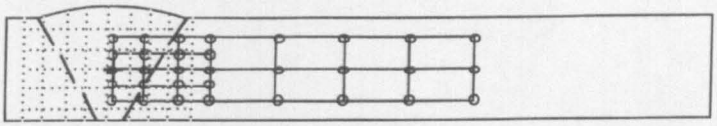

Fig. 1.11 Diagram of a transverse section of a welded plate showing the location of the sampling grid on a section through the middle of the welded plate [35].

The difference between the lattice parameters within the weld zone and the base metal was used to correct the strain obtained in the diffraction measurement of strain. Lattice strains were measured on a grid of points on the transverse section of the weldment shown in Fig. 1.11.

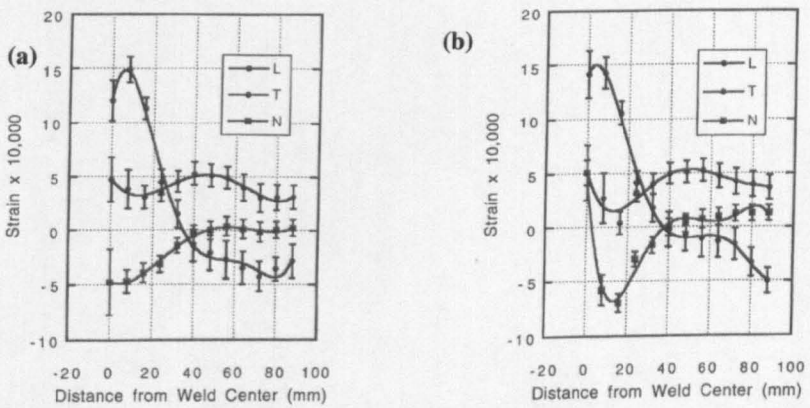

Fig. 1.12 (a) the corrected strains in the as welded plate (b) the strains in the plate with the vibration treated weld. L, N and T stand for longitudinal, transverse and normal [35].

The weld metal composition was slightly different from the base metal and could contain up to 9% of ferrite. The lattice parameter variation due to composition was corrected in the measured strains as an effective compressive strain error. The measured residual strains are shown in Fig. 1.12. The longitudinal strains decreased rapidly from high tensile values to relatively large compressive strains in the base metal. Over the base metal of the welded plate the normal and transverse strain components were observed to vary very little.

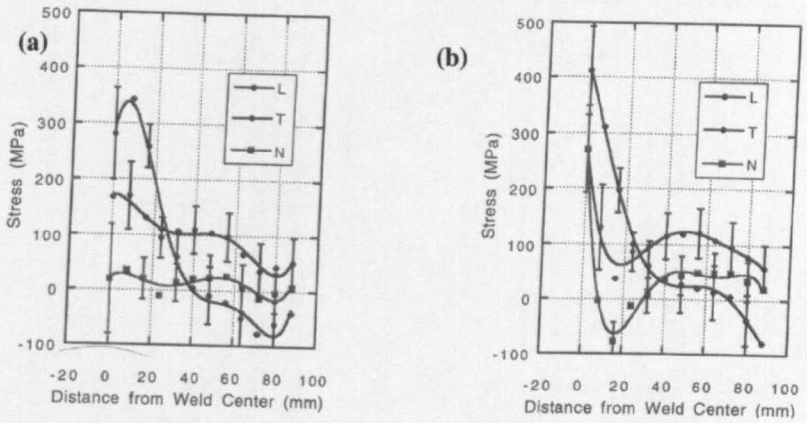

Fig. 1.13 (a) The stresses in the as welded plate (b) The stresses in the plate with the vibration treated weld. L, N and T stand for longitudinal, transverse and normal [35].

The residual stress distribution without vibratory treatment and with vibratory treatment is shown in Fig. 1.13. The longitudinal tensile stresses peak in the fusion zone and in the HAZ. The stresses become small and compressive at distances beyond 40 mm from the weld center line. The residual stresses exhibit small differences in the conventionally welded plate and in the vibratory treated plate.

Carr et al [36] investigated the residual stress distribution in a zircaloy-4 weld using neutron diffraction. The residual strains were measured in a Zr-4 butt weld in the as welded condition using time of flight neutron diffraction. Tungsten inert gas welding was used to prepare the weld. The Zr-4 material was hot rolled and annealed and the thickness of each plate was 8.6 mm. The rolling direction in the plate was kept

parallel to the weld longitudinal direction. For d_0 measurement the coupons were cut from a companion weld to the intact weld. In the coupons the macroscopic stress field was destroyed and the corresponding strain was absent. The strain corresponding to the macroscopic weld stress for each reflection is given by the difference between the lattice spacing of the intact weld and and the coupon at the same location. Fig. 1.14 shows the weld setup geometry.

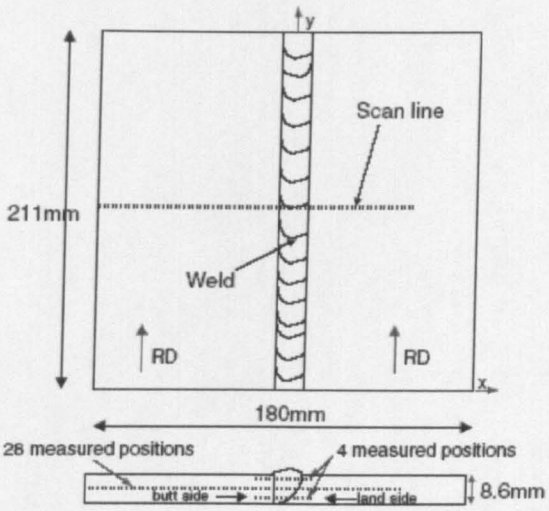

Fig. 1.14 Schematic of the weld and experimental setup [36].

Fig. 1.15 shows the variation of the macroscopic longitudinal strain as a function of position through the weld at the mid thickness of the plate for all accessible reflections.

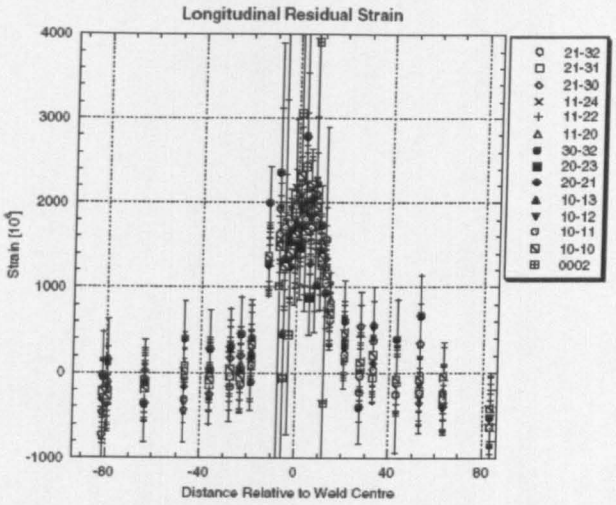

Fig. 1.15 Variation of the longitudinal strain across the weld for all the accessible reflections at the mid thickness of the plate [36].

Similar behaviour is exhibited by all reflections in the Fig. 1.15 to within the experimental uncertainty. The variation of the longitudinal, transverse and normal residual stresses determined by fitting ≈20 reflections in each of the three sample directions, as a function of position across the weld at mid thickness of the plate is shown in Fig. 1.16.

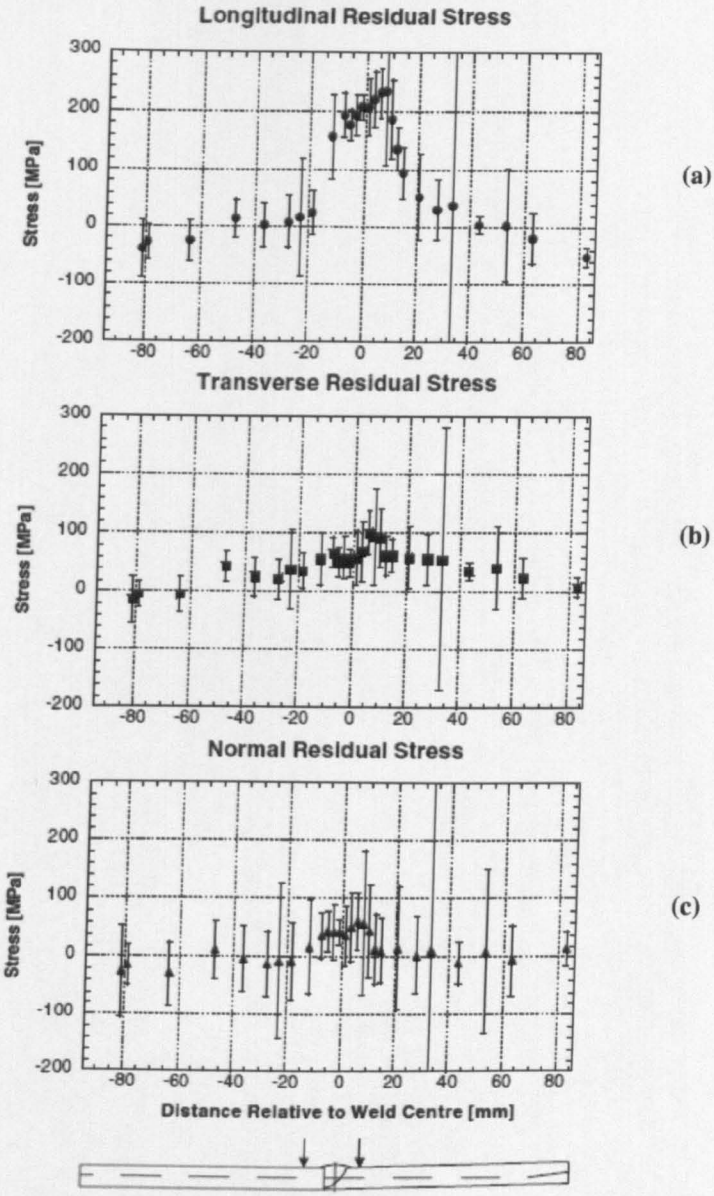

Fig. 1.16 Variation of (a) longitudinal (b) transverse and (c) normal stress across the weld at mid thickness of the plate [36].

Todd et al [37] investigated the inter-phase and inter-grain residual stresses in alumina/SiC nano-composites using neutron diffraction. Alumina/SiC nano-composites are structural ceramics in which an alumina matrix contains a dispersion

of fine SiC particles. Residual stresses are generated during cooling from processing temperatures because of the thermal expansion mismatch between the SiC particles and the alumina matrix. These are referred to as inter-phase stresses. Those residual stresses which arise from the mutual constraint of the grains during changes in the grain shape in a polycrystal are referred to as inter-grain stresses. Hot pressed discs were used for neutron diffraction. For reference specimens a monolithic alumina disc and the as received SiC powder was used.

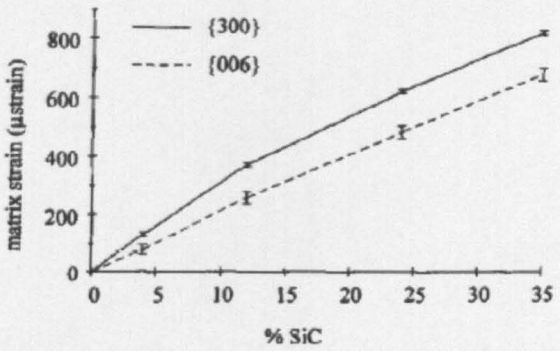

Fig. 1.17 Measured strain in the alumina matrix normal to the plane of the hot pressed discs [37].

Fig. 1.17 shows the average strains, ε_{hkl}, measured normal to the plane of the disc using the {300} and {600} reflections.

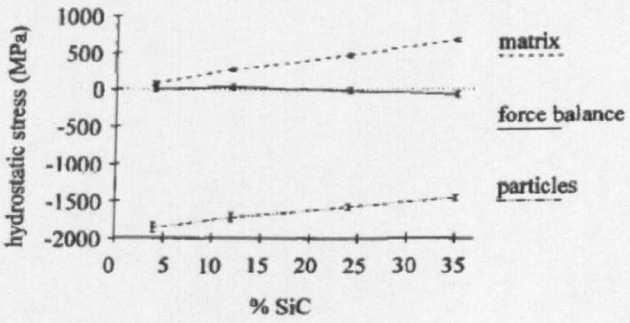

Fig. 1.18 Average hydrostatic stress measured in matrix, particles and composite as a whole ("force balance") as a function of SiC content [37].

The volume averaged strains in both the matrix and the particles were expected to be hydrostatic for isotropic conditions with spherical particles. The hydrostatic strain in

the matrix/particles was calculated from the mean strains measured parallel and perpendicular to the plane of the disc. The calculated hydrostatic stresses are shown in Fig. 1.18 which shows that in the SiC particles high pressures approaching 2 GPa were present. The tensile hydrostatic stresses in the matrix increase with SiC content from 80 MPa for f = 0.04 to 680 MPa for f = 0.35, where f is the fraction of SiC. The requirement that equilibrium is maintained between the forces in the two phases demands that the sum of hydrostatic stresses in both the phases should be zero. This provided an essential check on the suitability of the reference specimens. This force balance is also plotted in Fig. 1.18 and is zero to within two standard deviations. Stacey et al. [18] measured the residual stresses in thick walled tubing in the as manufactured condition and after autofrettage, using neutron diffraction. The tube material investigated was a high strength low-alloy steel designated as 4333 M4. The nominal bore diameter was 30 mm, and the outside diameter 62 mm. The tubing was supplied in the hot rolled and cold reduced conditions. A section of the tubing was autofrettaged to a pressure of 662 MN/m^2 to cause yielding from the bore to approximately half way through the wall. During the autofrettage process the tubing was not loaded axially and plane stress conditions prevailed.

The hoop and radial strains determined from the shifts in the 211 peak are presented in Fig. 1.19. The data have been plotted as a function of radial distance from the bore, *r*, normalised with respect to the wall thickness, *W*. The radial strain is found to change from positive at the bore to negative at mid-wall position to almost zero near the outer diameter. The residual strain distribution for the as received ring is shown in Fig. 1.20

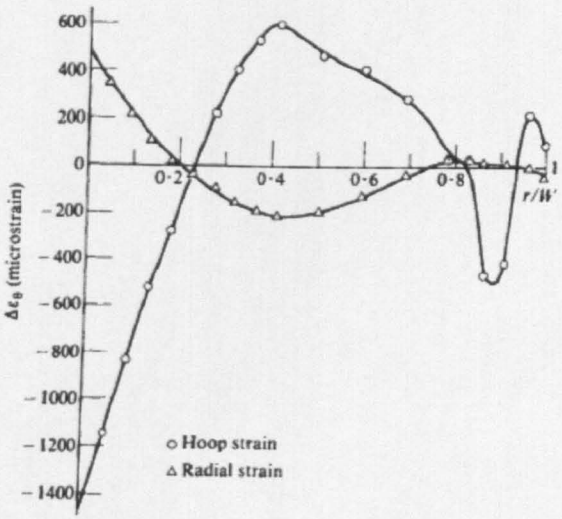

Fig. 1.19 Hoop and radial strains in the 5 mm thick autofrettaged sample obtained using neutron diffraction [18].

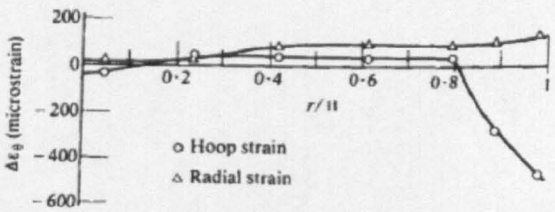

Fig. 1.20 Hoop and radial strains in the 5 mm thick as received sample obtained using neutron diffraction [18].

Except near the outside little strain is present. The compressive hoop strain measured at the outside is a result of the tubing manufacturing procedure.

1.11 Texture in Materials

This section provides details about the fundamentals of texture analysis. The experimental techniques used to measure crystallographic texture e.g. EBSD and neutron diffraction are also discussed. A literature review related to recrystallization texture has been carried out.

1.11.1 Definition of Texture

The texture of a polycrystalline, single phase material is defined by the orientation distribution function (ODF) of the constituent crystallites of the material [38]. This function is assumed to be the volume fraction of the crystallites having a crystallographic orientation 'g' with reference to a fixed sample coordinate system. This general definition of texture neither includes any information about the size, shape, and arrangement of the grains nor takes into account the possible presence of any lattice defects within the grains.

1.11.2 Definition of an Orientation

In a polycrystalline material, in order to specify an orientation g of a grain, a crystal coordinate system has to be chosen in each crystal. It consists of three deliberately chosen, mutually perpendicular crystal directions, which are the same in each crystal. (In cubic crystals these are the three cubic axes).

A sample coordinate system K_A has to be defined consisting of three prominent sample directions (in a rolled sheet these are the rolling (RD), the transverse (TD) and the normal (ND) directions) (Fig. 1.21).

The crystal orientation within a polycrystalline sample is then defined by the rotation g which transforms the sample fixed coordinate system K_A into the crystal fixed coordinate system K_B [39].

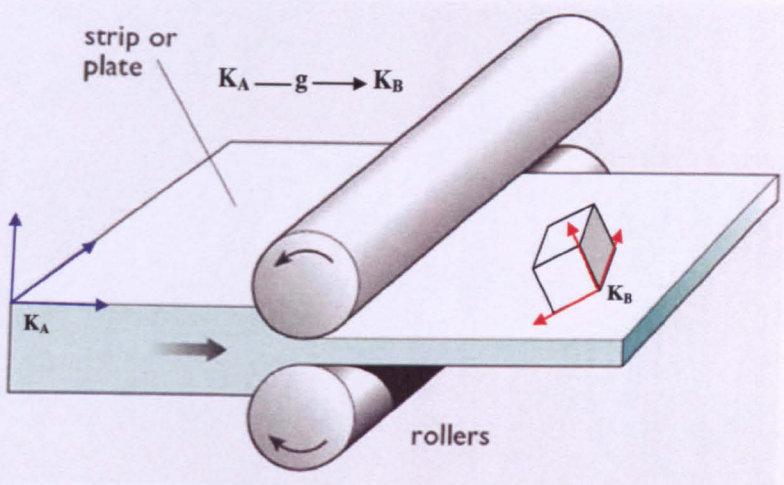

Fig. 1.21 Orientation 'g' of crystal coordinate system K_B with reference to the sample coordinate system K_A [40].

There are many ways in which a rotation g can be specified and hence the orientation distribution function is represented. The most important methods are described below:

Using the Euler angles:

$$g = \{\varphi_1, \phi, \varphi_2\} \tag{1.30}$$

Specifying an orientation by means of an orientation matrix,

$$g = [g_{ij}], \quad g_{ij} = \cos\langle x_i x'_j \rangle$$

The orientation matrix consists of the direction cosines of the axes x_i of the crystal coordinate system K_B with reference to the direction cosines x_j of the sample coordinate system K_A.

Specifying the Miller indices (*hkl*), of the crystallographic plane, parallel to the rolling plane and the indices [*uvw*] of the crystal direction parallel to the rolling direction.

$$g = (hkl)[uvw]$$

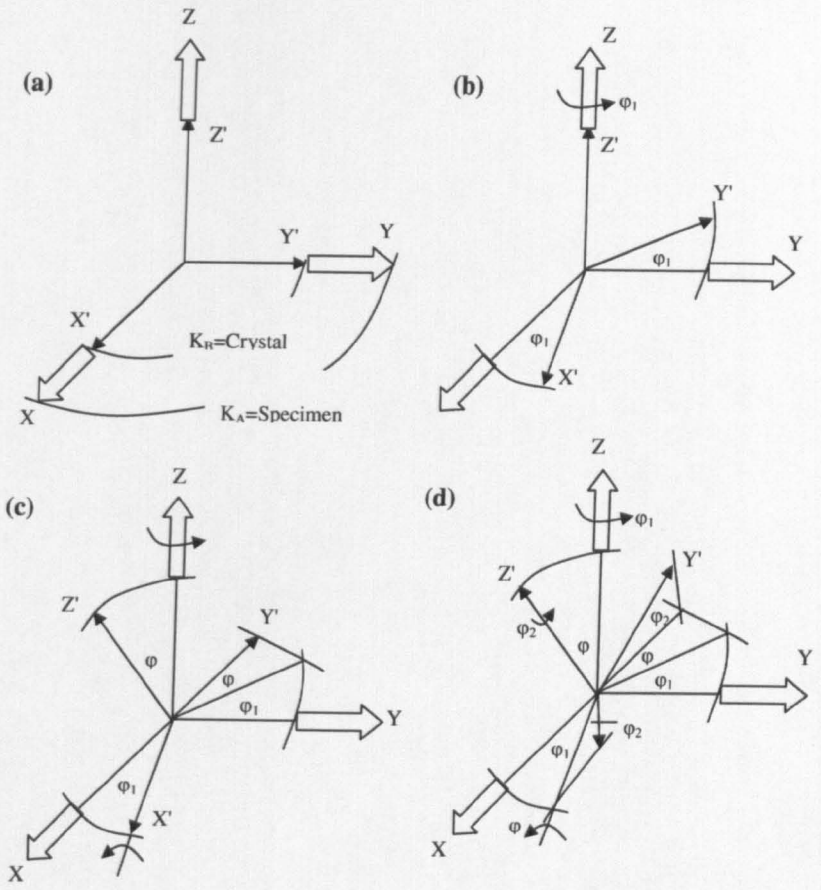

Fig. 1.22 The definition of the Euler angles φ_1 φ φ_2: (a) the crystal coordinate system K_B lies parallel to the sample coordinate system K_A (so called cube orientation); (b) the crystal coordinate system is rotated about the Z'-axis through the angle φ_1; (c) the crystal coordinate system is rotated with respect to the orientation (b) around the X'-axis through the angle φ; (d) the crystal coordinate system is rotated with respect to the orientation (c) around the Z'-axis through the angle φ_2 [39].

The texture of a polycrystalline material is most often described by a three dimensional orientation distribution function represented in terms of the Euler angles:

$$\frac{dV}{V} = f(\phi_1, \varphi, \phi_2)\frac{\sin\varphi}{8\pi^2} d\varphi\, d\phi_1\, d\phi_2 \qquad (1.31)$$

Where the factor sin φ represents the size of the volume element in the orientation space and the factor $8\pi^2$ takes care of the usual normalisation of the texture function in multiples of the random orientation density.

1.11.3 Measurement of Texture

The texture function represented by equation (1.31) cannot be measured directly [41]. It has to be constructed from pole figure measurements followed by pole figure inversion. Pole figure inversion can be achieved by the series expansion method. Pole figures can be measured by one of the following methods:

(a) Electron diffraction.

(b) Neutron diffraction.

As the neutrons can probe into the bulk of the material, they are suitable for global texture measurements. Also specimen surface preparation is not necessary in neutron diffraction texture measurements. Electron diffraction can be used for measuring local texture. However in the case of texture measurement by electron diffraction a mirror finish is required on the specimen surface in order to obtain a good diffraction pattern.

1.11.4 Texture Measurement using Electron Diffraction

Electrons can be diffracted from a periodic crystal lattice owing to their wave nature [42]. The diffracted beams are produced after the interaction of the electrons with the periodic lattice and using the relation $\lambda = h/mv$, where λ is the wavelength of the electrons, h is Planck's constant and mv is the momentum.

A highly evacuated container is required for electron diffraction in which a collimated stream of electrons is accelerated through a constant potential and strikes a specimen. The diffraction pattern can be recorded photographically or viewed on a fluorescent screen.

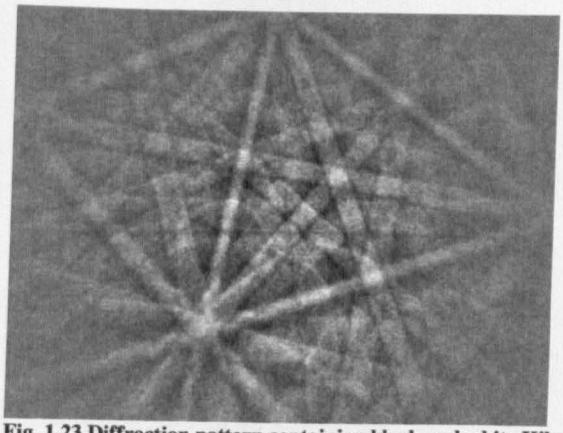

Fig. 1.23 Diffraction pattern containing black and white Kikuchi lines from stainless steel weld metal.

Black and white lines called Kikuchi lines appear on the diffraction pattern. A typical diffraction pattern containing black and white Kikuchi lines from stainless steel weld metal is shown in Fig. 1.23. Kikuchi lines are formed by those electrons which are diffusely scattered with some loss of energy. Some of these diffusely scattered electrons are reflected from some crystal planes. A set of parallel reflecting planes in a crystal is represented by AB and $A'B'$ in Fig. 1.24. Diffusely scattered electrons that would have followed the path OP are reflected to P', while the scattered ray OQ is reflected to Q'.

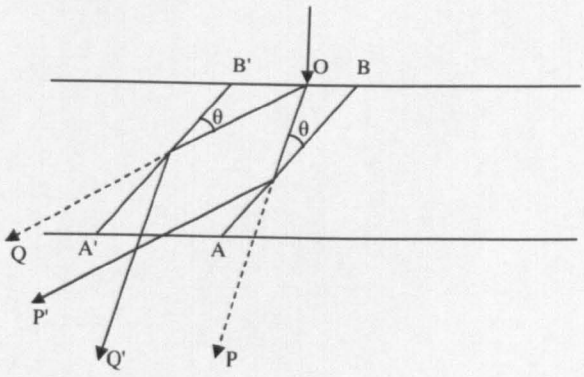

Fig. 1.24 Origin of Kikuchi lines [42]

1.11.5 EBSD Texture Analysis

The general experimental set-up for an EBSD texture experiment is shown in Fig. 1.25 [43].

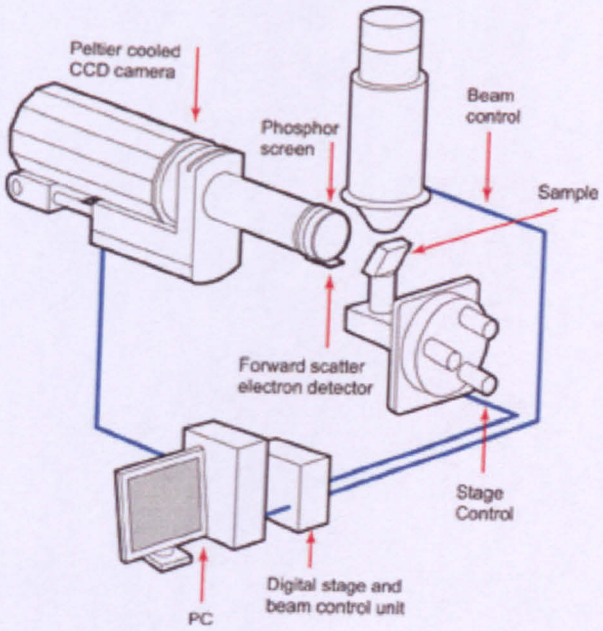

Fig. 1.25 The experimental set-up for EBSD [35]

In an EBSD texture experiment the local orientations in a polycrystalline material are measured by analysing electron back scattering Kikuchi diffraction patterns [44]. The polycrystalline sample is mounted in a scanning electron microscope so that its surface normal is tilted 70° away from the incident electron beam. A highly collimated beam is directed on to the sample. Backscattered electrons are diffracted off a small volume of the sample on to a phosphor coated viewing screen which has been mounted on the microscope chamber. Photons are emitted when the diffracted electrons collide with the phosphor screen. This image is transmitted in to a computer by a high gain video camera. The crystallographic planes in the sample are represented by bands in the diffraction pattern. Crystallographic directions are denoted by the intersections of these bands (zone axes). The orientation of the

crystallite can be determined by identifying the miller indices and the location of the zone axes in a back scattered Kikuchi diffraction pattern.

1.11.6 Texture Measurement by Neutron Diffraction

Neutron diffraction texture measurement involves pole figure measurement based on Bragg's law for diffraction of radiation from the crystal planes [45]. Consider Bragg diffraction from a single crystallite (Fig. 1.26a) which is irradiated with monochromatic radiation and a detector is set at angle 2θ with respect to the incident beam. There will be no diffraction in this case as the *hkl* planes are not parallel to the sample surface.

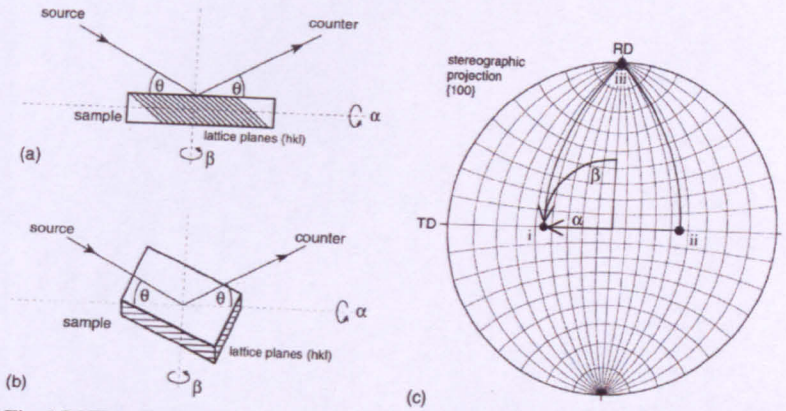

Fig. 1.26 The effect of sample rotation and diffraction from hkl planes. (a) untilted position ($\alpha = \beta = 0°$); (b) sample tilted to satisfy the Bragg condition ($\alpha > 0°$, $\beta > 0°$); (c) diffraction peaks of a Goss {111}<100> oriented crystal in the stereographic projection (i) $\alpha = 45°$, $\beta = 90°$ (ii) $\alpha = 45°$, $\beta = 270°$ (iii) $\alpha = 90°$, $\beta = 0°$ [45].

The sample has to be rotated and/or tilted until the *hkl* planes are in the diffraction condition (Fig. 1.26b). When a Goss (i.e. {110} <100>) oriented crystal (Fig. 1.26c) is irradiated at the Bragg angle for the (200) planes, diffraction peaks will be obtained for a sample tilt of 45° plus an additional rotation by either 90° or 270°.

In order to determine the orientation of crystals the sample is systematically rotated in a texture goniometer (Fig. 1.27) through three angles $\omega\chi\varphi$ in such a way that all possible lattice planes are successively brought into the diffraction condition and the diffracted intensities are recorded as a function of these rotation angles. The pole figure angles α (radial) and β (azimuthal) are directly related to the rotation angles and the diffracted intensities can be represented in a pole figure.

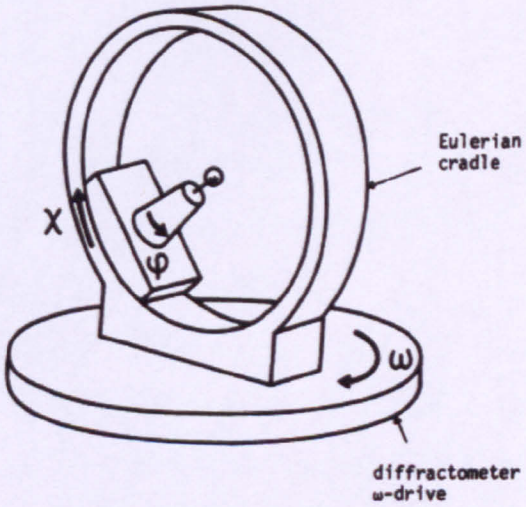

Fig. 1.27 Principle of pole figure measurements using an Eulerian cradle [46].

Pole figures are the direction distribution functions of specific crystal directions *h*, perpendicular to diffracting lattice planes (*hkl*)

$$\frac{dV}{V} = P_{hkl}\, y(dy); \quad \begin{cases} y = \{\alpha, \beta\} \\ dy = \sin\alpha \, d\alpha \, d\beta \end{cases} \tag{1.32}$$

where the orientation of the crystal direction h with reference to the sample coordinate system is described by two orientation parameters which may be the spherical polar

coordinates α, β [47]. dV/V is the volume fraction of crystals whose direction h is parallel to the sample direction y.

For the present work neutron diffraction texture measurements were performed at the Stress-Spec instrument of the FRM II research reactor, Munich.

The scans were performed with steps of 5° each for χ and φ.

The following pole figures were obtained for the austenite phase:

experimental: {200}, {111}, {311}{220}

The following pole figures were obtained for the ferrite phase:

experimental: {211}{110}

recalculated: {200}

1.11.7 Recrystallization Texture

Preferred orientations or textures characteristic of the mode of deformation, e.g. rolling, drawing etc are exhibited in a deformed polycrystalline aggregate [48]. Preferred orientations even stronger than the deformation textures are observed when such an aggregate is annealed.

The preferred orientations may arise from:

- In the deformed grains the dislocations are rearranged.
- In the deformed grains recrystallization (primary recrystallization) takes place.
- In the recrystallized grains there is subsequent growth of selected grains. Only a few grains are involved in the grain growth process and a coarse-grained structure results. This phenomenon has been called secondary recrystallization.

Amongst metals of the same crystal structure there are many kinds of recrystallization textures. When the annealing conditions are changed often one metal will have different textures. In a single sample two textures may co-exist.

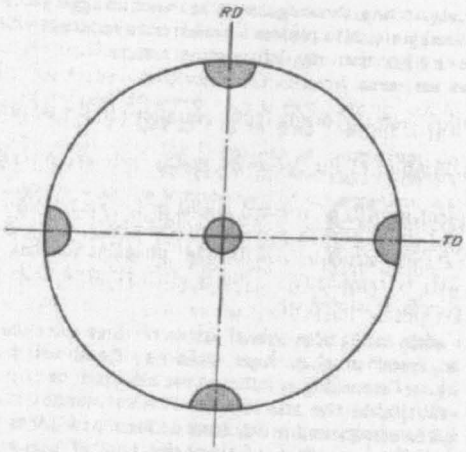

Fig. 1.28 {100} pole figure for an iron-50 wt percent nickel alloy rolled heavily followed by annealing at 1100° C. Cube texture [48].

A cube texture {100} <001> is the best example of a sharp recrystallization texture which is obtained in many face-centred cubic metals on recrystallization after the cold rolling of sheet material. In its extreme form the individual recrystallized grains are so closely oriented to the ideal orientation (Fig. 1.28) that the material resembles a single crystal. The distribution of orientations can be very sharp which is evident from the pole figure obtained from X-ray data. In the case of cube texture all the crystals are oriented in a way that a cube face lies nearly parallel to the plane of the sheet and a cube edge points approximately in the rolling direction. Then the transverse direction is also approximately a cube edge direction (Fig. 1.29).

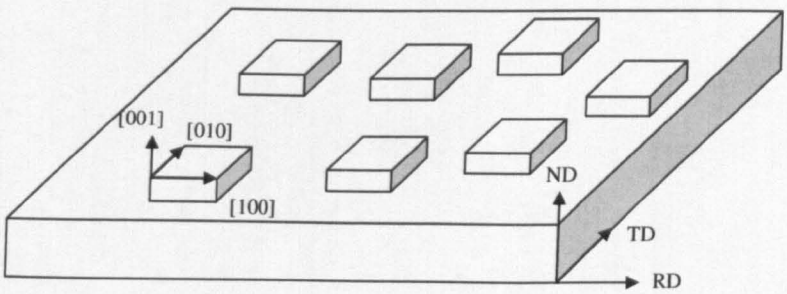

Fig. 1.29 Schematic representation of the cube texture in a sheet (ND, TD and RD stands for normal, transverse and rolling direction) [39].

Sindel et al [49] investigated heavily rolled coarse grained copper. A plate of 99.995% Cu was prepared to have a thickness of 17 mm and grain size 50 μm. The plate was rolled homogeneously on a two high mill to 95% reduction using paraffin lubricant and cooling between each pass. Annealing was carried out in an oil bath to 250° C.

Rolling Texture: Typical "copper type" rolling texture (Fig. 1.30 and Fig. 1.31) has been observed in the pole figure and corresponding true ODFs derived from the sheet surface in 50 μm grain sized copper after rolling 95%.

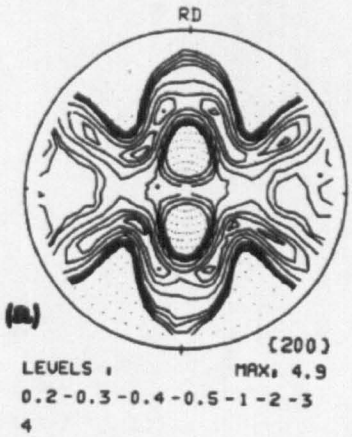

Fig. 1.30 {200} pole figure of cold rolled copper, 50 μm, cold rolled 95% [49].

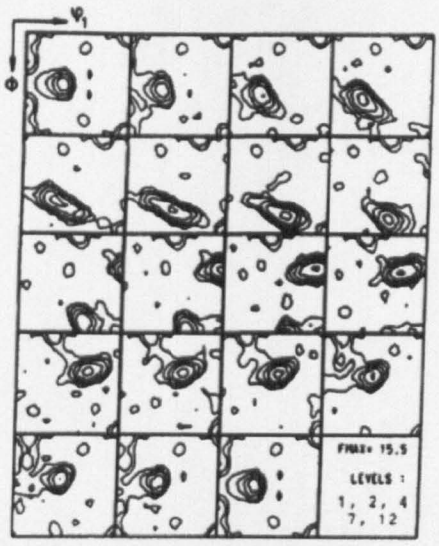

Fig. 1.31 ODFs of 50 μm grain sized copper after rolling to 95% reduction (from longitudinal sections) [49].

Annealing Texture: Very strong cube texture (Fig. 1.32 and Fig. 1.33) was observed in 50 μm grain size copper. After rolling 95% and annealing of 250°C the maximum intensity of {001} <100> in the ODF deduced from longitudinal section measurements reaches 85R (in multiples of times random intensity). In the {200} pole figure this corresponds to the level of 37R.

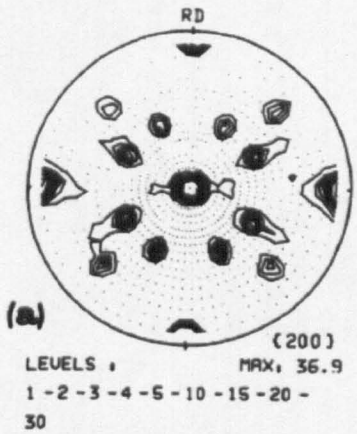

Fig. 1.32 {200} pole figure of fully annealed copper, 50 μm, colled rolled 95% [49].

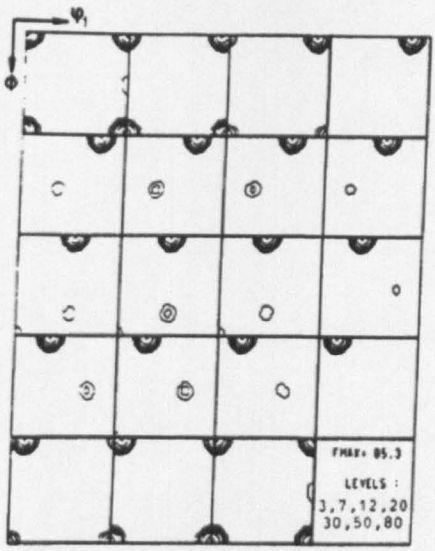

Fig. 1.33 ODFs of 50 μm grain sized copper after rolling 95% and full annealing at 250° C (from longitudinal sections) [49].

1.11.8 Crystallographic Orientation Relationship (OR)

In certain processes e.g. precipitation from solid solution, the martensitic transformation, epitaxial growth and solidification the crystallographic orientation relationship (OR) between two phases with different crystal structures is an important parameter affecting microstructure-property relationships [50]. In the solidification microstructures an OR between two phases is often found where the relationship is established either during solidification or during subsequent solid state transformation during cooling. For example the weld microstructures of austenitic stainless steels usually contain about 2% to 10% delta ferrite. Whether or not an OR is established between delta ferrite and austenite depends upon composition and solidification/cooling conditions. For bcc and fcc lattices Kurdjumov-Sachs and Nishiyama-Wassermann OR have been proposed. An OR is described by a set of planes that are parallel in the two lattices and a set of directions within those planes that are parallel.

Table 1.1 Summary of bcc-fcc orientation relationships [50].

Name	Orientation Relationship
K-S	$(111)_{fcc}$ //$(110)_{bcc}$, $[\bar{1}10]_{fcc}$ //$[\bar{1}11]_{bcc}$, $[11\bar{2}]_{fcc}$ //$[\bar{1}1\bar{2}]_{bcc}$
N-W	$(111)_{fcc}$ //$(110)_{bcc}$, $[\bar{1}01]_{fcc}$ //$[001]_{bcc}$, $[\bar{1}2\bar{1}]_{fcc}$ //$[\bar{1}10]_{bcc}$

Weld texture of 316L stainless steel weldment was also investigated by G Bouche et al [51]. In the weld microstructure, thin dendrites of δ-ferrite were observed between the columnar grains of γ-austenite matrix. Texture of both phases was investigated using neutron diffraction for global texture and and local orientation mapping using EBSD. Neutron diffraction results (Fig. 1.34) showed a fiber like texture <100> and γ- δ pole figures were very similar.

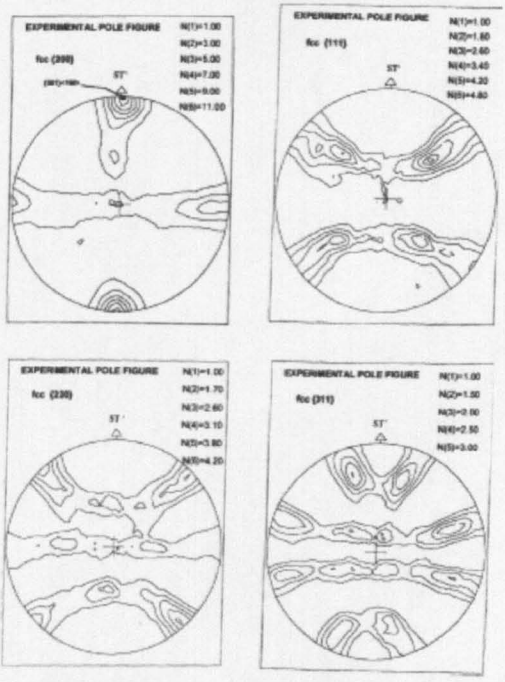

Fig. 1.34 Pole figures obtained for austenite by neutron diffraction analysis [51].

The growing direction of the grains <100> was found to be parallel to transformed normal direction (the pole figures were tilted to have the growing direction of the

grains perpendicular to the pole figure). By tilting the pole figures the exact angular deviation α between the <100> direction of solidification and the normal direction of the sample was calculated. It was observed that on the macroscopic scale the phases were not in a classical orientation relationship like Kurdjumov-Sachs or Nishiyama-Wassermann but more in a cube-cube one. EBSD results also confirmed that the γ/δ relationships were not always described by the classical KS or NW relationships, and that for the δ located at the low angle boundaries most of them were very near (within a 10° scatter) a cube-cube orientation, whereas in the high angle boundaries more γ/δ misorientation relationships were described by the KS relationships, but only one side of the grain.

1.12 In-situ Deformation of Materials

Daymond et al. [52] used a neutron diffractometer and in-situ tensile tester to measure the response of austenitic stainless steel. The macroscopic strain was measured using an extensometer and the lattice plane spacings parallel and perpendicular to the loading direction were measured simultaneously. Stainless steel was selected because of its good scattering properties and relatively large degree of anisotropy.

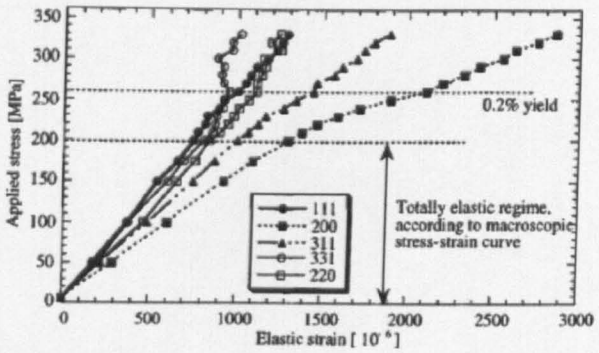

Fig. 1.35 Applied stress versus elastic lattice strain of different reflections measured using neutron diffraction [52].

The anisotropic response of the first five lattice reflections along with 0.2% yield limit for plasticity is plotted against the applied stress (Fig. 1.35). Deviations from linearity of the individual reflections occur close to the onset of macroscopic plasticity. After plastic deformation begins, the yield of preferentially oriented grains relative to their neighbours causes strain redistribution and a divergence from the linear response. Rietveld refinement was used for calculation of the average lattice parameter over all lattice planes oriented to a specific 2θ.

The stress strain response of three lattice planes, the Rietveld fits and the macroscopic strain are shown in Fig. 1.36.

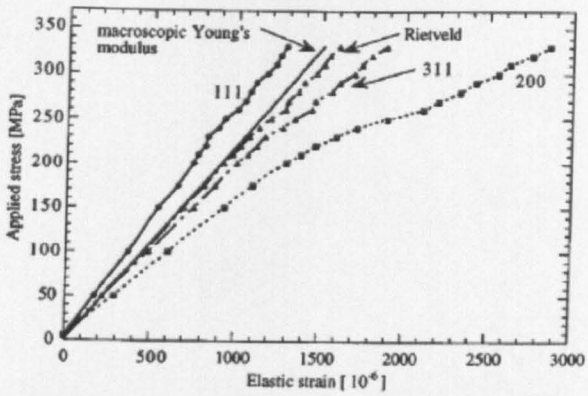

Fig. 1.36 Applied stress versus elastic lattice strain response of {111}, {200} and {311} reflections compared with Rietveld refinement [52].

The agreement of the Rietveld result with the macroscopic gradient is good in the elastic region. The {200} and {111} lattice planes represent the extremes of elastic stiffness in a cubic material with the {311} lying halfway between. The {311} lattice reflection in stainless steel is considered to be least affected by inter-granular strain and is commonly used for residual strain measurement at reactor neutron sources. Stone et al [7] measured the plane specific diffraction elastic constants for Waspaloy (a high strength nickel based superalloy). The experiment was carried out using neutron diffraction and in-situ tensile testing. The test pieces with a cross section of 5 mm x 5mm and a gauge length of 70 mm were machined from Waspaloy stock material. No inter-granular strain is observed for {111} planes (Fig. 1.37a). However, tensile inter-granular strains were accumulated beyond the elastic regime in the {200} lattice planes ((a) (b) Fig. 1.37b). The inter-granular strains were accumulated in the polycrystalline material because of the elastic and plastic anisotropy.

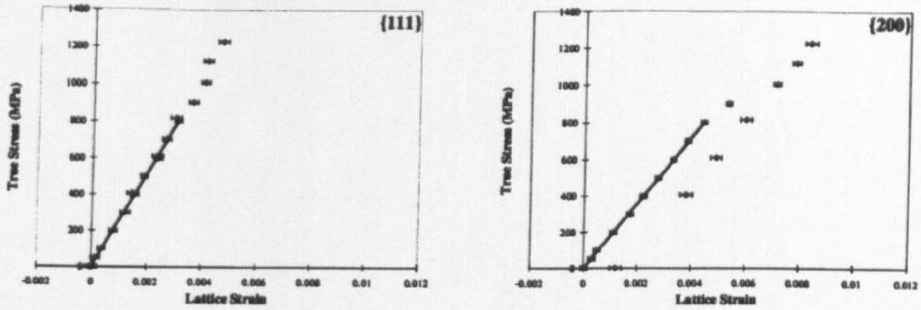

(a) (b)

Fig. 1.37 The variation of the lattice strain (longitudinal) on {111} and {200} diffraction peaks with true stress measured on a tensile test piece using in-situ neutron diffraction [7].

Holden et al [53] measured the diffraction elastic constants of a ferritic stainless steel using neutron diffraction. The (200), (111) and (110) reflections were used and some of the results are shown in Fig. 1.38.

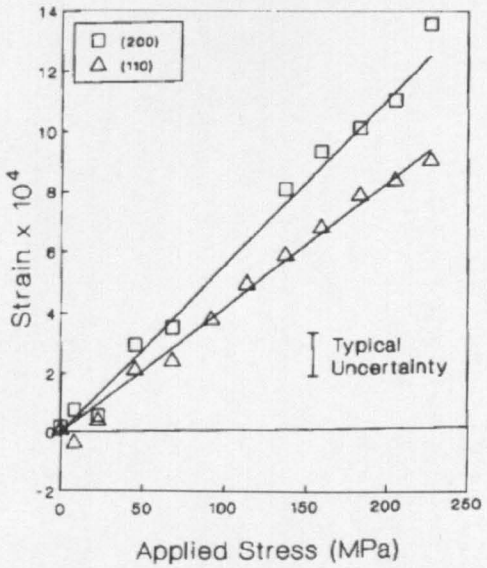

Fig. 1.38 Measurements of the lattice strain versus applied stress in ferritic steel. (110) and (200) reflections were used [53].

The measured diffraction elastic constants were compared with the theoretical values and they are summarised in table 1.2.

Table 1.2 Diffraction elastic constants for ferritic steel [53].

hkl	E (GPa)	ν	E_{Kroner}	ν_{Kroner}
(200)	182 ± 6	0.31 ± 0.02	176	0.33
(220)	243 ± 5	0.28 ± 0.01	225	0.28
(222)	268 ± 17	0.30 ± 0.03	248	0.25
Bulk	224		213	0.29

Withers et al [54] investigated the load partitioning in continuous Ti/SiC composites using neutron diffraction. The material investigated was a composite laminate containing a Ti-6Al-4V matrix reinforced with 35 vol. % SCS-6 SiC monofilamentary fibres. Initially the unreinforced material was loaded and the strain response was monitored. The macroscopic stress-strain curve is shown in Fig. 1.39.

The response of the composite after loading axially was strongly influenced by the presence of the fibres, which can be observed by comparing Fig. 1.39 and Fig. 1.40. The maximum load in the composite was 250 MPa higher than the unreinforced alloy but the plastic strain in the composite was over 50 times smaller than the unreinforced alloy because of the load borne by the reinforcing fibres.

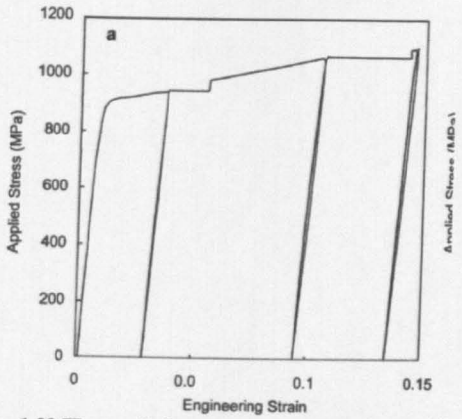

Fig. 1.39 The applied stress vs engineering strain Curve for the unreinforced Ti-6Al-4V alloy [54].

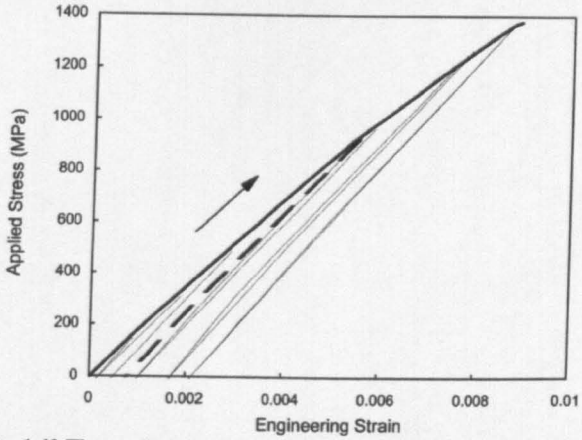

Fig. 1.40 The applied stress vs engineering strain response of the composite applied parallel to the fibre alignment direction. The thin lines delineate the loading/unloading stages of the cycle. [54].

1.13 Modelling of Inter-granular Stresses

1.13.1 Introduction

This section provides details about the elastic anisotropy of single crystals. Various modelling techniques for estimating the properties of polycrystalline materials are also reviewed.

1.13.2 Elastic Anisotropy in Single Crystals

All crystalline materials have different properties in different directions. In a single crystal the variation in elastic properties with direction is called elastic anisotropy. In plasticity the crystals deform on well defined crystal planes (slip planes) in specific directions (slip directions), and this property is called plastic anisotropy.

The inverse of the Young's modulus [55] E, for cubic systems, as a function of direction (orientation) may be expressed as:

$$(1/E_{hkl}) = S_{11} - 2\left(((S_{11} - S_{12}) - \frac{1}{2}S_{44})(l_1^2 l_2^2 + l_2^2 l_3^2 + l_3^2 l_1^2)\right) \tag{1.33}$$

with the orientation dependency governed by the latter term of direction cosines

$$(l_1^2 l_2^2 + l_2^2 l_3^2 + l_3^2 l_1^2) \tag{1.34}$$

The direction cosines can be expressed in the form of Miller indices,

$$\begin{aligned} l_1 &= h/\sqrt{h^2 + k^2 + l^2} \\ l_2 &= k/\sqrt{h^2 + k^2 + l^2} \\ l_3 &= l/\sqrt{h^2 + k^2 + l^2} \end{aligned} \tag{1.35}$$

Eq. (1.28) can be written as

$$(1/E_{hkl}) = S_{11} - 2\left(((S_{11} - S_{12}) - \frac{1}{2}S_{44})\frac{(k^2l^2 + l^2h^2 + h^2k^2)}{(h^2 + k^2 + l^2)^2}\right) \tag{1.36}$$

For an isotropic material, $1/E$ is independent of direction. This requires

$S_{44} = 2(S_{11}-S_{12})$.

The degree of anisotropy is often expressed in terms of the ratio given below, which will be equal to unity for isotropic crystal properties and deviating from unity with increasing degree of anisotropy:

$$\frac{2(S_{11}-S_{12})}{S_{44}} \tag{1.37}$$

If the degree of anisotropy is greater than unity, the <111> family of directions is the most stiff and the <100> family of directions is most compliant. If this term is less than unity, the stiff and compliant directions are interchanged.

The values of elastic moduli for selected crystallographic directions (*hkl*) as well as the values of the degree of anisotropy for a range of bcc and fcc materials, are tabulated in table 1.4 and 1.5 (pp 77-78).

A broad range in the degree of anisotropy for bcc materials is presented in table 1.4, from nearly isotropic tungsten to the highly anisotropic iron. For materials like molybdenum and chromium, the degree of anisotropy is less than unity giving rise to the situation where the <111> family of directions become the most compliant and <200> family of directions the stiff one.

Similar data is given for common fcc materials in table 1.5.

For aluminium, the maximum deviation in stiffness from the typical macroscopic value of 70 GPa amounts to 8-9%, whereas for austenite, with a typical macroscopic modulus near 200 GPa, the deviation in stiffness exceeds 50%. For the fcc materials presented in table 1.5 the parameter describing the degree of anisotropy is larger than unity. The tabulated fcc materials show the <111> to be the most stiff direction and <200> to be the most compliant.

1.13.3 Young's Modulus in Crystals

Assume a bar of crystal is loaded in tension and is cut with its length parallel to some arbitrary direction Ox'_1. Longitudinal and lateral strains (because of Poisson's ratio) will be produced in an isotropic material. However in a crystal shear strains will also be produced [56]. The ratio of the longitudinal stress to the longitudinal strain is defined as the Young's modulus for the direction of the tension, i.e. in matrix notation $1/S'_{11}$.

The expression for the reciprocal of Young's modulus in the direction of the unit vector l_i, namely S'_{11} for the cubic crystals is given in equation (1.33).

The variation of the elastic behaviour of a crystal with direction cannot be represented by a single surface. A surface that is useful in practice is one that shows the variation of Young's modulus with direction, its radius vector being proportional to $1/s'_{11}$.

Fig. 1.41 shows examples for some of the cubic crystals. Each figure has not only the symmetry elements of the crystal, but also a centre of the symmetry, the property of elasticity being inherently centro-symmetric.

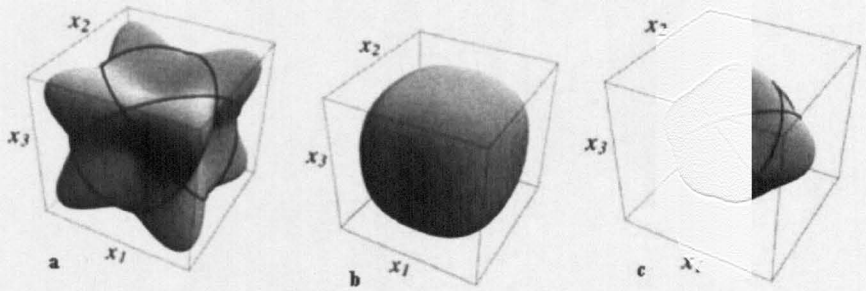

Fig. 1.41 Radius vector in each part is proportional to the magnitude of Young's modulus, $1/S'_{11}$, in that direction. (a) copper, cubic (b) diamond, cubic (c) rock-salt, cubic [56].

In a cubic system the variation of the Young's modulus with direction depends on $l_1^2 l_2^2 + l_2^2 l_3^2 + l_3^2 l_1^2$, which is zero in the <100> directions and a maximum in the <111> directions. Usually $\left(S_{11} - S_{12} - \frac{1}{2}S_{44}\right)$ is positive, so that Young's modulus is

a maximum in the <111> directions and a minimum in the <100> directions. The surface for copper in Fig. 1.41 has the form of a cube with rounded corners and depressions at the centres of the faces. Their central sections normal to <111> are circles, as indicated. For rock salt, Young's modulus is least for <111>.

1.14 Modelling of Bulk Properties:

Several theoretical models have been proposed to describe the fundamental properties of polycrystalline materials based on single crystal elastic constants. Various modelling schemes have been suggested for this purpose and these are reviewed in the following sections.

1.15 Crystal Plasticity Models

1.15.1 Taylor Model

The Taylor model [57] postulates that each grain inside a polycrystalline material experiences the same strain as the surrounding material in the bulk. All the grain boundaries necessarily remain in contact with this strain and no holes forming between them. For example, in a drawn wire, the crystal grains are all elongated in the direction of extension and contracted in the perpendicular direction.

1.15.2 Sachs Model

The Sachs model [58] is one of the earliest crystal plasticity models. The model postulates that the shear stresses on the principal slip systems are the same for all slip systems. A proportional relation between the single crystal stress state and the average stress state, results because of this assumption.

1.16 Elastic and Self-consistent Models

1.16.1 Voigt Modelling Scheme for bulk properties (Uniform Strain Approach)

In the Voigt modelling scheme each grain in the aggregate is assumed to experience the same uniform strain, and the aggregate's elastic properties are calculated by averaging the elastic stiffness, C_{ij}, over all elements of the aggregate [59]. The elastic properties of the aggregate are independent of the crystallographic direction. The uniform strain approach represents an upper bound (UB) for the elastic energy of the aggregate [60]. Compatibility is fulfilled in the uniform strain approach, but equilibrium is not fulfilled [61].

1.16.2 Reuss model for bulk properties (Uniform Stress Approach)

In the Reuss modelling scheme each grain is assumed to experience the average stress applied to the aggregate, and the aggregate properties are calculated by averaging the elastic compliances, S_{ij}, over all elements of the aggregate [59]. Continuity of displacement at grain boundaries is not allowed in this model, as the strains in two adjacent crystallites are different. Each crystallite develops a strain that is proportional to the anisotropic modulus in a particular direction [60]. The elastic constants therefore depend on the crystallographic orientation. This model represents a lower bound (LB) for the elastic energy of the aggregate [61].

For cubic materials:

Table 1.3 Voigt and Reuss Modelling Techniques

	K	G	E	ν
Voigt	$(C_{11} + 2C_{12})/3$	$[(C_{11} - C_{12}) + 3C_{44}]/5$	$3K^V(1 - 2\nu^V) = 2(1 + \nu^V)G^V$	$(3K^V - 2G^V)/2(3K^V + G^V)$
Reuss	$(C_{11} + 2C_{12})/3$	$5/[4(S_{11} - S_{12}) + 3S_{44}]$	$3K^R(1 - 2\nu^R) = 2(1 + \nu^R)G^R$	$(3K^R - 2G^R)/2(3K^R + G^R)$

Based on these expressions, the overall elastic properties have been calculated for a range of bcc and fcc materials, and the results are presented in table 1.4 and 1.5.

Table 1.4 Bulk, shear, Young's moduli and Poisson's ratio for polycrystalline aggregates following the Voigt and Reuss modelling scheme based on the single crystal elastic constants for bcc crystals [62, 63, 64, 65].

Modulus	Units	Temp. (K)	Cr	V	Mo	W	Ta	Fe
			298	300	300	300	300	300
C_{11}	10^{11}Pa		3.50	2.28	4.41	5.23	2.61	2.33
C_{12}	10^{11}Pa		0.68	1.19	1.72	2.05	1.57	1.35
C_{44}	10^{11}Pa		1.01	0.43	1.22	1.61	0.82	1.18
S_{11}	$10^{11}Pa^{-1}$		0.30	0.68	0.29	0.24	0.70	0.75
S_{12}	$10^{11}Pa^{-1}$		-0.05	-0.23	-0.08	-0.07	-0.26	-0.28
S_{44}	$10^{11}Pa^{-1}$		0.99	2.35	0.82	0.62	1.22	0.85
$2(S_{11}-S_{12})/S_{44}$			0.71	0.78	0.90	1.00	1.58	2.41
E_{200}	GPa		328	147	344	408	142	134
E_{310}	GPa		303	137	336	409	157	156
E_{411}	GPa		300	136	335	409	159	160
E_{321}	GPa		266	123	323	411	191	223
E_{112}	GPa		266	123	323	411	191	223
E_{110}	GPa		266	123	323	411	191	223
E_{111}	GPa		250	117	316	411	215	287
K^V	GPa		162	155	262	311	192	168
G^V	GPa		117	47	127	160	70	90
ν^V			0.21	0.36	0.29	0.28	0.34	0.27
E^V	GPa		283	129	327	410	187	230
K^R	GPa		162	155	262	311	192	168
μ^R	GPa		114	47	126	160	66	75
ν^R			0.22	0.36	0.29	0.28	0.34	0.31
E^R	GPa		277	127	327	410	179	196

Table 1.5 Bulk, shear, Young's moduli and Poisson's ratio for polycrystalline aggregates following the Voigt and Reuss modelling scheme based on the single crystal elastic constants for fcc crystals [66, 67,68, 69, 70, 71].

Modulus	Units	Al	Ni	Ag	Au	Cu	Austenite
	Temp. (K)	293.2	298	300	300	300	300
C_{11}	10^{11}Pa	1.13	2.44	1.24	1.92	1.68	2.05
C_{12}	10^{11}Pa	0.67	1.58	0.94	1.63	1.21	1.38
C_{44}	10^{11}Pa	0.28	1.02	0.46	0.42	0.75	1.26
S_{11}	$10^{11}Pa^{-1}$	1.57	0.83	2.31	2.74	1.50	1.07
S_{12}	$10^{11}Pa^{-1}$	-0.58	-0.33	-0.99	-1.08	-0.63	-0.43
S_{44}	$10^{11}Pa^{-1}$	3.59	0.98	2.17	2.38	1.33	0.79
$2(S_{11}-S_{12})/S_{44}$		1.20	2.38	3.04	3.20	3.21	3.79
E_{200}	GPa	64	120	43	36	67	93
E_{311}	GPa	66	140	52	44	81	115
E_{420}	GPa	67	143	54	45	83	118
E_{531}	GPa	72	201	83	70	130	193
E_{110}	GPa	72	201	83	70	130	193
E_{331}	GPa	72	201	83	70	130	193
E_{111}	GPa	75	259	121	101	191	299
K^V	GPa	82	187	104	173	137	160
G^V	GPa	26	78	34	31	55	89
ν^V		0.36	0.32	0.35	0.42	0.32	0.27
E^V	GPa	70	206	91	88	145	225
K^R	GPa	82	187	104	173	137	160
μ^R	GPa	26	66	25	22	40	60
ν^R		0.36	0.34	0.39	0.44	0.37	0.33
E^R	GPa	70	177	70	64	109	159

1.16.3 Hill's Averaging Scheme

In the method proposed by Voigt the forces between the grains could not usually be in equilibrium. In the method proposed by Reuss the distorted grains could not fit together. In general both methods are approximate.

Hill [72] proposed that the measured moduli for an aggregate of crystals invariably lie between the Reuss and Voigt values, the latter being greater.

For a macroscopically isotropic aggregate

$$K^R \leq K \leq K^V; \quad G^R \leq G \leq G^V \tag{1.38}$$

$$E^R \leq K \leq E^V$$

K and G are the measured bulk and shear moduli.

1.16.4 Hashin and Shtrikman Bounds

Lower and upper bounds for the elastic moduli of the constituting crystals have been calculated using variational principles for anisotropic and non-homogeneous elasticity [73]. An important feature of the treatment is that no assumptions concerning shape or behaviour of the crystals are involved. Voigt and Reuss bounds present exact theoretical results only when the concept of an effective elastic modulus of a polycrystal is accepted, according to which an aggregate of randomly oriented crystals may be replaced by an equivalent isotropic and homogeneous elastic body. These bounds are not close enough to provide a good estimate for the effective elastic moduli except for the case when the anisotropy of the crystals is small. The bounds obtained by variational principles are much closer than the Voigt and Reuss bounds give good estimates for the effective elastic moduli even in cases when the anisotropy of the crystal is large.

The elastic moduli of a crystal of cubic symmetry are completely specified by the three moduli C_{11}, C_{12} and C_{44}, in six by six matrix notation. The bulk modulus and the two shear moduli of such a crystal are defined by

$$\left.\begin{aligned} K &= \frac{1}{3}(C_{11}+2C_{12}) \\ G_1 &= \frac{1}{2}(C_{11}-C_{12}) \\ G_2 &= C_{44} \end{aligned}\right\} \tag{1.39}$$

The Voigt and Reuss bounds for the bulk modulus of an aggregate of cubic crystals coincide and both are given by above equation.

Hashin and Shtrikman bounds for the shear modulus:

$$\left.\begin{aligned} G_1^* &= G_1 + 3\left(\frac{5}{G_2-G_1} - 4\beta_1\right)^{-1} \\ G_2^* &= G_2 + 2\left(\frac{5}{G_1-G_2} - 6\beta_2\right)^{-1} \end{aligned}\right\} \tag{1.40}$$

where

$$\beta_1 = -\frac{3(K+2G_1)}{5G_1(3K+4G_1)}$$

$$\beta_2 = -\frac{3(K+2G_2)}{5G_2(3K+4G_2)}$$

The Voigt and Reuss bounds for the shear modulus of a polycrystalline aggregate are given by

$$\left.\begin{aligned} G_V^* &= \frac{1}{5}(2G_1+3G_2) \\ G_R^* &= \frac{5G_1G_2}{2G_2+3G_1} \end{aligned}\right\} \tag{1.41}$$

Table 1.6 Calculated bounds and experimental results for shear modulus of cubic polycrystalline metals (GPa) [73]

Metal	C_{11}	C_{12}	C_{44}	G_R^*	G_1^*	$G_{(obs)}$	G_2^*	G_V^*
Copper	171	122	691	40	448	455	472	54
Gold	186	157	42	24	27	277	29	31
α-iron	237	141	116	74	80	831	83	89

1.17 Elasto-Plastic Solutions

1.17.1 Kröner model for macroscopic bulk properties

The Kroner model [59, 60, 74] allows both stresses and strains to vary from grain to grain in contrast to the idealised approach by Voigt and Reuss which prescribes either the strain or the stress to be uniform in the aggregate. In the model proposed by Kroner, all the grains of one crystallographic orientation (within a certain small range) are represented by a single spherical grain. The surrounding matrix is represented by an isotropic continuum. The Eshelby method [67] can be used to solve this problem of an inclusion embedded in an isotropic medium. The spherical grain is cut out of the isotropic matrix. The surface tractions are applied to the matrix at infinity which gives rise to the macroscopic average stress $\bar{\sigma}$. The surface tractions are also applied at the hole such that the surrounding material is under the same stress state as it would be if the hole were filled with the isotropic continuum also. There will be uniform elastic and plastic deformation of the matrix. The plastic strain of the hole may be described by $\bar{\varepsilon}$. The elastic strains in the grain and the matrix are assumed to be identical. The surface tractions which were applied to the inside surface of the hole are applied, with opposite sign, to the separated grain. The grain will yield under these surface tractions and the plastic strain of the grain is ε. The grain can not be inserted back into the matrix as the compatibility conditions have been violated. The grain and matrix are

treated as elastic and a distribution of the internal stresses and the elastic strains is found that will make the grain fit back into the hole.

The internal stress is uniform inside any grain of ellipsoidal shape and it is directed opposite to the difference between the plastic strains of the grain and hole.

$$\sigma - \bar{\sigma} = -\alpha G(\varepsilon - \bar{\varepsilon}) \tag{1.42}$$

where σ is the total stress inside the grain, G is the appropriate elastic modulus and α is a scalar constant.

In the case of cubic crystals, the bulk modulus can be calculated in the same way as in Voigt and Reuss models:

$$K^{Kroner} = (C_{11} + 2C_{12})/3 = K^{Voigt} = K^{Reuss} \tag{1.43}$$

The shear modulus, G, can be calculated by solving the cubic equation:

$$G^3 + \alpha G^2 + \beta G + \gamma = 0 \tag{1.44}$$

Where $\alpha = \dfrac{(5C_{11} + 4C_{12})}{8}$

$\beta = \dfrac{-C_{44}(7C_{11} - 4C_{12})}{8}$

$\gamma = \dfrac{-C_{44}(C_{11} - C_{12})(C_{11} + 2C_{12})}{8}$

The bulk modulus, K, shear modulus, G, the Poisson's ratio, ν, and the Young's modulus, E, have been calculated based on the Kroner modeling scheme, for various bcc and fcc materials and shown in table 1.7 and table 1.8.

Table 1.7 Bulk, shear, Young's moduli and Poisson's ratio for polycrystalline aggregates following the Kroner modelling scheme for bcc materials.

Modulus		Fe	Cr	V	Mo	W	Ta
G	GPa	83	115	47	127	160	68
K	GPa	168	162	155	262	311	192
v		0.29	0.21	0.36	0.29	0.28	0.34
E^{Kroner}	GPa	215	280	128	327	410	183

Table 1.8 Bulk, shear, Young's moduli and Poisson's ratio for polycrystalline aggregates following the Kroner modelling scheme for fcc materials.

Modulus		Al	Ni	Ag	Au	Cu	Austenite	Pb
G	GPa	26	73	30	28	48	76	9
K	GPa	820	187	104	173	137	160	42
v		0.48	0.33	0.37	0.42	0.34	0.30	0.40
E^{Kroner}	GPa	77	193	82	80	129	196	24

1.18 Elasto-Plastic Self Consistent Modelling

The upper and lower bound models of Taylor and Sachs neglect the strain and stress variation from grain to grain [76]. In practice the deformation within a particular grain is usually heterogeneous. Self consistent approaches are used to account for inter-granular heterogeneties during elastic-plastic deformation of polycrystalline materials. Polycrystalline material properties can be calculated by assuming the grain as an ellipsoidal inclusion (which is generally heterogeneous) inside a homogeneous isotropic medium. The stress and strain inside the grain are related to the stress and strain at infinity and can be calculated using Eshelby's formalism.

This section introduces the fundamental concepts of the EPSC formalism based on Hutchinson's implementation [77] of the EPSC model proposed by Hill. The behaviour of a grain inside a polycrystalline aggregate under applied external stress is investigated in the self-consistent model of elasto-plastic deformation. The properties of materials must be studied at different scales using this approach [78]. This approach is particularly suitable for analyzing inter-granular stresses, as neither the strain nor the stress are assumed a priori inside the grains [79].

1.18.1 Stress – Strain behaviour for single crystals

Schmid's Law: Single crystals deform plastically by slip in certain directions on specific crystallographic planes after the resolved shear stress on one or more of these slip systems reaches a critical value.

If a crystallite is under the stress σ_c,

Resolved shear stress on the slip system = $\sigma_{ckl}\alpha_{kl}^{\ i}$ or $\sigma_c\alpha^i$ (1.45)

where $\alpha_{kl}^i = \frac{1}{2}(m_k^i n_l^i + m_l^i n_k^i)$ (no sum on i)

n_j^i is the normal to the plane of ith slip system and m_j^i is its slip direction.

The multiplication of dislocations and evolution of their spatial distribution inside a grain leads to hardening of the slip systems during plastic deformation (the critical resolved shear stress increases with deformation). The rate of the critical shear stress on the i^{th} slip system τ^i is given by.

$$\dot{\tau}^i = \sum_j h^{ij} \dot{\gamma}^j \tag{1.46}$$

h^{ij} = the instantaneous hardening coefficients (which depend upon the previous deformation history).

A slip system is active if the rate of resolved stress is equal to the rate of its critical value and using Schmid's law,

$$\dot{\sigma}_c \alpha_i = \dot{\tau}^i \tag{1.47}$$

The local tangent modulus L_c relating the grain stress rate $\dot{\sigma}_c$ and the grain strain rate $\dot{\varepsilon}_c$ can be calculated for the known set of active slip systems.

$$\dot{\sigma}_c = L_c \dot{\varepsilon}_c \text{ and } \dot{\varepsilon}_c = M_c \dot{\sigma}_c \tag{1.48}$$

1.18.2 Self – consistent calculation of the overall instantaneous moduli

The shape and orientation of a particular grain is approximated by a similarly aligned ellipsoidal single crystal which is taken to be embedded in an infinite homogeneous matrix whose moduli L are the overall instantaneous moduli of the polycrystal to be determined. In this approximate way the interaction between the grain under consideration and its plastically deforming neighbours is taken into account.

Using Eshelby's formalism, the stress and strain rates in the ellipsoidal inclusion, $\dot{\sigma}_c$ and $\dot{\varepsilon}_c$, will be uniform and can be related to the stress and strain rates at infinity by fourth order tensors A_c and B_c according to

$$\dot{\varepsilon}_c = A_c \dot{\bar{\varepsilon}} \text{ and } \dot{\sigma}_c = B_c \dot{\bar{\sigma}} \tag{1.49}$$

where $\dot{\bar{\sigma}}, \dot{\bar{\varepsilon}}$ = the stress and strain rates at infinity in the matrix.

The calculation of A_c and B_c is facilitated by the introduction of a constraint tensor L^* with inverse M^*. These are defined by considering a matrix containing an ellipsoidal void with the same orientation and shape as the grain and subject to a traction rate, $\dot{\sigma}^*_{ij} n_j$, over the surface of the void where n is the inward unit normal to the void surface and $\dot{\sigma}^*$ is constant. The associated uniform straining of the void $\dot{\varepsilon}^*$ is given by

$$\dot{\sigma}^* = -L^* \dot{\varepsilon}^* \text{ or } \dot{\varepsilon}^* = -M^* \dot{\sigma}^* \tag{1.50}$$

L^* and M^* depend only on L and the shape of the orientation of the ellipsoid, and if the void is spherical, only on L.

With the use of L^* and M^* the differences between the stress and strain rates in a given single crystal inclusion and the rates in the matrix at infinity are related by

$$\dot{\bar{\sigma}} - \dot{\sigma}_c = -L^* (\dot{\bar{\varepsilon}} - \dot{\varepsilon}_c) \text{ or } (\dot{\bar{\varepsilon}} - \dot{\varepsilon}_c) = -M^* (\dot{\bar{\sigma}} - \dot{\sigma}_c) \tag{1.51}$$

or

$$(L^* + L_c)\dot{\varepsilon}_c = (L^* + L)\dot{\bar{\varepsilon}} \text{ and } (M^* + M_c)\dot{\sigma}_c = (M^* + M)\dot{\bar{\sigma}} \tag{1.52}$$

or

$$A_c = (L^* + L_c)^{-1} = (L^* + L) \text{ and } B_c = (M^* + M_c)^{-1} = (M^* + M) \tag{1.53}$$

The final step in the formulation equates the overall stress and strain rates of the polycrystal with the weighted averages of these same quantities over all the grain orientations and shapes. For a particular grain $\dot{\sigma}_c = L_c A_c \dot{\bar{\varepsilon}}$; and if the average over all the grains is denoted by { }, then

$$\{\dot{\sigma}_c\} = \dot{\bar{\sigma}} \Rightarrow L = \{L_c A_c\} \tag{1.54}$$

Similarly,

$$\{\dot{\bar{\varepsilon}}_c\} = \dot{\bar{\varepsilon}} \Rightarrow M = \{M_c B_c\} \tag{1.55}$$

1.18.3 Examples: EPSC Modelling

Clausen et al investigated the response of austenitic stainless steel using in-situ tensile testing [8]. They also compared the experimental results with a self consistent model. Initial texture of the material was relatively weak cube texture. The elastic response of several reflections was recorded parallel and perpendicular to the tensile axis. Rietveld refinement was used to fit the entire diffraction spectrum. For the model calculations, an exponentially decreasing hardening law was used, which enabled a very accurate representation of the measured macroscopic stress-strain curve as shown in Fig. 1.42.

The lattice strain of different planes was also measured and compared with the model as shown in Fig. 1.43. The comparison between the experiment and model is easy to make due to the similarities between some of the assumptions in the modelling and

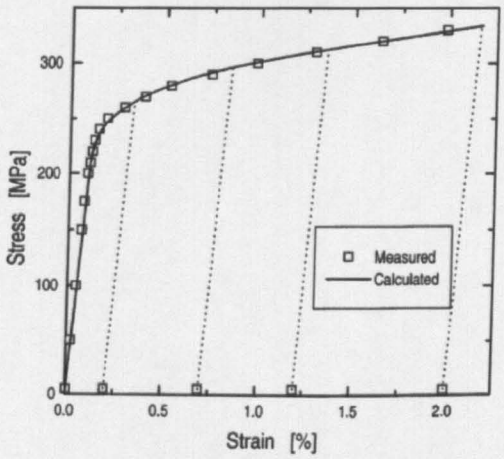

Fig. 1.42 Measured and calculated macroscopic stress-strain curve [8].

the characteristics of neutron diffraction measurements. Neutron diffraction measurement grains have different neighbouring grains and surroundings and the measured average strain for a reflection is therefore determined for an average surrounding which is very similar to the homogeneous equivalent medium assumption used in the Eshelby calculations in the model.

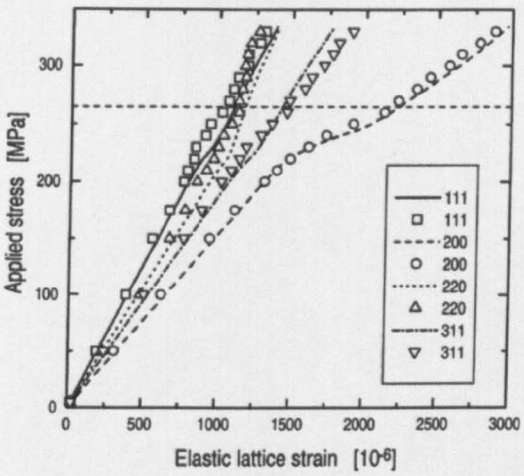

Fig. 1.43 The applied stress versus the elastic lattice strain. Symbols are for measured strain and lines for calculated strain [8].

Clausen et al [80] investigated the development of elastic lattice strains in three f.c.c. materials using self consistent modelling. The materials chosen were aluminium, copper and stainless steel representing different degrees of elastic anisotropy. To make the macroscopic stress-strain response of the model resemble the real macroscopic behaviour of the materials, the initial critical resolved shear stress and the hardening coefficients were used as the fitting parameters. Fig. 1.44 shows the calculated macroscopic stress-strain response for the three materials.

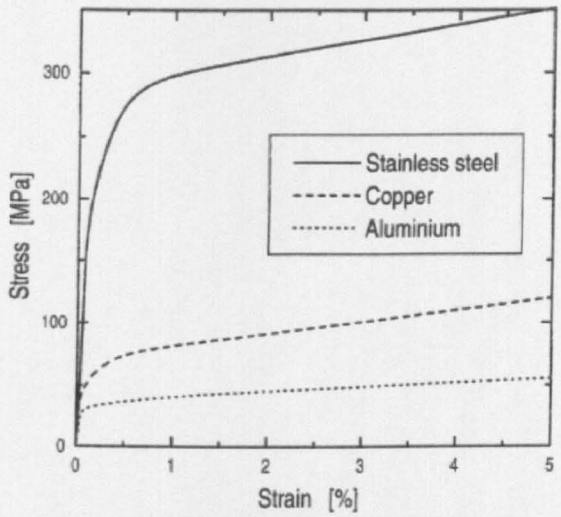

Fig. 1.44 The calculated stress-strain curves for the selected materials [80].

The lattice strains were derived from the model calculations by simulating the tensile deformation of initially texture free samples of aluminium, copper and stainless steel with 5000 grains. The relation between the applied stress and the elastic lattice strains parallel to and perpendicular to the tensile axis for the six reflections in the three materials is shown in Fig. 1.45 and Fig. 1.46 respectively. At the onset of plastic deformation the degree of redistribution of the load between the reflections increases with the increase in elastic anisotropy; the elastic anisotropy of aluminium is weakest and that of stainless steel is the strongest. In stainless steel and copper the strain redistribution is quite similar. The elastically soft reflections {200} and {311} remain the softest in the plastic region along the tensile axis. The {200} reflection becomes the stiffest direction and experiences the largest redistribution in lattice strain perpendicular to the tensile axis. In aluminium, along the tensile axis, the elastically stiffest reflection {111} becomes the softest reflection and the elastically softest reflection {200} becomes one of the stiffest in the plastic region. The redistribution is almost the same perpendicular to the tensile axis.

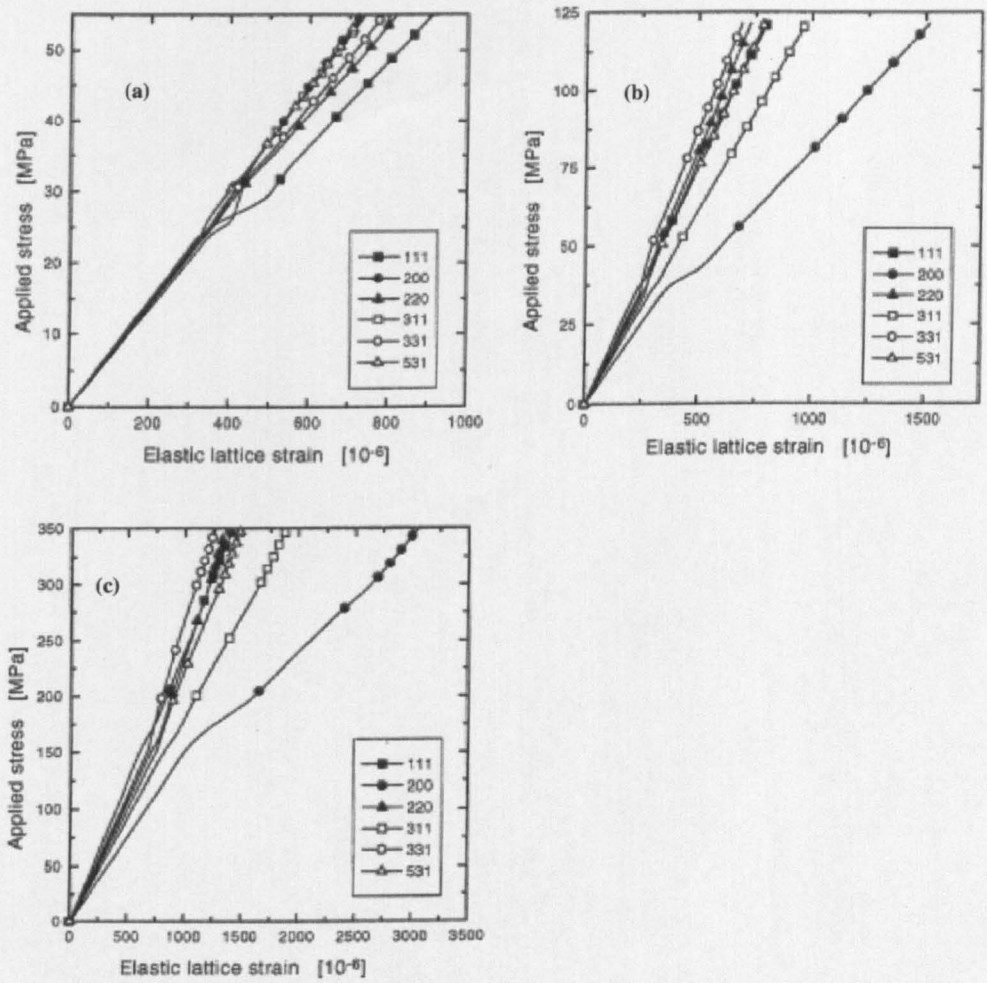

Fig. 1.45 Stress strain response parallel to the tensile axis. (a) aluminium (b) copper (c) stainless steel [80].

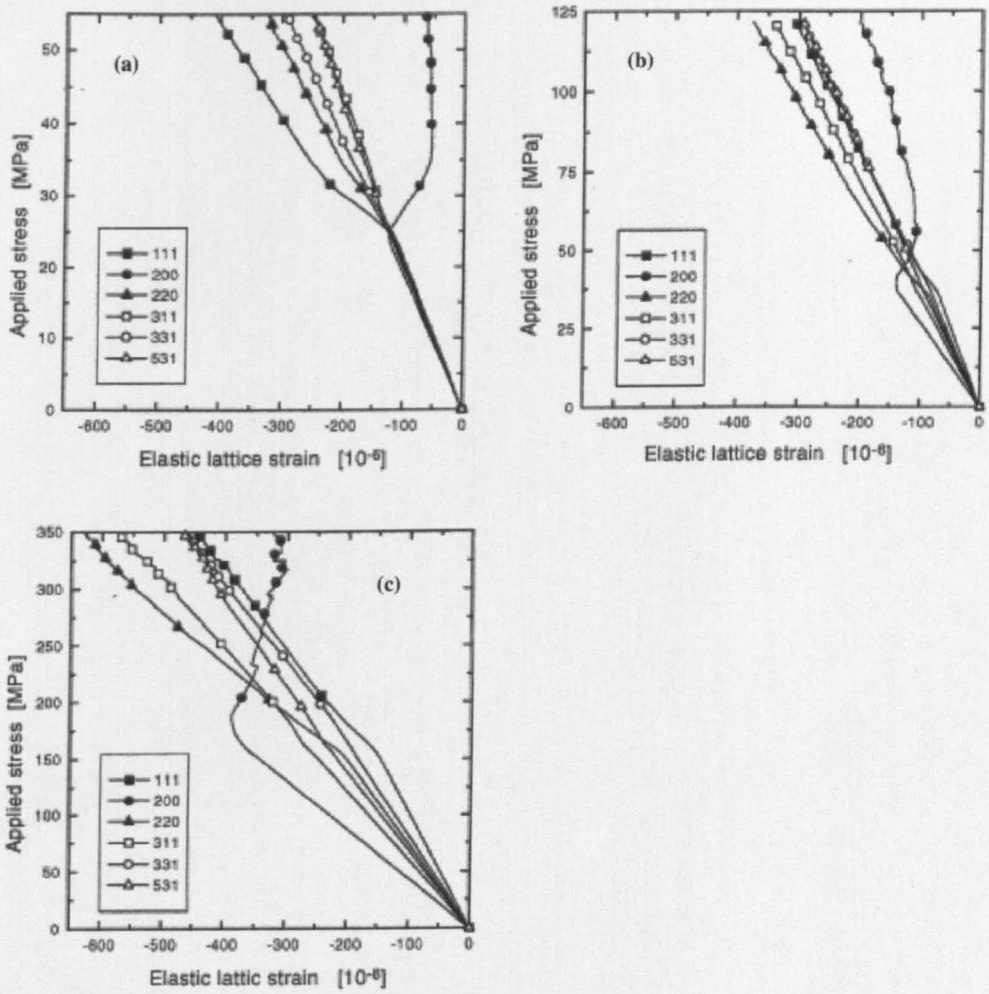

Fig. 1.46 Stress strain response perpendicular to the tensile axis. (a) aluminium (b) copper (c) stainless steel [80].

Daymond et al [81] investigated the deformation behaviour of a heat-treated ferritic steel specimen using in-situ neutron diffraction and self-consistent modelling. The material investigated was a 38MnS6 steel consisting mainly of a pearlitic microstructure. Fig. 1.47 shows the macroscopic stress-strain curve obtained from the experiment and the model.

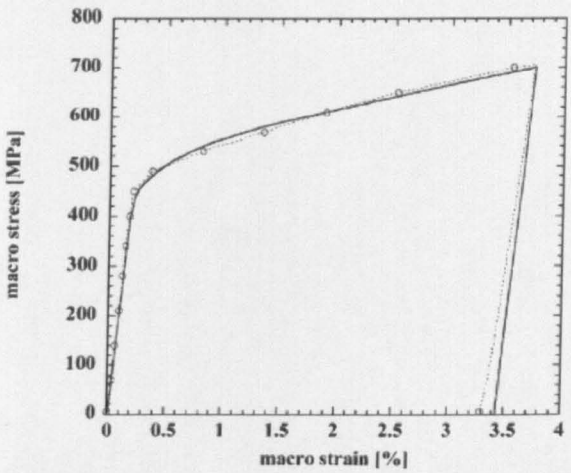

Fig. 1.47 The macroscopic response of the iron sample. Experimental (dotted line) and model (continuous line) data. The open circles indicate the macrostresses at which neutron measurements were made [81].

The agreement between the experiment and the model is reasonable except for a few discrepancies such as the presence of a reverse yield at the base of the experimental unload which is not there in the model.

Fig. 1.48 shows the bulk or average strains in each phase obtained from the Rietveld refinement. The cementite elastic response is the same in both axial and transverse directions. The iron strains show excellent agreement with the model.

Fig. 1.49 shows the response of four (first order) lattice reflections plotted against the macroscopic applied stress parallel to the loading direction. These strains were determined using single peak fitting.

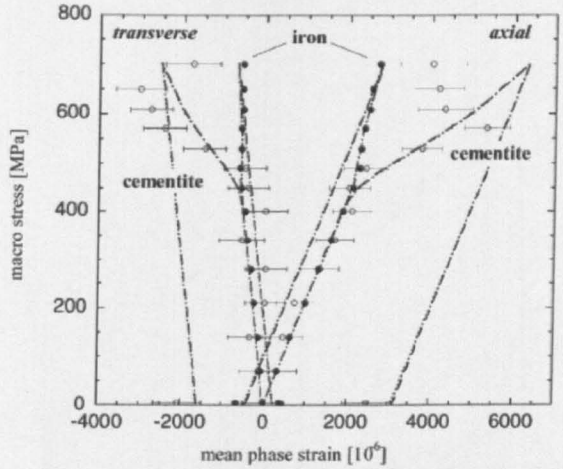

Fig. 1.48 The mean phase strains in iron (experimental closed symbols) and cementite (experimental open symbols) measured using in situ neutron diffraction. Data from the self consistent model is shown as the mean phase elastic strain (long broken lines) [81].

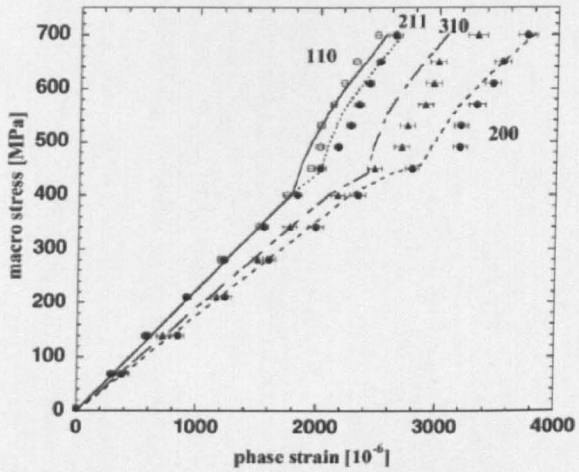

Fig. 1.49 The axial strains in different families of Fe grains compared with model predictions, as a function of applied macroscopic stress [81].

The model {200} and {310} peak strains show a deviation from the elastic gradient first becoming softer than elastic and then harder. The peaks {110} and {211} instead deviate to stiffer behaviour.

The elastic response of ferrite is similar to that of austenite because of similar elastic constants. After reaching the yield point the austenite phase deforms plastically while the ferrite phase remains in the elastic range.

Ledbetter [82] has provided detail on how the single crystal elastic constants, the C_{ij}s, can be obtained from polycrystalline elastic constants and then used to calculate the macroscopic elastic constants of textured aggregates. Ultrasonic study of welds requires knowledge and understanding of the weld's single crystal elastic constants and how these constants relate to the macroscopic elastic constants of the textured aggregate. A stainless steel 316 weld has been investigated in this study, which developed a [001] fiber texture which is transversely isotropic. This type of texture has macroscopically hexagonal symmetry with five independent elastic constants (C_{11}, C_{12}, C_{44}, C_{13}, C_{33}). In an ideal [001] fiber texture [001] type directions are parallel to the unique axis x_3 (the solidification direction in this case), and the (100) type planes perpendicular to x_3 are distributed randomly with respect to rotation about x_3. (Fig. 1.50) relates cubic and hexagonal coordinate systems to weld geometry.

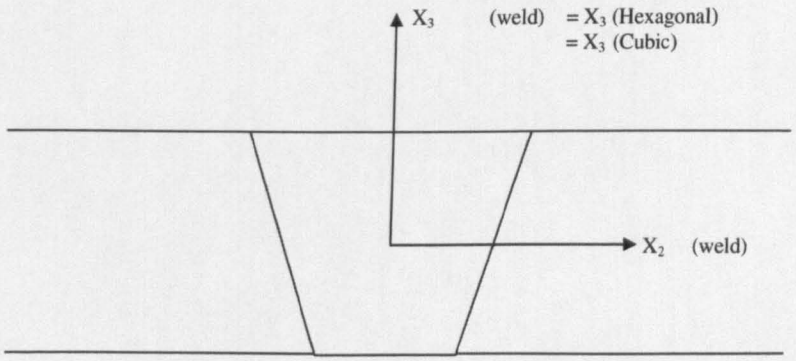

Fig. 1.50 Relationship between cubic and hexagonal coordinate systems and weld geometry. Cubic directions x_1 and x_2 are distributed randomly, perpendicular to x_3. Since the hexagonal x_1-x_2 plane is elastically isotropic, x_2 (hex) can be any direction perpendicular to x_3 (hex) [82].

In the x_1-x_2 plane, crystallites were orientated randomly because no preferred heat-flow direction occurred in that plane. Thus, an effective fiber texture occurred with x_3

being the fiber axis. Macroscopically, such a material exhibited transverse-isotropic symmetry, with five independent elastic constants. This was equivalent to hexagonal symmetry. Thus, the theoretical problem was to express the five hexagonal symmetry elastic constants, C_{ij}^{H}, in terms of the three cubic symmetry elastic constants C_{11}, C_{12} and C_{44}.

Elastic constant bounds (Fig. 1.51) were calculated for textured aggregates using Voigt (constant strain) and Reuss (constant stress) formalisms and also using Hill's suggestion of an arithmetic average. For the important [001] texture case, the bounds coincided for three elastic constants C_{13}^{H}, C_{33}^{H} and C_{44}^{H}.

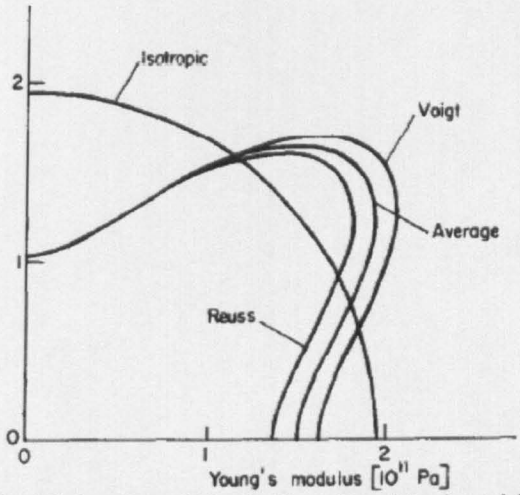

Fig. 1.51 Angular variation for Young's modulus for stainless steel 316 for [001] texture. The vertical direction is x_3(hex), about which the figure has complete rotational symmetry. Average denotes simple arithmetic average of Voigt and Reuss bounds, which correspond to constant strain and constant stress, respectively [82].

1.18.4 Summary

Basic concepts of stress, strain and constitutive relations have been reviewed in this chapter. Residual stresses and measurement of residual stresses by diffraction have also been reviewed. Finally, a literature review on strain measurement by diffraction in different types of components has been carried out.

The next chapter will provide details about welding solidification, metallurgy and weld microstructure, and the geometry of the specimens used in various tests.

Chapter 2 Specimens Detail, Welding Metallurgy and Microstructure

This chapter provides details about the various specimens and their manufacturing details, which were used in the neutron diffraction, metallography and texture experiments. Several types of welds were tested in-situ in tension and compression. This chapter also provides details about the principles of dendritic solidification in the welds and the metallurgy and microstructure of welds. Optical microstructures obtained from various specimens have been discussed.

2.1 Introduction to the Specimens

The specimens which are used in the present work are described in the following sections. These specimens were produced by British Energy for Young's modulus measurement and fatigue testing [83]. It was decided by The Open University that these specimens should be used for in-situ neutron diffraction measurements to measure the diffraction Young's modulus of the weld metal.

2.2 Chemical Composition of the Weld Metal

Both the multi-pass weld pad and the single-pass weld were fabricated by Mitsui Babcock on behalf of British Energy [83]. All the welds were deposited using Babcock 'S' type 5mm electrodes. The welding process used was the manual metal arc welding. The chemical composition of these electrodes is provided in table 2.1:

Table 2.1 Chemical composition (wt%) of the Babcock 'S' type 5 mm electrode [83]

C	Si	Mn	P	S	Cr	Ni	Mo	Cu	N
0.032	0.26	1.09	0.016	0.008	18.4	11.41	2.05	0.06	0.059

2.3 Manufacturing Details of the Multi-Pass Weld-Pad

The multi-pass weld-pad (Fig. 2.1) was built up on a type 316 stainless steel backing plate 150mm long, 100mm wide and 25mm thick. A photograph of the weld-pad is shown in Fig. 2.2. The pad was built up to a height of 100mm using a total of 239 overlapping weld runs of approximately 150mm in length. The table of recorded parameters for the weld-pad is shown in appendix–A.

2.4 Manufacturing Details of the Single-Pass Weld

The single pass welds (Fig. 2.7) were deposited in U preparation grooves, approximately 15mm deep, machined into 25mm thick type 316 stainless steel plates. These grooves had flank angles inclined at 20 degrees from the vertical. Four plates were used, each of dimensions 100mm long and 100mm wide, with the grooves machined parallel to the plate length. Ten grooves were machined into each plate; five per side, in order to ensure the plate remained flat following welding. The weld grooves were individually numbered before welding in order to subsequently identify the weld runs. The test specimens were manufactured such that the gauge length of the specimen was parallel to the longitudinal direction of the weld bead. The table of recorded parameters for the single-pass weld is shown in appendix–B.

2.5 Specimens for in-situ Tension Test

The in-situ tension test was carried out on multi-pass and single-pass austenitic stainless steel weld metal. A requirement of the tests was that the specimen designs had to be consistent between those manufactured from the weld pad and those from the single weld beads, for the purpose of mounting the specimens in the grips of the stress-rig.

2.5.1 Specimens from the Multi-Pass Weld-Pad

The test specimen blanks were taken from this pad such that their gauge lengths were parallel to the weld beads, i.e. in the 150mm longitudinal direction. Note that the locations from which the test specimens were machined from the weld pad were not recorded. Fig. 2.3 shows the multi–pass specimen no. 4. This specimen is shown inside the grips. This specimen is not electron beam welded at the ends. Fig. 2.4 shows a sketch of the multi–pass specimen no. 4.

Fig. 2.5 shows the multi–pass specimen no. 15. This specimen is electron beam welded at the ends. Fig. 2.6 shows a sketch of the multi–pass specimen no. 15.

2.5.2 Specimens from the Single-Pass Weld

Since the single weld beads were of approximately 5 mm diameter and there was a limited length of pedigree material, it was necessary to fabricate the specimen with welded end pieces which would mate with the test machine grips.

For the single pass weld specimens the weld bead was cut from the welded plate and machined into a cylinder, approximately 100mm in length, containing only weld metal. The individual weld beads and surrounding parent material were etched using Nital to ensure that the parent plate had been completely removed. The ends of the cylinders were cut off to remove the run-in and run-out of the welds and the cylinders cut such that 32mm long blanks were produced for the tensile specimens. This cutting process used a spark erosion technique to minimise the material wastage and to ensure the ends of the blanks were normal to the length of the blank.

These cylindrical blanks were then electron beam welded onto end pieces machined from type 316 stainless steel supplied by British Energy. Particular care was taken during the electron beam (EB) welding of these blanks to ensure that the amount of porosity was kept to an absolute minimum. In addition, the specimens were designed such that the electron beam weld was in the shoulder radius to ensure that the heat

affected zone produced by the EB welding process was at the extremes of the gauge length. The resulting components were then machined into test specimens.

Fig. 2.7 shows the single bead deposited in the groove and Fig. 2.8 shows the single–pass specimen no. 13/26. This specimen was also electron beam welded at the ends.

Fig. 2.9 shows a sketch of the single–pass specimen no. 13/26.

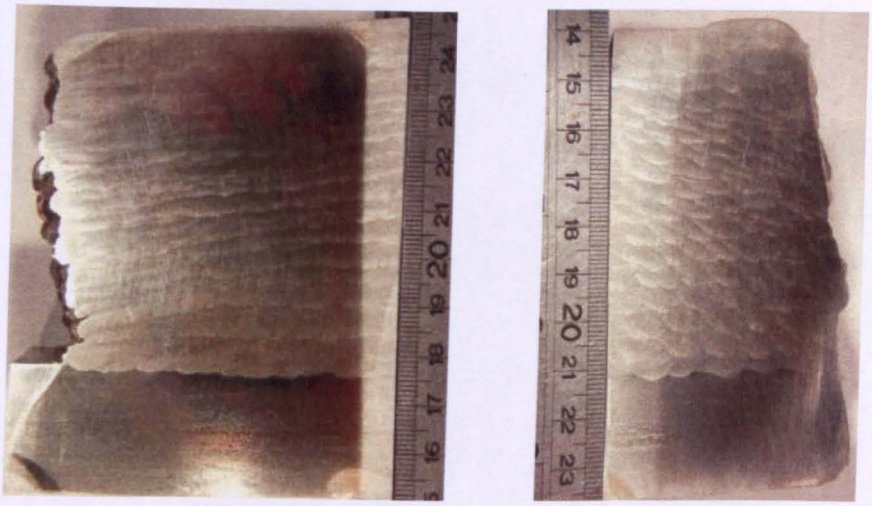

Fig. 2.1 Various views of multi–pass weld-pad (316 austenitic stainless steel). The surface was polished to show the weld beads. All the dimensions are in mm.

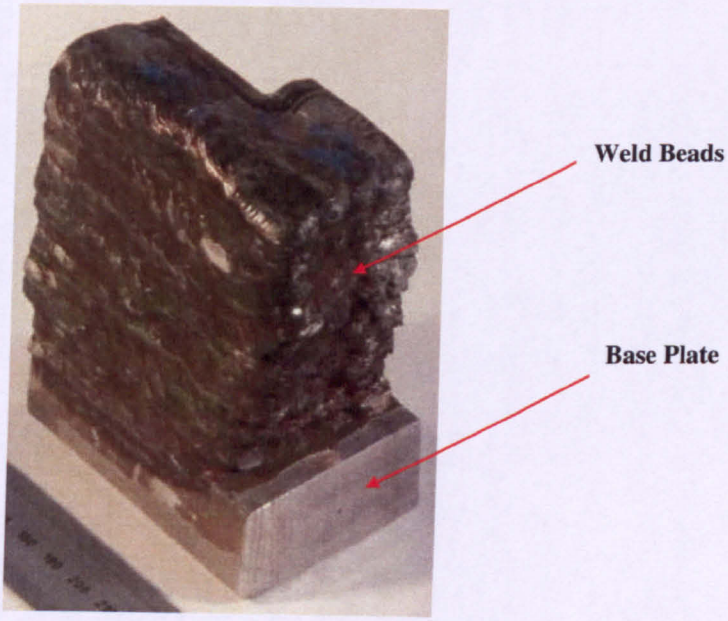

Fig. 2.2 3D view of multi–pass weld-pad

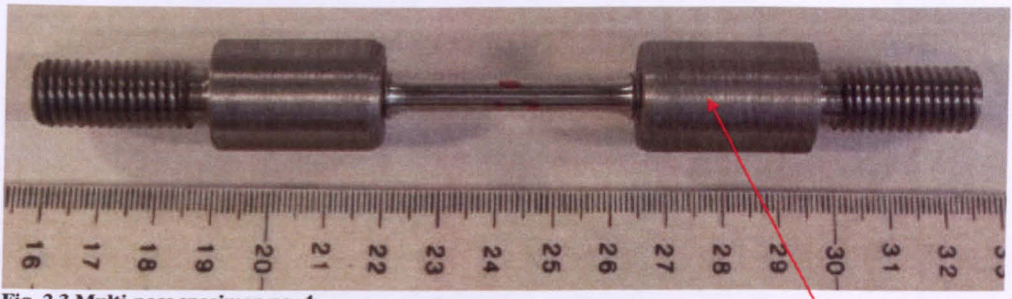

Fig. 2.3 Multi-pass specimen no. 4

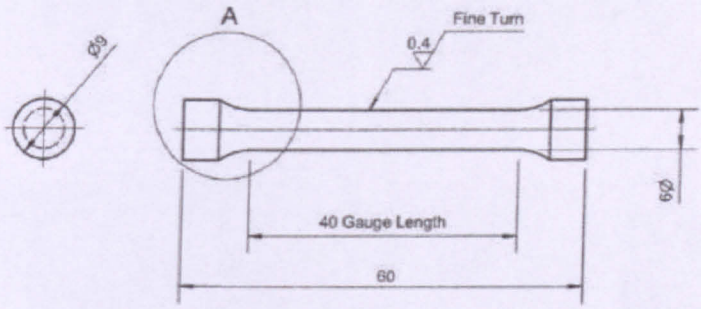

Fig. 2.4 Sketch of multi-pass specimen no. 4

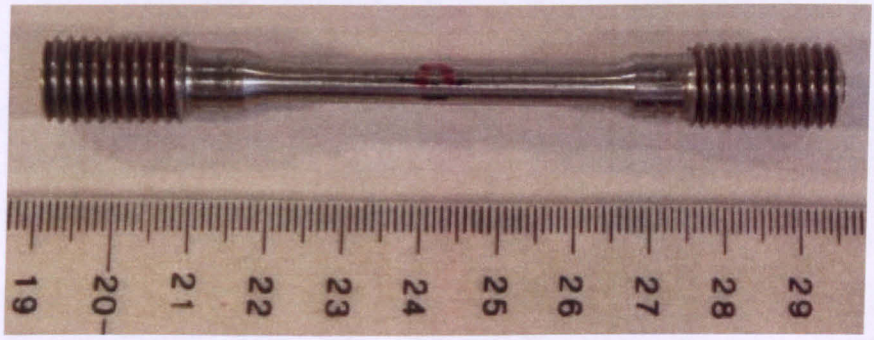

Fig. 2.5 Multi–pass specimen No. 15

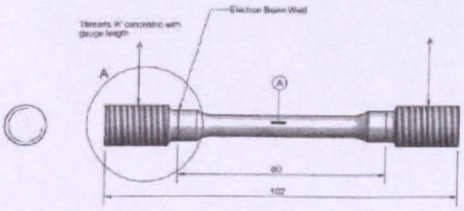

Fig. 2.6 Sketch of Multi-pass specimen no. 15

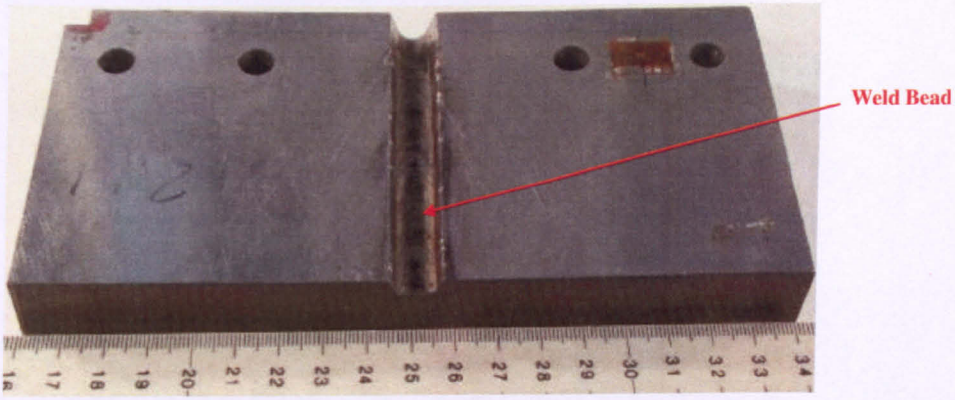

Fig. 2.7 Schematic view of single bead weld (316 austenitic stainless steel)

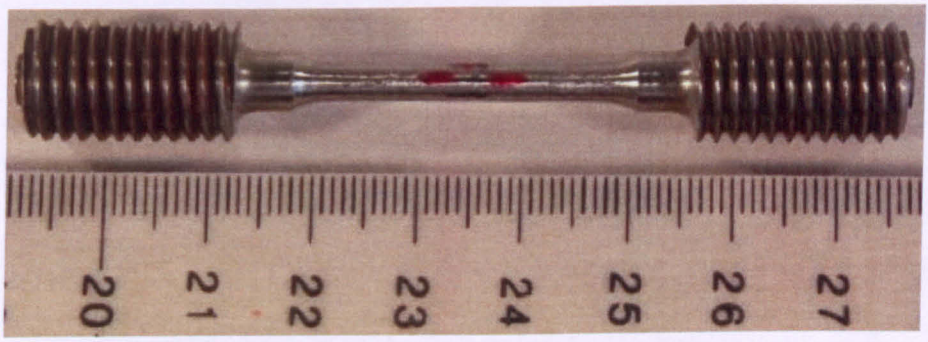

Fig. 2.8 Single Pass Specimen No. 13/26

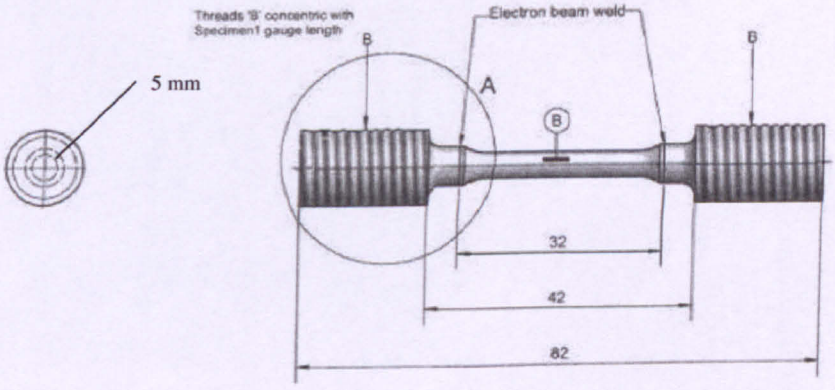

Fig. 2.9 Sketch of single-pass specimen no. 13/26

2.6 Specimens for in–situ Compression Tests

In-situ compression tests were carried out on several types of welds. The details of the specimens used in the in-situ compression tests are discussed in the following sections.

2.6.1 Cuboids from the Multi – Pass 316 Weld Pad

For the in–situ compression test, cuboids were machined from the weld pad. The details of the weld pad have been discussed in the previous sections. The size of the cuboid was 10 mm x 7 mm x 7mm. The cuboids were machined in such a way that the loading axis for each orientation was always the 10 mm dimension of the cuboid. The location of the cuboids in the weld-pad is shown in Fig. 2.10. The different orientations of the cuboids e.g. LD, TD and ND are shown in Fig. 2.11.

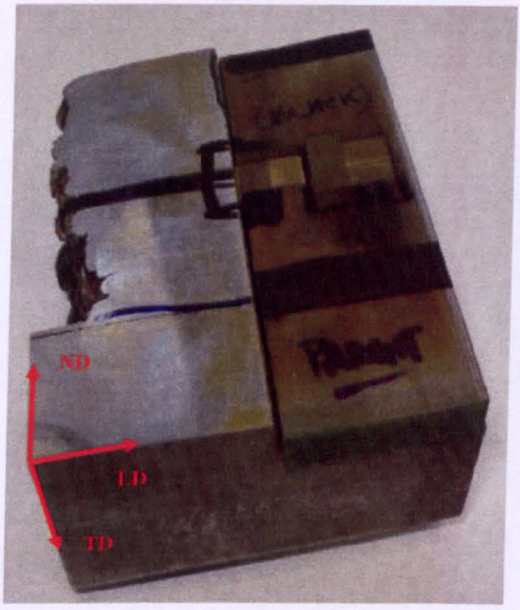

Fig. 2.10 Location of the cuboids in the weld-pad

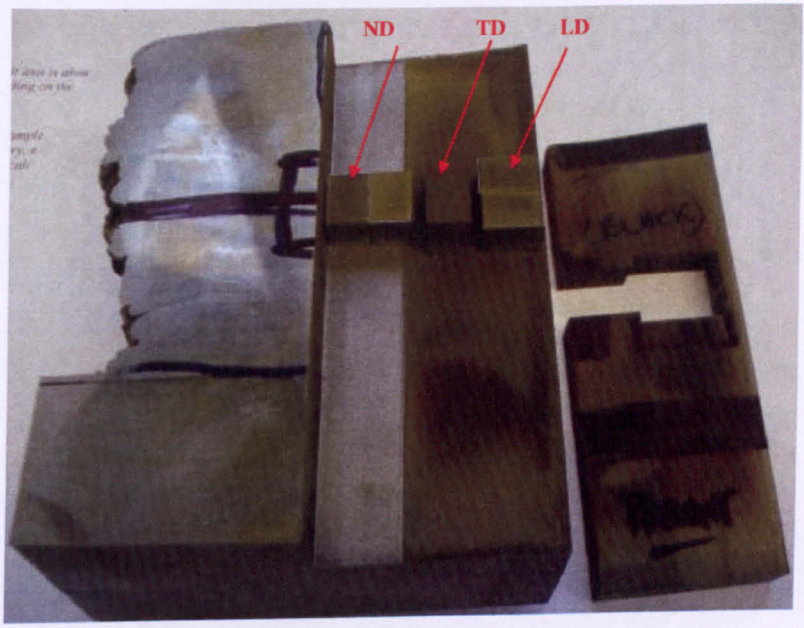

Fig. 2.11 Orientation of the cuboids in the weld-pad

2.6.2 Multi–Pass 316 TRAINSS Pipe Butt Weld [84, 85, 86]

TRAINSS Butt Weld Specimen (Training Industry in Neutron Strain Scanning).

As part of a wide ranging programme of investigations into the effect of repair welds in thick section austenitic butt welds on residual stress distributions, a series of specimens was commissioned by British Energy Generation Ltd for manufacture. Two programs were being considered, the effect of weld repair length and repair weld depth on residual stress profiles in addition to providing verification of predicted residual stress levels using a finite element model. A photo view of the TRAINSS pipe is shown in Fig. 2.12.

2.6.3 Method of Manufacture

A 19 mm thick pipe butt weld was required to study the effect of repair weld length, with one short repair (20° circumferential extent) and one long repair (60° circumferential extent) being introduced in to the original as-welded butt weld. Two ex-Heysham 1 power station headers (432 mm outside diameter by 63.5 mm thick)

were utilised as the base material for the test specimen. The material specification of the original header was ASME II: 1968 Part A: SA-182F-316H. The headers were bore machined to achieve the required thickness of 19.6 mm and then solution heat treated (for one hour at 1050°C followed by air cooling) to remove all residual stresses from machining operation. The pipe ends were then machined with weld preparations according to original manufacturing welding specifications for Heysham 1 PS Boiler spines and the two matching sections were welded together in accordance with original welding parameters (Fig. 2.13a). The following two deviations from the original weld specifications were agreed:

The original weld procedures were specified for the horizontal fixed position, which would have required positional welding and therefore a variation of heat input around the circumference. It was therefore decided to rotate the specimens during welding in order to carry out welding in a constant position, thereby minimising any circumferential variation in heat input.

The internal purge was originally specified as 8 – 10 cubic ft/hr. The use of nitrogen is not common practice and a more conventional high purity argon purge was applied. This would have no influence on the development of residual stress.

The root was made using Tungsten inert gas welding method utilising a BS 2901 Part 2 316S92 2.4 mm diameter filler wire. The remainder of the weld was filled using manual metal arc (MMA) welding method using Babcock 'Type S' electrodes of varying size conforming to BS 2926 19.12.3LBR. A sketch of the weld bead deposition sequence is shown in Fig. 2.13b and a macrograph of part of the weld in Fig. 2.14. Table 2.2 summarises the MMA electrode sizes and welding conditions used. The average electrical heat input of the passes is estimated to be 1.4 kJ/mm.

Fig. 2.12 TRAINSS Pipe

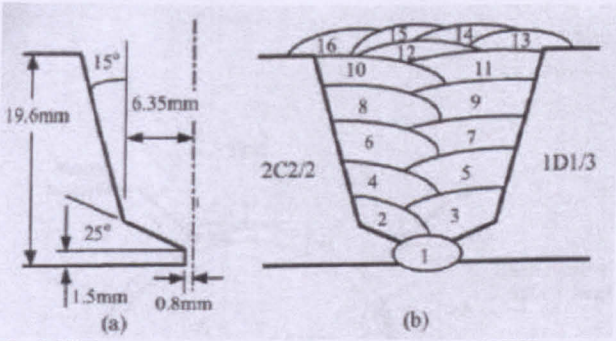

Fig. 2.13 Test component geometry showing girth weld [85]

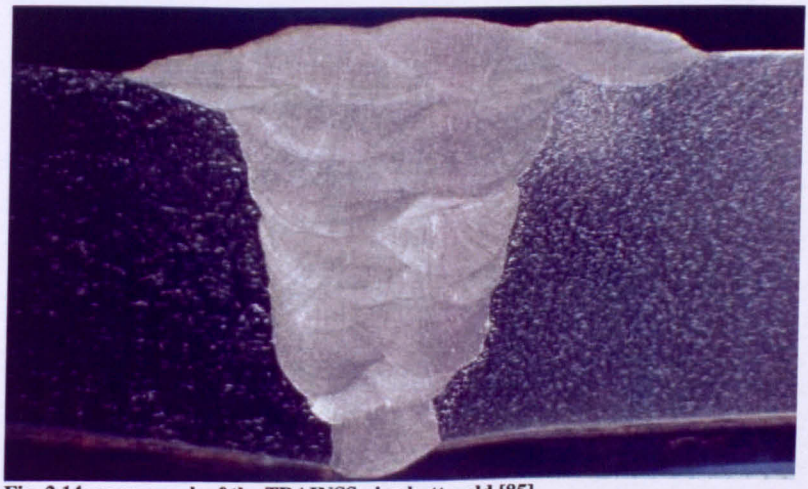

Fig. 2.14 macrograph of the TRAINSS pipe butt weld [85]

The location and orientation of the TRAINSS cuboids is shown in Fig. 2.15. A section of the weld was removed from the location as shown in Fig. 2.15. The cuboids were machined from this section in various orientations e.g. axial, hoop and radial. Both

ends of the removed section were etched (Fig. 2.16) to confirm that the cubes were machined from the weld metal only. The size of the cuboids was 10 mm x 7 mm x 7mm. The cuboids were machined in such a way the loading axis for each orientation was always the 10 mm dimension of the cube.

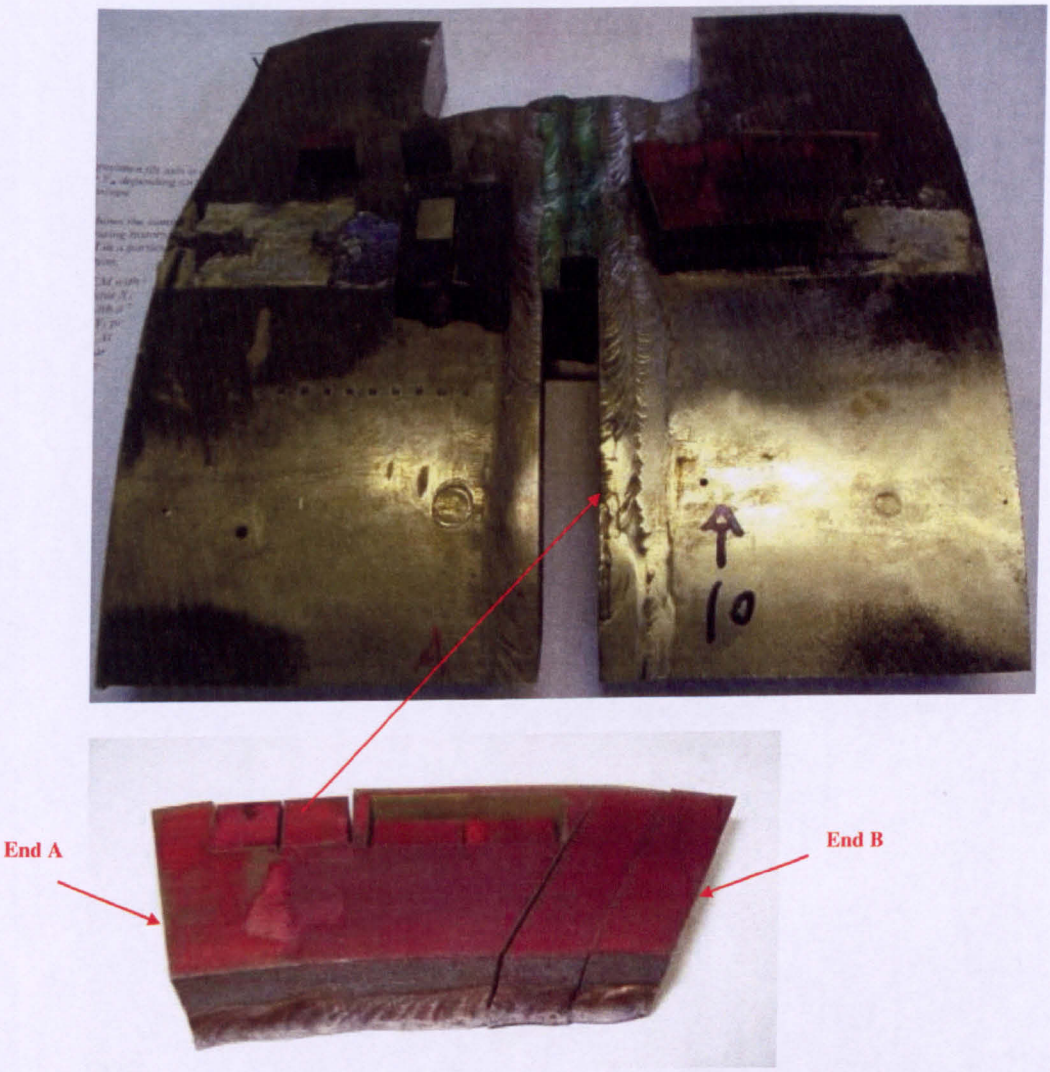

Fig. 2.15 Schematics of cuboids machined from the pipe butt weld

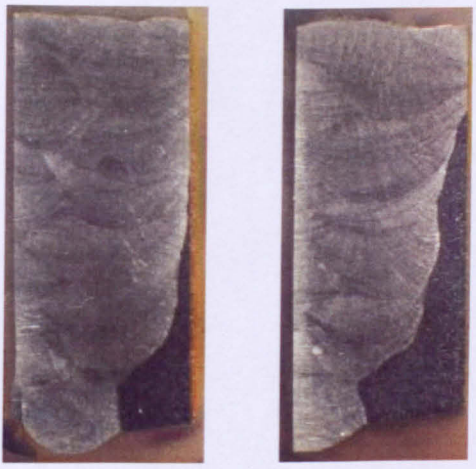

Fig. 2.16 **(a) end A** **(b) end B**
Ends of the pipe butt weld were etched to confirm that the cuboids have been machined from the weld metal

Table 2.2 Girth weld pass data [85]

Weld Passes	**Electrode Diameter (mm)**	**Current, I (A)**
1	2.4	90
2 - 3	2.4	70
4 - 5	3.2	120
6 - 9	3.2	135
10 - 12	4.0	155
13 - 16	3.2	135

2.6.4 Multi-Pass TIG Weld Cuboids

TIG weld cuboids were machined from an 8 pass TIG groove weld (Fig. 2.17 and Fig. 2.18). A 304 stainless steel plate was machined to 200x150x20 mm blanks to produce the groove weld plate specimens [87]. In the center of each specimen, a 10 mm groove was machined. The specimens were solution annealed (in a vacuum furnace) at 1050°C, followed by gas fan quenching to relieve machining residual stresses from the blank after machining. Weld metal was laid down within each groove of the treated blank. TIG welding was carried out with a type 308L filler wire, 0.9 mm in diameter using argon as a shielding gas. The typical composition of an austenitic 308 weld is:

Table 2.3 Chemical composition (wt%) of the austenitic 308 weld.

C	Si	Mn	Cr	Ni	N
0.05	0.5	1.7	20.2	9.4	0.06

The tungsten electrode was the cathode and a pulsed current was used with the peak current ranging from 180 – 200 A and with the background current of 130 – 150 A. The peak current was applied for 50% duration of each cycle with a pulse frequency of 1 Hz. The nominal heat input was approximately 1.3 kJ/mm and the welding speed was 75 mm/min. The inter-pass temperature remained at 70°C for each pass and the plates were not restrained.

The first pass was placed along the groove centreline filling the base of the groove with subsequent passes being laid down at either side of the center line.

The TIG cuboids were compressed along two principal orientations LD and TD. The size of the cuboid for the LD orientation was 7.55 mm x 8.12 mm x 14.54 mm.

The size of the cuboid for the TD orientation was 8.01 mm x 7.28 mm x 14.68 mm.

The loading axis was always along the 14 mm dimension.

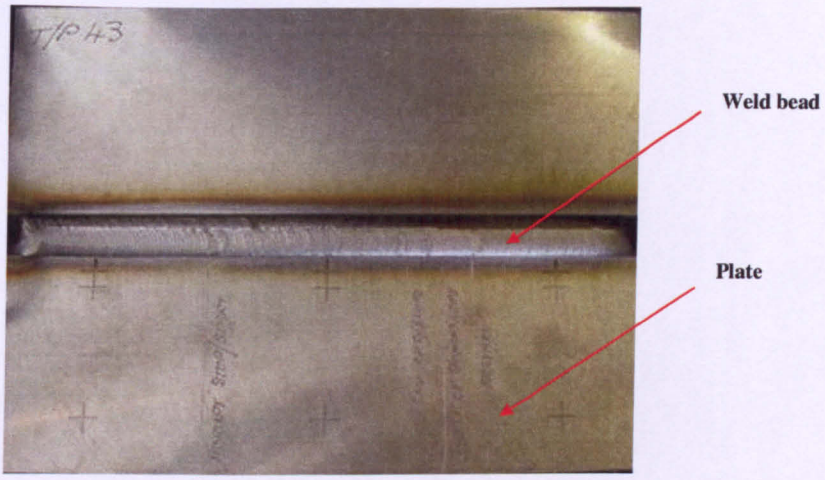

Fig. 2.17 TIG groove weld plate (plan view)

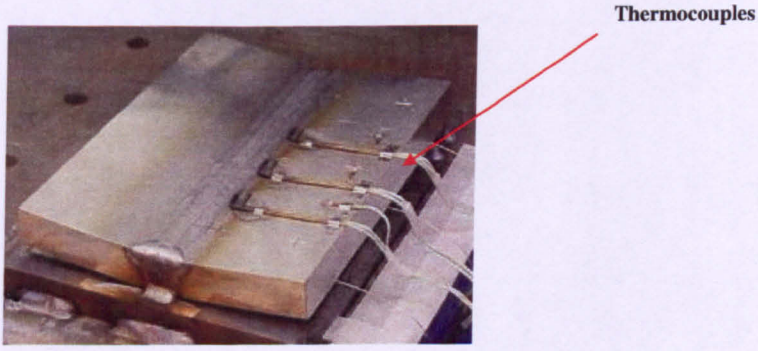

Fig. 2.18 TIG groove weld plate (3D view)

2.7 Principles of Fusion Welding

Fusion welding involves melting the area to be welded with a localised heat input as shown in Fig. 2.19 [88].

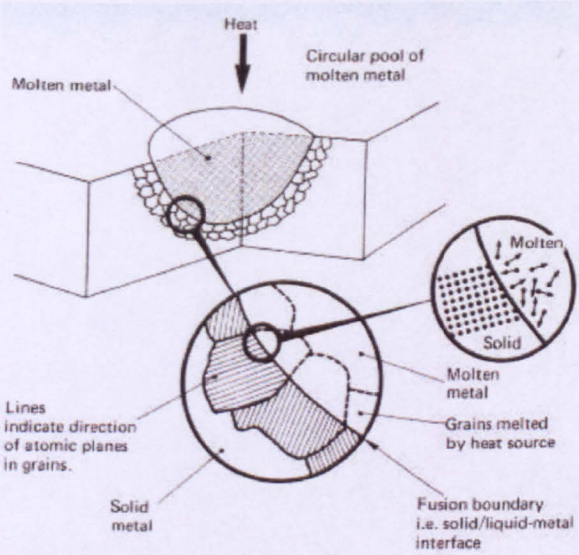

Fig. 2.19 Formation of molten pool [88]

Molten metal intersects the solid metal at the fusion boundary. The molten pool is devoid of any lattice structure and the atoms move randomly. Solidification takes place when the molten metal cools and the direction of solidification is opposite to that of heat flow, as shown in Fig. 2.20.

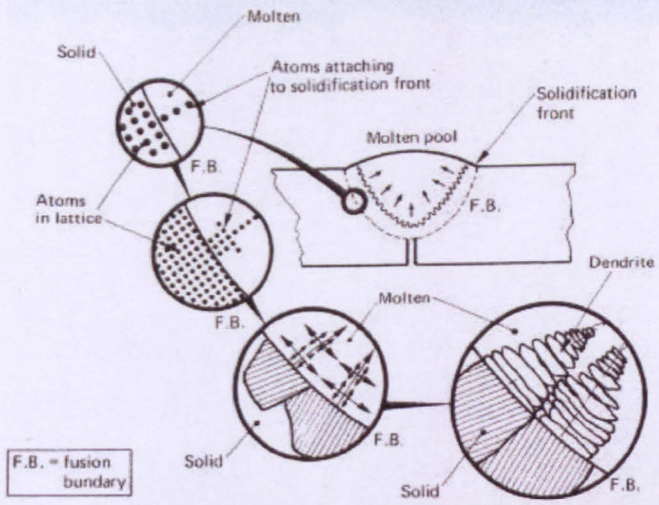

Fig. 2.20 Stages in solidification and formation of dendrites [88]

Dendritic solidification takes place when the atoms in the solid metal provide spare bonds to the solidifying atoms and the lattice plane is extended into the molten pool. Dendrites are formed in the liquid metal and these dendrites also grow laterally.

2.7.1 The Heat Affected Zone

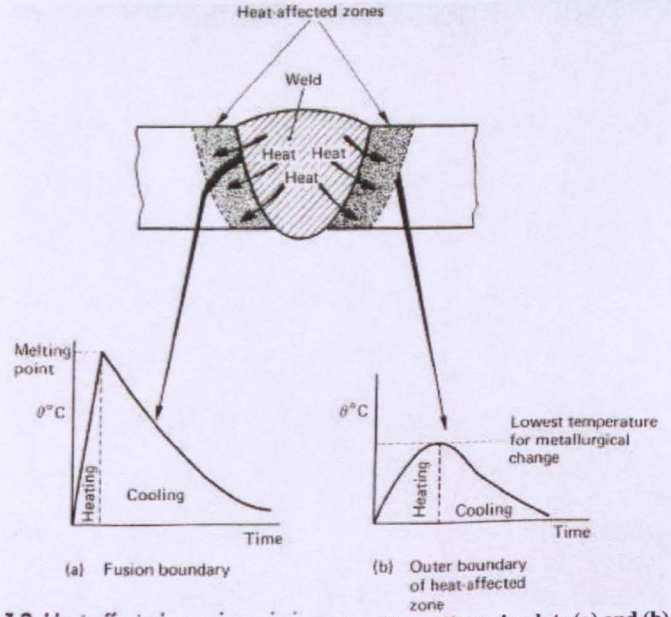

Fig. 2.21 Heat affected zone boundaries. The ordinate in plots (a) and (b) is temperature. [88]

During the solidification the majority of the heat flows through the parent metal on each side of the joint and a small amount of heat escapes through the surface of the pool (Fig. 2.21). The parent metal is subjected to heating and cooling cycles. This thermal cycle causes metallurgical change in the affected region and this region is called the heat-affected zone.

2.8 Optical Microstructure of Welds

Homogeneous wrought austenitic stainless steels generally exhibit an austenitic microstructure at room temperature [2]. However, during welding these materials may solidify with a structure containing some retained ferrite at room temperature. This depends on the composition of the austenitic stainless steel as well. Using a Schaeffler diagram and alloy chemical composition the as-welded ferrite content can be predicted by plotting the calculated Ni and Cr equivalents (Ni_{eq} and Cr_{eq}) [8].

Cr_{eq} = [wt % Cr] + 1.5 [wt % Si] + [wt % Mo] + 0.5 [wt % Nb] + 2 [wt % Ti]

Ni_{eq} = [wt % Ni] + 0.5 [wt % Mn] + 30 [wt % C] + 30 [wt % N-0.06]

The fusion zone of austenitic stainless steels exhibits a room-temperature microstructure which is dependent upon the solidification behaviour and subsequent solid-state transformations [89]. The solidification occurs as either primary ferrite or primary austenite in the austenitic stainless steels, depending upon the specific composition. A shift from primary ferrite to primary austenite may take place with small changes in the composition. Both solidification modes are possible in the composition range of many austenitic stainless steels. In the solid state additional transformations can occur upon cooling to room temperature after solidification. For austenitic stainless steel weld metals there are four solidification and solid-state transformation possibilities. Table 2.4 lists these reactions and these are related to the Fe-Cr-Ni phase diagram in Fig. 2.22.

Table 2.4. Solidification Types, Reactions, and Resultant Microstructures [90]

Solidification Mode	Reaction	Microstructure
A	$L \rightarrow L + A \rightarrow A$	Fully austenitic, well-defined solidification structure
AF	$L \rightarrow L + A \rightarrow L + A + (A + F)_{eut} \rightarrow A + F_{eut}$	Ferrite at cell and dendrite boundaries
FA	$L \rightarrow L + F \rightarrow L + F + (F + A)_{per/eut} \rightarrow F + A$	Skeletal and/or lathy ferrite resulting from ferrite to austenite transformation
F	$L \rightarrow L + F \rightarrow F \rightarrow F + A$	Acicular ferrite or ferrite matrix with grain boundary austenite and Widmanstätten side plates

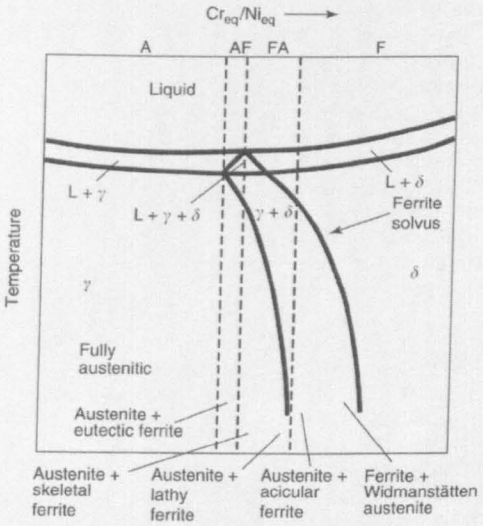

Fig. 2.22 Relationship of the solidification type to the pseudo-binary phase diagram [90]

Austenite is the first phase to form upon solidification in the A and AF modes of solidification. Delta ferrite is the primary phase in the FA and F solidification modes. Ferrite being unstable at lower temperatures, additional micro-structural modification occurs in the solid state for the FA and F types after solidification.

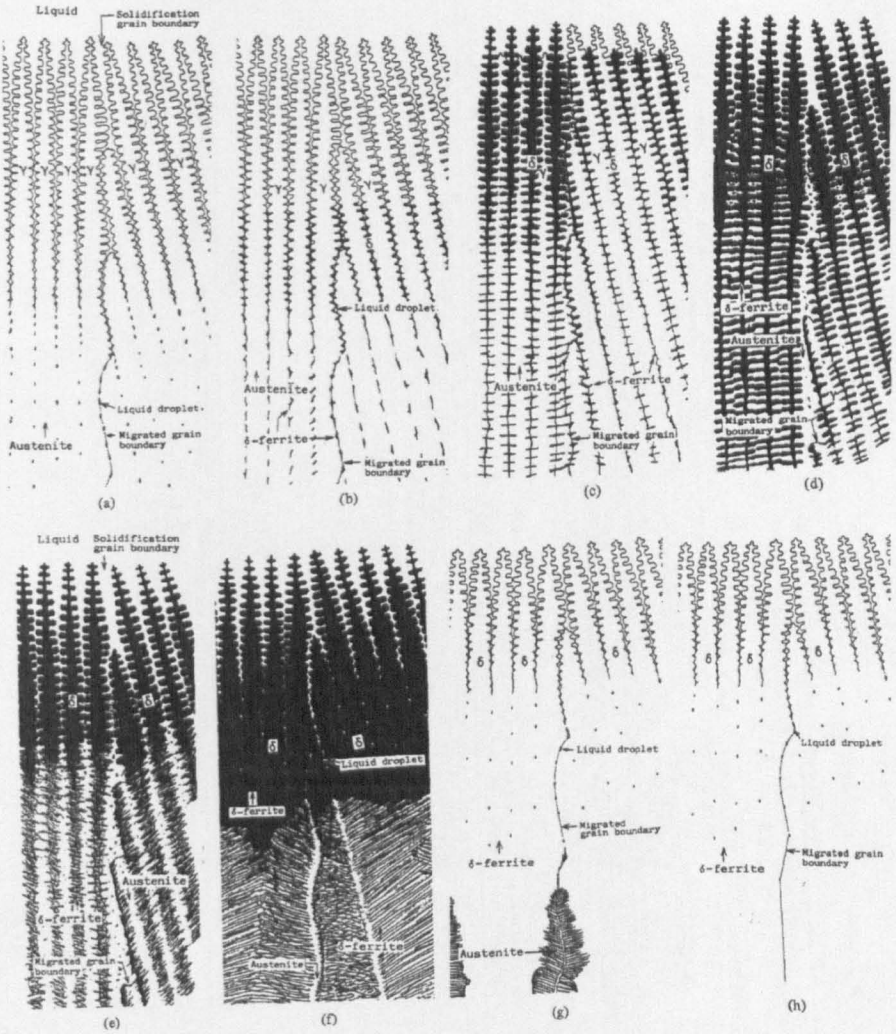

Fig. 2.23 Schematic representation of solidification and solid-state transformation behaviour resulting in different characteristic morphologies of weld metal microstructures [4]:
(a) Mode A (fully austenite)
(b) Mode AF (Intercellular eutectic ferrite)
(c) Mode EF (eutectic ferrite)
(d) Mode FA (vermicular ferrite)
(e) Mode FA (lathy ferrite)
(f) Mode F (acicular ferrite)
(g) Mode F (Widmanstatten austenite)
(h) Mode FF (Fully ferrite)

2.9 Mode A: Fully Austenitic Solidification

The welds which solidify as primary austenite have relatively high nickel equivalent ($Cr_{eq} < 1.48\ Ni_{eq}$) [91]. These welds are usually ferrite free or have ferrite content less than 6%. The general structure of mode A welds is characterised by large growth units; blocks which are often elongated in the direction of heat flow, i.e. in the growth direction. The grain structure of the austenite is approximately similar to the block structure, but generally the grain boundaries do not coincide exactly with the block boundaries. These are sometimes pinned by inclusions or by delta ferrite in low ferrite welds. The solidification is either cellular or cellular dendritic, the cell size being 10 to 15 μm. The delta ferrite is located only at the boundaries of the cells or dendrites, not at their axes. This solidification mode is shown schematically in Fig. 2.23a.

2.10 Ferritic-Austenitic Solidification Modes

This solidification mode is observed in those welds which have the equivalent ratio range ($1.48 < Cr_{eq}/Ni_{eq} < 1.95$) [92]. The ferrite content of these welds normally ranges from 4 to 18 % and it increases with the Cr_{eq}/Ni_{eq} ratio.

2.10.1 Mode AF Solidification

The solidification is termed mode AF if some ferrite forms at the end of the primary austenite solidification process via a eutectic reaction. This occurs if during solidification sufficient ferrite forming elements (mainly Cr and Mo) partition to the solidification sub-grain boundaries to promote the formation of ferrite as an end solidification product. Relatively stable ferrite forms along the boundary and during weld cooling it resists transformation to austenite as it is already enriched in the ferrite forming elements. Fig. 2.23b shows a schematic of Mode-AF solidification.

2.10.2 Mode FA Solidification

The solidification is termed mode FA when some austenite forms at the end of solidification and the solidification occurs as primary ferrite. The austenite exists at the ferrite solidification boundaries at the end of the solidification and forms via a peritectic-eutectic reaction. The ferrite becomes increasingly unstable as the weld metal cools through the two phase delta ferrite + austenite field and a diffusion controlled reaction the austenite starts to consume the ferrite.

A vermicular or skeletal ferrite morphology results when the weld cooling rates are moderate and/or when the Cr_{eq}/Ni_{eq} is low but still within the FA range. The skeletal microstructure is shown schematically in Fig. 2.23d and in the micrograph in Fig. 2.24a.

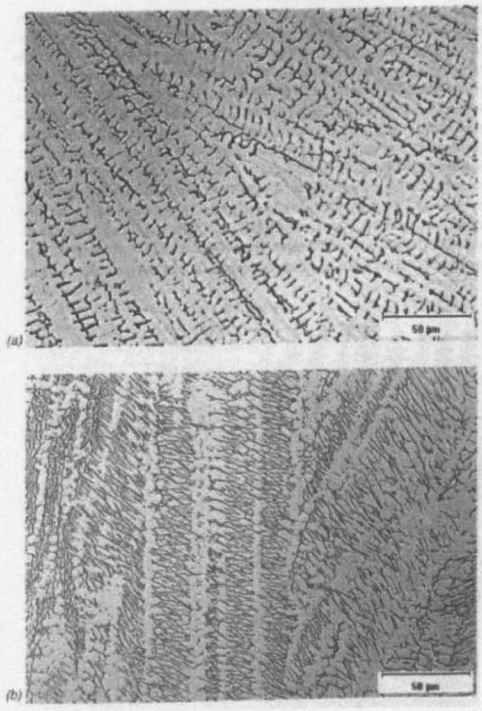

Fig. 2.24 Fusion zone microstructure resulting from mode FA solidification: (a) skeletal ferrite; (b) lathy morphology [90].

Lathy ferrite morphology results when the cooling rates are high and/or when the Cr_{eq}/Ni_{eq} increases within the FA range. Due to restricted diffusion during the ferrite-austenite transformation the lathy morphology forms in place of the skeletal morphology. Fig. 2.23e shows the schematic of lathy ferrite morphology and the micrograph is shown in Fig. 2.24b.

2.11 Mode F solidification

The solidification is termed as Mode F when $Cr_{eq}/Ni_{eq} > 1.95$ and the ferrite content is 10 to 85% [93]. The typical lathy ferrite structure occurs at the low values of the ratio of the equivalents ($1.95 < Cr_{eq}/Ni_{eq} < 2.3$), when the austenite forms a matrix at room temperature i.e. it is the majority phase. At higher values ($Cr_{eq}/Ni_{eq} > 2.3$) the ferrite forms a matrix at the room temperature and the austenite is present in lathy form. The microstructure resulting from the Mode-F solidification is a function of composition and cooling rate. An acicular or lathy ferrite structure (Fig. 2.23f) will form within the ferrite grains at low Cr_{eq}/Ni_{eq} values within the F range. The microstructure will consist of ferrite matrix with grain boundary austenite and Widmanstatten austenite (Fig. 2.23g) plates that nucleate at the grain boundary austenite or within the ferrite grains, at higher Cr_{eq}/Ni_{eq} values.

2.12 Optical Microstructures from Present Work

Several types of welds have been investigated in the present work. These include 316 multi-pass weld-pad, 316 multi-pass pipe butt weld and 308 multi-pass TIG weld. The following sections provide details about the sample preparation details for metallographic examination and optical microstructures observed in the welds.

2.12.1 Sample Preparation for Metallographic Examination and EBSD

For metallographic examination the specimens were mounted in Bakelite moulds using a Metaserv automatic mounting press. After mounting in Bakelite the specimens

were ground using a Buehler grinder with grit sizes of 220, 500 and 1200. The force was set to 10 lb at 140 RPM and each grit size was used for 5 minutes.

After grinding the specimens were polished in a Struers polisher. A Struers Roto Force–4 polisher was used. The force was set to 20 N and the RPM to 150. The specimen was polished with diamond suspension of 9 μm, 6 μm and finally 1 μm to get a mirror finish.

For EBSD texture analysis, the specimens were electrolytically polished at 22 V, 300 mA for 20 s. The electrolyte used was Struers A2-1 electrolyte. A map was obtained on a 2mm x 2mm region, with 5 μm steps between each measurement. EBSD measurements were carried out on a Zeiss SUPRA 55 VP SEM. The SEM was operated at 20 kV with the sample tilted at 70°.

2.12.2 Multi-Pass Weld Pad

Cr_{eq} = [18.4] + 1.5 [0.26] + [2.05] = 20.84

Ni_{eq} = [11.41] + 0.5 [1.09] + 30 [0.032] + 30 [0.059-0.06] = 12.885

Cr_{eq}/Ni_{eq} = 1.617

The optical microstructures from the multi-pass weld-pad are shown in Fig. 2.25. The microstructure exhibits a skeletal ferrite morphology as shown in Fig. 2.23d and Fig. 2.24a. The dark phase is ferrite and the lighter phase is austenite. The direction of the dendrites is along the sample normal direction. The dendrites are several mm long along the heat flow direction.

2.12.3 Multi-Pass TRAINSS Pipe Butt Weld

TRAINSS pipe butt weld has a chemical composition similar to that of the weld-pad. The optical microstructures from the TRAINSS weld are shown in Fig. 2.26. The microstructure exhibits a skeletal ferrite morphology as shown in Fig. 2.23d and Fig. 2.24a. The dark phase is ferrite and the lighter phase is austenite. The direction of the

dendrites is along the sample normal direction. The dendrites are several mm long along the heat flow direction.

2.12.4 Multi-Pass TIG Weld

Cr_{eq} = [20.2] + 1.5 [0.5] = 20.95

Ni_{eq} = [9.4] + 0.5 [1.7] + 30 [0.05] + 30 [0.06-0.06] = 11.75

Cr_{eq}/Ni_{eq} = 1.78

The optical microstructures from the multi-pass TIG weld are shown in Fig. 2.27. The microstructure exhibits a skeletal ferrite morphology as shown in Fig. 2.23d and Fig. 2.24a. The dark phase is ferrite and the lighter phase is austenite. The direction of the dendrites is along the sample normal direction. The dendrites are several mm long along the heat flow direction.

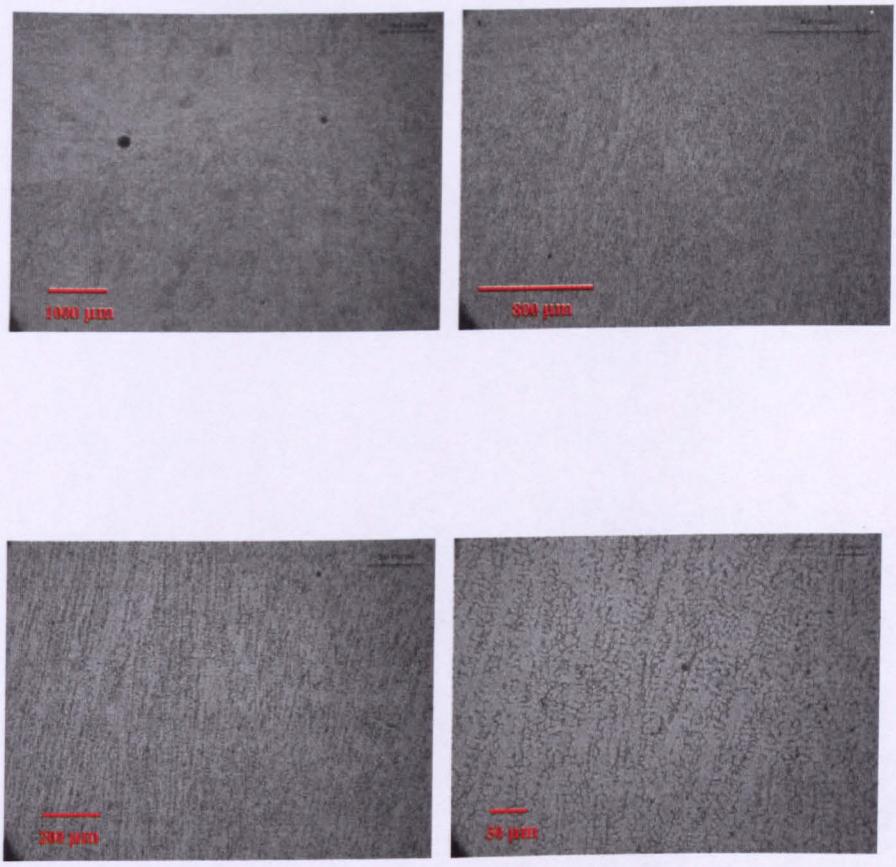

Fig. 2.25 Multi-pass weld-pad: Optical micrographs at different magnifications

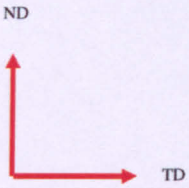

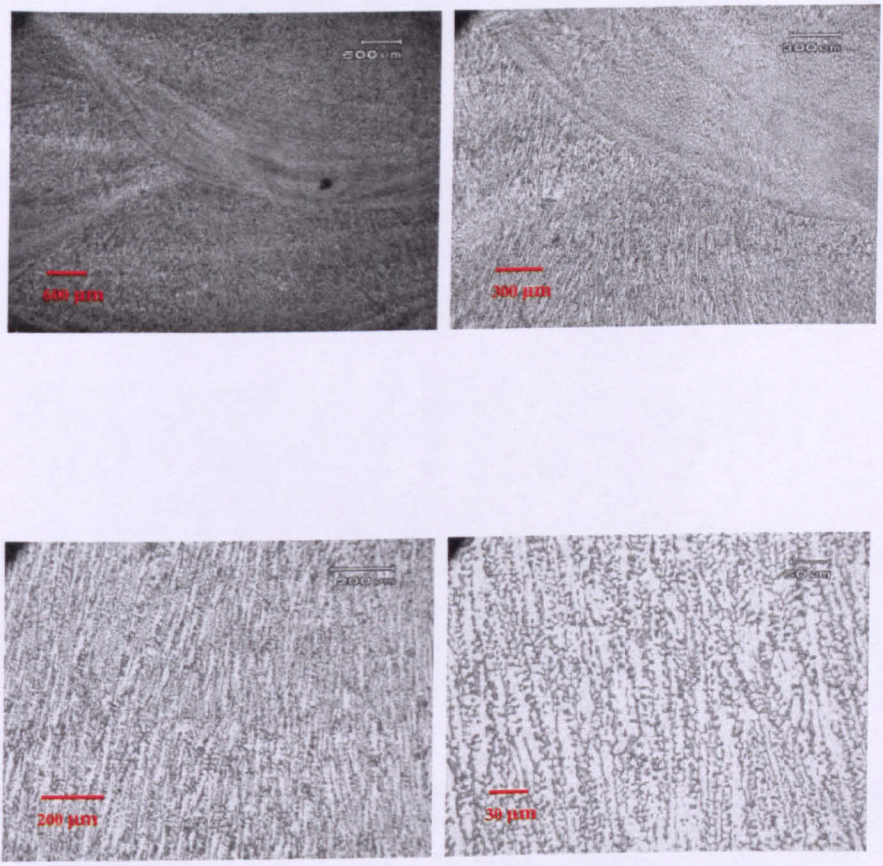

Fig. 2.26 Multi-pass TRAINSS pipe butt weld: Optical micrographs at different magnifications

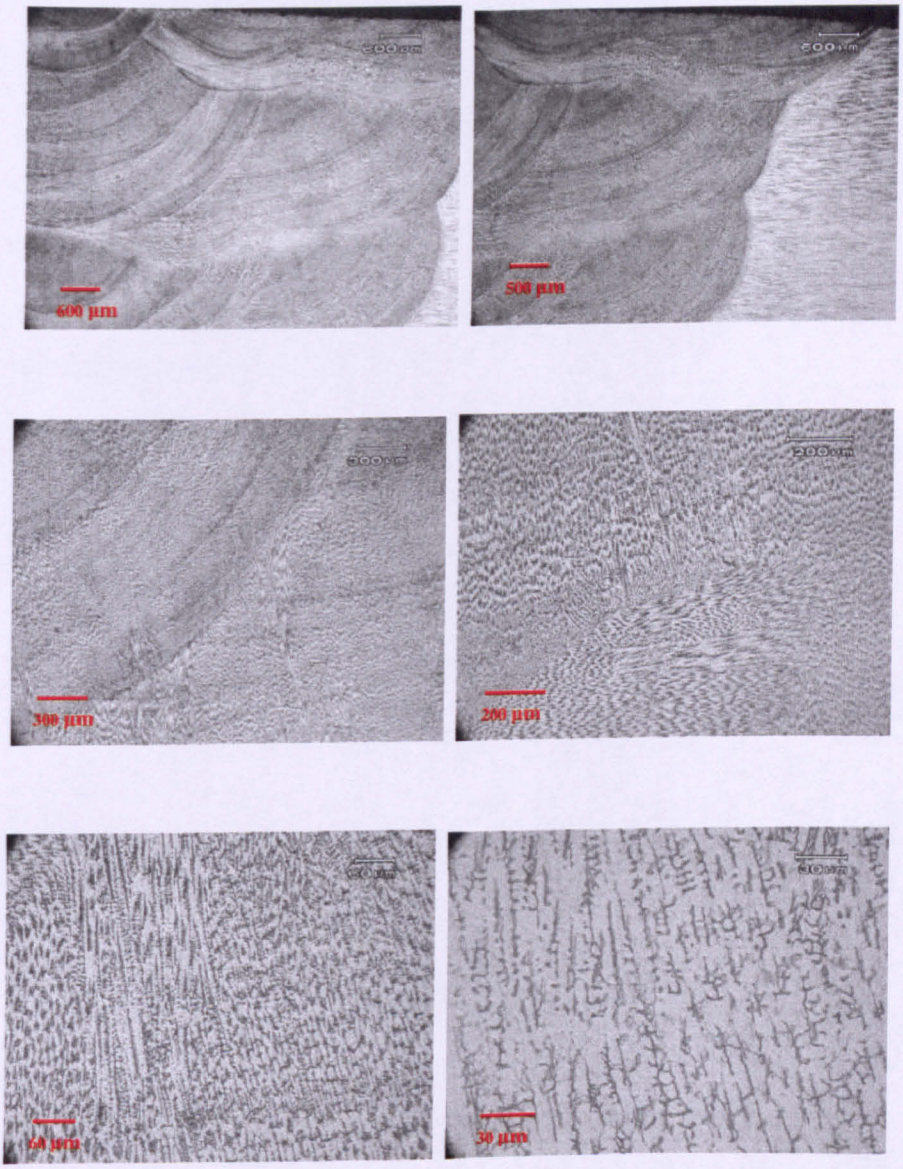

Fig. 2.27 Multi-pass TIG weld: Optical micrographs at different magnifications.

2.13 Summary

The geometry and manufacturing details of various specimens used in various tests have been described. Welding solidification, metallurgy and microstructure have been reviewed in this chapter. Weld microstructure results obtained using optical microscopy have been presented. The next chapter will provide details on fundamentals of texture and measurement of texture using electron and neutron diffraction on various types of weld specimens.

Chapter 3 Texture Analysis of Welds

This chapter provides details about the results obtained from EBSD and neutron diffraction texture measurements on various types of welds. The welds investigated were 316 multi-pass MMAW Weld-Pad, 316 multi-pass MMAW pipe butt weld and 308 multi-pass TIG weld. The fundamentals of texture analysis and the details about the techniques used to measure texture have been described in chapter 1. The manufacturing details about various specimens have been described in chapter 2.

3.1 Results and Discussion

3.1.1 The ODF Sections

The texture results are presented in the form of pole figures and ODF sections in the following sections. In those cases where the texture is simple e.g. in the case of the Weld-Pad which represents a recrystallization cube texture it can be interpreted that the ODF sections are also showing the cube orientations. Similarly for the TIG weld where the pole figures show a nearly random texture it can be interpreted that the ODF sections show the random texture. However, certain other orientations maybe present in the ODF sections which are difficult to interpret.

3.1.2 Multi-Pass Weld-Pad

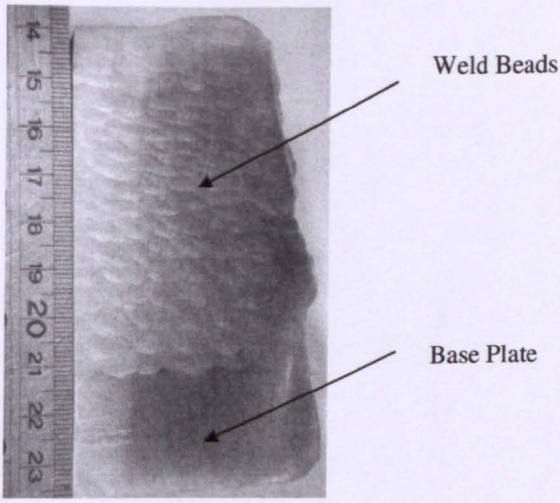

Fig. 3.1 Bead size in weld-pad

For production of the multi-pass weld-pad, a 5 mm diameter electrode was used. This resulted in a larger bead size as shown in Fig. 3.1 (approximate height 5mm and the width varies from 5mm to 10 mm). The amount of heat generated during the process was high (about 2 kJ/mm).

Because of the bigger bead size and high heat generated, the weld-pad remains at higher temperatures during the welding process and develops a very intense cube texture. This cube texture is a typical recrystallization texture.

Several samples were investigated for EBSD and neutron texture analysis. These included the actual samples (sample 4 and sample 15) which were tested in-situ using neutron diffraction (For details please refer to chapter 4), and cubes machined from the weld-pad.

The experimental pole figures for austenite from neutron texture for the sample 4 are shown in. The most intense texture is observed in the {200} pole figure with a times random intensity of 12.14. The recalculated and experimental pole figures for ferrite are shown in Fig. 3.5 and respectively. The ferrite {200} pole figure looks similar to

the austenite {200} pole figure. The ODF sections for austenite and ferrite are shown in Fig. 3.7 and Fig. 3.8 respectively.

The experimental pole figures for austenite from neutron diffraction texture for the sample 15 are shown in Fig. 3.9. The most intense texture is observed in the {200} pole figure with a times random intensity of 9.49. The recalculated and experimental pole figures for ferrite are shown in Fig. 3.10 and Fig. 3.11 respectively. The ferrite {200} pole figure looks similar to the austenite {200} pole figure. The ODF sections for austenite and ferrite are shown in Fig. 3.12 and

Fig. 3.13 respectively. The texture is more intense in the case of sample 15 as compared with the sample 4 which is evident from the ODF sections for austenite. The times random intensity for sample 15 is 13.06 as compared with 7.20 for the sample 4.

EBSD and neutron diffraction texture measurements were also carried out on the cubes machined from the weld. The details of these cubes are given in chapter 2. The EBSD map obtained from the cube machined from weld-pad is shown in Fig. 3.14. The grains are columnar and oriented towards the sample normal direction.

The EBSD pole figures for austenite and ferrite are shown in Fig. 3.15 and Fig. 3.16 respectively. The austenite and ferrite pole figures look similar and the {100} pole figures are the most intense. The experimental pole figures for austenite from neutron diffraction texture for the cubes machined from the weld-pad are shown in Fig. 3.17. The {200} pole figure is more intense with a times random density of 20.55. The recalculated and experimental pole figures for ferrite are shown in Fig. 3.18 and Fig. 3.19 respectively. The austenite {200} pole figure looks similar to ferrite {200} pole figure. The EBSD and neutron diffraction pole figures look similar. The ODF sections for the austenite from EBSD and neutron diffraction are shown in Fig. 3.20 and Fig.

3.21 respectively. The ODF sections for ferrite from EBSD and neutron diffraction are shown in Fig. 3.22 and Fig. 3.23 respectively.

The crystallographic texture generated in the weld-pad is the typical recrystallization cube texture. This type of texture has been reported in the literature and has been discussed in the chapter 1.

This texture is also called fiber texture in which certain crystallites orient themselves along a particular crystallographic direction. In the case of the weld-pad, the {200} planes orient themselves along the heat flow direction. This heat flow direction is at a certain angle from the sample normal direction.

3.1.3 TRAINSS Pipe Butt Weld

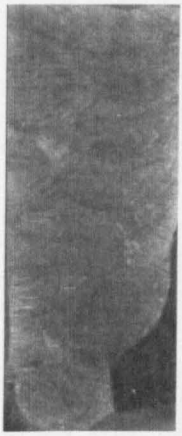

Fig. 3.2 Bead size in TRAINSS

During the welding of the TRAINSS pipe butt weld, the diameter of the electrode varied from 2.4 mm to 4.0 mm. The bead size in the TRAINSS pipe butt weld is smaller as compared to the Weld-Pad as shown in Fig. 3.2. The average heat input in this case is 1.4 kJ/mm. Also the cooling rate can be assumed faster as compared with the weld-pad as the heat generated during weld bead deposition is taken away by the surrounding material.

The TRAINSS pipe butt weld also develops a similar texture as the weld-pad, but the texture is less intense. The EBSD and neutron diffraction texture measurements were carried out on the cubes machined from the TRAINSS pipe butt weld. The details of these cubes are described in chapter 2. The EBSD microstructure map is shown in Fig. 3.24. The microstructure is columnar with the grains oriented towards the sample normal direction. The EBSD pole figures for austenite and ferrite are shown in Fig. 3.25 and Fig. 3.26 respectively. The austenite and ferrite pole figures from EBSD results look similar. The experimental pole figures for austenite from neutron diffraction texture measurement are shown in Fig. 3.27. The most intense texture is exhibited by the 200 pole figure with a times random density of 5.03. The recalculated and experimental pole figures for ferrite from neutron diffraction texture measurements are shown in
Fig. 3.28 and Fig. 3.29 respectively. The austenite {200} pole figure looks similar to the ferrite {200} pole figure. The ODF sections for the austenite from EBSD and neutron diffraction are shown in Fig. 3.30 and Fig. 3.31 respectively. The ODF sections for ferrite from EBSD and neutron diffraction are shown in Fig. 3.32 and Fig. 3.33 respectively. The texture exhibited by the TRAINSS pipe butt weld is much less intense as compared with the weld-pad.

3.1.4 Multi-Pass TIG Weld

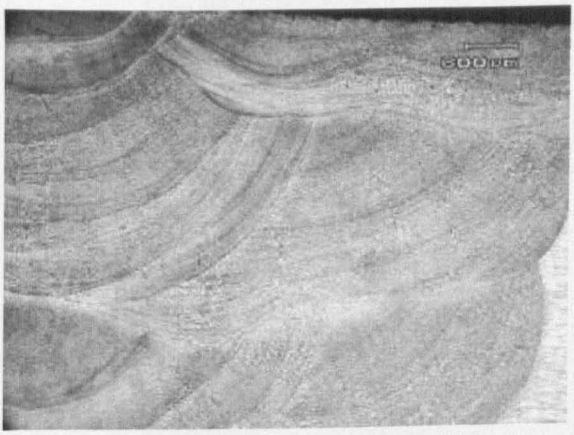

Fig. 3.3 Bead size in TIG weld

During the TIG welding a filler wire of diameter 0.9 mm was used. This has resulted in a very small bead size as shown in Fig. 3.3. The average heat input was 1.3 kJ/mm which is comparable to the heat input in TRAINSS pipe butt weld. However this heat input is lesser as compared with the multi-pass weld-pad. The EBSD and neutron diffraction texture investigations were carried out on the cubes machined from the TIG weld. The details of these cubes are described in chapter 2.

The EBSD microstructural map is shown in

Fig. 3.34. The EBSD pole figures for austenite and ferrite are shown in Fig. 3.35 and Fig. 3.36 respectively. The austenite pole figures from EBSD measurements exhibit very nearly a random texture. The experimental pole figures for austenite from neutron diffraction texture measurements are shown in Fig. 3.37. The {200} and {111} pole figures exhibit an intense texture with a times random intensity of 4.17 and 4.41 respectively. The recalculated and experimental pole figures for ferrite from neutron diffraction texture measurements are shown in

Fig. 3.38 and Fig. 3.39 respectively. The ODF sections for the austenite from EBSD and neutron diffraction are shown in

Fig. 3.40 and

Fig. 3.41 respectively. The ODF sections for ferrite from EBSD and neutron diffraction are shown in

Fig. 3.42 and

Fig. 3.43 respectively. The texture exhibited by the TIG weld is much less intense as compared with the weld-pad and it can be considered as nearly random texture.

3.1.5 B. E. Single Pass Weld

The neutron diffraction texture measurements were carried out on the cube machined from the B. E. Single Pass Weld. The details about the B. E. single pass weld are described in chapter 2. The experimental pole figures for austenite from neutron diffraction texture measurements are shown in Fig. 3.44. The {200} and {111} pole figures exhibit an intense texture with a times random intensity of 4.67 and 3.64 respectively. It appears like a {200} fiber texture where the {200} poles are oriented at an angle from the sample normal direction. The recalculated and experimental pole figures for ferrite from neutron diffraction texture measurements are shown in

Fig. 3.45 and

Fig. 3.46 respectively. The austenite {200} pole figure looks similar to the ferrite {200} pole figure. The ODF sections for the austenite and ferrite from neutron diffraction texture measurements are shown in Fig. 3.47 and

Fig. 3.48 respectively.

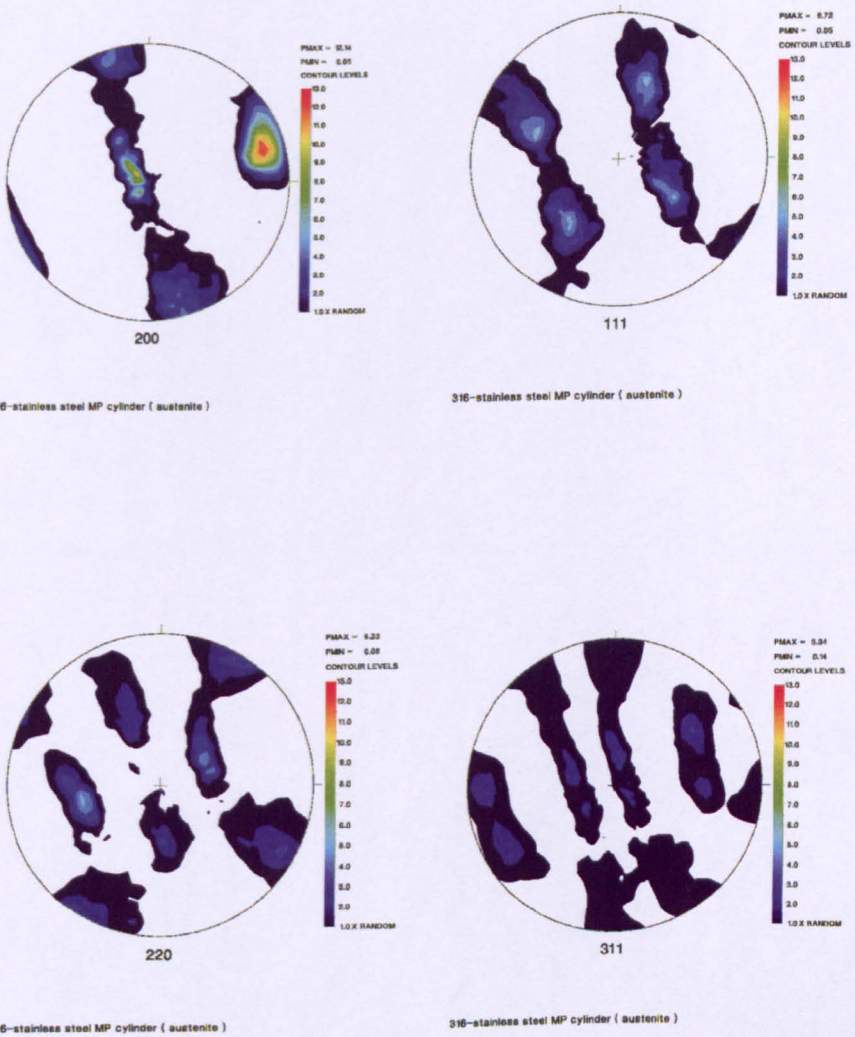

Fig. 3.4 Experimental pole figures (austenite): neutron diffraction texture: sample 4 (weld-pad)

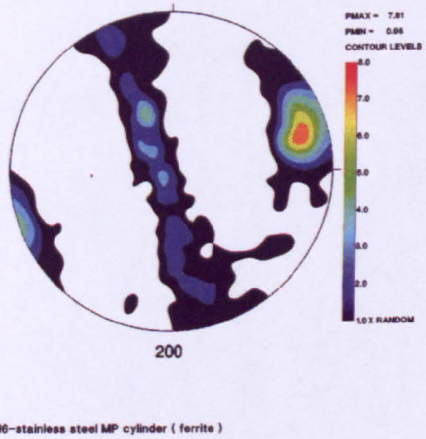

Fig. 3.5 Recalculated pole figure (ferrite): neutron diffraction texture sample 4 (weld-pad)

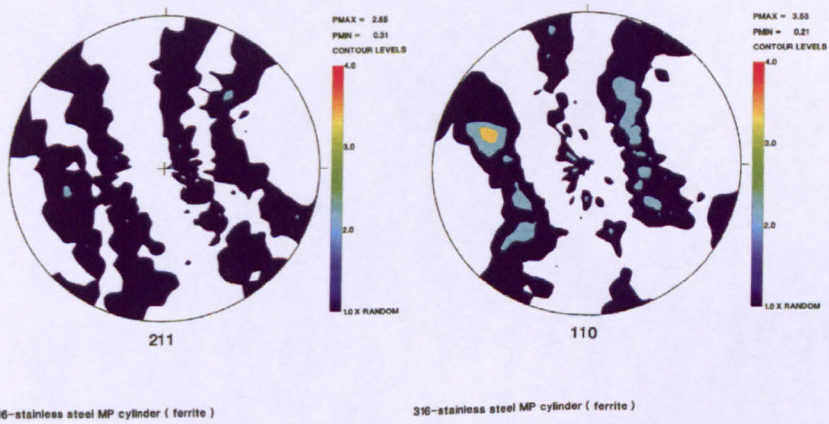

Fig. 3.6 Experimental pole figures (ferrite): neutron diffraction texture sample 4 (weld-pad)

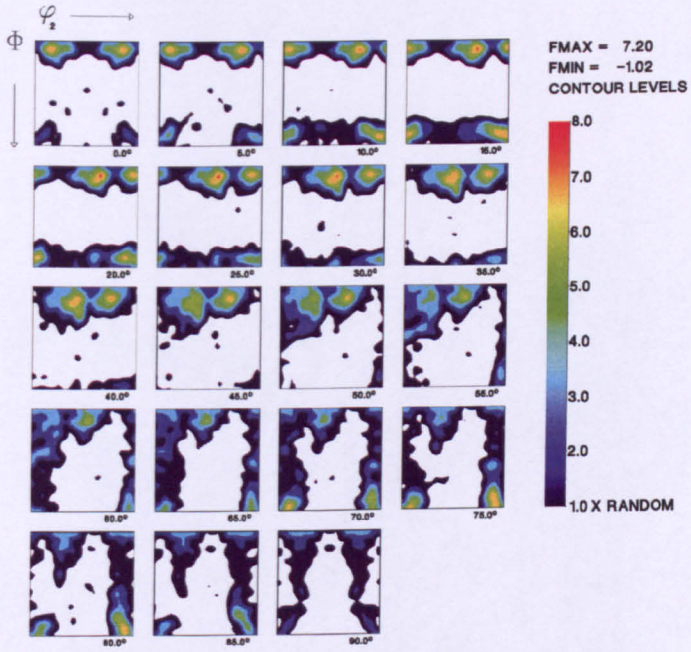

Fig. 3.7 ODF sections (austenite): neutron diffraction texture sample 4 (weld-pad)

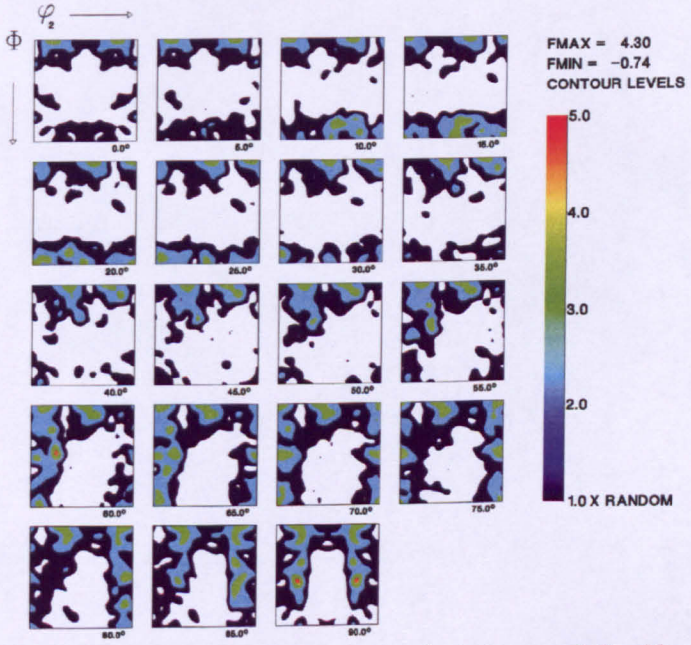

Fig. 3.8 ODF sections (ferrite): neutron diffraction texture sample 4 (weld-pad)

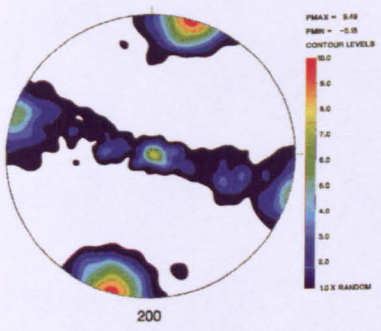

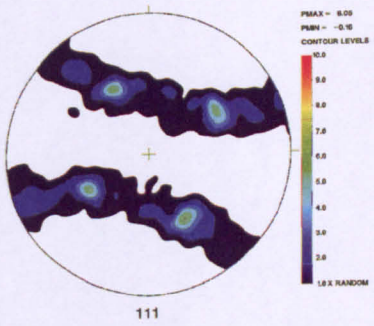

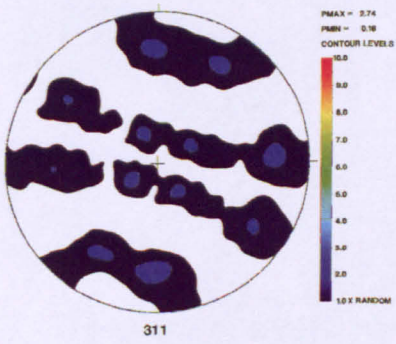

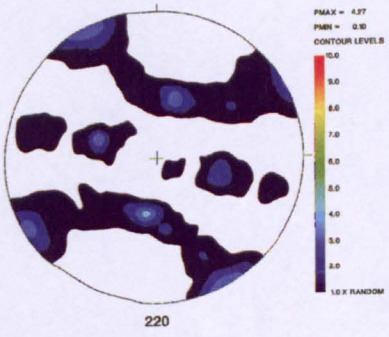

Fig. 3.9 Experimental pole figures (austenite): neutron diffraction texture sample 15 (weld-pad)

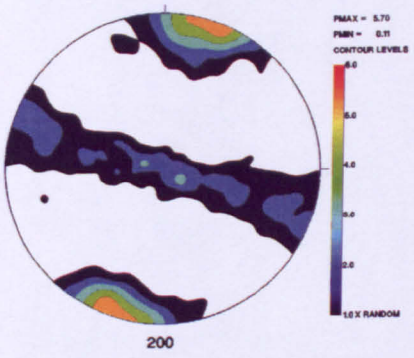

Fig. 3.10 Recalculated pole figure (ferrite): neutron diffraction texture sample 4 (weld-pad)

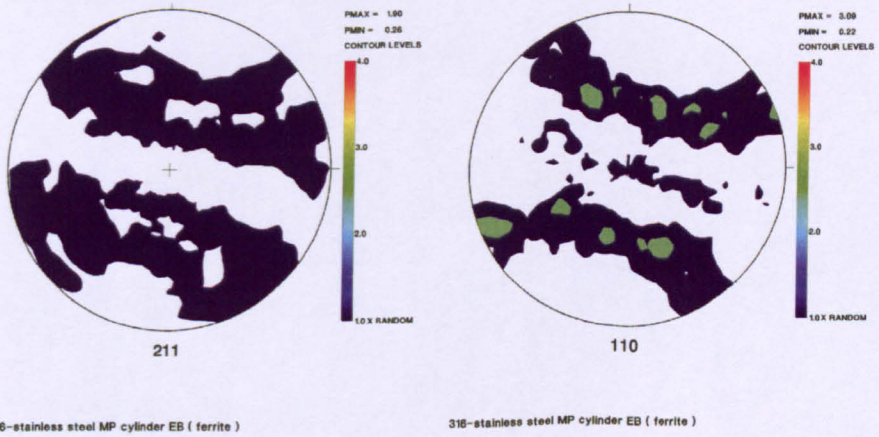

Fig. 3.11 Experimental pole figures (ferrite): neutron diffraction texture sample 15 (weld-pad)

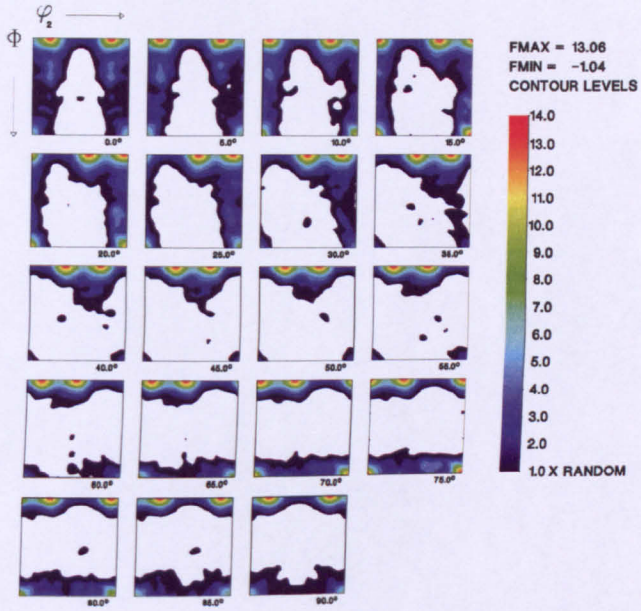

Fig. 3.12 ODF sections (austenite): neutron diffraction texture sample 15 (weld-pad)

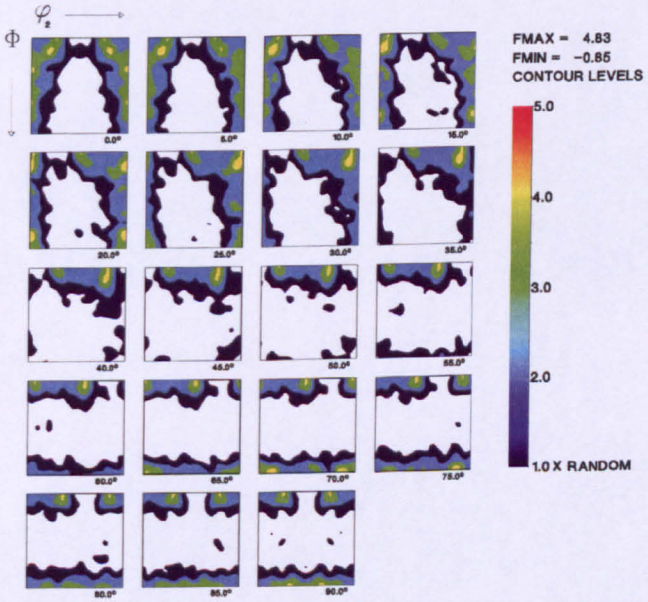

Fig. 3.13 ODF sections (ferrite): neutron diffraction texture sample 15 (weld-pad)

Fig. 3.14 EBSD microstructure map: cubes machined from 316 multi-pass weld-pad

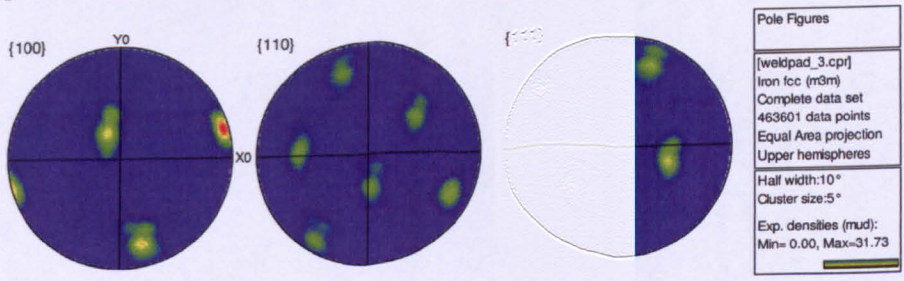

Fig. 3.15 Austenite pole figures: EBSD (cubes machined from weld-pad)

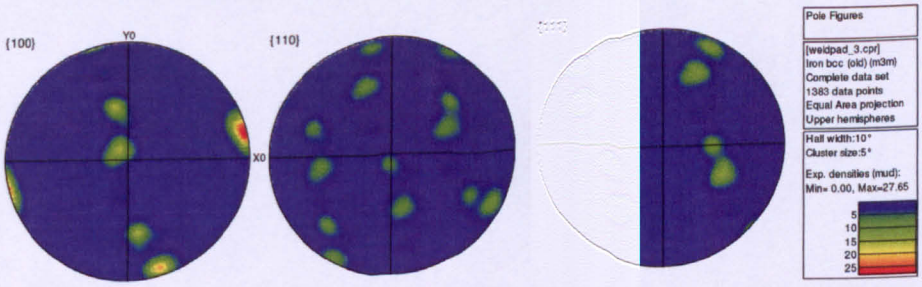

Fig. 3.16 Ferrite pole figures: EBSD (cubes machined from weld-pad)

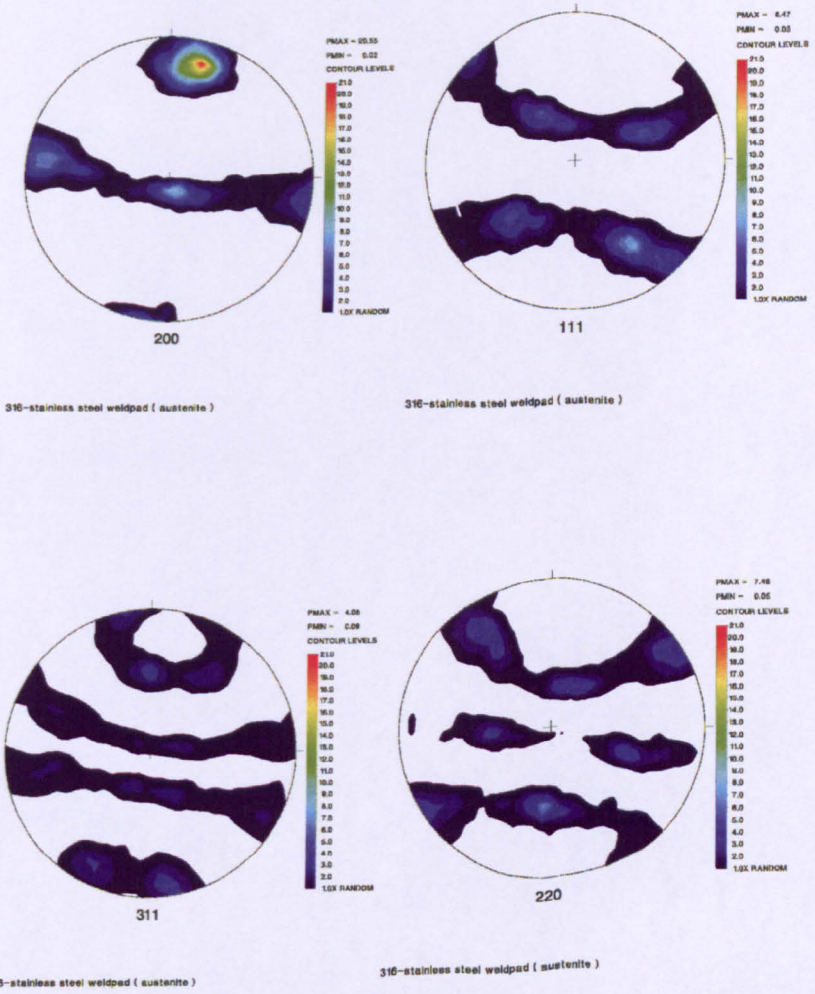

Fig. 3.17 Experimental pole figures (austenite): Neutron diffraction texture (cubes machined from weld-pad)

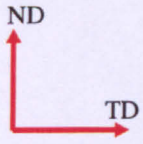

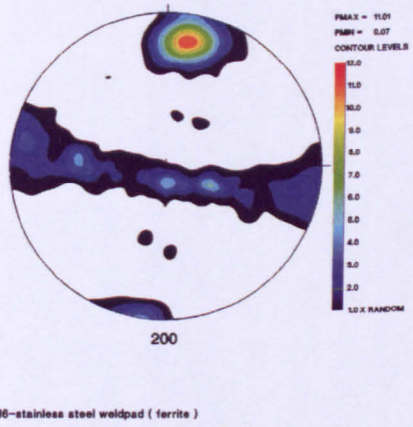

Fig. 3.18 Reclaculated pole figure (ferrite): Neutron diffraction texture (cubes machined from weld-pad)

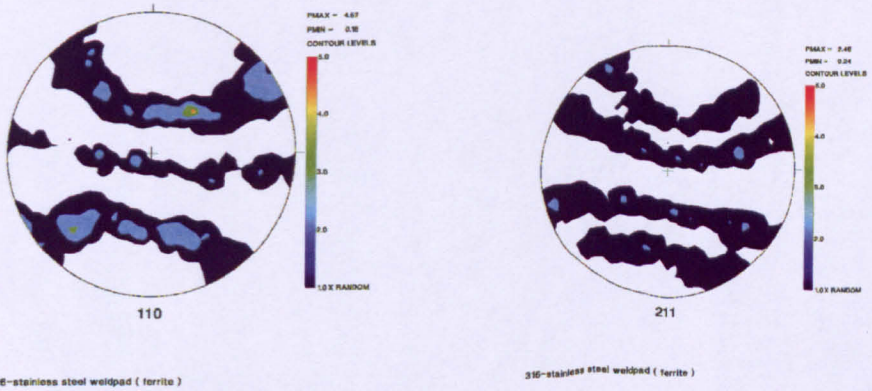

Fig. 3.19 Experimental pole figures (ferrite): Neutron diffraction texture (cubes machined from weld-pad)

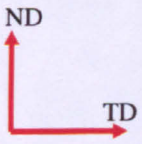

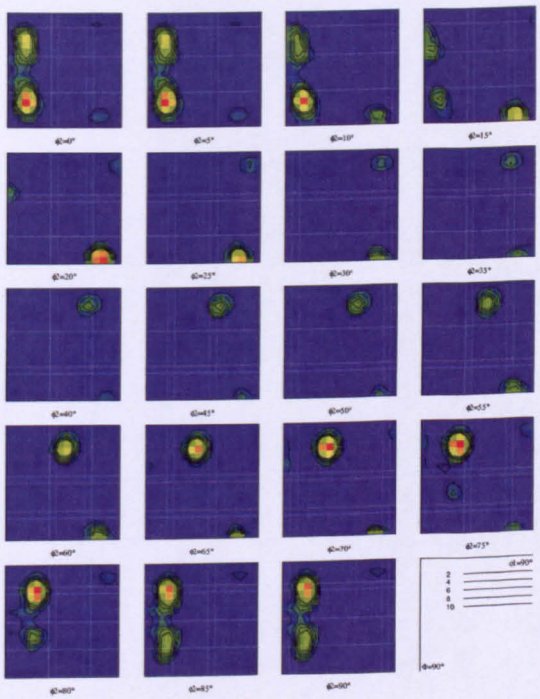

Fig. 3.20 ODF sections (austenite): EBSD (cubes machined from weld-pad)

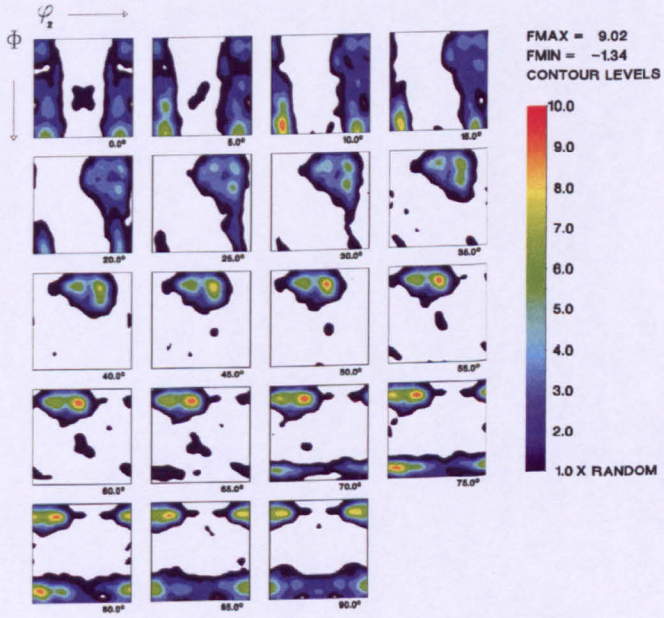

Fig. 3.21 ODF sections (austenite): neutron diffraction texture (cubes machined from weld-pad)

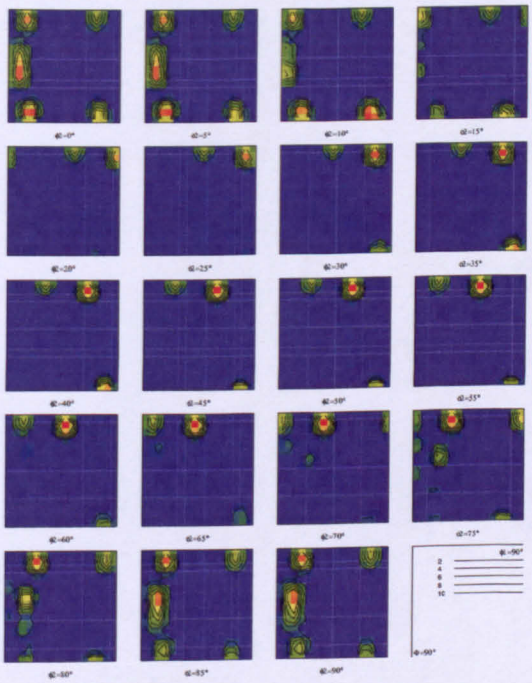

Fig. 3.22 ODF sections (ferrite): EBSD (cubes machined from weld-pad)

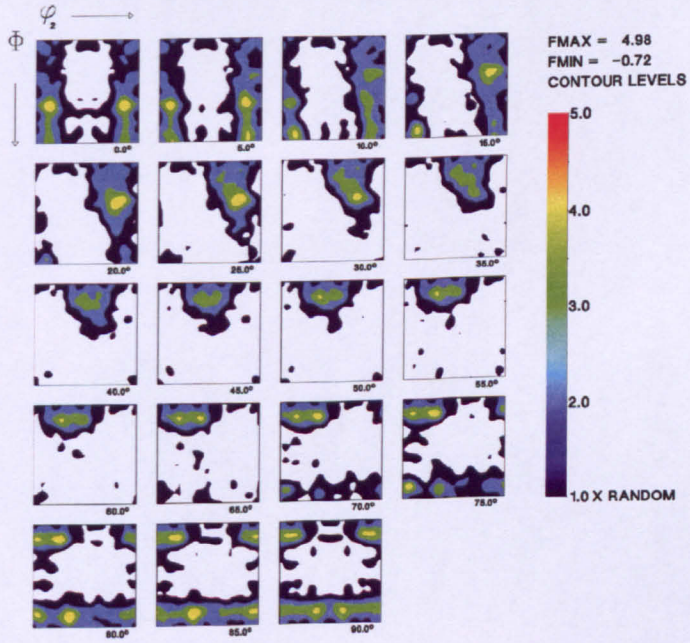

Fig. 3.23 ODF sections (ferrite): neutron diffraction texture (cubes machined from weld-pad)

Fig. 3.24 EBSD microstructure map (cubes machined from TRAINSS pipe butt weld)

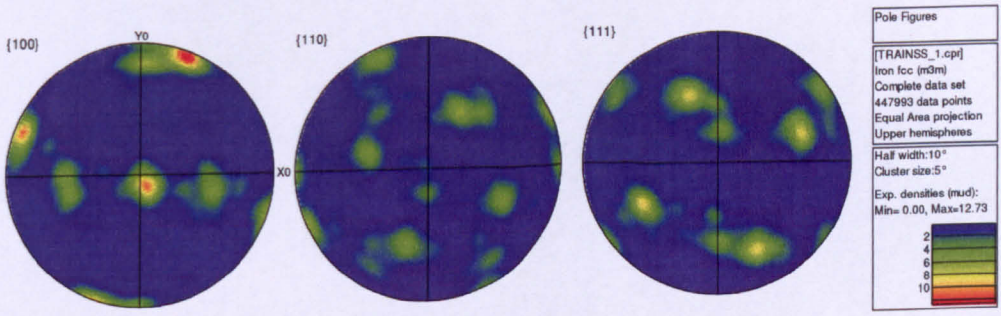

Fig. 3.25 Austenite pole figures: EBSD (cubes machined from TRAINSS pipe butt weld)

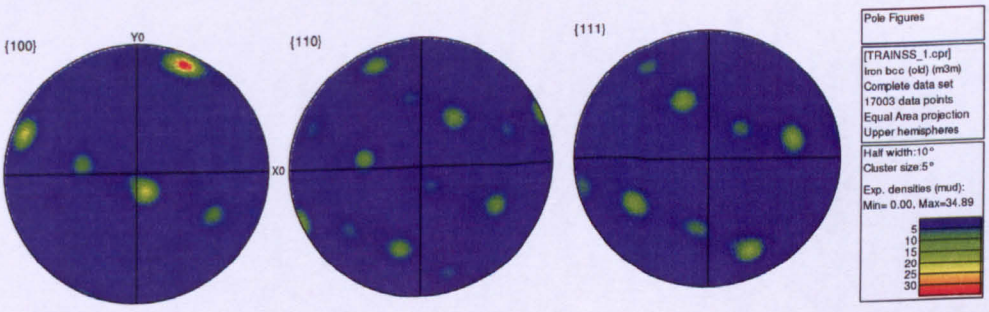

Fig. 3.26 Ferrite pole figures: EBSD (cubes machined from TRAINSS pipe butt weld)

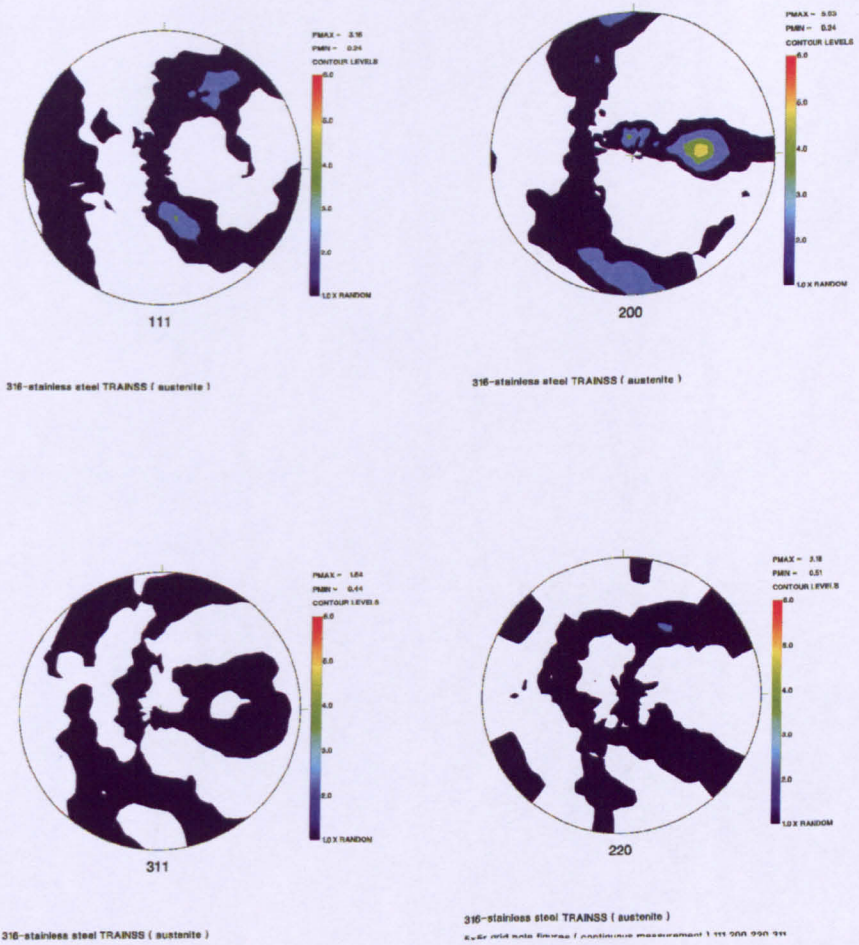

Fig. 3.27 Experimental pole figures (austenite): Neutron diffraction texture (cubes machined from TRAINSS pipe butt weld)

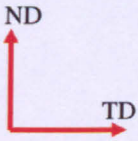

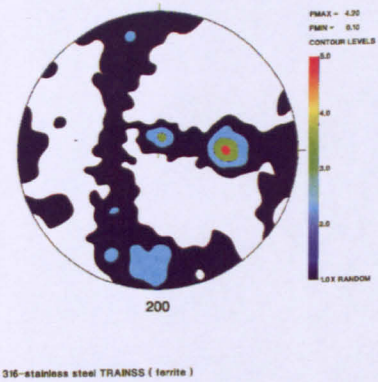

Fig. 3.28 Recalculated pole figure (ferrite): neutron diffraction texture (cubes machined from TRAINSS pipe butt weld)

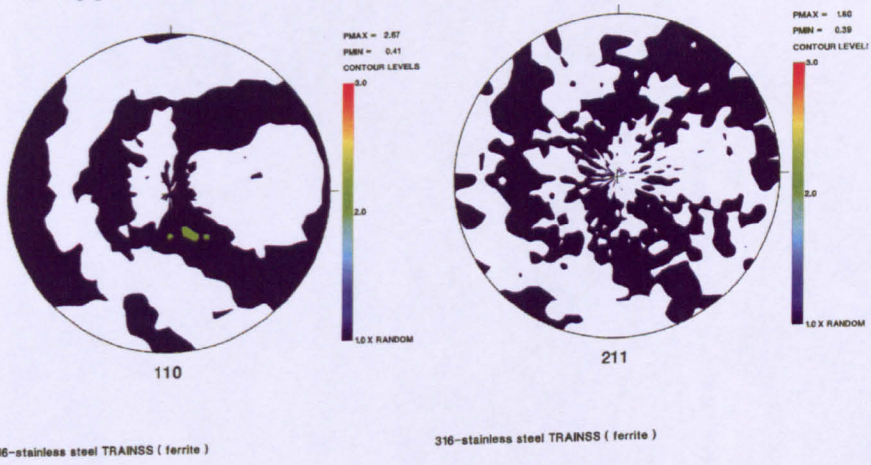

Fig. 3.29 Experimental pole figures (ferrite): neutron diffraction texture (cubes machined from TRAINSS pipe butt weld)

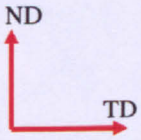

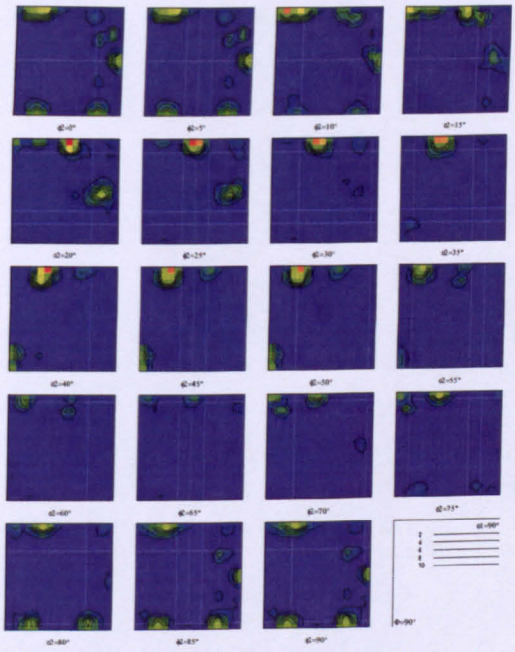

Fig. 3.30 ODF sections (austenite): EBSD (cubes machined from TRAINSS pipe butt weld)

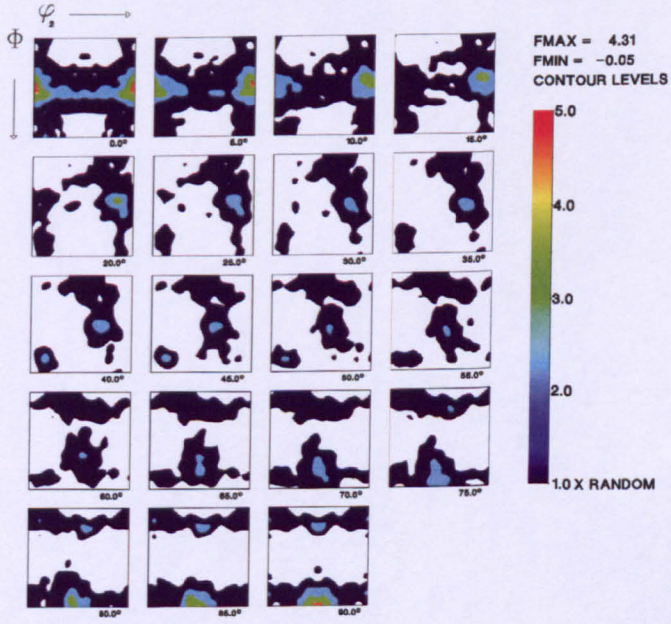

Fig. 3.31 ODF sections (austenite): neutron diffraction texture (cubes machined from TRAINSS pipe butt weld)

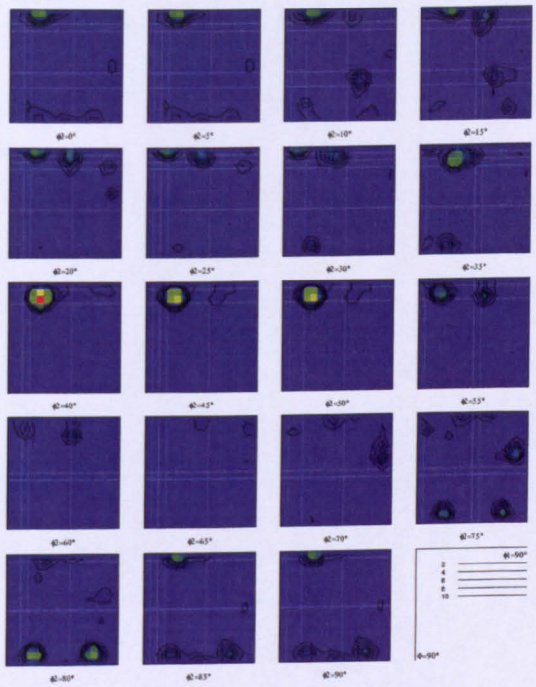

Fig. 3.32 ODF sections (ferrite): EBSD (cubes machined from TRAINSS pipe butt weld)

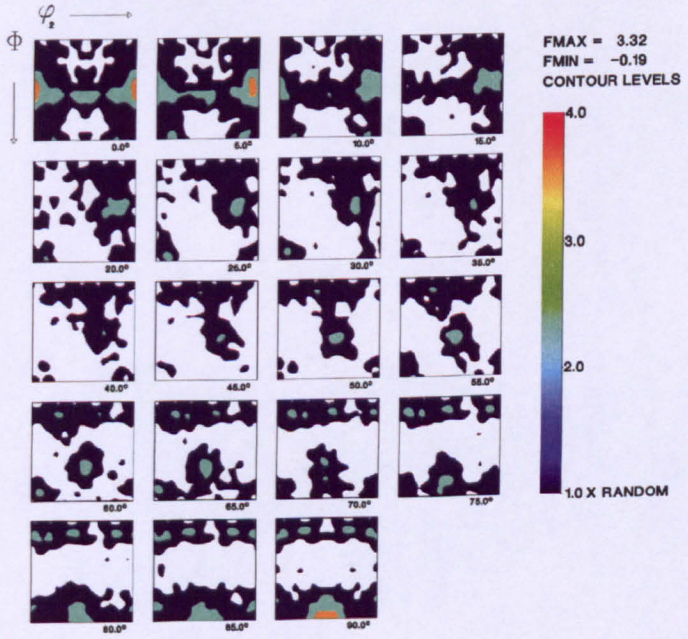

Fig. 3.33 ODF sections (ferrite): neutron diffraction texture (cubes machined from TRAINSS pipe butt weld)

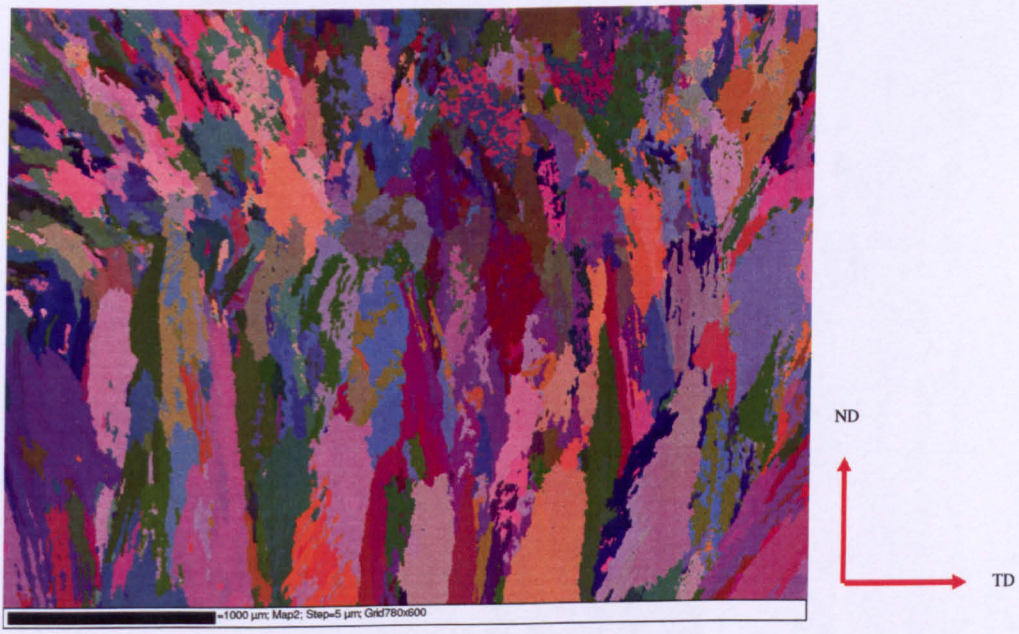

Fig. 3.34 EBSD microstructure map (cubes machined from TIG weld)

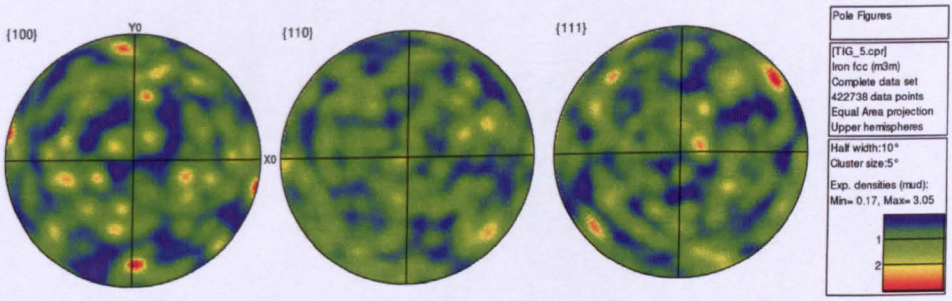

Fig. 3.35 Austenite pole figures: EBSD (cubes machined from TIG weld)

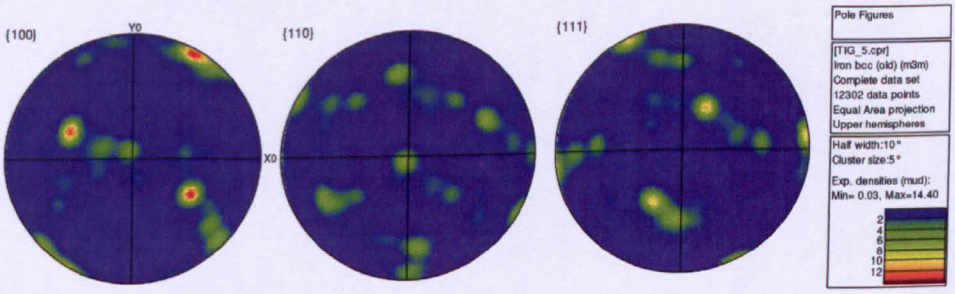

Fig. 3.36 Ferrite pole figures: EBSD (cubes machined from TIG weld)

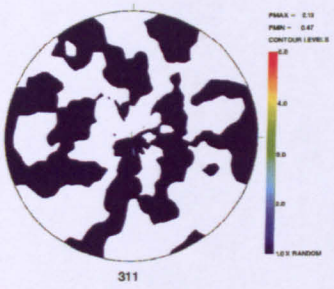

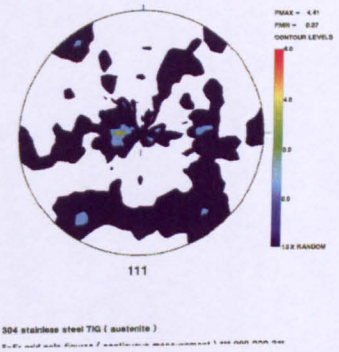

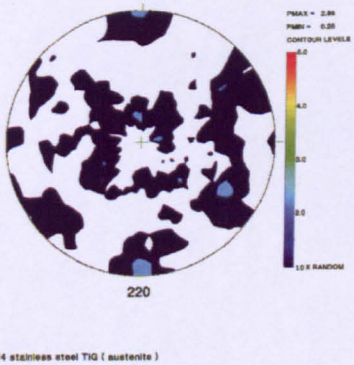

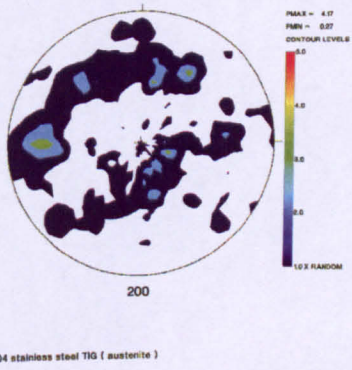

Fig. 3.37 Experimental pole figures (austenite): neutron diffraction texture (cubes machined from TIG weld)

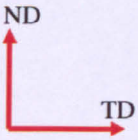

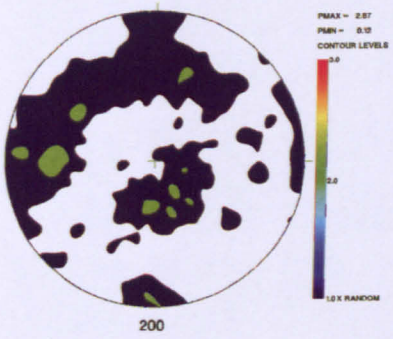

Fig. 3.38 Recalculated pole figure (ferrite): neutron diffraction texture (cubes machined from TIG weld)

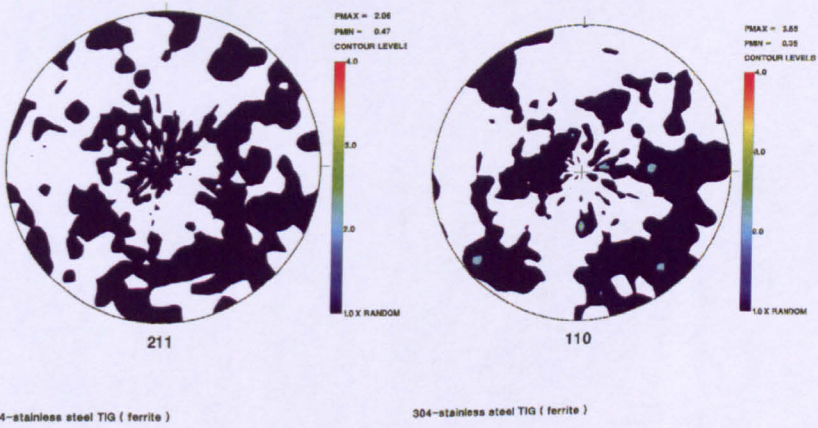

Fig. 3.39 Experimental pole figures (ferrite): neutron diffraction texture (cubes machined from TIG weld)

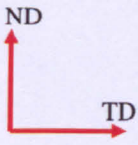

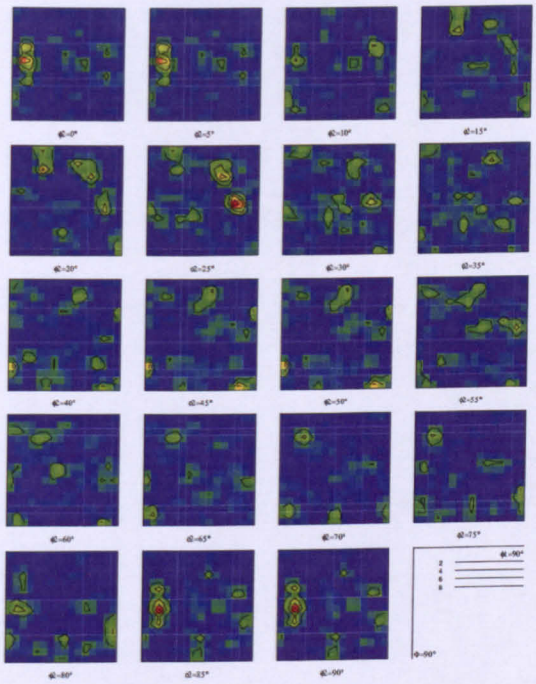

Fig. 3.40 ODF sections (austenite): EBSD Texture (cubes machined from TIG weld)

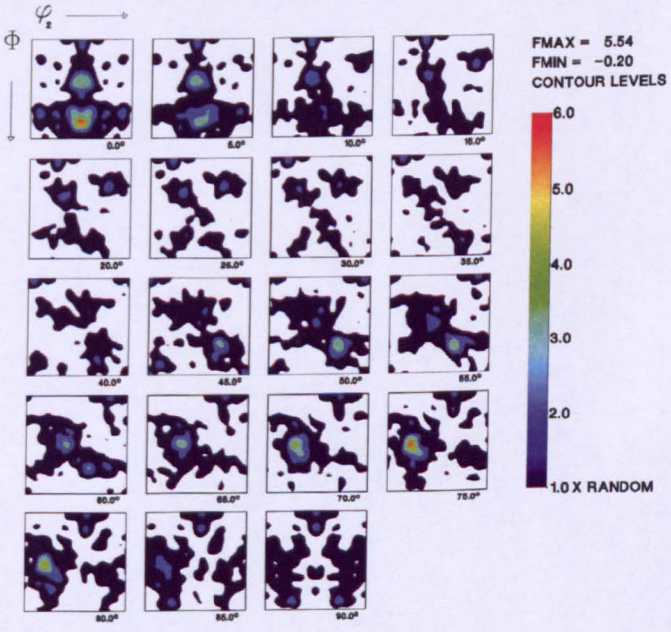

Fig. 3.41 ODF sections (austenite): neutron diffraction texture (cubes machined from TIG weld)

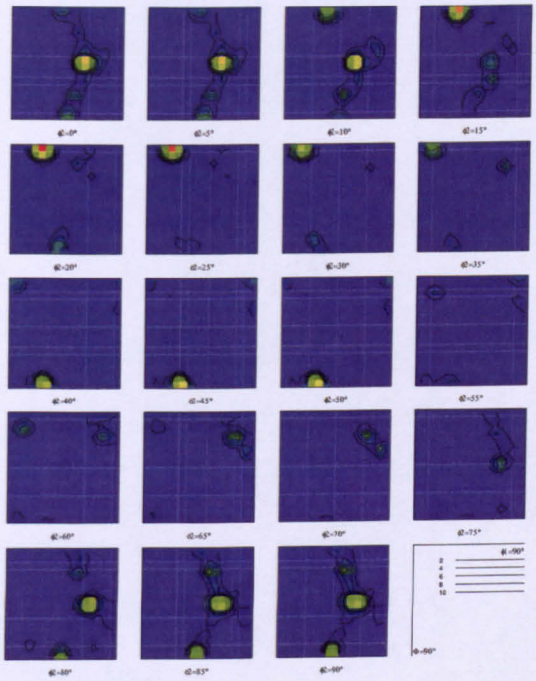

Fig. 3.42 ODF sections (ferrite): EBSD texture (cubes machined from TIG weld)

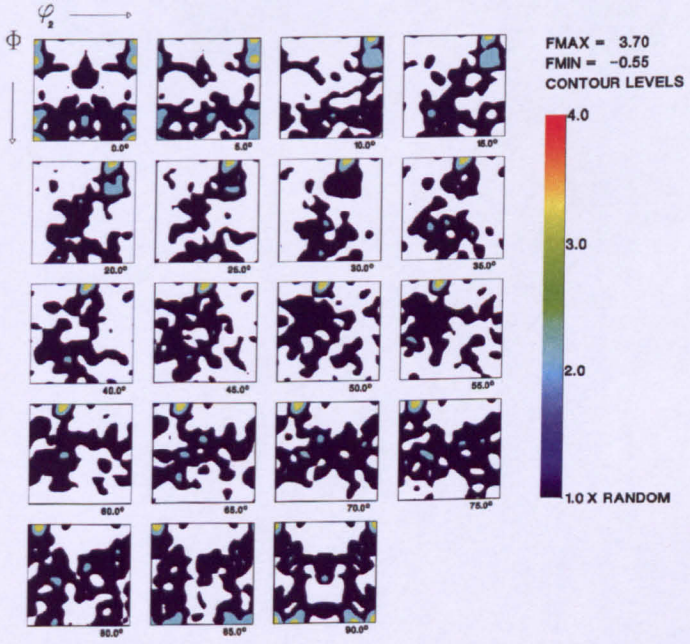

Fig. 3.43 ODF sections (ferrite): neutron diffraction texture (cubes machined from TIG weld)

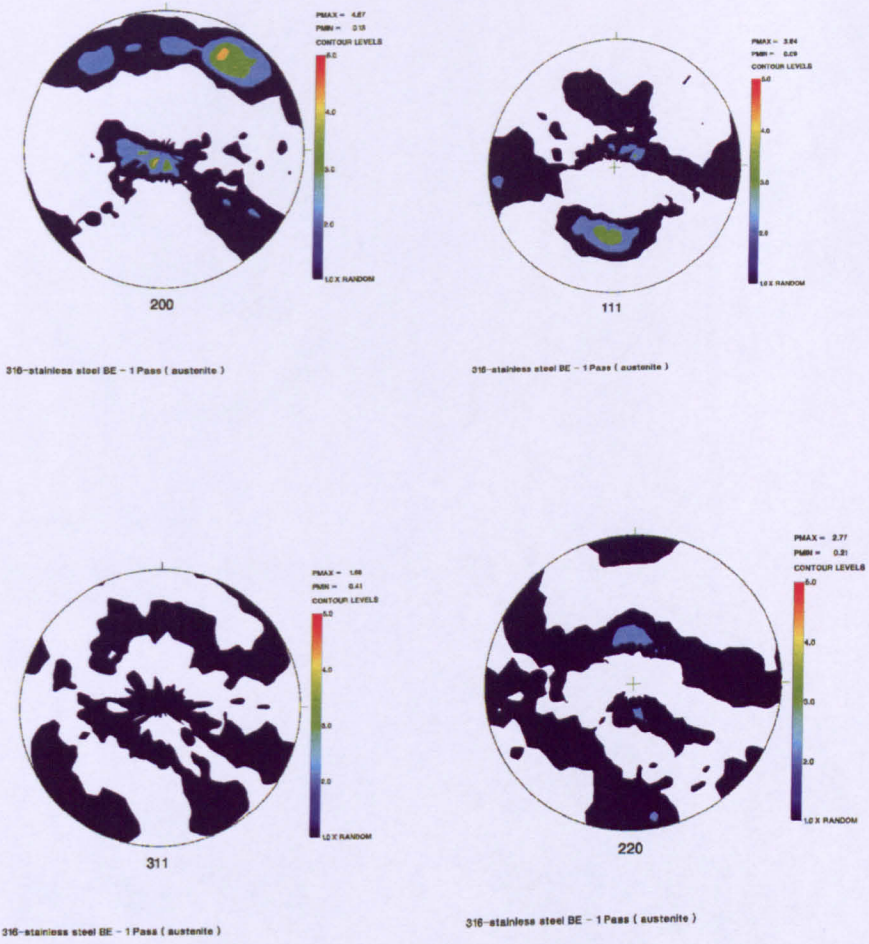

Fig. 3.44 Experimental pole figures (austenite): neutron diffraction texture (cubes machined from B.E. I pass weld)

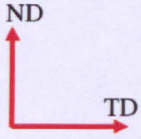

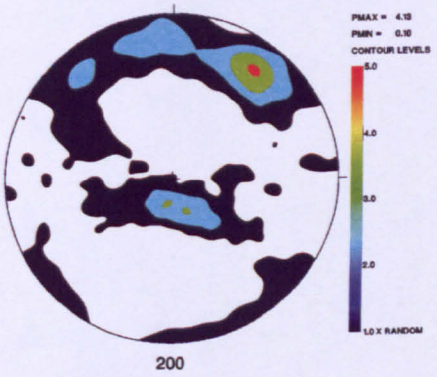

Fig. 3.45 Recalculated pole figure (ferrite): neutron diffraction texture (cubes machined from B.E. I pass weld)

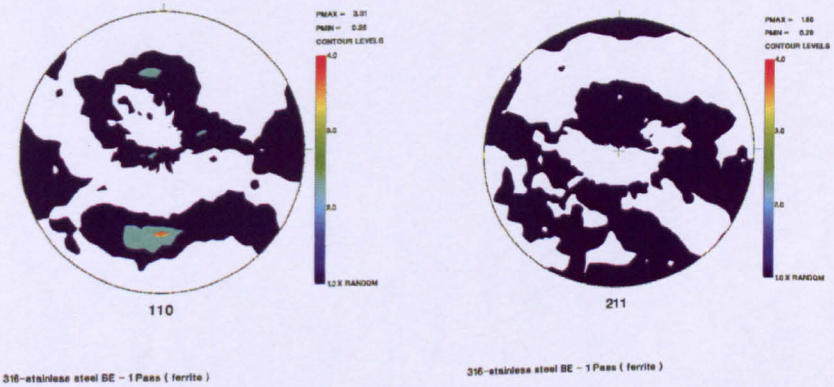

Fig. 3.46 Experimental pole figures (ferrite): neutron diffraction texture (cubes machined from B.E. I pass weld)

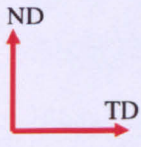

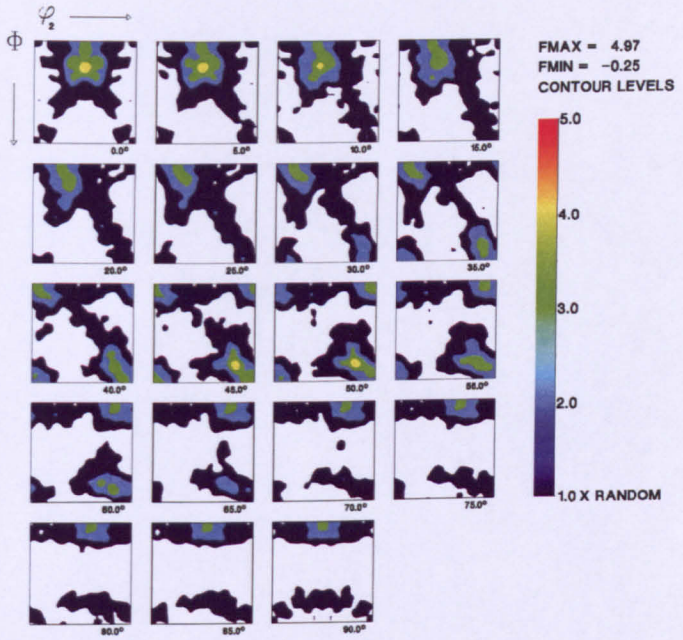

Fig. 3.47 ODF sections (austenite): neutron diffraction texture (B.E. I pass weld)

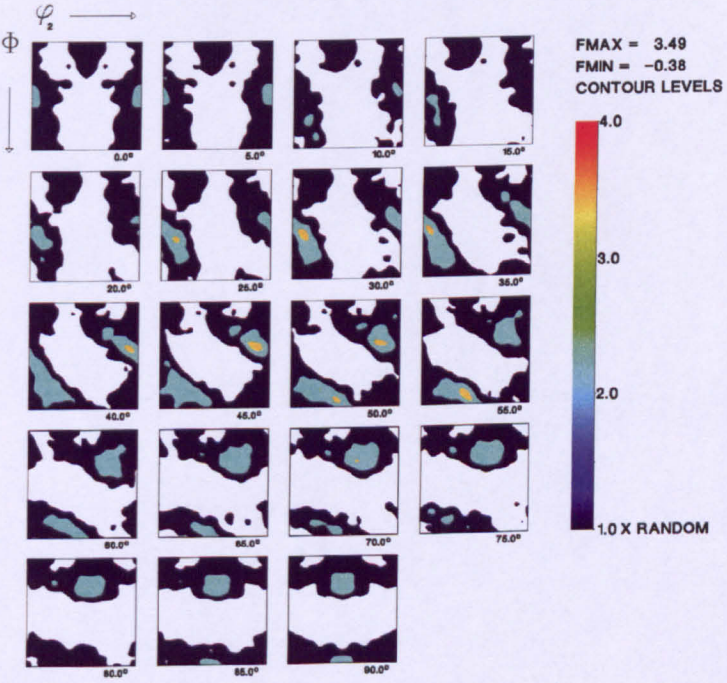

Fig. 3.48 ODF sections (ferrite): neutron diffraction texture (B.E. I pass weld)

3.2 Summary

Texture results from EBSD and neutron diffraction measurements, on various types of welds have been presented in the form of pole figures and ODF sections.

The next chapter will provide details on in-situ neutron diffraction experiments on various types of weld specimens.

Chapter 4 In-situ Neutron Diffraction Testing

4.1 Introduction

This chapter provides details about the in-situ tests using neutron diffraction. In-situ tensile and compression tests were conducted on several types of welds. Lattice strain has been calculated using Pawley refinement and the macro-strain monitored using an extensometer. Single peak strain has also been computed after fitting the individual peaks. Young's modulus has been calculated from the linear region of the applied stress vs Pawley lattice strain curve and applied stress vs extensometer strain curve.

4.2 In-situ Tension Test

The diffraction elastic constants of a material of interest can be measured by installing a tensile test rig on the neutron diffractometer. In this way the Young's modulus of the material and the Poisson's ratio can be calculated. The present experiment was carried out in-situ on the ENGIN-X time of flight neutron diffractometer at the ISIS facility of the Rutherford-Appleton Laboratory. A 50kN Instron servo hydraulic stress rig (Fig. 4.1) available on ENGIN-X for in situ mechanical loading was used for this experiment.

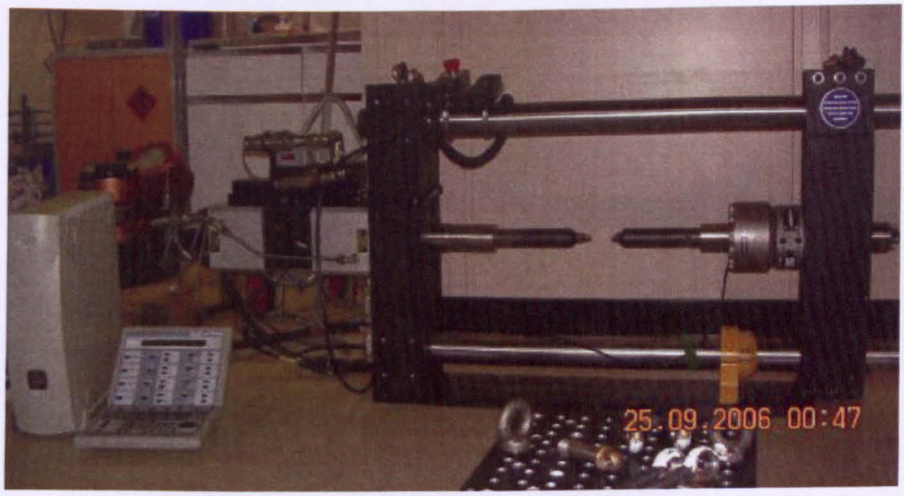

Fig. 4.1 50 kN Instron servo hydraulic stress rig available at ENGIN-X.

The in-situ tensile test was carried out on two types of specimens:

- multi-pass welds
- single-pass welds

The specimen geometry and manufacturing details have been discussed in the second chapter. The advantage of doing the uniaxial test in the beam was twofold. The macroscopic response was measured by using an extensometer and the elastic response of individual reflections was simultaneously recorded by neutron diffraction. The loading axis was horizontal and at 45° to the incident neutron beam, allowing simultaneous measurements of the lattice plane spacing parallel and perpendicular to the loading direction, in opposing 90° detector banks.

4.2.1 The Tensile Test Procedure

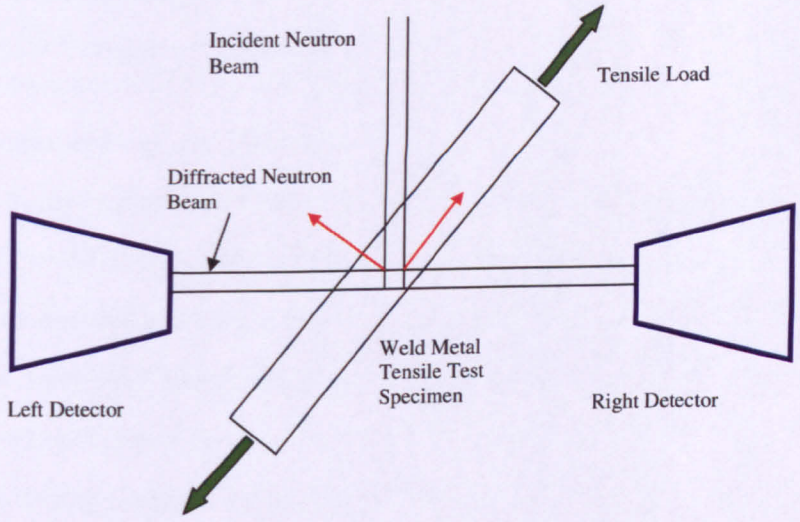

Fig. 4.2 Experimental arrangement for in–situ tensile testing in neutron beam

The experimental arrangement for the in-situ tension test is shown in Fig. 4.2. Deformation of the specimen in tension was carried out in strain control mode. Strain control was achieved by fitting a clip gauge in the gauge length of the specimen. The initial orientation of the sample to the beam was determined by rotating the specimen in different positions (along axis of loading). The specimen was rotated in 45° increments (about the axis of loading) to obtain the best diffraction pattern. The lattice plane spacing measured at a load of 5 MPa was assumed to be d_0 (the stress free reference spacing).

The loading was carried out initially at small strain increments, with interruptions during measurement time.

After the peak load was achieved, unloading was carried out in load control mode, in order to allow a number of measurements to be made on unloading, for Young's modulus measurement.

4.3 Data Analysis

4.3.1 Fitting the whole spectrum

The advantage of doing an experiment at a time of flight neutron source is that the complete diffraction spectrum is recorded. Pulses of neutrons, each of which has a continuous range of velocities and therefore wavelengths, are directed at the specimen [52]. The diffraction spectra of the detected (diffracted) neutrons can be recorded after calculating the wavelengths by measuring the flight times. All possible lattice planes in an orientation defined by the fixed detector angle are recorded in each measurement as the incident spectra are polychromatic. All the peaks for the polycrystalline aggregate can be recorded simultaneously, in contrast to a single peak measurement on a reactor source. The scattering vectors for all reflections recorded in one detector lie in the same direction, and thus measure the strain in the same direction. Different families of grains are oriented in a way that the given hkl plane diffracts to the detector and produces the reflection. As the weld metal is highly textured, Rietveld refinement fails to converge. Therefore Pawley refinement has been applied.

The refinement was carried out using EX-SBA, the ENGIN-X script based analysis software, written using the Open Genie programming language developed at ISIS [94].

EX-SBA uses the software package GSAS for automatic Rietveld/Pawley refinement of the diffraction spectra [95]. Initially a RAW data file is generated containing information about individual TOF spectra recorded by the data acquisition electronics for every single detector element. The individual spectra of this RAW file are summed together, taking account of the differences in time of flight, to create a single diffraction spectrum from all the elements in a bank. The focusing technique is called time focusing. The focussed spectra are stored in the .his file. The diffraction

spectrum was fitted using a TOF scale from 10,000 μs to 40,000 μs. This scale covers all the peaks appearing in the diffraction spectrum.

The neutron diffraction spectrum from stainless steel weld metal carries the austenite phase as well as ferrite phase. We have refined only the austenite phase as the ferrite phase is present in a very small quantity (up to 6%).

The unit cell lattice parameter a along with the error in fitting 'a' was computed after the fitting of the data.

4.3.2 Single Peak Fitting

Single peak fitting was also carried out using EX-SBA. In the single peak fitting routine, each peak was fitted individually and the inter-planar spacing d_{hkl} was computed along with the error in peak fitting.

4.3.3 Calculation of Diffraction Elastic Constants

Several diffraction elastic constants e.g. the Young's modulus, the Poisson's ratio for the bulk of the material as well as plane specific can be calculated from the present results. However, only Young's modulus results have been presented in this thesis. The Young's modulus has been calculated by fitting the linear region of the applied stress vs Pawley longitudinal lattice strain curve and the applied stress vs. clip gauge strain curve as shown in Fig. 4.3. The diffraction Young's modulus is the ratio of an applied macroscopic stress to the strain measured by diffraction in the family of grains whose plane normals (hkl) lie along the scattering vector. Similarly the diffraction Poisson's ratio can be calculated from the linear region of the applied stress vs. Pawley transverse strain curve. The slope of the applied stress vs transverse strain curve is equal to the Young's modulus divided by the Poisson's ratio.

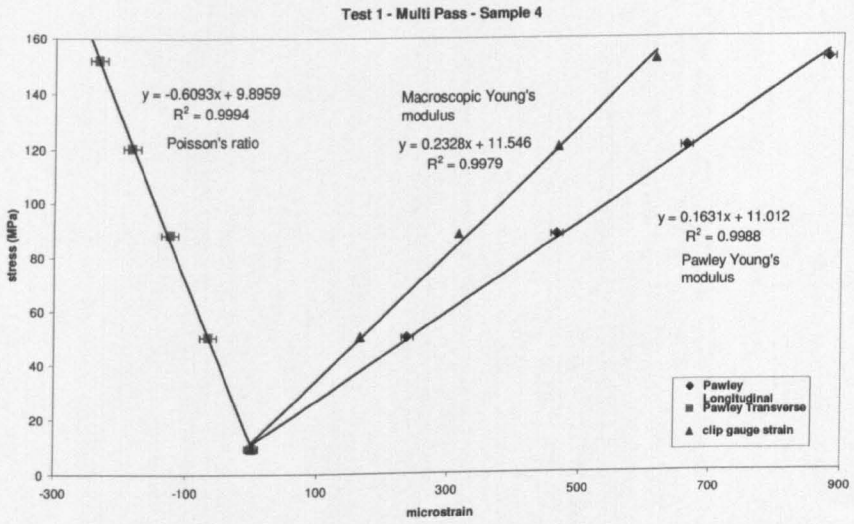

Fig. 4.3 An example showing the calculation of the diffraction elastic constants. The black continuous line is the trend line. The R value shows the quality of the fit with R=1 the best fit.

4.4 Orientations of the Multi-Pass Weld Specimens

As the weld metal was highly textured, the diffraction spectrum contained only one or two peaks with high intensity, the other peaks being less intense. Therefore, the sample was rotated in the neutron beam (about the axis of the cylinder) to get a best diffraction spectrum. Some orientations were marked along the circumference of the sample. The reference orientation 0° was marked arbitrarily.

Two different specimens were tested in these experiments.

4.4.1 Sample 4

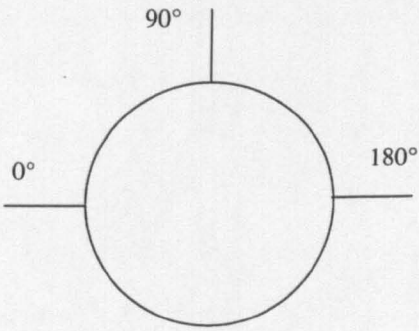

Fig. 4.4 Orientations marked on sample 4.

Three orientations were marked on the surface of the specimen covering a total angle of 180°. The diffraction spectrum was recorded in 0° orientation, then rotated by 90° and finally to 180°.

4.4.2 Sample 15

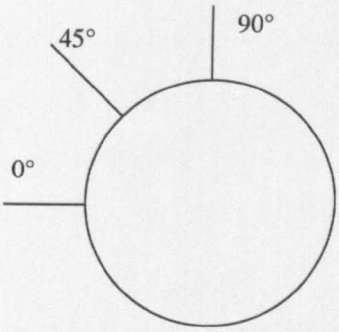

Fig. 4.5 Orientations marked on sample 15.

Three orientations were marked on the surface of the specimen covering a total angle of 90°. Diffraction spectra were recorded in 0° orientation, then rotated by 90°, and finally rotated back to 45° orientation.

4.5 Effect of Texture on Young's Modulus

The crystallographic texture of various specimens has been discussed in chapter 3. The specimens obtained from the Weld-Pad exhibit {100} fibre texture in which most of the {200} planes are aligned along the solidification direction. This is evident from the {200} pole figures shown in chapter 3. The consequence of this texture is that the diffraction spectrum will show usually a {200} dominant peak. However, with the change in the orientation of the specimen with reference to the neutron beam other peaks such as {311} or {111} may become dominant.

The Young's modulus will be high or low depending upon whether the diffraction spectrum is dominant in {111} or {200} peak.

In the case of the TIG weld, the texture is nearly random. Therefore a Young's modulus value comparable to a random textured material is obtained.

4.6 Results from the Multi-Pass Weld Specimens

4.6.1 Test 1 (Sample 4)

Test 1 was carried out on the cylindrical specimen in the 180° orientation. The diffraction spectrum at the beginning of the experiment, for longitudinal strain is shown in Fig. 4.6. In the diffraction spectrum, the {200} peak is dominant. The Pawley lattice strain for longitudinal and transverse directions along with the clip gauge strain is shown in Fig. 4.7.

The specimen was loaded up to 100 MPa in tension. The single peak strain, along with Pawley lattice strain is shown in Fig. 4.8. In the longitudinal as well as the transverse direction the {200} planes are the most compliant planes whereas the {111} planes are the stiffest. The Pawley response curve is close to that of the {200} lattice plane. The Young's modulus from the Pawley fit and the clip gauge data was found to be 163 GPa and 232 GPa respectively.

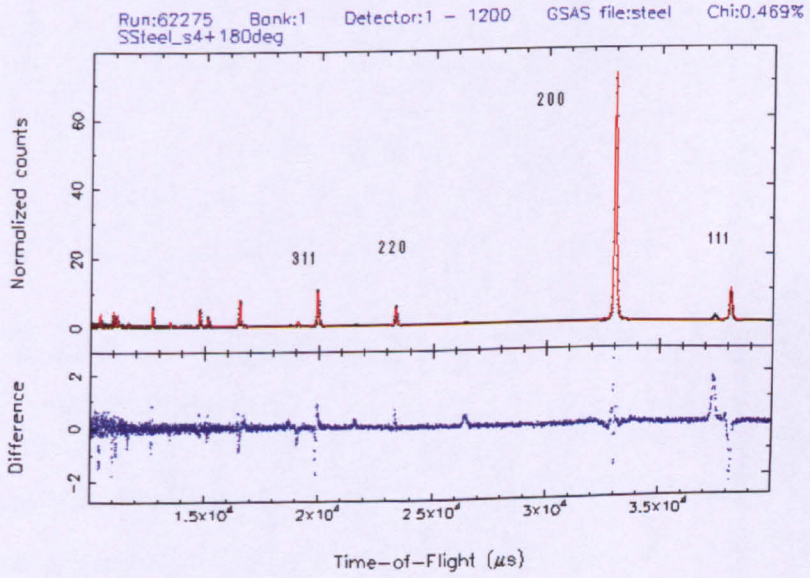

Fig. 4.6 Test 1: Diffraction spectrum for sample 4 under 5 MPa load (180° orientation).

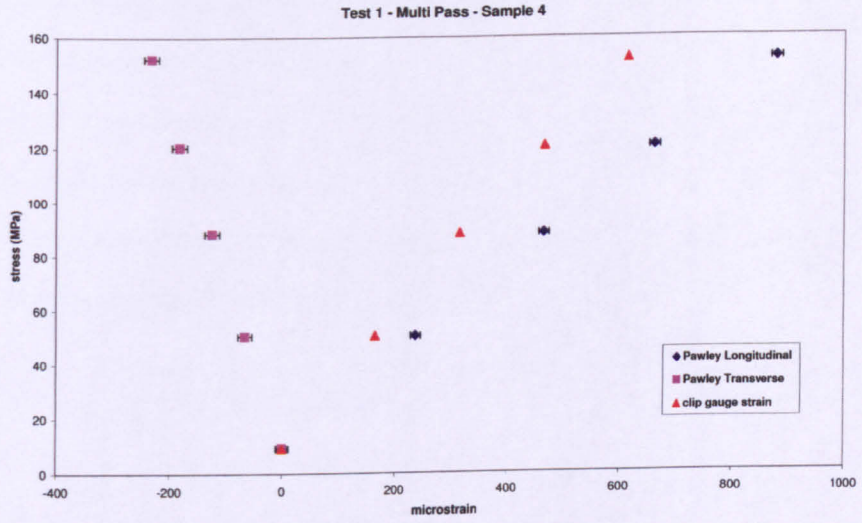

Fig. 4.7 Test 1: Applied stress vs elastic strain [10^{-6}]

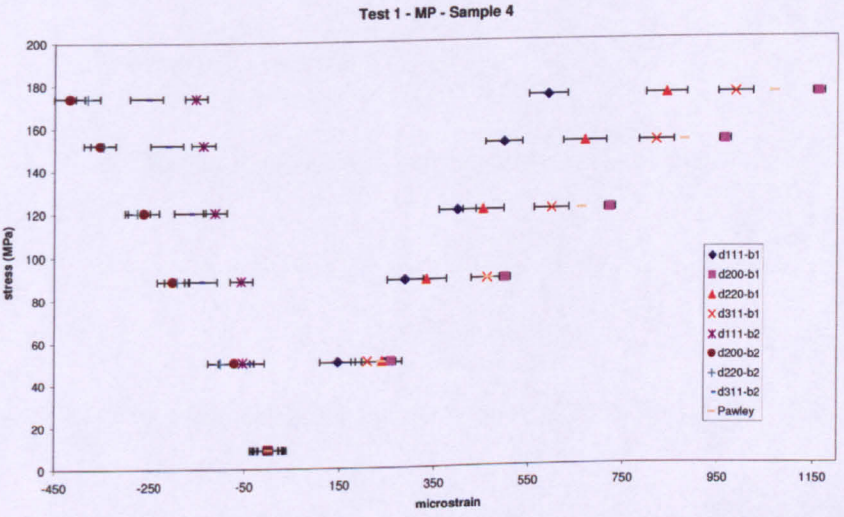

Fig. 4.8 Test 1: Multi-pass 316 MMAW tension (sample 4-180° orientation). Applied stress vs elastic lattice strain [10^{-6}] (single peak strain).

4.6.2 Test 2 (Sample 4)

In the second test the specimen was rotated back to the 90°orientation. The diffraction spectrum at the beginning of the experiment, for longitudinal strain is shown in Fig. 4.9. In the diffraction spectrum, the 200 and 311 peaks are dominant. The Pawley lattice strain for the longitudinal and transverse directions along with the

corresponding clip gauge strain is shown in Fig. 4.10. The specimen was loaded up to 80 MPa in tension. The single peak strain, along with Pawley lattice strain is shown in Fig. 4.11. In the longitudinal as well as the transverse direction the {200} planes are the most compliant and the {111} planes are the stiffest. The Pawley lattice strain response is close to the {311} lattice planes. The Young's modulus from Pawley fit and clip gauge data is found to be 172 GPa and 189 GPa respectively.

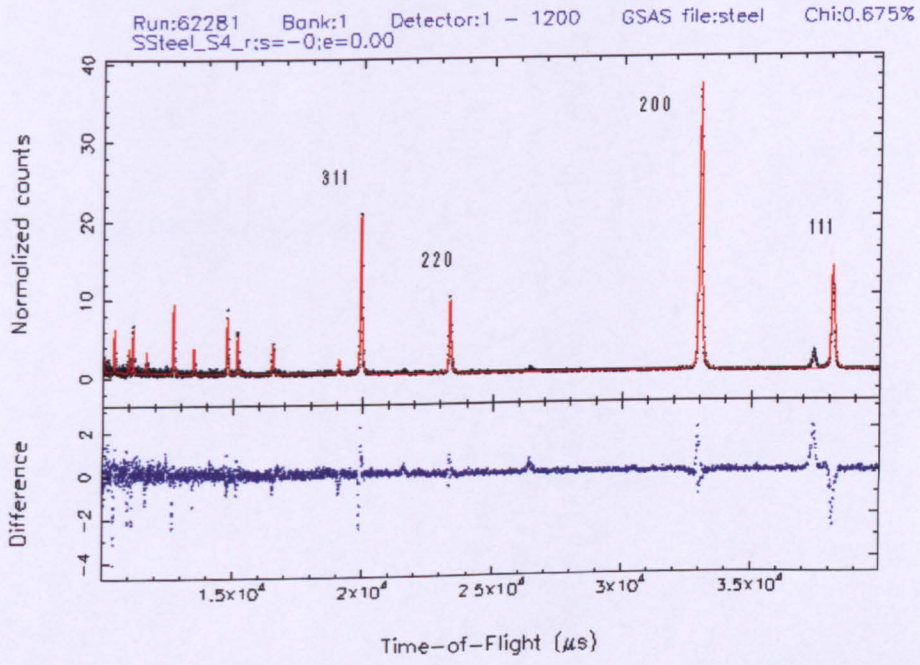

Fig. 4.9 Test 2: Diffraction spectrum for stainless steel weld metal under 0 MPa load (sample 4-90° orientation).

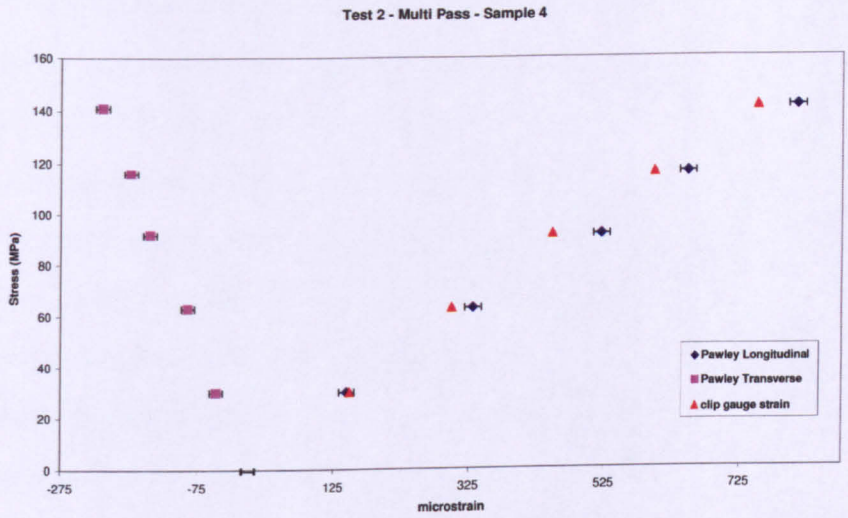

Fig. 4.10 Test 2: Applied stress vs elastic strain (sample 4-90° orientation).

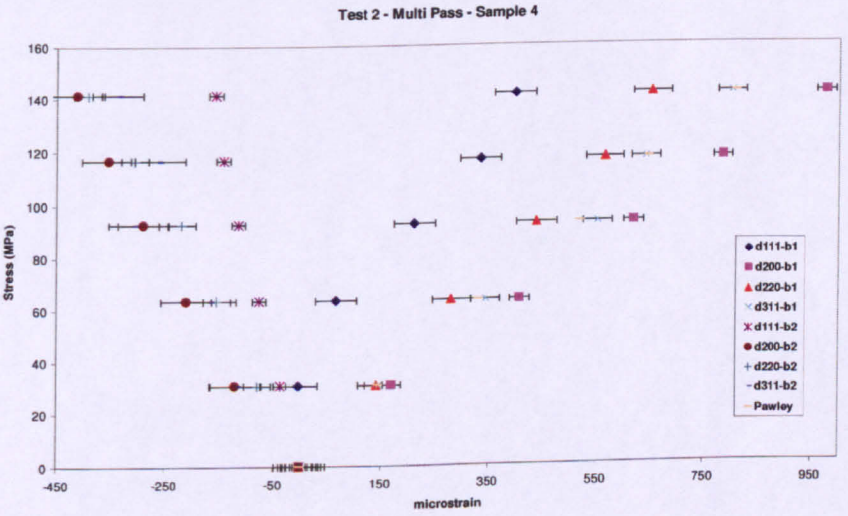

Fig. 4.11 Test 2: Applied stress vs single peak strain (sample 4-90° orientation).

4.6.3 Test 3 (Sample 4)

Test 3 was carried out in the same orientation as test 2. The diffraction spectrum at the beginning of the experiment, for the longitudinal strain is shown in Fig. 4.12. In the diffraction spectrum the {200} and {311} peaks are dominant. In this test, the

specimen was deformed plastically, up to 1% plastic strain. The Pawley lattice strain for the longitudinal and transverse directions along with the clip gauge strain is shown in Fig. 4.13. The elastic region of this curve is shown in Fig. 4.14. The single peak strain, along with the Pawley lattice strain is shown in Fig. 4.15. In the elastic region and the longitudinal as well as the transverse direction the {200} are the most compliant planes and the {111} stiffest. However, in the plastic region and in the longitudinal direction the {200} are the most compliant planes and the {111} and {200} are the stiffest. In the plastic region and the transverse direction the {220} planes are the most compliant and the {111} planes stiffest. The response of Pawley lattice strain curve is close to the {311} single peak strain curve in the elastic region. Above the elastic region the Pawley response diverges from the {311} peak. The reason for this diversion being that the Pawley curve yields more as compared with the {311} set of planes. The Young's modulus from the Pawley fit and the clip gauge data is found to be 160 GPa and 162 GPa respectively.

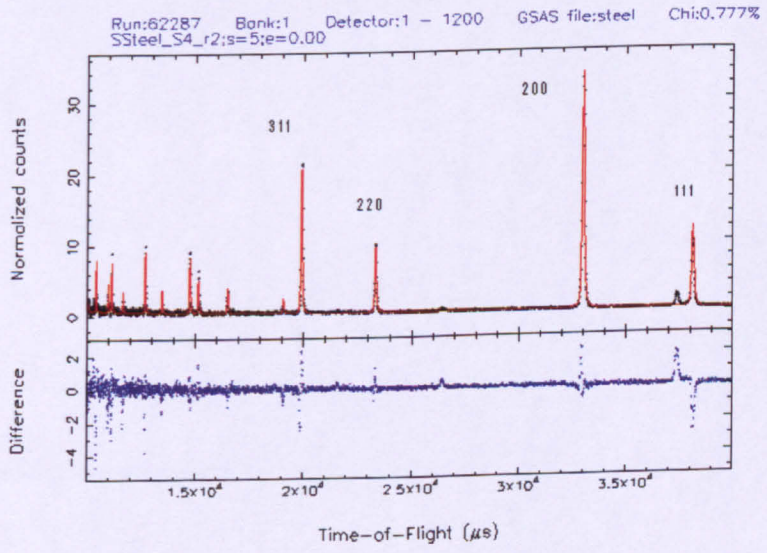

Fig. 4.12 Test 3: Diffraction spectrum for stainless steel weld metal under 5 MPa load (sample 4-90° orientation).

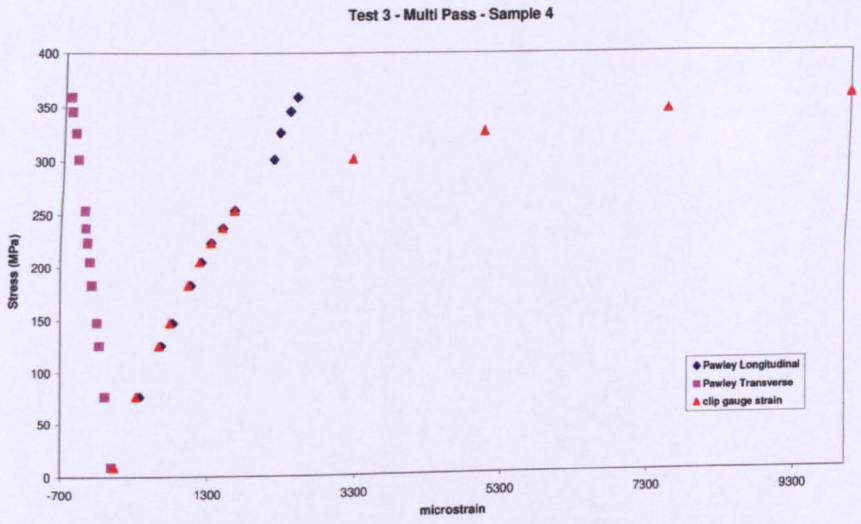

Fig. 4.13 Test 3: Multi–pass 316 MMAW tension–sample 4 (90° orientation). Applied stress vs Pawley lattice strain and extensometer strain.

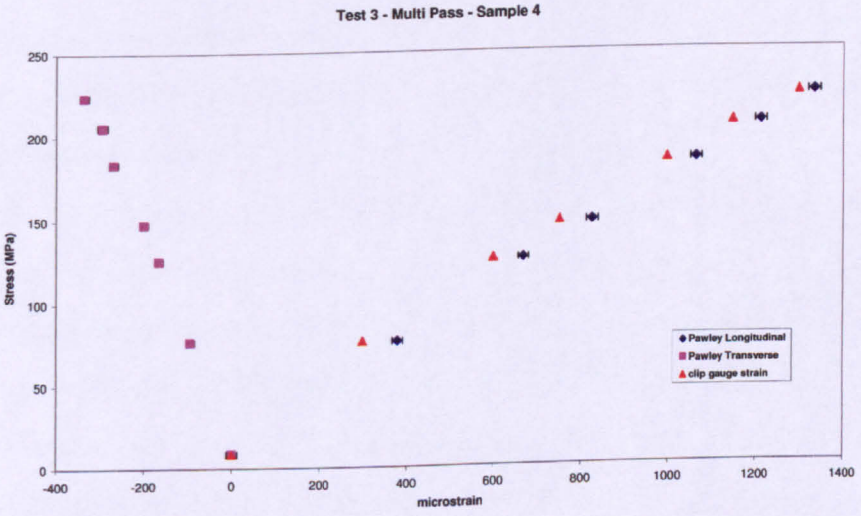

Fig. 4.14 Elastic region of the curve in Fig. 4.13

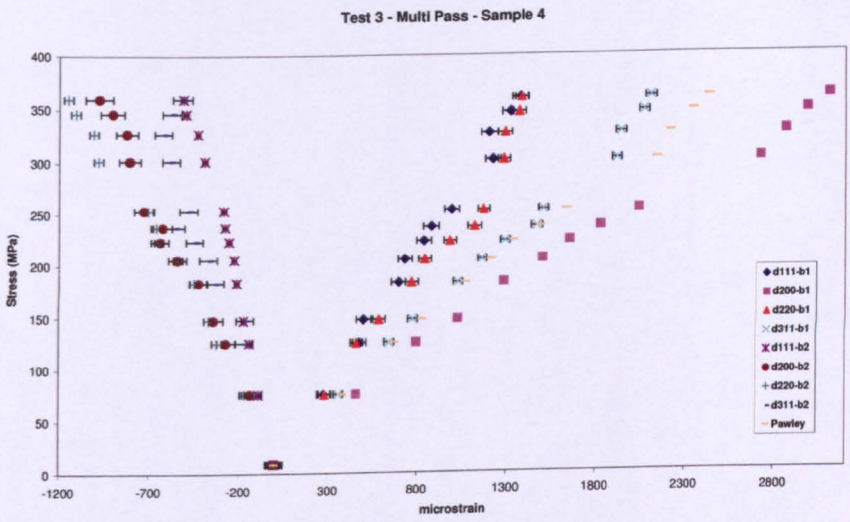

Fig. 4.15 Test 3: Multi–pass 316 MMAW tension. (sample 4-90° orientation). Applied stress vs single peak strain.

4.6.4 Test 4 (Sample 15)

This test was carried out in the 0° orientation. The diffraction spectrum at the beginning of the experiment and at 367 MPa for longitudinal strain is shown in Fig. 4.16 and Fig. 4.17. At the beginning of the experiment the 200 peak is dominant in the diffraction spectrum. The {311} and {111} peaks become more intense as the specimen is deformed plastically. The specimen was deformed plastically up to 5% plastic strain. Pawley lattice strain for longitudinal and transverse directions along with clip gauge strain is shown in Fig. 4.18. The elastic region of the stress–strain curve is shown in Fig. 4.19. The single peak strain, along with the Pawley lattice strain is shown in Fig. 4.20. In the elastic region and along the longitudinal direction the {200} planes are the most compliant and the {111} stiffest. In the elastic region and along the transverse direction the {200} planes are the most compliant and the {220} stiffest upto 150 MPa. In the plastic region and along the transverse direction the {200} and {311} remain compliant upto 310 MPa and after that the {200} are the most compliant planes. In the plastic region and along the transverse direction the

{111} planes remain stiffest. The response of Pawley lattice strain is close to {311} single peak strain in the elastic region and then it deviates from {311}. The Young's modulus from Pawley fit and clip gauge data is found to be 130 GPa and 126 GPa respectively.

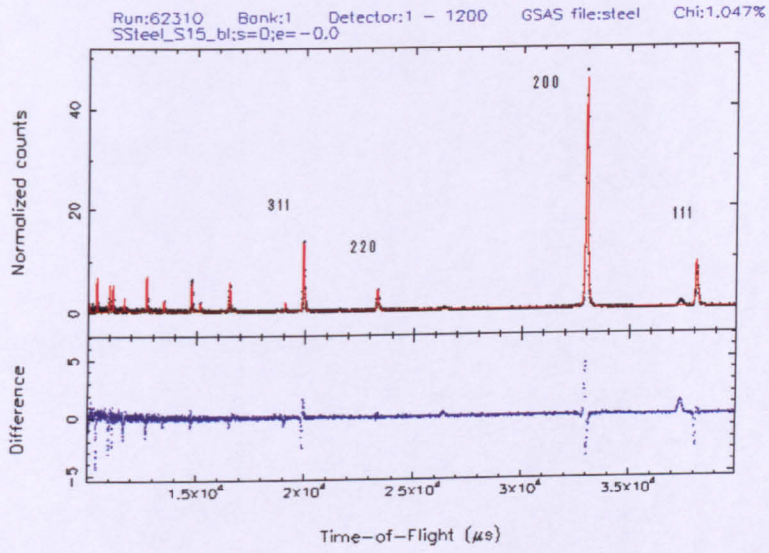

Fig. 4.16 Test 4: Diffraction spectrum for stainless steel weld metal under 0 MPa load. Sample 15.

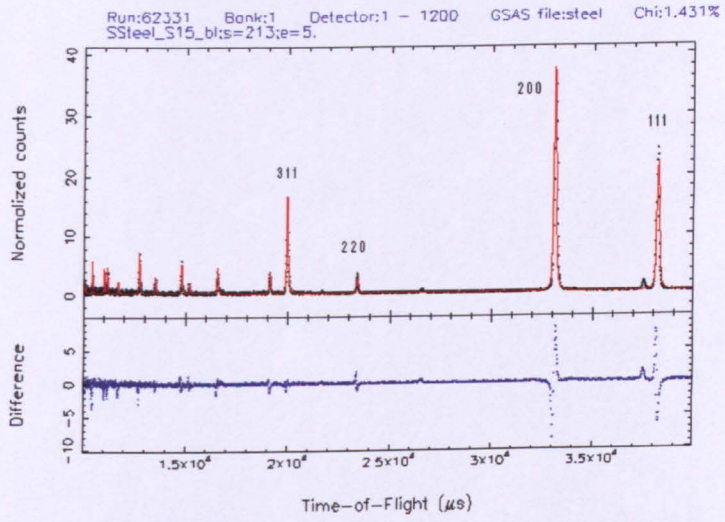

Fig. 4.17 Test 4: Diffraction spectrum for stainless steel weld metal under 367 MPa load. Sample 15.

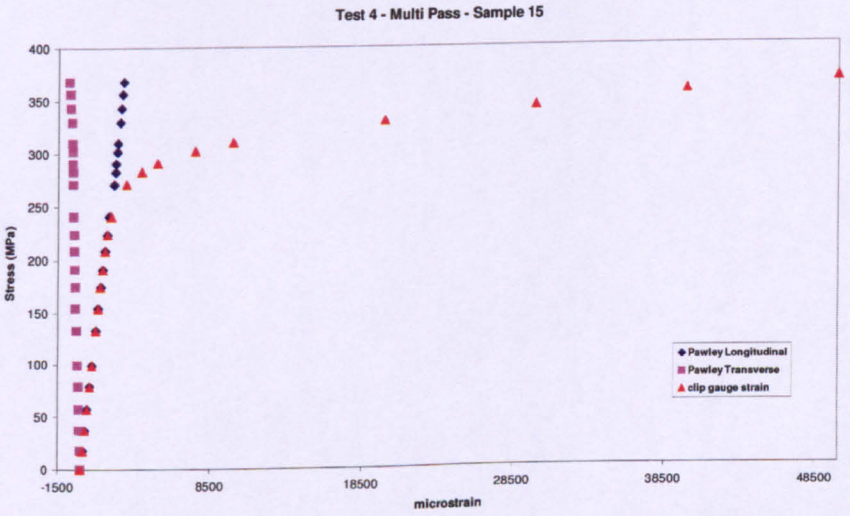

Fig. 4.18 Test 4: Applied stress vs Pawley lattice strain and extensometer strain (complete data). Sample 15.

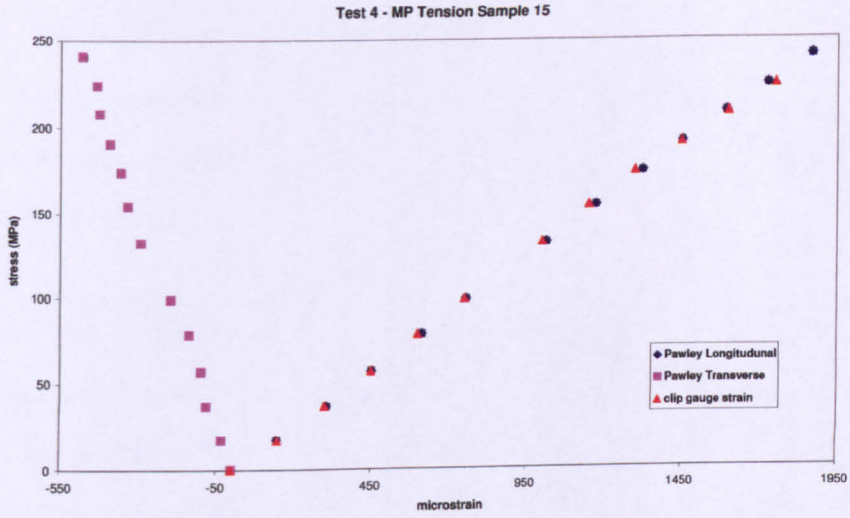

Fig. 4.19: Elastic region of the curve shown in fig. 4.17.

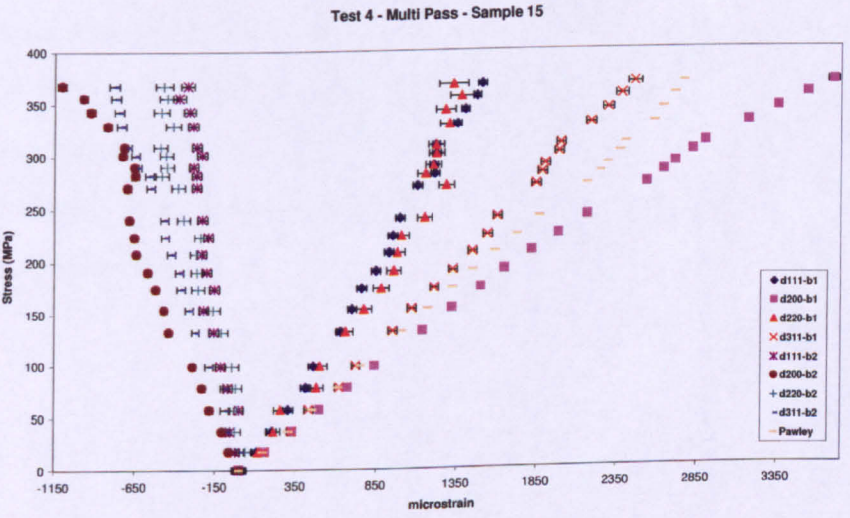

Fig. 4.20 Test 4: Applied stress vs single peak strain. Sample 15.

4.7 Results from the Single–Pass Weld Specimen

Only one specimen was tested in these experiments. Three orientations were marked on the surface of the specimen, 0°, 45° and 90°. The reference orientation 0° was selected arbitrarily.

4.7.1 Test 1 (Sample 13/26)

The first test was carried out at 45° orientation. The diffraction spectrum at the beginning of the experiment, for longitudinal strain is shown in Fig. 4.21. In the diffraction spectrum the {111} and {311} peaks are dominant, and almost equal in intensity. The specimen was deformed elastically, up to 0.075% elastic strain. The Pawley lattice strain for longitudinal and transverse directions along with the clip gauge strain is shown in Fig. 4.22. The single peak strain, along with the Pawley lattice strain is shown in Fig. 4.23. A non-linear behaviour is exhibited by all the peaks. Along the longitudinal direction the {200} planes are the most compliant and the {111} are the stiffest. Along the transverse direction the {200} planes are the most compliant and the {111} and the {220) are the stiffest.

The Young's modulus from Pawley fit and clip gauge data was found to be 223 GPa and 146 GPa respectively.

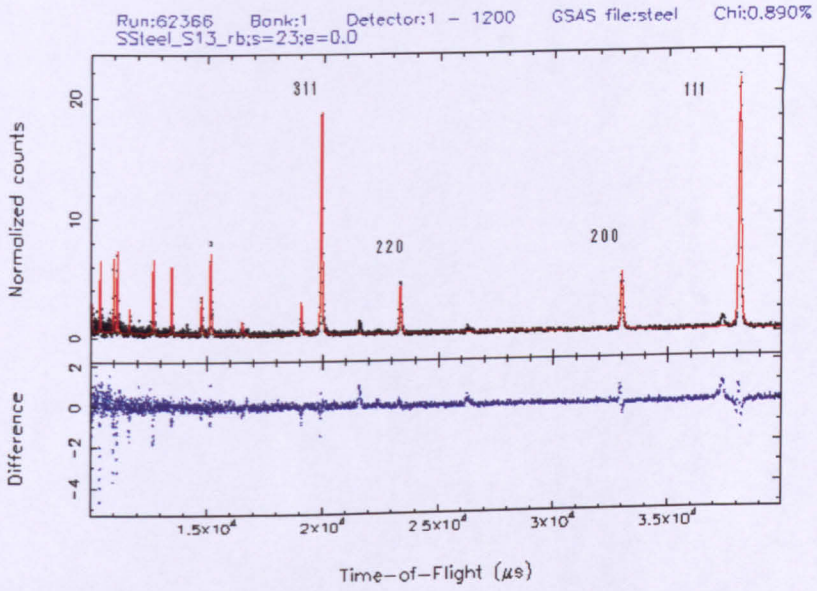

Fig. 4.21 Test 1: Diffraction spectrum for stainless steel weld metal under 17 MPa load. Sample 13/26.

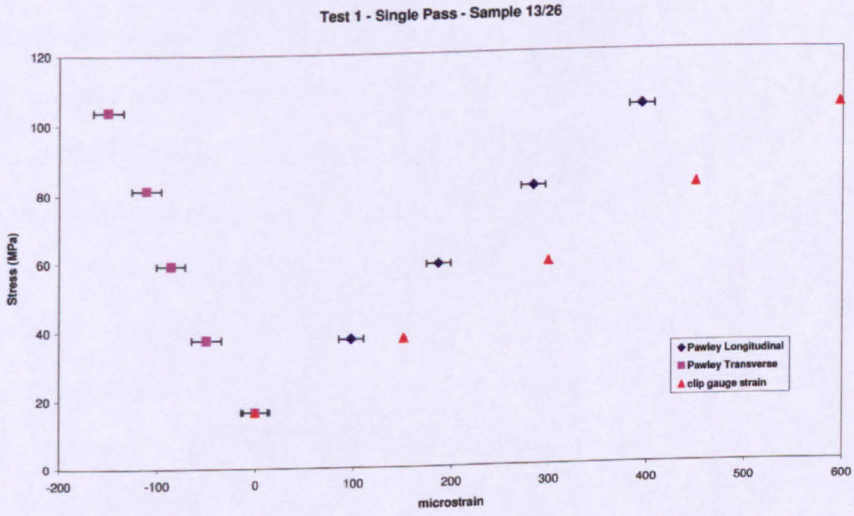

Fig. 4.22 Test 1: Applied stress vs Pawley lattice strain and extensometer strain. Sample 13/26.

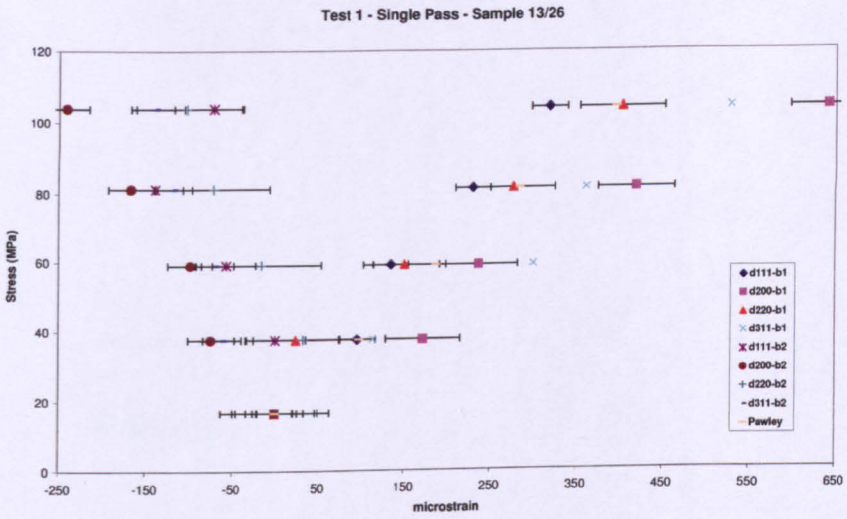

Fig. 4.23 Test 1: Applied stress vs single peak strain. Sample 13/26.

4.7.2 Test 2 (Sample 13/26)

The specimen was rotated back to the 0° orientation. The diffraction spectrum at the beginning of the experiment, for longitudinal strain is shown in Fig. 4.24. In the diffraction spectrum the {111} and {311} peaks are dominant, {111} being more intense than {311}. The specimen was deformed elastically, up to 0.075% elastic strain. Pawley lattice strain for longitudinal and transverse directions along with clip gauge strain is shown in Fig. 4.25. The single peak strain, along with Pawley lattice strain is shown in Fig. 4.26. A non-linear behaviour is exhibited by all the peaks. Along the longitudinal and the transverse direction the {200} planes are the most compliant and the {111} are the stiffest. The response of the Pawley lattice strain curve lies in between the {111} and {220} single peak strain curves. The Young's modulus from Pawley fit and clip gauge data is found to be 240 GPa and 159 GPa respectively.

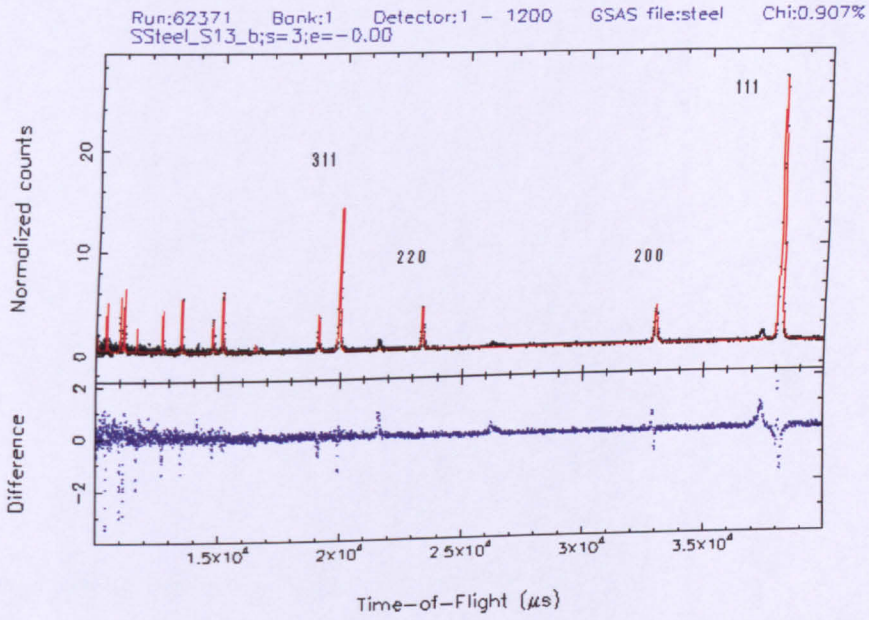

Fig. 4.24 Test 2: Diffraction spectrum for stainless steel weld metal under 9 MPa load. Sample 13/26.

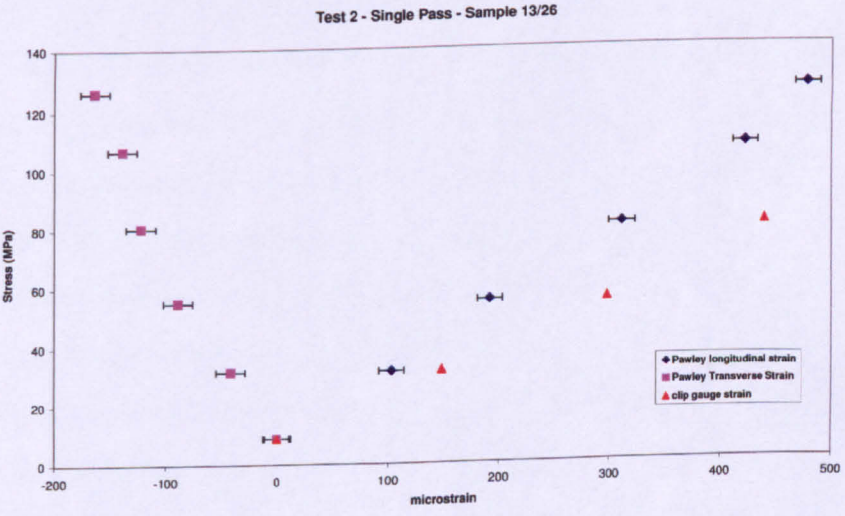

Fig. 4.25 Test 2: Applied stress vs Pawley lattice strain and extensometer strain. Sample 13/26.

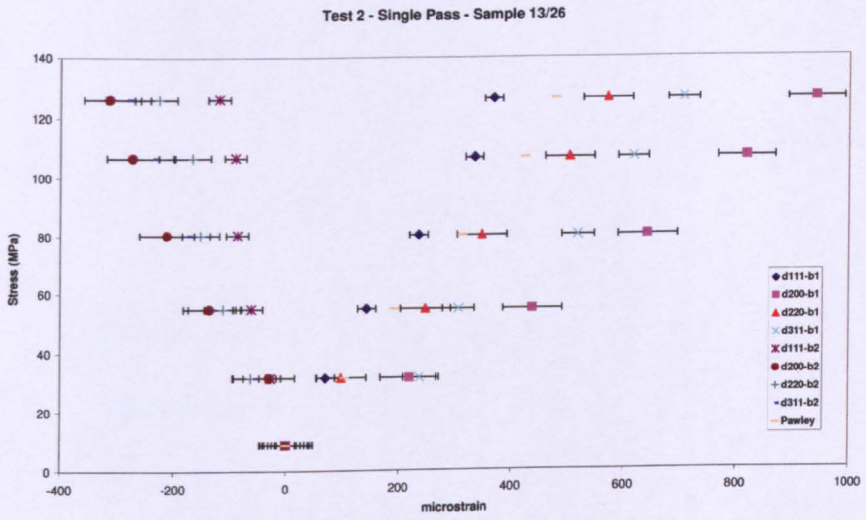

Fig. 4.26 Test 2: Applied stress vs single peak strain. Sample 13/26.

4.7.3 Test 3 (Sample 13/26)

The diffraction spectrum at the beginning of the experiment, for the longitudinal strain is shown in Fig. 4.27. In the diffraction spectrum the {111} and {311} peaks are dominant. The specimen was deformed plastically, up to 5% plastic strain and then unloaded to zero strain. The Pawley lattice strain for longitudinal and transverse directions along with the clip gauge strain is shown in Fig. 4.28. The elastic region of the stress strain curve is shown in Fig. 4.29. The single peak strains, along with the Pawley lattice strain is shown in Fig. 4.30. In the longitudinal direction the {200} planes are the most compliant and the {111} stiffest. Along the transverse direction the {200} planes are the most compliant and the {111} and {220} stiffest. The response of the Pawley lattice strain curve is close to the {220} peak upto 275 MPa. After that the {220} planes become stiffer than the Pawley curve. The Young's modulus from Pawley fit and clip gauge data is found to be 223 GPa and 141 GPa respectively.

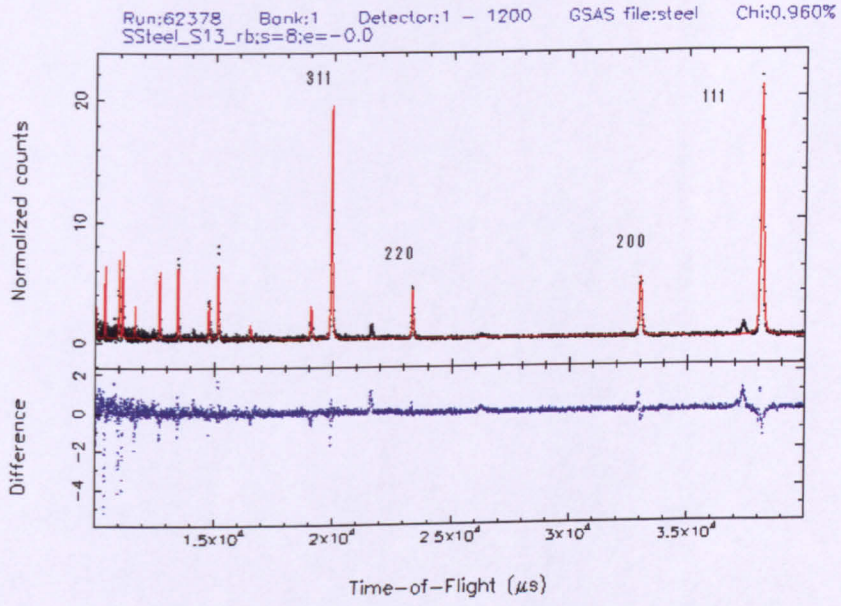

Fig. 4.27 Test 3: Diffraction spectrum for stainless steel weld metal under 8 MPa load. Sample 13/26.

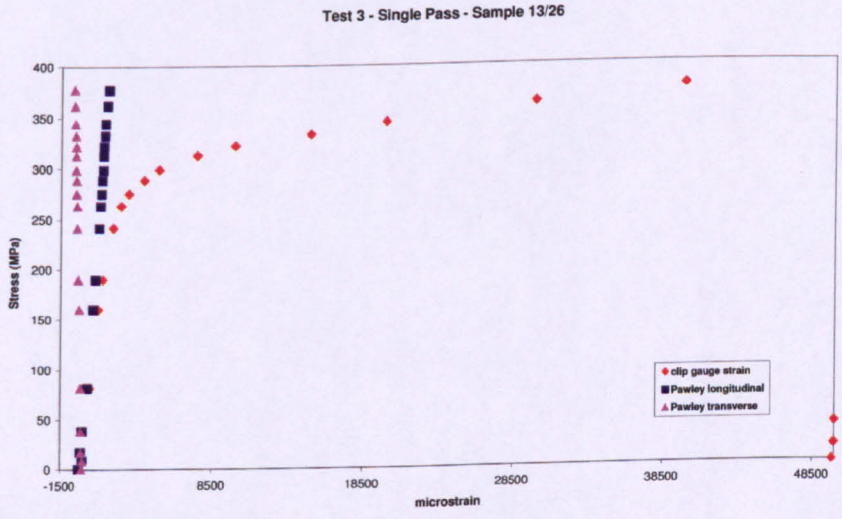

Fig. 4.28 Test 3: Applied stress vs Pawley lattice strain and extensometer strain. Sample 13/26.

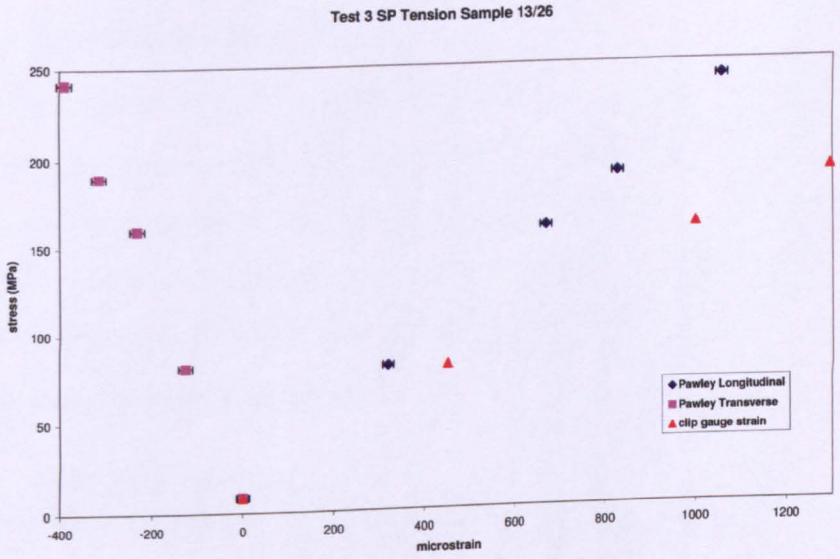

Fig. 4.29 Test 3: Applied stress vs Pawley lattice strain and clip gauge strain. Sample 13/26.

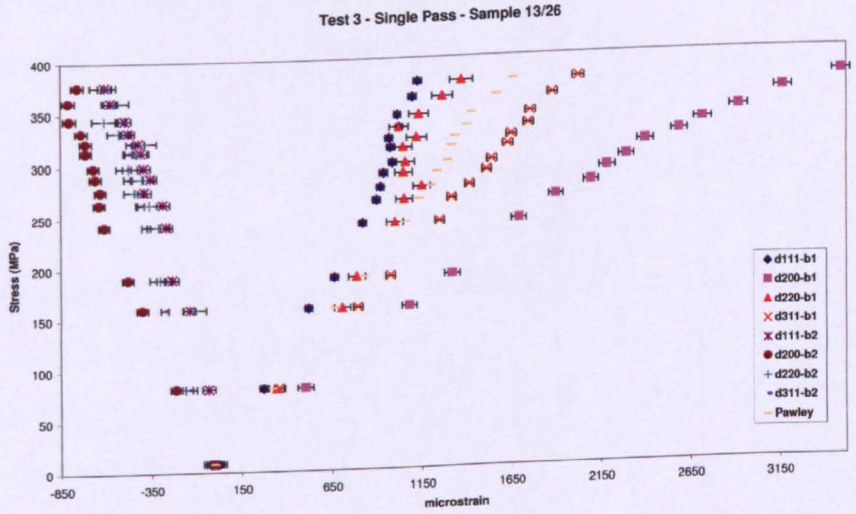

Fig. 4.30 Test 3: Applied stress vs single peak strain. Sample 13/26.

4.8 Discussion about the results

The macroscopic Young's modulus has been measured in non-standard conditions; e.g. without the use of strain gauges on the opposite sides of the cylinder to check the bending of the specimen. Therefore the values of macroscopic Young's modulus may not be reliable. As the Young's modulus measurement is a high precision work it may not be possible to estimate the magnitude of the error which might have been resulted because of non-standard conditions.

4.8.1 Multi–Pass Welds

The values of the macroscopic Young's modulus calculated from the extensometer strain and the diffraction elastic modulus calculated from the Pawley lattice strain are summarised in table 4.1. The Young's modulus derived from the extensometer strain and the Pawley fit is in close agreement in tests 2 and 3 for the sample 4. However, in the test 1 the moduli are not in close agreement.

However the Pawley Young's modulus values are in close agreement in all the tests on sample 4.

The Young's modulus derived from the extensometer strain and the Pawley fit is in close agreement for the sample 15. However, between the sample 4 and the sample 15 the Pawley Young's modulus differs, which may be attributed to the difference in the texture between two samples. The texture results for the sample 4 and the sample 15 are discussed in the chapter 3. The sample 15 has more intense texture as compared with the sample 4.

Table 4.1: Summary of the macroscopic Young's modulus and Pawley Young's modulus values for the Weld-Pad.

Sample	Test	Pawley Young's Modulus (GPa)	Macroscopic Young's Modulus (GPa)
4	1	163	233
4	2	172	189
4	3	160	162
15	4	130	126

4.8.2 Single–Pass Weld

The Young's modulus derived from the Pawley fit is around 220 GPa in all the tests. However, the macroscopic Young's modulus calculated from the extensometer strain is around 140 GPa. In all the tests 111 and 311 peak is dominant. The response of the Pawley lattice strain lies in between 111 and 311. Therefore a high Pawley modulus is expected. The texture of a single-pass weld has been discussed in the chapter 3. The texture of the single-pass weld is not very intense. Therefore Young's modulus comparable to randomly textured materials is expected.

4.9 In Situ Weld Compression

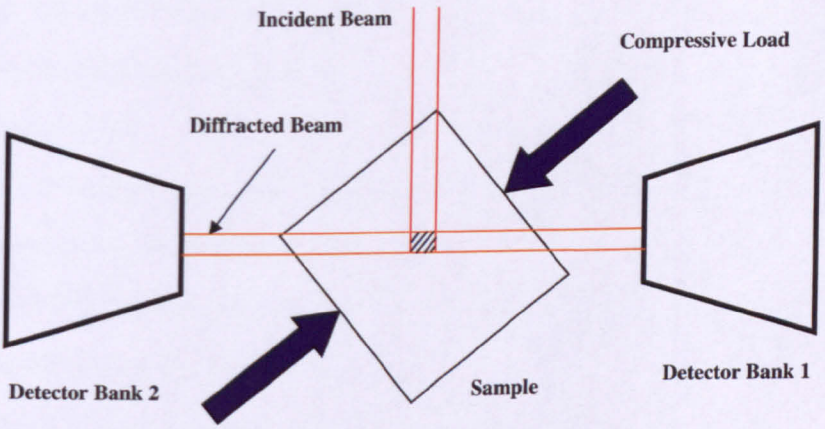

Fig. 4.31: In-situ weld compression experimental arrangement at ENGIN-X.

4.9.1 Introduction

Weld compression experiments were conducted on cubes machined from various weld types. The experiments were conducted in-situ at ENGIN-X. The general setup for the experiment is shown in Fig. 4.31. The compression specimen is held in a stress rig. The neutron beam incident upon the specimen is diffracted by the specimen, and the diffracted beam hits the detectors placed at right angles to the incident beam. One of the detectors measures the longitudinal component of the strain and the other detector measures the transverse component. The gauge volume used was 4x4x4 mm^3. Deformation was achieved using the strain control mode during the loading cycle. Load control mode was used during the unloading cycle.

Although an extensometer was attached to the specimens during the compression tests, it was not possible to get a reasonable macroscopic elastic modulus. The reason for this may be attributed to the fact that the extensometer was mounted very close to

the grips of the stress-rig and it may be recording the compliance of the grips of the rig.

The various weld types tested were:

(a) Multi–Pass Weld Pad

(b) TRAINSS Pipe Butt Weld

(c) TIG Weld

The tests were carried out in several orientations of the cubes with reference to the neutron beam. The orientations are discussed below:

LD – TD: The cube compressed along the longitudinal direction and detector bank 2 recording the transverse direction strain.

TD – LD: The cube compressed along the transverse direction and detector bank 2 recording the longitudinal direction strain.

ND – TD: The cube compressed along the normal direction and detector bank 2 recording the transverse direction strain.

4.9.2 Multi-Pass Weld Pad (LD-TD)

Fig. 4.32 shows the complete cycle of loading for the test.

The specimen was loaded up to 2% strain and then unloaded to zero stress. It was then loaded to 4% strain and unloaded to zero stress. The Young's modulus has been calculated for various loading/unloading Pawley lattice strain and is summarised in table 4.2.

Table 4.2 Young's modulus calculated from Pawley lattice strain for the Weld-Pad (LD-TD).

% Strain	Young's modulus (GPa)
2% strain (loading)	128
2% strain (unloading)	135
4% strain (unloading)	143

Fig. 4.33 shows the diffraction spectrum at the beginning of the test. In the diffraction spectrum {200} is the dominant peak, and {311} is second in intensity. Pawley lattice strain for various load and unload cycles is shown in Fig. 4.34. The single peak strain along with Pawley lattice strain is shown in Fig. 4.35. In the elastic region and in the longitudinal direction, the response of Pawley strain curve is very close to {200} and {311} single peak strain curve. Beyond the elastic region it lies in between {200} and {311} single peak strain. The {200} planes are the most compliant and the {111} stiffest. The {111} planes exhibit non-linearity. In the transverse direction the {200} planes are the most compliant and the {111} stiffest.

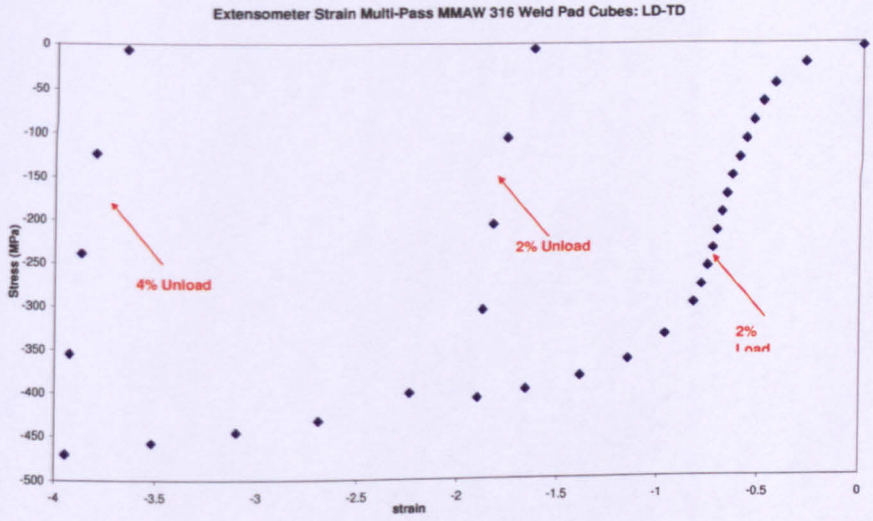

Fig. 4.32 Test LD-TD: complete cycle of loading.

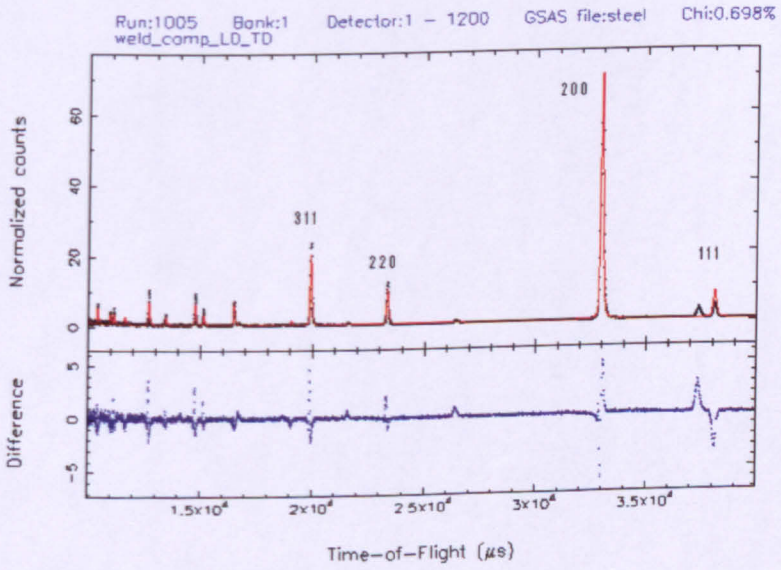

Fig. 4.33 Test LD-TD diffraction spectrum at 5 MPa

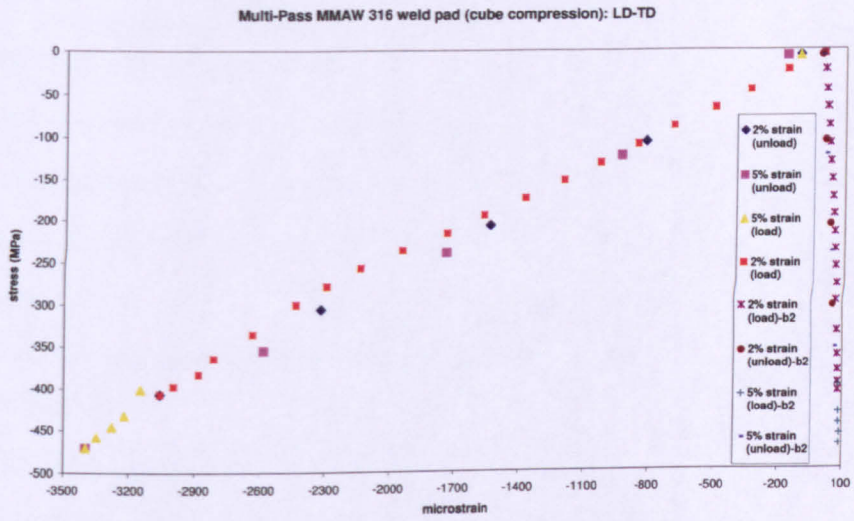

Fig. 4.34 Test LD-TD applied stress vs Pawley lattice strain (longitudinal and transverse).

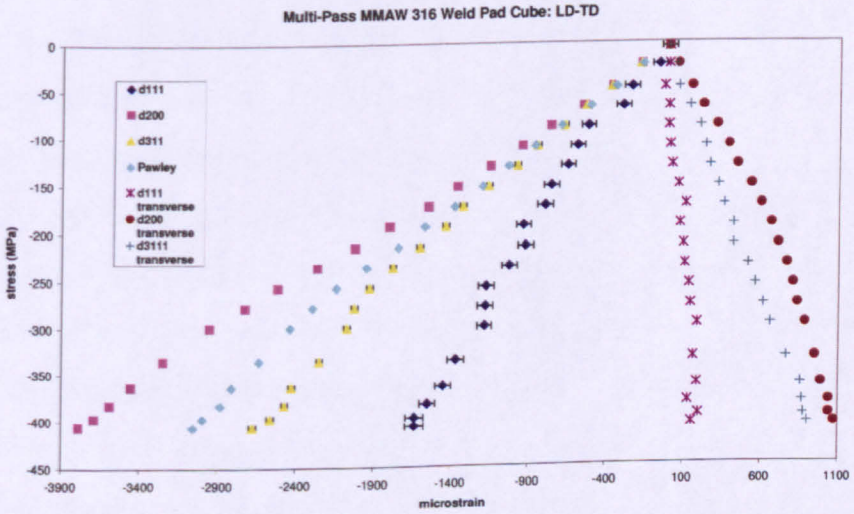

Fig. 4.35 Test LD-TD applied stress vs single peak strain with Pawley lattice strain.

4.9.3 Multi–Pass Weld Pad (TD–LD)

Fig. 4.36 shows the complete cycle of loading for the test.

The specimen was loaded up to 1.6% strain and then unloaded to zero stress. Again it was loaded to 3.6% strain and unloaded to zero stress. The Young's modulus has been calculated for various loading/unloading Pawley lattice strain and is summarised in table 4.3.

Table 4.3 Young's modulus calculated from Pawley lattice strain for the Weld-Pad (TD-LD).

% Strain	Young's modulus (GPa)
1.6% strain (loading)	121
1.6% strain (unloading)	127.8
3.6% strain (unloading)	130

Fig. 4.37 shows the diffraction spectrum at the beginning of the test. In the diffraction spectrum {200} is the dominant peak, and {311} is second in intensity. Pawley lattice strain for various load and unload cycles is shown in Fig. 4.38. The single peak strain along with Pawley lattice strain is shown in Fig. 4.39. In the elastic region and along the longitudinal direction the response of Pawley strain curve is very close to {200} and {311} single peak strain. Beyond the elastic region it lies in between {200} and {311} single peak strain. The {200} planes are the most compliant and the {111} stiffest. The {111} planes exhibit non-linearity. Along the transverse direction non-linear behaviour is exhibited by all the peaks with the exception of {200} which have some offset points from the linear behaviour.

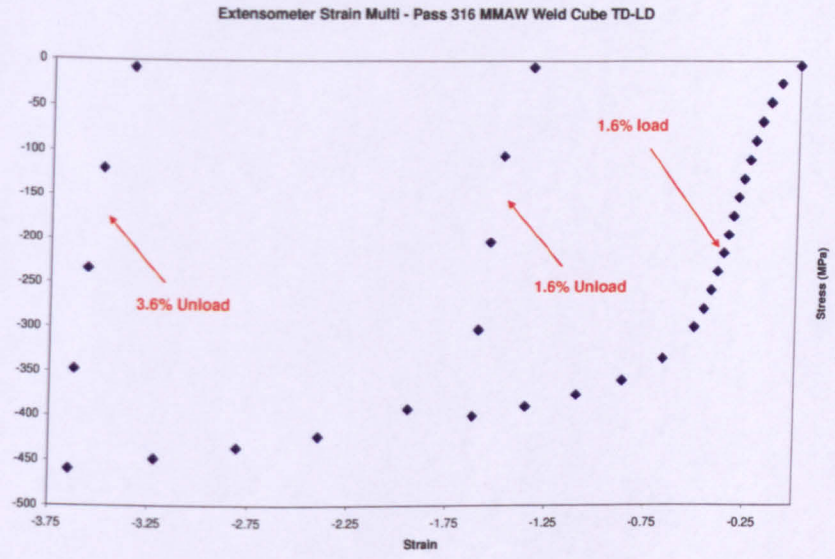

Fig. 4.36 Test TD-LD complete cycle of loading.

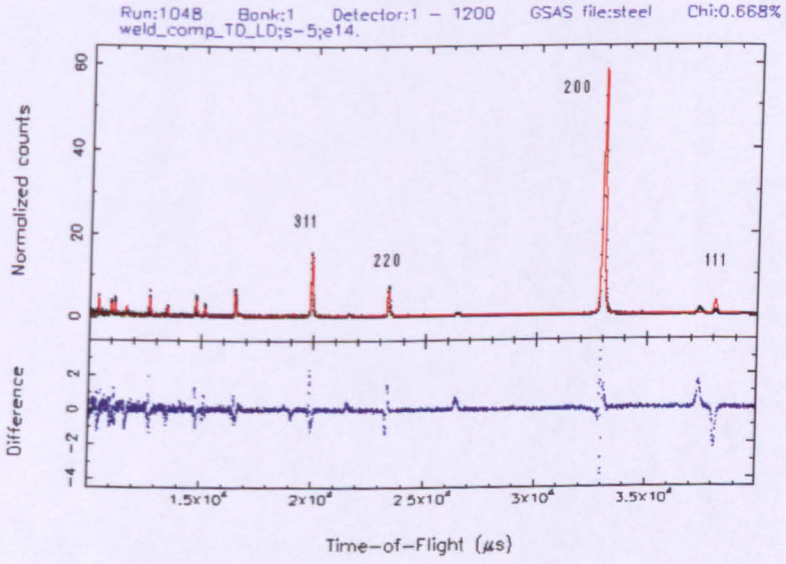

Fig. 4.37 Test TD-LD diffraction spectrum at 5 MPa.

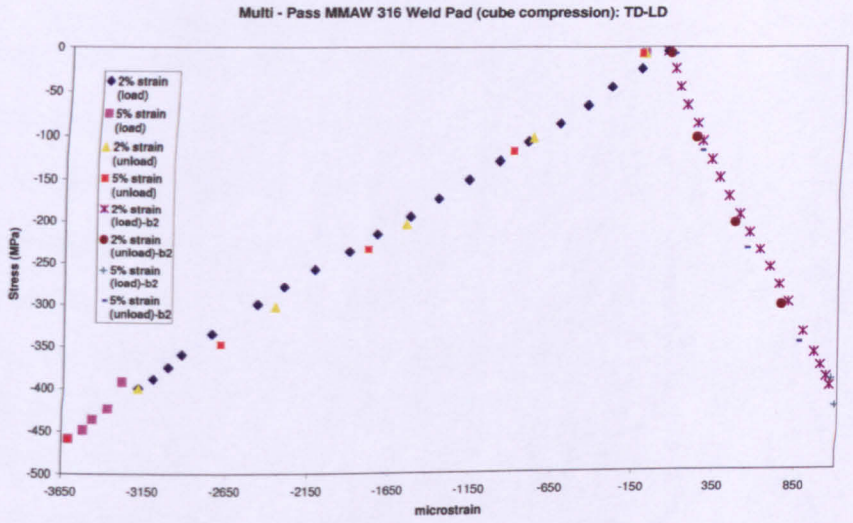

Fig. 4.38 Test TD-LD applied stress vs Pawley lattice starin.

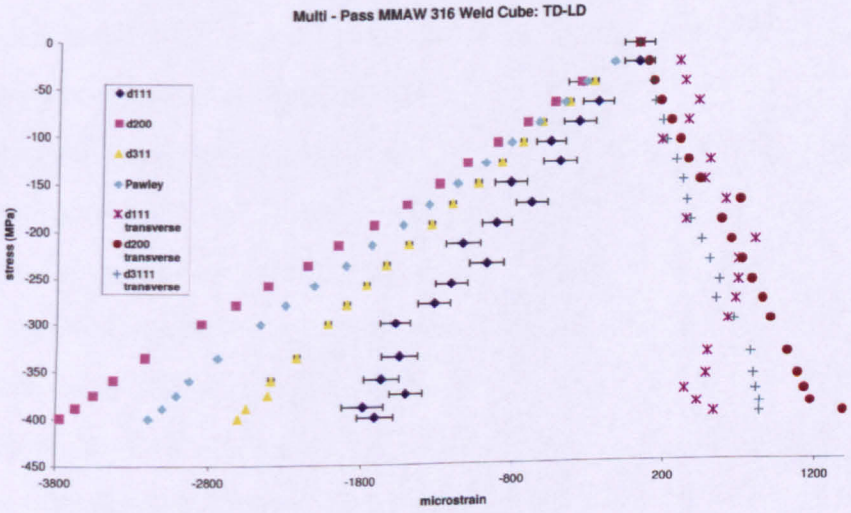

Fig. 4.39 Test TD-LD applied stress vs single peak strain with Pawley strain.

4.9.4 Multi–Pass Weld Pad (ND–TD)

Fig. 4.40 shows the complete cycle of loading for the test.

The specimen was loaded up to 2% strain and then unloaded to zero stress. Again it was loaded to 4% strain and unloaded to zero stress. The Young's modulus has been calculated for various loading/unloading Pawley lattice strain and is summarised in table 4.4.

Table 4.4 Young's modulus calculated from Pawley lattice strain for the Weld-Pad (ND-TD).

% Strain	Young's modulus (GPa)
2% strain (loading)	123
2% strain (unloading)	119.4
4% strain (unloading)	126.2

Fig. 4.41 shows the diffraction spectrum at the beginning of the test. In the diffraction spectrum {200} is the dominant peak, and {311} is second in intensity. Pawley lattice strain for various load and unload cycles is shown in Fig. 4.42. The single peak strain along with Pawley lattice strain is shown in Fig. 4.43. The response of Pawley lattice strain curve is very close to {200} single peak strain curve. Non-linear behaviour is exhibited by all the peaks in the longitudinal and the transverse direction. In the longitudinal direction the {311} peak strain is the most compliant upto 215 MPa. After that the {200} becomes the most compliant. The {200} peak strain the stiffest upto 67 MPa. After that the {111} peak strain is the stiffest. In the transverse direction the {200} planes are the most compliant and the {111} stiffest.

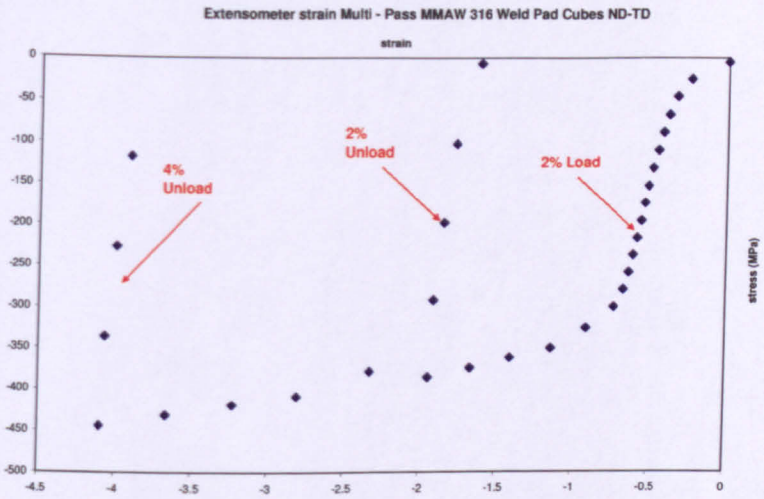

Fig. 4.40 Test ND-TD complete loading cycle.

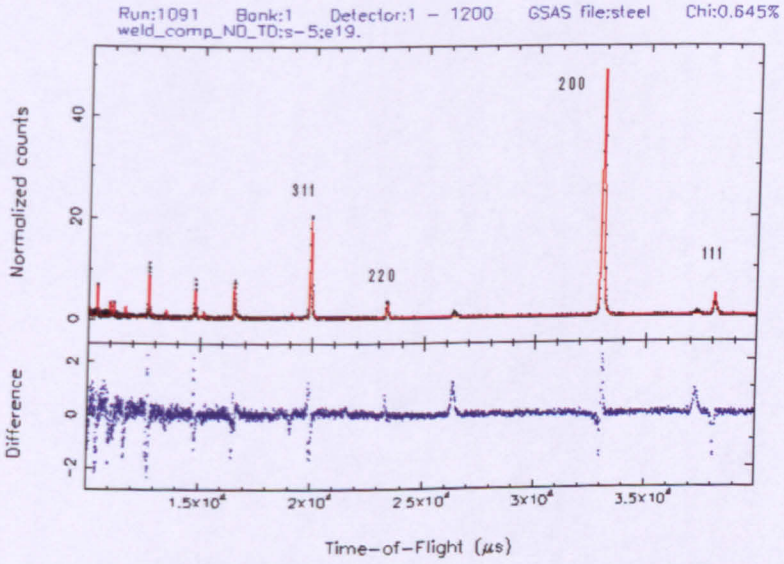

Fig. 4.41 Test ND-TD diffraction spectrum at 5 MPa

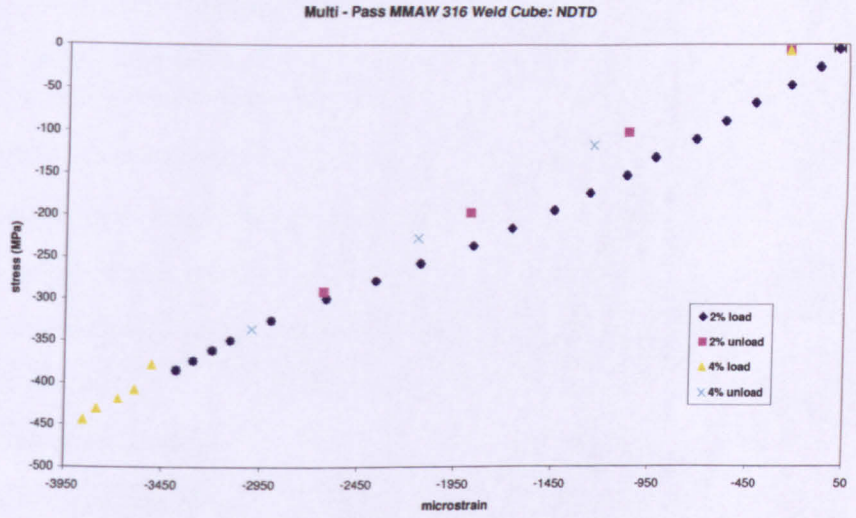

Fig. 4.42 Test ND-TD applied stress vs Pawley lattice strain.

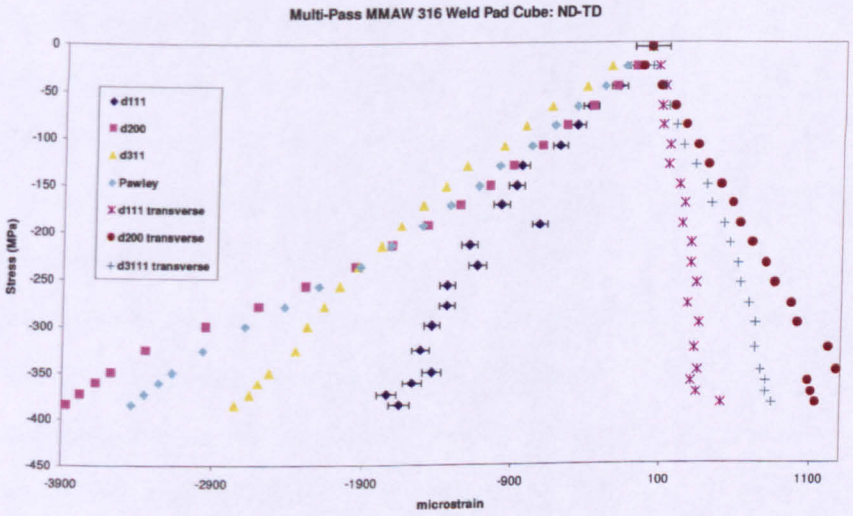

Fig. 4.43 Test ND-TD applied stress vs single peak strain with Pawley response.

4.10 Discussion

As the 200 peak is dominant in the loading diffraction spectrum for all the orientations, the Pawley elastic modulus remains low at around 120 GPa.

4.11 Weld Compression – TRAINSS Pipe Butt Weld

4.11.1 Test 1–LD-TD

Fig. 4.44 shows the complete loading cycle. The specimen was loaded to 1.6% strain and then unloaded to zero stress. It was reloaded again to 4% strain and then unloaded to zero stress. The Young's modulus has been calculated for various loading/unloading Pawley lattice strain and is summarised in table 4.5.

Table 4.5 Young's modulus calculated from Pawley lattice strain for the TRAINSS (LD-TD).

% Strain	Young's modulus (GPa)
1.6% strain (loading)	139
1.6% strain (unloading)	147
4% strain (unloading)	153

Fig. 4.45 shows the diffraction spectrum at the beginning of the experiment. In the diffraction spectrum {200} is the dominant peak, {311} being second in intensity. Fig. 4.46 shows the Pawley lattice strain (longitudinal and transverse) for various load – unload cycles. The Young's modulus calculated from first load cycle is 139 GPa. Single peak strain along with Pawley lattice strain is shown in Fig. 4.47. In the longitudinal direction the {111} planes exhibit non-linear behaviour and they are the stiffest planes. The {311} planes are the most compliant up to 130 MPa. After that the {200} planes become most compliant. The response of Pawley lattice strain is very close to {200} single peak strain. In the transverse direction the {311} and the {200} are the most compliant planes up to 130 MPa. After that the {200} planes are the most compliant. The {111} planes are the stiffest.

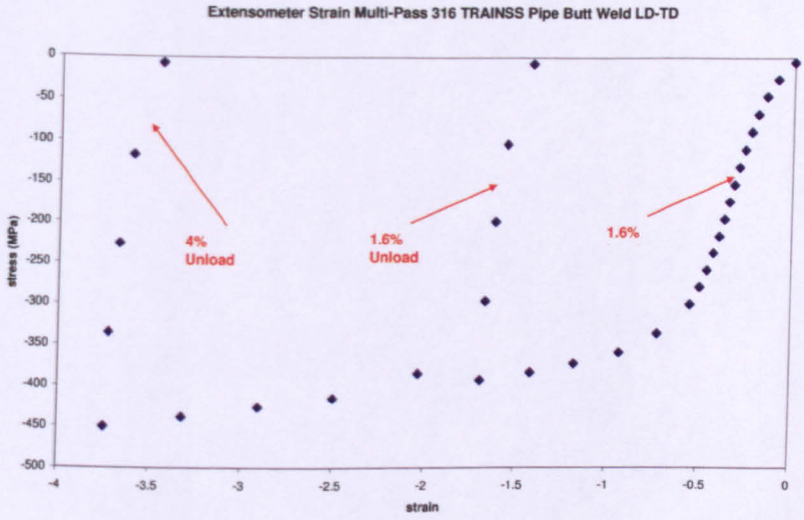

Fig. 4.44 Test LD-TD complete loading cycle.

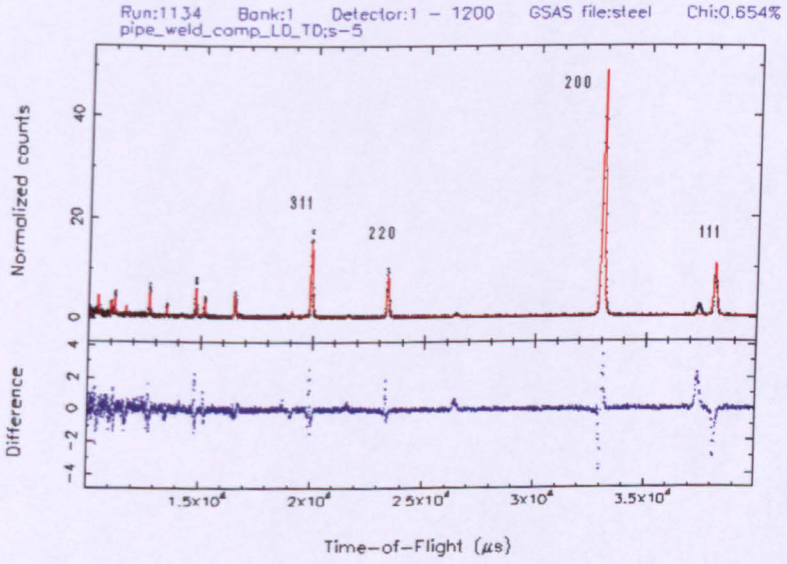

Fig. 4.45 Test LD-TD diffraction spectrum at 5 MPa.

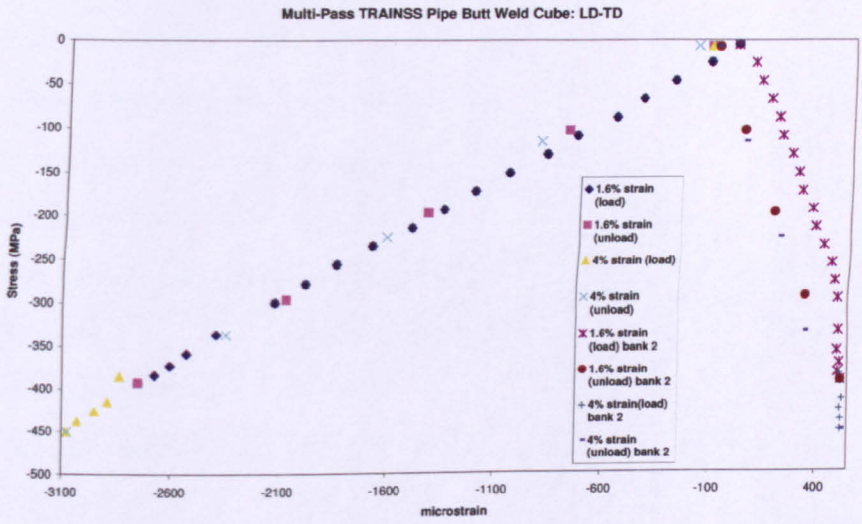

Fig. 4.46 Test LD-TD applied stress vs Pawley lattice strain (longitudinal and transverse).

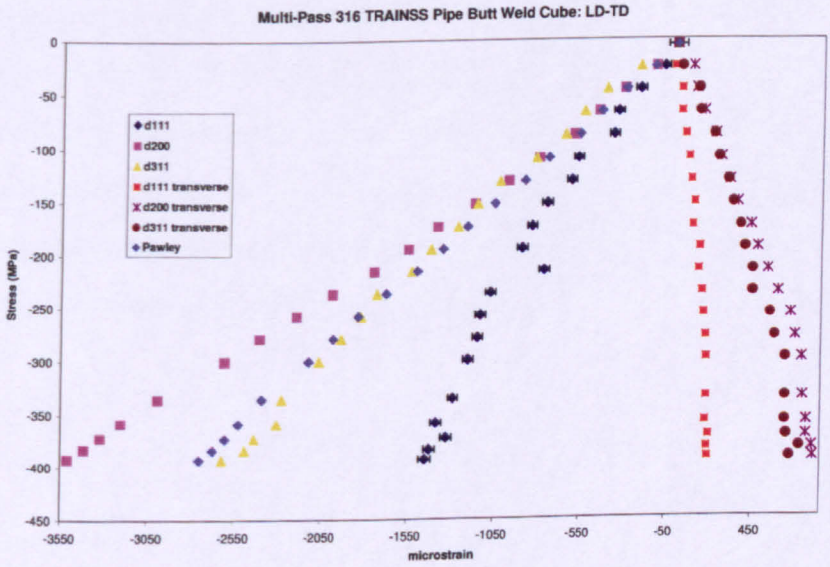

Fig. 4.47 Test LD-TD applied stress vs single peak strain with Pawley lattice strain.

4.11.2 Test 2–TD-LD

Fig. 4.48 shows the complete loading cycle. The specimen was loaded to 1.6% strain and then unloaded to zero stress. It was reloaded again to 4% strain and then unloaded to zero stress. The Young's modulus has been calculated for various loading/unloading Pawley lattice strain and is summarised in table 4.6.

Table 4.6 Young's modulus calculated from Pawley lattice strain for the TRAINSS (TD-LD).

% Strain	Young's modulus (GPa)
1.6% strain (loading)	126
1.6% strain (unloading)	143.6
4% strain (unloading)	154

Fig. 4.49 shows the diffraction spectrum at the beginning of the experiment. In the diffraction spectrum {200} is the dominant peak, {311} and {111} being second in intensity. Fig. 4.50 shows the Pawley lattice strain (longitudinal and transverse) for various load – unload cycles. Single peak strain along with Pawley lattice strain is shown in Fig. 4.51. In the longitudinal direction the {111} planes are the stiffest and exhibit non-linear behaviour. The {200} planes are the most compliant. The response of Pawley lattice strain is very close to {311} single peak strain. In the transverse direction all the planes exhibit non-linear behaviour. The {200} planes are the most compliant and the {111} stiffest.

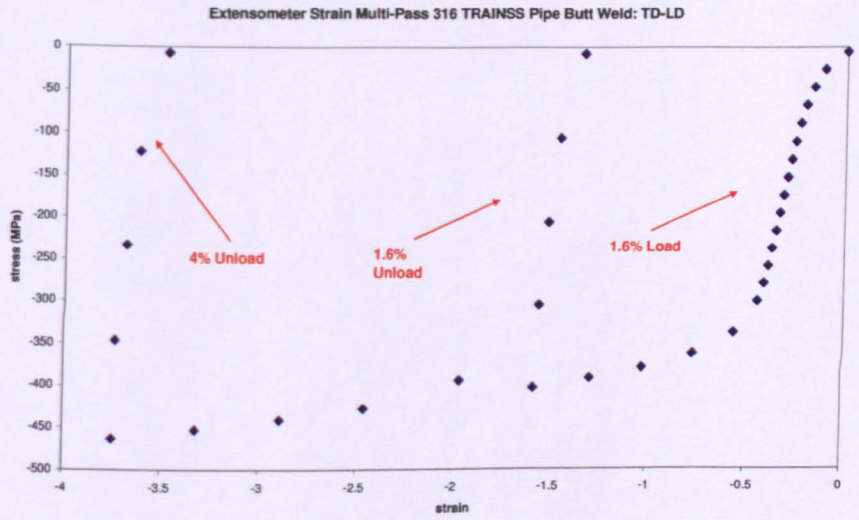

Fig. 4.48 Test TD-LD complete loading cycle.

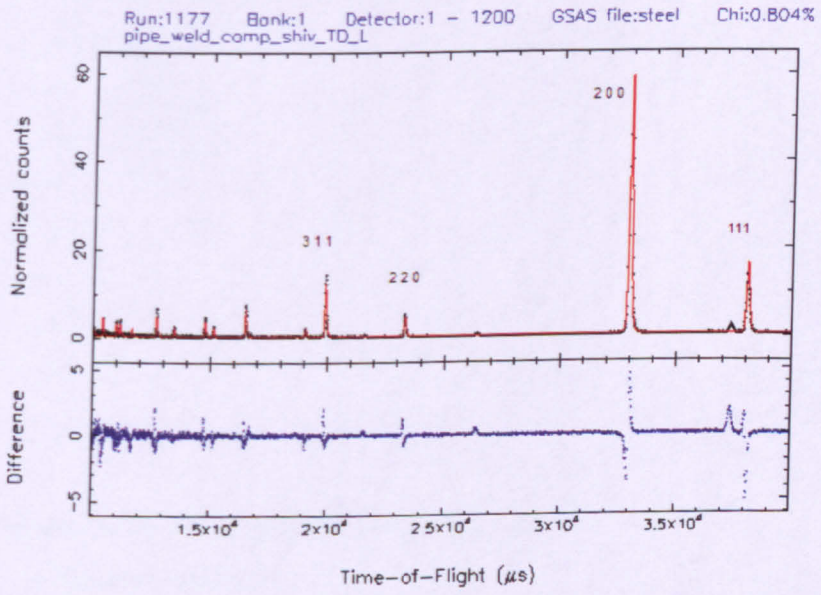

Fig. 4.49 Test TD-LD diffraction spectrum at 5 MPa.

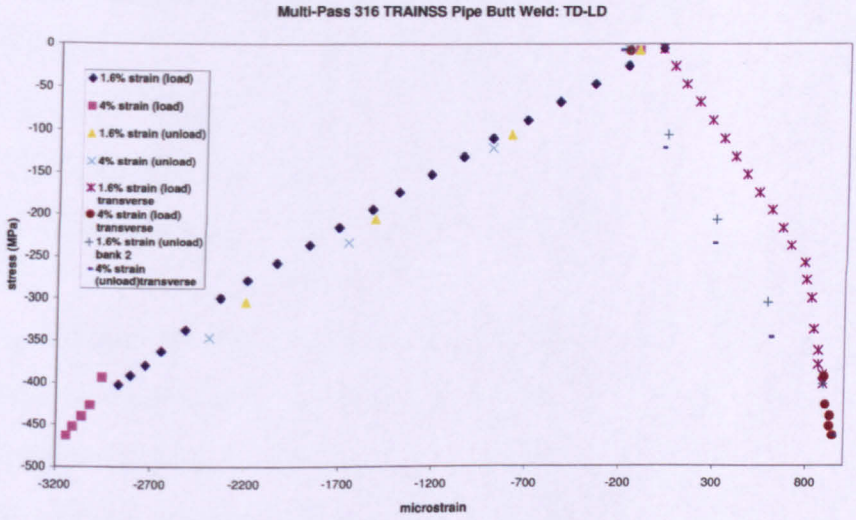

Fig. 4.50 Test TD-LD Pawley lattice strain (longitudinal and transverse).

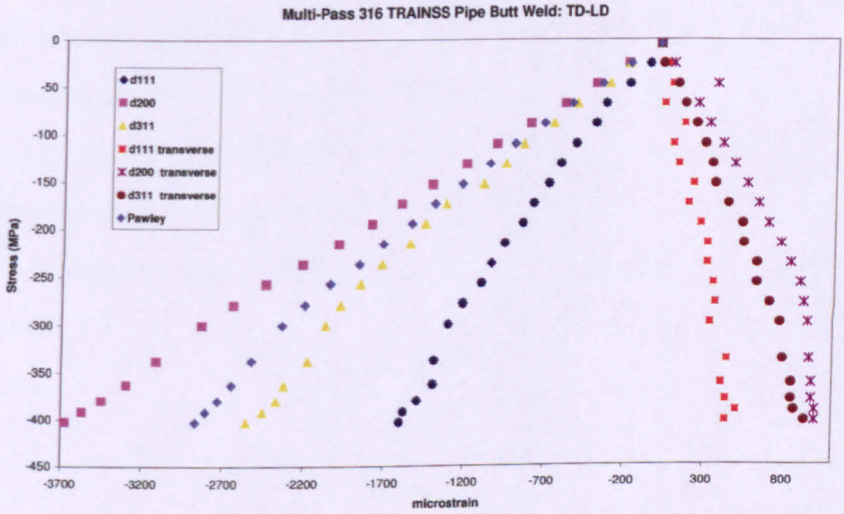

Fig. 4.51 Test TD-LD single peak strain with Pawley lattice strain.

4.11.3 Test 3–ND-TD

Fig. 4.52 shows the complete loading cycle. The specimen was loaded to 1.76% strain and then unloaded to zero stress. It was reloaded again to 4% strain and then unloaded to zero stress. The Young's modulus has been calculated for various loading/unloading Pawley lattice strain and is summarised in table 4.7.

Table 4.7 Young's modulus calculated from Pawley lattice strain for the TRAINSS (ND-TD).

% Strain	Young's modulus (GPa)
1.76% strain (loading)	180
1.76% strain (unloading)	217
4% strain (unloading)	225

Fig. 4.53 shows the diffraction spectrum at the beginning of the experiment. In the diffraction spectrum {111} is the dominant peak, {220} and {311} being second and third in intensity. Fig. 4.54 shows the Pawley lattice strain (longitudinal and transverse) for various load–unload cycles. Single peak strain along with Pawley lattice strain is shown in Fig. 4.55. The response of Pawley lattice strain curve is very close to {111} single peak strain curve in the elastic region. In the longitudinal direction the {111} and {311} are the stiffest planes up to 130 MPa. After that the {111} planes are the stiffest. As the {200} peak is very small in the diffraction spectrum there are big error bars. The response of the {200} planes is very non-linear. In the transverse direction the {200} planes are the most compliant and the {111} stiffest.

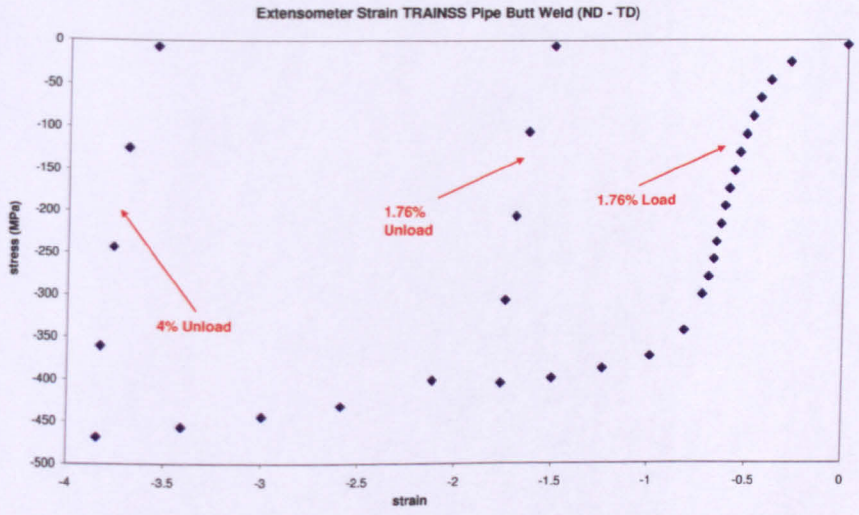

Fig. 4.52 Test ND-TD complete loading cycle.

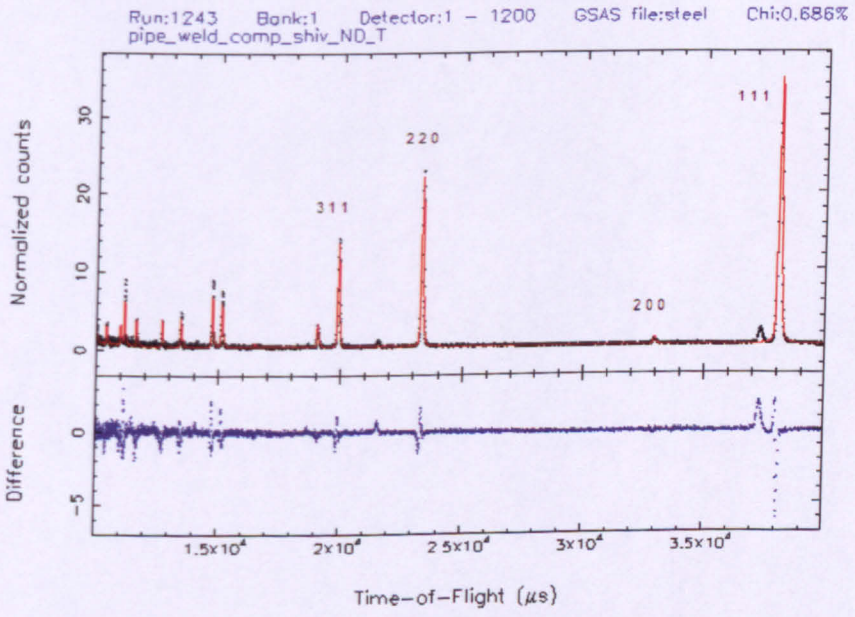

Fig. 4.53 Test ND-TD diffraction spectrum at 5 MPa

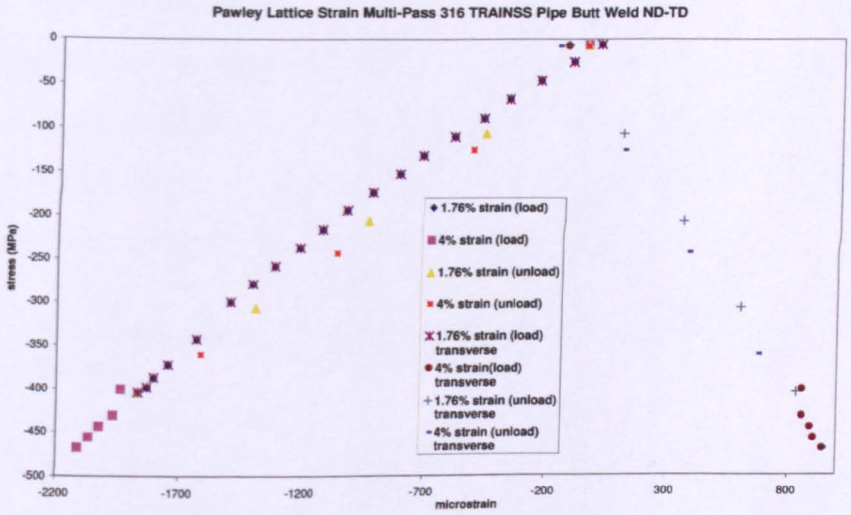

Fig. 4.54 Test ND-TD applied stress vs Pawley lattice strain (longitudinal and transverse).

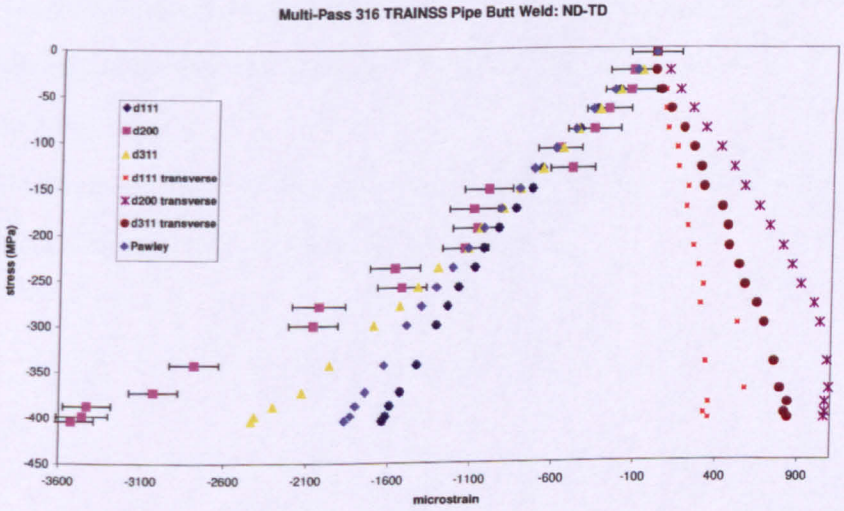

Fig. 4.55 Test ND-TD Applied Stress vs Single peak strain with Pawley lattice strain.

4.12 Discussion

The Pawley elastic modulus in the LD and TD orientations during the loading cycles is 139 and 126 GPa respectively. This can be attributed to pronounced 200 peak in the diffraction spectrum. However in the ND diffraction spectrum 111 peak is dominant, which results in high value of Pawley elastic modulus (139 GPa).

4.13 Compression Tests On Multi-Pass 308 TIG Weld Metal Cubes

4.13.1 Test 1–LD–TD

Fig. 4.56 shows the loading cycle for LD–TD orientation. The specimen was loaded to 2% strain and then unloaded to zero strain. Fig. 4.57 shows the diffraction spectrum at the beginning of the experiment. In the diffraction spectrum {111} is the dominant peak, followed by {311}. The Pawley lattice strain (longitudinal and transverse) for the loading and unloading part of the test is shown in Fig. 4.58. Single peak strain along with Pawley lattice strain is shown in Fig. 4.59. The response of Pawley lattice strain lies in between {111} and {311}. The {200} planes are the most compliant and the {111} stiffest.

The Young's modulus calculated from Pawley lattice strain at 1.4% strain during load is 226 GPa and at 1.4% strain during unload 206 GPa.

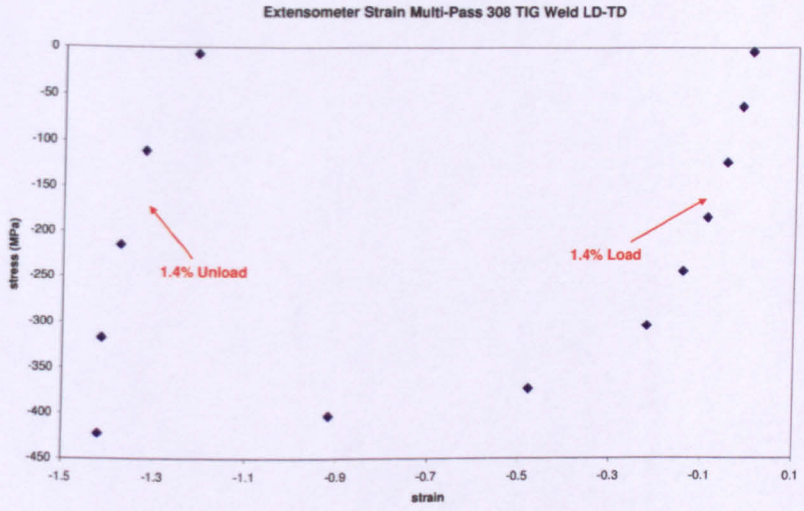

Fig. 4.56 Test LD-TD complete loading cycle.

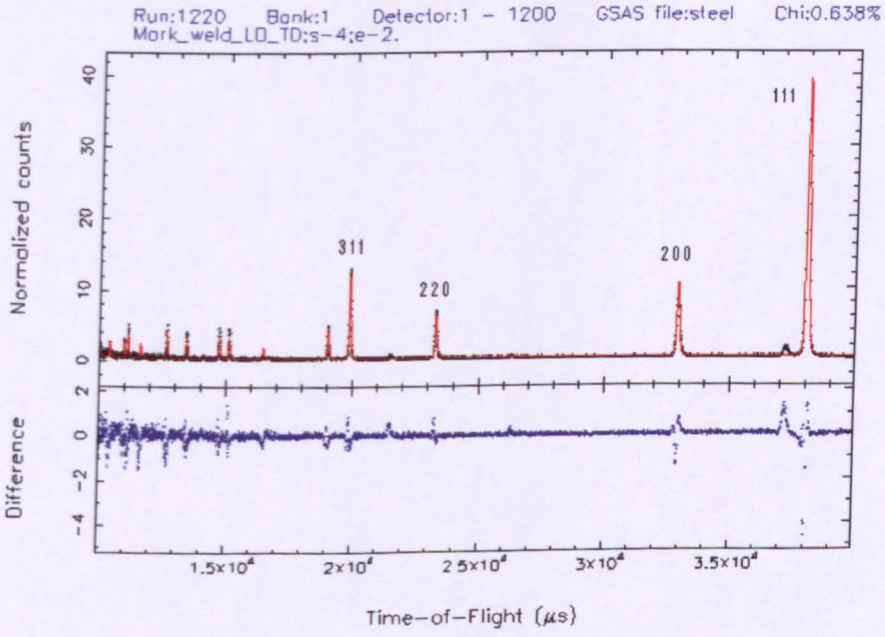

Fig. 4.57 Test LD-TD diffraction spectrum at 5 MPa.

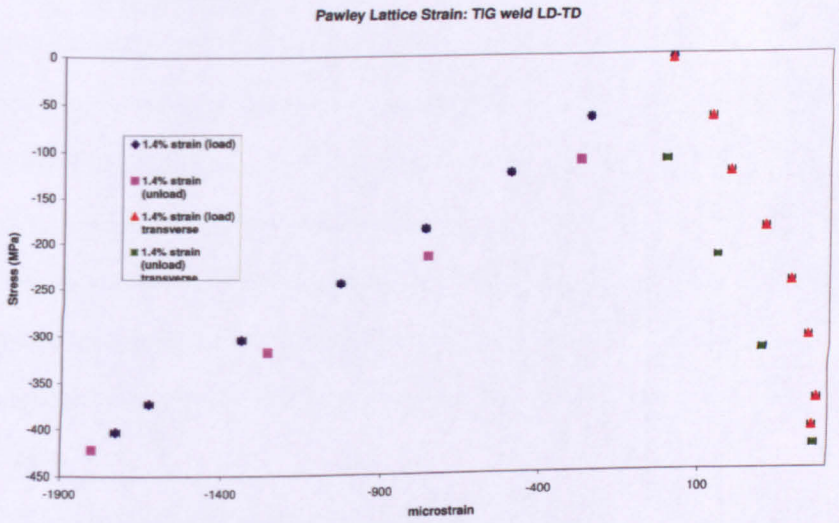

Fig. 4.58 Test LD-TD applied stress vs Pawley lattice strain (longitudinal and transverse).

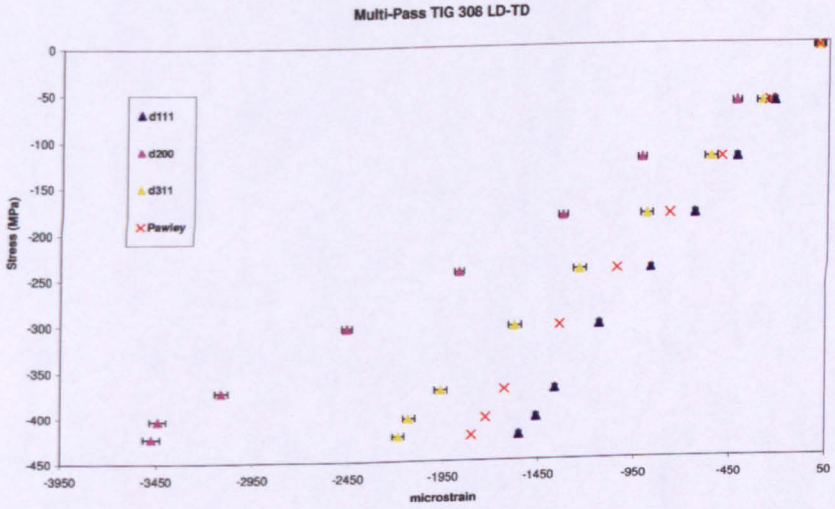

Fig. 4.59 Test LD-TD applied stress vs single peak strain with Pawley lattice strain.

4.13.2 Test 2–TD–LD

Fig. 4.60 shows the loading cycle for LD–TD orientation. The specimen was loaded to 2% strain and then unloaded to zero strain. Fig. 4.61 shows the diffraction spectrum at the beginning of the experiment. In the diffraction spectrum {111} is the dominant peak, followed by {200}. Pawley lattice strain (longitudinal and transverse) for the loading part of the test is shown in Fig. 4.62. *Single peak strain along* with Pawley lattice strain is shown in Fig. 4.63. The response of Pawley lattice strain lies in between {111} and {311}. The {200} planes are the most compliant and the {111} stiffest.

The Young's modulus calculated from Pawley lattice strain at 1.7% strain during load is 220 GPa.

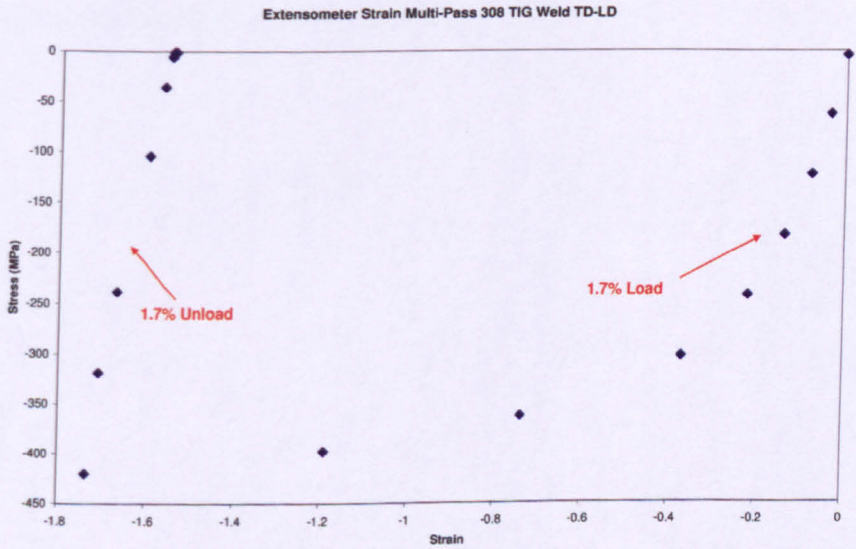

Fig. 4.60 Test TD-LD complete loading cycle.

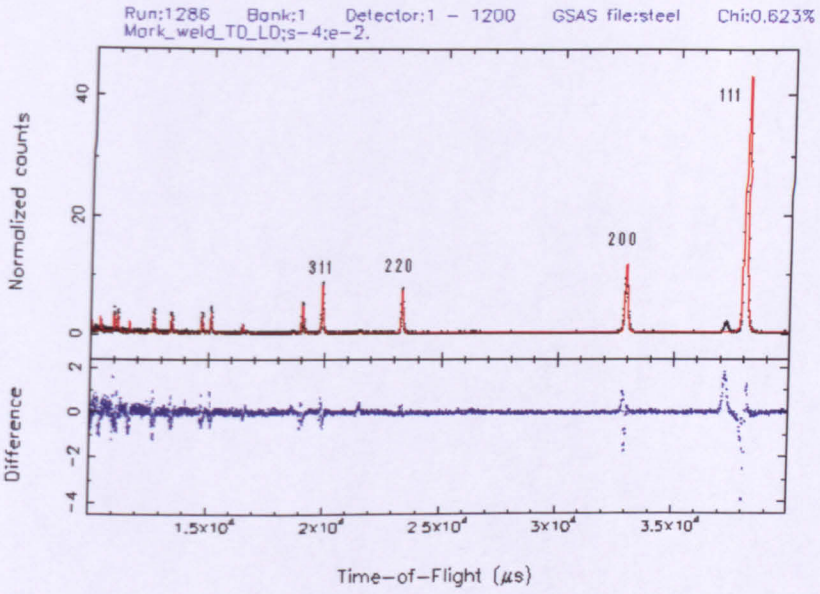

Fig. 4.61 Test TD-LD diffraction spectrum at 5 MPa.

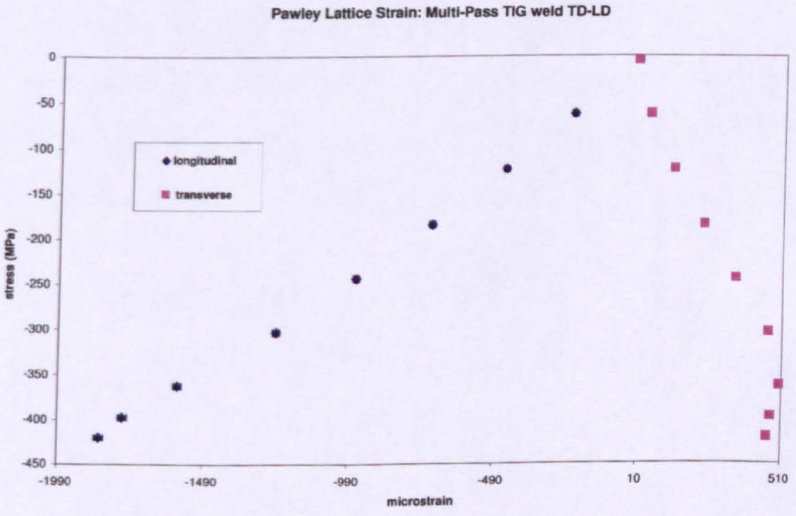

Fig. 4.62 Test TD-LD applied stress vs Pawley lattice strain (longitudinal and transverse).

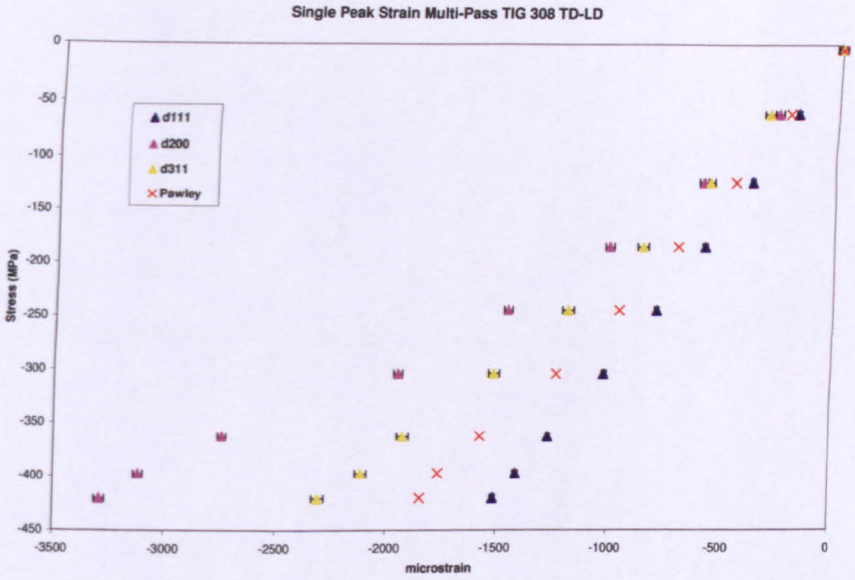

Fig. 4.63 Test TD-LD applied stress vs single peak strain with Pawley lattice strain.

4.14 Discussion

The diffraction spectrums for LD and TD orientations during the loading cycles show a dominant {111} peak. Therefore the Pawley elastic modulus remains high at around 220 GPa. The TIG welds show a nearly random texture. Therefore the elastic modulus of TIG weld is comparable with the parent metal.

4.15 Summary

In-situ neutron diffraction tests on various types of weld specimens have been discussed. The results are presented in the form of diffraction spectra, Pawley lattice strain and single peak strains. Literature review on in-situ neutron diffraction tests have been carried out.

Next chapter will provide details about various modelling techniques and EPSC results.

Chapter 5 Discussion and Link to Modelling

The development of texture in various welds and the implications for Young's modulus measurement has been discussed. The Young's modulus results obtained from the EPSC modelling are compared with the neutron diffraction results. The angular variation of the Young's modulus has been measured.

5.1 Modelling of Weld Residual Stresses

For predicting weld residual stresses using finite element modelling a good estimate of the Young's modulus is necessary. For an isotropic material the stress calculations are straightforward. Most of the engineering materials such as the welds are highly anisotropic and complications arise in estimating a suitable value of the Young's modulus.

The previous work [96, 97, 98, 99] assumes the weld metal to be homogeneous and assigns a Young's modulus value of the parent metal. No texture measurements are carried out on the weld metal to check the orientation dependency of the Young's modulus.

Shan et al [96] have used the finite element method for the thermo-mechanical modelling of a single weld bead on plate of austenitic stainless steel. The Young's modulus value of 171 GPa for the weld and 195.6 GPa for parent metal has been used.

Ficquet et al [97] used a finite element model for predicting the residual stresses generated by single weld bead on an austenitic stainless steel (AISI Type 316L) plate. The Young's modulus value of 168.2 GPa for the weld and 195.6 GPa for parent metal has been used.

The work in references [96] and [97] was carried out as part of the NeT (European Network on Neutron Techniques Standardization for Structural Integrity [98])

programme to validate the use of finite element simulations in order to accurately predict residual stresses

Deng et al [99] used ABAQUS software to investigate the temperature fields and residual stress states in multi-pass welds in SUS304 stainless steel pipe. Although the base metal and the weld metal were defined as different materials, the weld metal was assigned the same elastic modulus as the parent metal. The Young's modulus value of 198.5 GPa was used.

Brown et al [100] used the finite element model to predict the residual stresses in a series of rectangular repair welds in P275 and S690 steels. This work was carried out as part of the European Union FP-5 project ELIXIR to validate the numerical modelling techniques used in the determination of the residual stresses generated during the repair process. The Young's modulus value of 199 GPa was used for the S275 plate material and 209 GPa for the weld material. For the S690 plate and weld material an elastic modulus value of 210 GPa was used.

From the present work it has been found that the Young's modulus is highly orientation dependent in the case of a highly textured material such as the Weld-Pad. But in the case of a TIG weld the Young's modulus approaches a value comparable to an isotropic material.

5.2 Texture Development in the Weld Metal

5.2.1 Weld-Pad

The weld-pad exhibits a very strong recrystallization cube texture which is evident from the {200} pole figures as shown in Fig. 5.1. The texture strength in multiples of the random intensity is 20.55 for the {200} pole figure and 8.47 for the {111} pole figure.

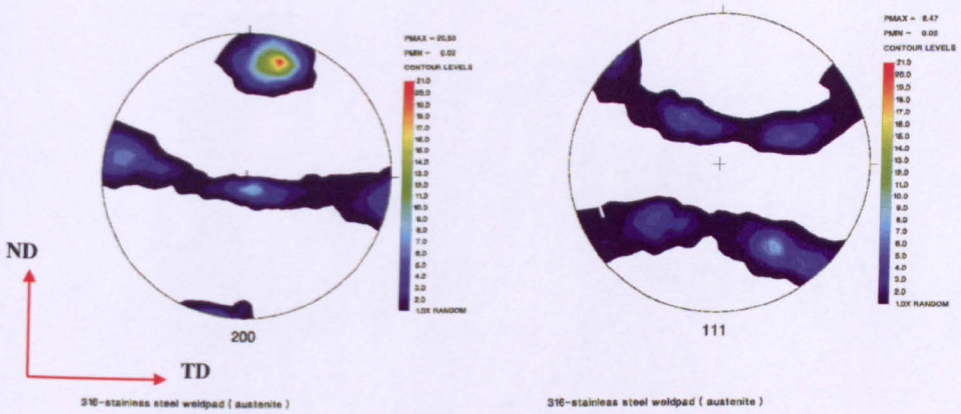

Fig. 5.1 The {200} and {111} pole figures for the weld-pad.

The [200] directions are the softest in austenitic stainless steels of fcc crystal structure. In the textured weld-pad material these planes are tilted from the sample normal direction. In the literature this type of texture has been termed as the fiber texture where certain crystallographic planes ([001] in the case of austenitic stainless steel welds) align themselves along the solidification direction as shown in Fig. 5.2 [82, 101].

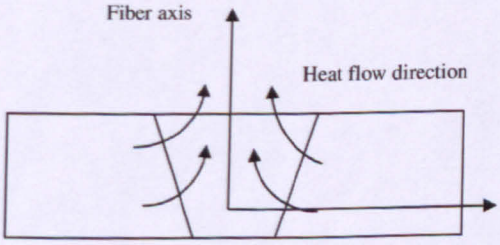

Fig. 5.2 Fiber axis in a typical weld geometry.

5.2.2 TRAINSS

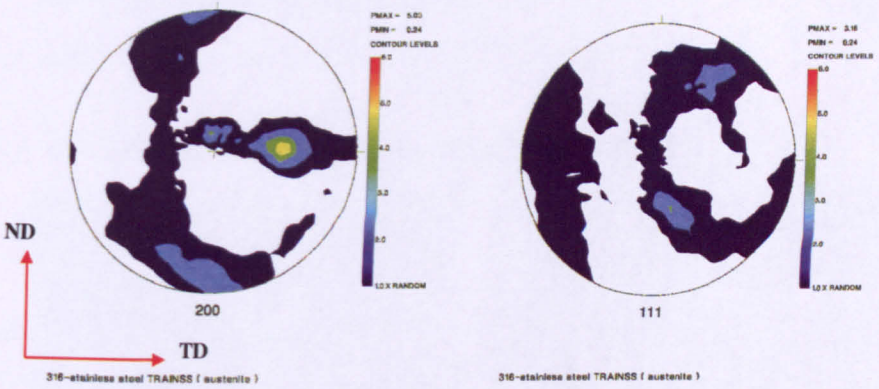

Fig. 5.3 The {200} and {111} pole figures for the TRAINSS weld.

The texture exhibited by the TRAINSS weld is mild as compared with the weld-pad which is evident from the {200} and {111} pole figures as shown in Fig. 5.3. The texture strength in multiples of the random intensity is 5.03 for the {200} pole figure and 3.16 for the {111} pole figure. The softest crystallographic planes are aligned along the sample transverse direction.

5.2.3 TIG

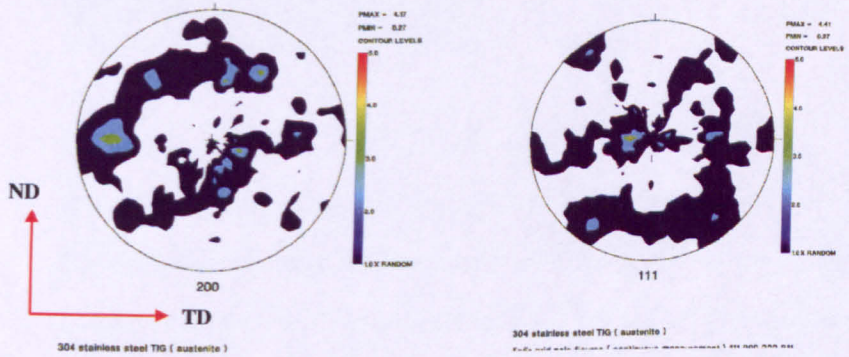

Fig. 5.4 The {200} and {111} pole figures for the TIG weld.

The texture exhibited by the TIG weld is nearly random which is evident from the {200} and {111} pole figures as shown in Fig. 5.4. The nearly random texture

exhibited by the TIG weld is surprising because a weld solidifies along a thermal gradient and significant texture is expected. The cause for the nearly random texture in the TIG weld needs to be investigated in more detail.

5.3 Symmetry Exhibited by the Weld Microstructure

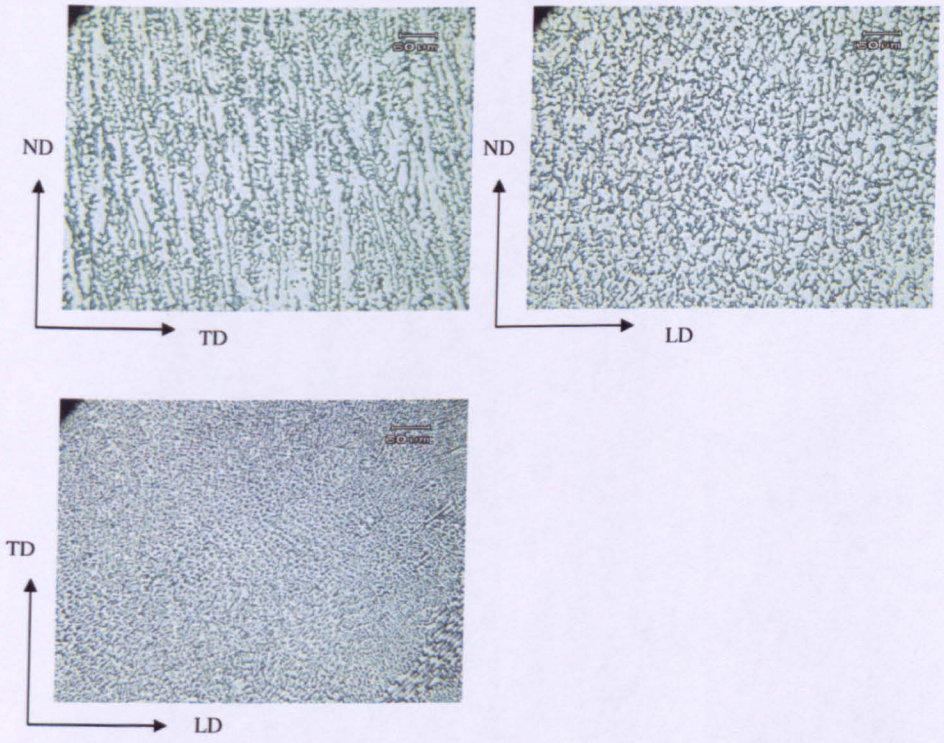

Fig. 5.5 Weld microstructure in different orientations (from TRAINSS weld).

The weld microstructure exhibits microstructural similarity in the (ND-TD) and the (ND-LD) planes as shown in Fig. 5.5 for the TRAINSS weld. However, this similarity has been observed in the Weld-Pad and the TIG weld as well. The (TD-LD) plane is expected to be a plane of isotropy. The weld metal is expected to have special orthotropic symmetry because of the apparent symmetry in the microstructure. This requires five elastic constants [5].

5.4 Implications for Young's Modulus Measurement

The texture exhibited by the weld-pad is complex and this type of texture has implications for the Young's modulus measurement as the softest or stiffest orientations are not aligned with any of the directions along which the samples have been machined for the Young's modulus measurement (Fig. 5.6).

Therefore it is very hard to predict the clip gauge response in this situation as the clip gauge is not measuring macroscopic strains along soft or stiff orientations.

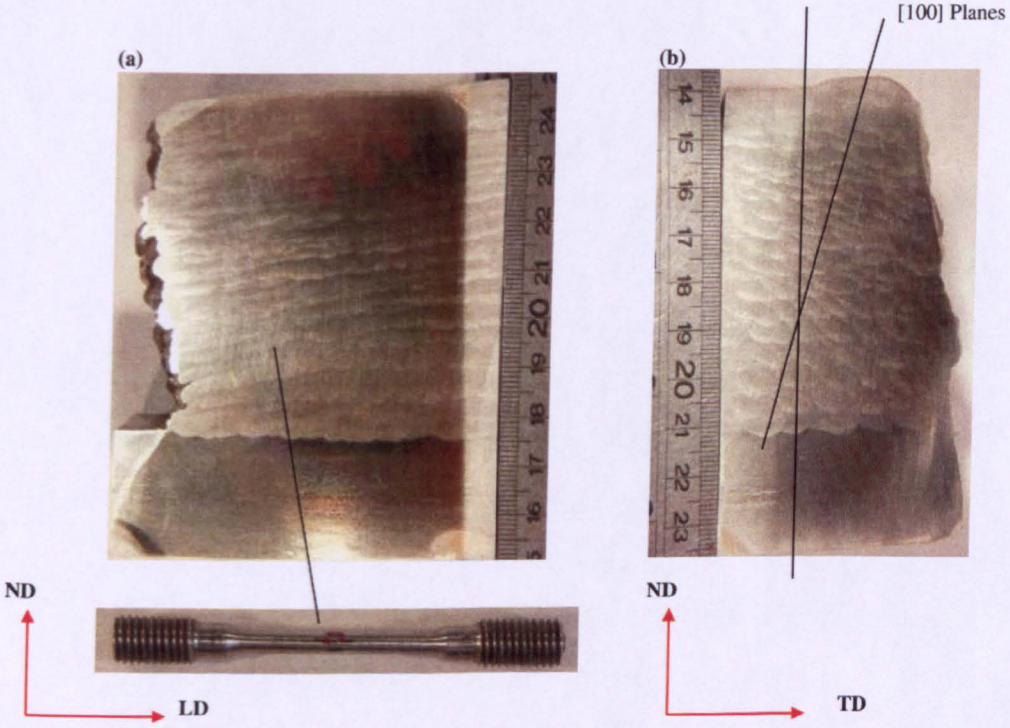

Fig. 5.6 (a) The orientation of specimen in the weld-pad (b) location of the compliant planes in the weld-pad.

In the case of the TRAINSS weld, as the most compliant planes are almost along the sample transverse direction, a lower value of the Young's modulus has been obtained in this orientation as compared with other orientations.

In the case of TIG weld, as the texture is nearly random, an identical value of the Young's modulus has been obtained in all the orientations.

5.5 EPSC Modelling

The theoretical framework for EPSC modelling has been described in the chapter 1. This section provides details about the practical data used to model the weld response under applied loading and also describes the calculation of the Young's modulus from EPSC.

The single crystal elastic constants used in the model (C_{11} =204.6 GPa , C_{12} = 137.7 GPa, C_{44} = 126.2 GPa) are those for austenite [70]. The critical resolved shear stress τ_0 is 87 MPa [80]. The slip systems for FCC {111} planes and <110> directions are used in the model. The FORTRAN sub-routine written by Carlos Tome and E. C. Oliver (EPSC manual) has been used for EPSC calculations based on the EBSD texture data.

The EPSC model takes as input the grain population file (e.g. texture information). This grain population information can be obtained by EBSD analysis or neutron diffraction. The grain population file contains the information about grain orientations in the form of Euler angles. For the present work the EBSD technique has been used to obtain the grain population file. The EBSD analysis was carried out on the Multi-pass weld pad, the TRAINSS pipe butt-weld and a TIG weld. The specimens used for EBSD texture analysis were described in chapter two.

5.5.1 Angular Variation of Young's Modulus

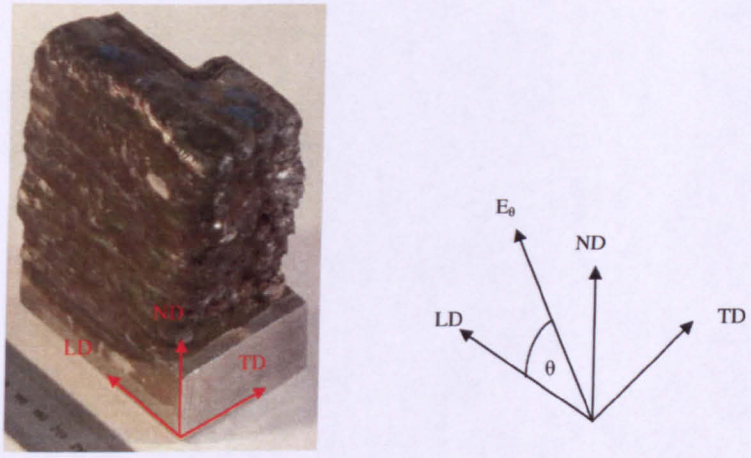

Fig. 5.7 Schematic showing the angular variation of the Young's modulus in the LD-ND plane.

Young's modulus has also been calculated as a function of angle in the LD-ND plane as shown in Fig. 5.7. As the texture is always measured in an orthogonal sample coordinate system which is related to an orthogonal EPSC coordinate system. It is not possible to apply a load to the measured texture at angles other than 90°. Therefore the texture measured in the sample coordinate system has been transformed to the loading coordinate system which facilitates the load application at any angle from 0° to 90°. The LD, TD and ND directions correspond to the sample coordinate system.

5.5.2 EPSC Modelling of Multi-Pass 316 Weld Pad

The response of the 316 weld-pad was investigated in the three principal processing directions i.e. LD, TD and ND using EPSC modelling. The elastic region of the macroscopic stress vs strain curve calculated using the EPSC model is shown in Fig. 5.8. The response of the weld-pad along the transverse direction is stiffer than along the more compliant normal direction. The Young's modulus results are compared with the neutron diffraction results and summarised in Table 5.1.

The EPSC results are in good agreement with the in-situ cube compression results. The Young's modulus calculated from EPSC is in general agreement with the diffraction Young's modulus except in the TD orientation. It is difficult to comment why there is disagreement in the TD orientation as a range of values for the diffraction Young's modulus has been observed even in the same orientation. Table 5.4 summarises the Young's modulus values obtained from various samples in various orientations. The angular variation of the Young's modulus for the weld-pad is shown in Fig. 5.9. The modulus is a minimum of approximately at angles 0° and 90°, which correspond to LD and ND directions respectively. It attains a maximum value at about 45°. The Young's modulus is 136 GPa in the LD and 115 GPa in the ND but attains a value of 202 GPa midway between LD and ND. The weld-pad is most anisotropic in the LD-ND plane as compared with the TRAINSS pipe butt-weld and the TIG weld.

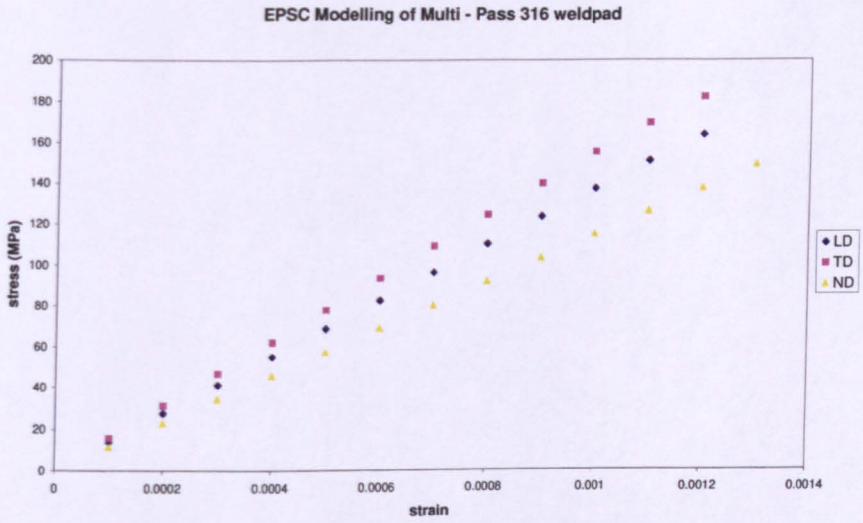

Fig. 5.8 EPSC modelling of the weld-pad response in three principal processing directions

Table 5.1 Comparison of EPSC *modelling* results of Young's modulus with neutron diffraction Young's modulus for the weld-pad.

Tension (Cylinder)	**LD**	**TD**	**ND**
Sample 4	**155**		
Sample 4	**172**		
Sample 4	**162**		
Sample 15	**130**		
Compression (Cubes)			
LD - TD	**128**		
TD - LD		**121**	
ND - TD			**123**
EPSC **(Texture from Cubes)**	**137.16**	**153.35**	**114.88**

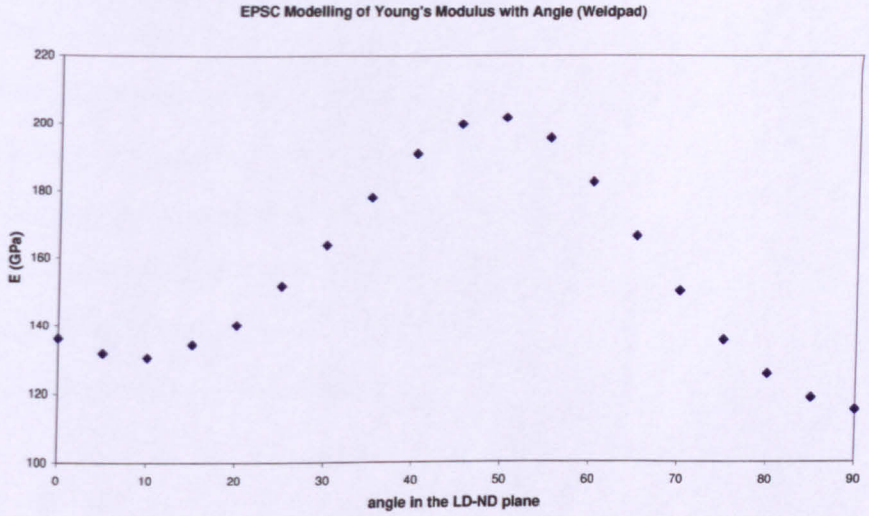

Fig. 5.9 Angular variation of the Young's modulus for the weld-pad.

5.5.3 EPSC Modelling of TRAINSS Pipe Butt Weld

The response of the 316 TRAINSS pipe butt weld was investigated along the three principal directions using EPSC modelling. The elastic region of the macroscopic stress vs strain curve is shown in *Fig. 5.10*. The response of the weld-pad along the normal direction is stiffer than along the more compliant transverse direction.

The Young's modulus results are compared with the neutron diffraction results and summarised in table 5.2. The Young's modulus calculated from EPSC is in general agreement with the diffraction Young's modulus except in the LD orientation.

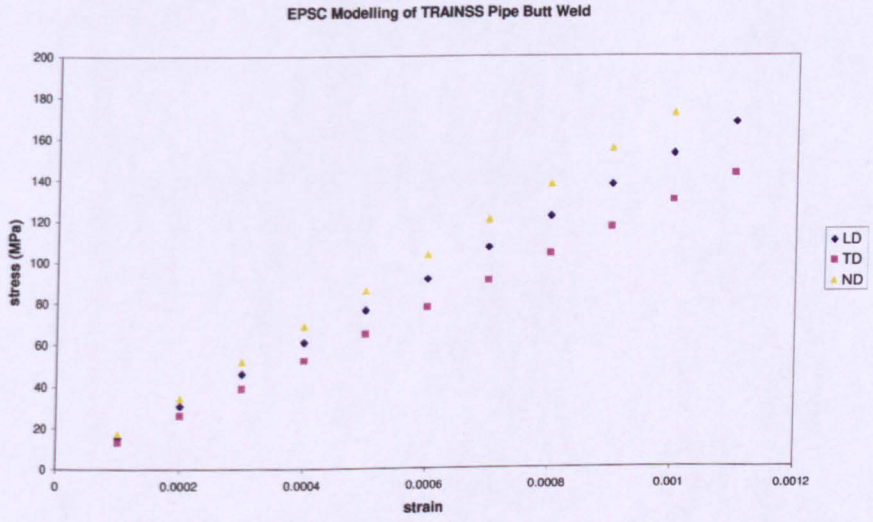

Fig. 5.10 EPSC modelling response of TRAINSS pipe butt weld in three principal processing directions

The angular variation of the Young's modulus is shown in Fig. 5.11. The modulus is a minimum at 0° and increases at higher angles. In the case of TRAINSS pipe butt-weld the Young's modulus is 153 GPa in the LD and attains a value of 174 GPa while going from LD towards ND. However the overall variation is lower as compared with that in the weld-pad.

Table 5.2 Comparison of EPSC modelling results of Young's modulus with neutron diffraction Young's modulus for the TRAINSS weld.

	LD	TD	ND
Compression			
LD - TD	**139**		
TD - LD		**126**	
ND - TD			***180***
EPSC **(Texture from Cubes)**	**152.5**	**129.73**	**172**

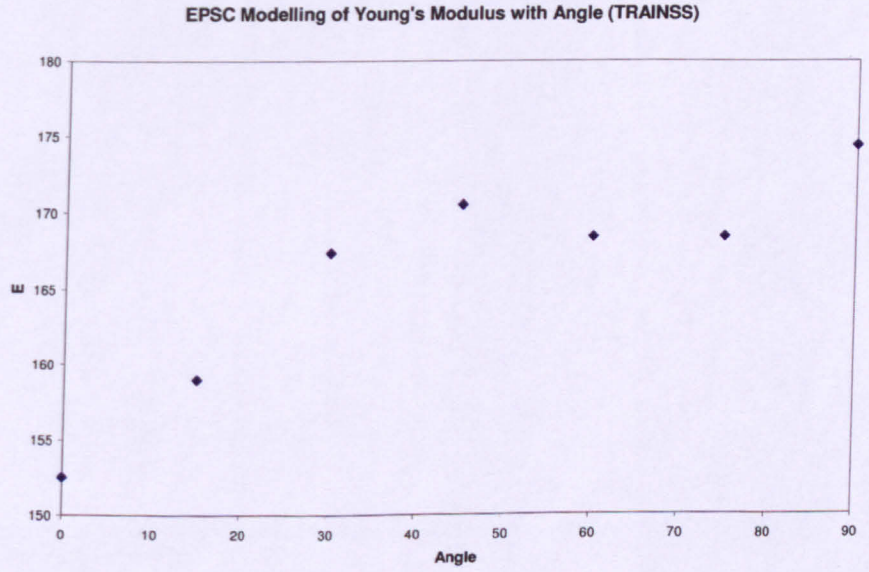

Fig. 5.11 EPSC modelling of E with angle (TRAINSS weld)

5.5.4 EPSC Modelling of 304 Multi–Pass TIG Weld

The response of the 316 TRAINSS pipe butt weld was investigated along three principal processing directions i.e. LD, TD and ND using EPSC modelling. The elastic region of the macroscopic stress vs strain curve is shown in Fig. 5.12.

The response of the TIG weld in the LD, TD and ND orientations is similar which shows that the TIG weld is nearly isotropic as compared with the weld-pad and TRAINSS weld.

The Young's modulus results are compared with the neutron diffraction results and summarised in Table 5.3. The EPSC results are in good agreement with the diffraction results.

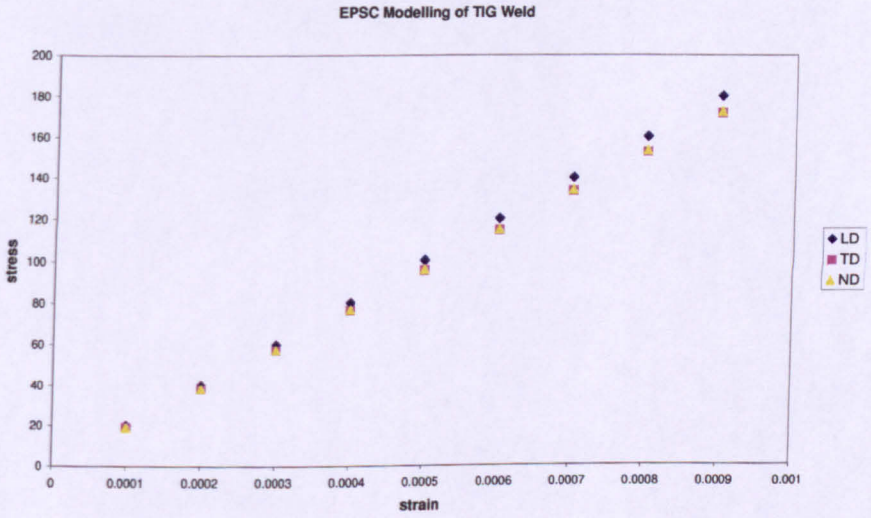

Fig. 5.12 EPSC modelling results for the TIG weld (macroscopic strain in three principal processing directions)

Table 5.3 Comparison of EPSC modelling results of Young's modulus with neutron diffraction Young's modulus for the TIG weld.

	LD	TD	ND
Compression			
LD - TD	**226**		
TD - LD		**220**	
ND - TD			
EPSC	**200.16**	**191**	**191.83**

The angular variation of the Young's modulus is shown in Fig. 5.13. The modulus reaches a maximum at 0° but drops at higher angles. In the case of the *TIG weld* the Young's modulus remains at about 190 GPa for all orientations.

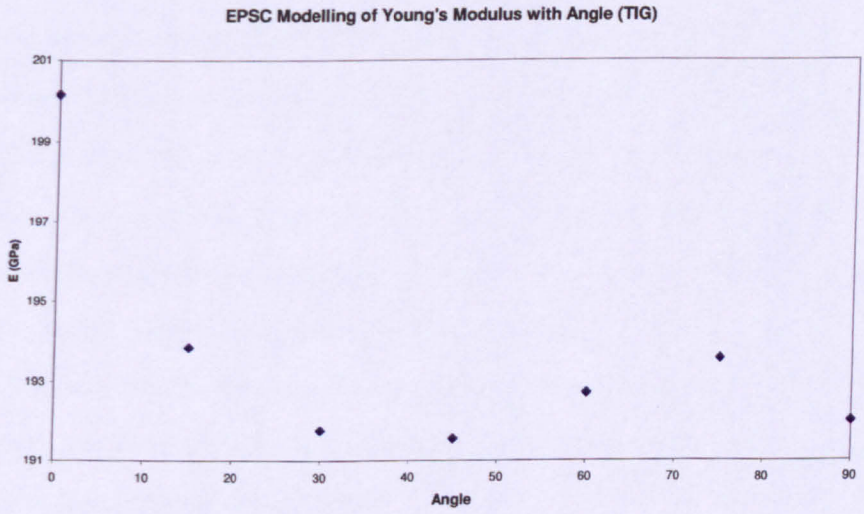

Fig. 5.13 EPSC modelling of E with angle

5.6 Young's Modulus Results from Present Work

Young's modulus results from the present work are summarised in table 5.4. The diffraction Young's modulus has been designated E_{Pawley} and the modulus measured using the clip gauge has been designated E_{mech}. The Young's modulus values from in-situ tensile and compression tests are presented in various orientations of the specimen. The orientations are with reference to the welding directions e.g. LD is the welding longitudinal direction.

5.6.1 Multi-Pass MMAW

The Pawley Young's modulus measured using in-situ tension in the longitudinal direction varies between 155 to 172 GPa for sample 4. However in the case of sample 15 the Pawley elastic modulus is 130 GPa. This discrepancy between the diffraction elastic modulus values of two samples can be attributed to the difference of texture between both the samples.

The texture results from both the samples have been discussed in Chapter 3. Sample 15 is more textured as compared with the sample 4, which is evident from the ODF sections. The texture strength (in multiples of times random) is 7.2 for the sample 4 and 13.06 for the sample 15. Due to the intense cube texture the sample 15 attains the properties of pseudo-single crystal which result in the anisotropic response. The Pawley Young's modulus measured using in-situ compression is in the range of 120 GPa to 124 GPa for various orientations of the specimen. The low value of the elastic modulus can be attributed to high texture of the weld-pad. The texture intensity (in multiples of times random) is 9.02.

5.6.2 Single-Pass MMAW

The Pawley Young's modulus measured using in-situ tension test is in the range of 223.5 to 240 GPa. The single-pass weld metal is less textured which is evident from the ODF sections and the texture intensity (in multiples of random texture intensity) is 4.97.

5.6.3 Multi-Pass TRAINSS Pipe Butt Weld

The Pawley Young's modulus measured using in-situ compression testing is 137 GPa in the LD and 127 GPa in the TD directions. The Young's modulus is very high in the ND direction.

5.6.4 Multi-Pass TIG Weld

The Pawley elastic modulus measured using in-situ compression testing, has been found to be 226 GPa in the longitudinal direction and 222 GPa in the transverse direction. The texture intensity (in multiples of times random) is much lower in the TIG weld, which is evident from the ODF sections. (Fig. 3.45a, Chapter 3). Being less textured the TIG weld tends to attain isotropic properties and therefore the values of the elastic modulus in the LD and TD directions are in close agreement.

5.7 Summary

The development of crystallographic texture in the welds has been reviewed and its implication for Young's modulus measurement has been discussed. EPSC modelling results are compared with the neutron diffraction results. A table of the Young's modulus values for different orientations for various weld types has been produced.

Material	Welding Technique	Orientation	In-situ Tension (at ISIS)			In-situ Compression (at ISIS)			Remarks (E_{mech} and E_{pawley} are Young's modulus values in GPa)
				E_{mech}	E_{pawley}	E_{mech}	E_{pawley}	Strain %	
316	MMAW Multi-pass pad (cylinders)	LD	Sample4	232	163			0.083	Gauge Volume: 4x4x4
			Sample 4	189	172			0.076	
			Sample 4	162	160			1	
			Sample 15	126	130			5	
316	Cubes from weld pad	LD					119.4	0.17	Gauge Volume: 4x4x4
		TD					119	0.17	
		ND					124.6	0.17	
316	MMAW single-pass cylinders	LD	Sample 13	146	223			0.075	Gauge Volume: 4x4x4
			Sample 13	159	240			0.075	
			Sample 13	141	223				
316	MMAW multi-pass pipe butt weld	LD					136.7	0.17	Gauge Volume: 4x4x4
		TD					126.1	0.17	
		ND					181.7	0.17	.
308	TIG multi-pass butt weld	LD					226.9	0.17	Gauge Volume: 4x4x4
		TD					221.9	0.17	

Table 5.4 Summary of Young's modulus values from present work.

Chapter 6 Conclusions

Several types of welds have been investigated in the present work. These included multi-pass weld-pad, multi-pass pipe butt weld, multi-pass TIG weld, single bead weld. The welds were fabricated using different welding process and under different conditions with different degrees of heat input. The welds exhibit similar microstructure with skeletal ferrite morphology. The welds exhibit a range of crystallographic texture from very intense cube texture to nearly random.

It has been observed that the crystallographic texture has consequences for anisotropy of the weld metal. The weld-pad with intense cube texture is very anisotropic as compared with TIG weld which is nearly isotropic. The anisotropy of the weld metal has implications for the Young's modulus values used in the calculation of residual stresses from measured strains and also in general design for structural integrity. With high anisotropy as observed in the weld-pad the Young's modulus value is highly orientation dependent. Therefore care must be taken to choose an appropriate value depending on the orientation for which residual stresses are calculated.

6.1 Future Work

It is proposed that the measurement of Young's modulus of a weld metal using diffraction techniques should be standardised. Round robin samples should be prepared from different weld geometries. Weld metal characterisation using metallography and texture should be carried out.

There are also some issues which require attention. It has been discussed in the previous chapter that a typical weld geometry has been attributed an orthotropic symmetry. This means that it requires nine elastic constants to fully describe the elastic stiffness tensor. However, with the existence of one plane of isotropy the number of elastic constants reduces to six.

This assumption has implication for the self consistent modelling of the weld metal. Now a question has to be answered whether a weld metal requires six elastic constants as input into the self consistent model even it is composed of cubic symmetry crystallites which requires three elastic constants.

It has to be investigated whether all welds, ranging from a highly textured weld-pad to a nearly random textured TIG weld exhibit special orthotropy.

References

1. Yoshiaki Arata, F. Matsuda, S. Katayama, Solidification crack susceptibility in weld metals of fully austenitic stainless steels (Report 1)–Fundamental investigation on solidification behaviour of fully austenitic and duplex microstructures and effect of ferrite on microsegregation, *Trans. of JWRI*, (1976), 135-151.

2. J. A. Brooks, A. W. Thompson, Microstructural development and solidification cracking susceptibility of austenitic stainless steel welds, *International Materials Reviews*, 36 (1991), 16-44.

3. M. F. McGuire, Austenitic stainless steels, *Encyclopaedia of Materials: Science and Technology*, (Elsevier Ltd., 2008), 406-410.

4. S. Katayama, T. Fujimoto, A. Matsunawa, Correlation among solidification process, microstructure, micro-segregation and solidification cracking susceptibility in stainless steel weld metals, *Trans. of JWRI*, 14 (1985), 123-138.

5. B. R. Dewey, L. Adler, R. T. King, K. V. Cook, Measurements of anisotropic elastic constants of type 308 stainless steel electroslag welds, *Experimental Mechanics*, 17 (1977), 420-426.

6. M. R. Daymond, Use of Rietveld refinement for elastic micro-strain determination and for evaluation for plastic strain history from diffraction spectra, *J Appl. Phys.* 82 (1987), 1554-1562.

7. H.J. Stone, T.M. Holden and R.C. Reed, Determination of the plane specific elastic constants of Waspaloy using neutron diffraction, *Scripta Materialia*, 40 (1999), 353-358.

8. Bjorn Clausen, Torben Lorentzen, Mark A. M. Bourke, Mark R. Daymond, Lattice strain evolution during uni-axial tensile loading of stainless steel, *Materials Science and Engineering*, A259 (1999), 17–24.

9. J. F. Nye, *Physical properties of crystals*, (Oxford University Press, 1957).

10. S. P. Timoshenko, J. N. Goodier, *Theory of Elasticity*, 3rd edn (McGraw Hill, 1970).

11. P.P. Benham, R. J. Crawford, C. G. Armstrong, *Mechanics of Engineering Materials*, (Prentice Hall, 1996).

12. J. M. Alexander, *Strength of Materials volume 1: Fundamentals*, (Ellis Horwood Ltd., 1981).

13. George E. Dieter, *Mechanical Metallurgy*, (McGraw Hill, 1988).

14. R. M. Christensen, *Mechanics of composite materials*, (John Wiley & Sons, 1979).

15. Von A. Reuss, Berechnung der fliesgrenze von mischkristallen auf grund der plastizitiatsbedingung fur einkristalle, *Ztschr. f. angew. Math. und Mech.*, (1929).

16. E. Macherauch, K. H. Kloos, Origin Measurement and Evaluation of Residual Stresses, *Proc. Of the Intl. Conf. on Residual Stresses*, Garmisch-Partenkirchen FRG, 1986, 167-174.

17. A. Stacey, H. J. MacGillivary, G. A. Webster, P. J. Webster, K. R. A. Ziebeck, Measurement of Residual Stresses by Neutron Diffraction, *Journal of strain analysis*, 20 (1985), 93-100.

18. P. J. Withers, H. K. D. H. Bhadeshia, Residual Stress Part 1 – Measurement Techniques, *Materials Sci. & Tech.*, 17 (2001), 355-365.

19. A Lodini, Calculation of residual stresses from measured strain, in *Analysis of residual stress by diffraction using neutron and synchrotron radiation*, Ed. by M. E. Fitzpatrick and A. Lodini, (Taylor and Francis, 2003).

20. M. E. Fitzpatrick, M. T. Hutchings, P. J. Withers, Separation of macroscopic, elastic mismatch and thermal expansion misfit stresses in metal matrix composite quenched plates from neutron diffraction measurements, *Acta Mater.*, 45 (1997), 4867-4876.

21. Philip J. Withers, Mapping residual and internal stress in materials by neutron diffraction, *C. R. Physique*, 8 (2007), 806-820.

22. I.C. Noyan, The theory of stress/strain analysis with diffraction, in *Measurement of residual and applied stress using diffraction*, Ed. by M. T. Hutchings, A. D. Krawitz, (Kluwer academic publishers, 1991), 51-65.

23. T. M. Holden, J. H. Root, R. A. Holt, M. Hayashi, Neutron diffraction measurements of stress, *Physica B*, 213-214 (1995), 793-796.

24. G. A. Webster, R. C. Wimpory, Non-destructive measurement of residual stress by neutron diffraction, *J. of Materials Processing Technology*, 117 (2001), 395-399.

25. M. T. Hutchings, Neutron diffraction measurements of residual stress fields: overview and points for discussion, in *Measurement of residual and applied stress using diffraction*, Ed. by M. T. Hutchings and A. D. Krawitz (Kluwer academic publishers, 1991), 3-18.

26. P. J. Webster, Spatial resolution and strain scanning, in *Measurement of Residual and Applied Stress using Neutron Diffraction*, Ed. by M. T. Hutchings and A. D. Krawitz, (Kluwer Academic Publishers, 1992), 235-251.

27. A. J. Allen, M. T. Hutchings, C. G. Windsor, C. Andreani, Neutron Diffraction methods for the study of residual stress fields, *Advances in Physics*, 34 (1985), 445-473.

28. H. G. Priesmeyer, J. Larsen, K. Meggers, Neutron diffraction for non-destructive strain/stress measurements in industrial devices, *J. of Neutron Research*, 2 (1994), 31-52.

29. L Pintschovius, Neutron diffraction methods, in *Structural and residual stress analysis by non-destructive methods* Ed. by Viktor Hauk, (Elsevier, 1997).

30. J. R. Santisteban, M. R. Daymond, J. A. James, L. Edwards, ENGIN-X: A third generation neutron strain scanner, *J. Appl. Crystallography*, 39 (2006), 812-825.

31. G. A. Webster, A. N. Ezeilo, Neutron scattering in engineering applications, *Physica B*, 234-236 (1997), 949-955.

32. R. A. Winholtz, the effect of assuming the principal directions in neutron diffraction measurement of stress tensors, *Materials Science and Engineering A*, 205 (1996) 257-258.

33. H. M. Rietveld, A profile refinement method for nuclear and magnetic structures, *J. App. Crystallography*, 2 (1969), 65-71.

34. W. I. F David, W. T. A. Harrison, The analysis of powder diffraction data, in *Neutron Scattering Data Analysis 1986*, Ed. by M. W. Johnson, (IOP Publishing Ltd, 1986), pp 1-25.

35. S. Spooner, Investigation of residual stresses in a multi-pass weld in 1" stainless steel plate, *Proceedings of the fourth international conference on residual stresses*, (SEM Inc, 1994) pp1205-1209.

36. D.G. Carr, M. I. Ripley, T. M. Holden, D. W. Brown, S. C. Vogel, Residual stress measurements in a zircaloy-4 weld by neutron diffraction, *Acta Materialia*, 52, (2004), 4083-4091.

37. R. I. Todd, M. A. M. Bourke, C. E. Borsa and R. J. Brook, Neutron diffraction measurements of residual stresses in Alumina/SiC nano-composites, *Acta Mater.*, 45 (1997), 1791-1800.

38. H. J. Bunge, Three dimensional texture analysis, *International materials reviews*, 32 (1987), 265-291.

39. H.J. Bunge, *Texture analysis in materials science: Mathematical methods*, (Butterworths, 1982).

40. http://openlearn.open.ac.uk/mod/resource/view.php?id=198370 (accessed on 15/09/2009).

41. M. Dahms, H. J. Bunge, The iterative series expansion method for quantitative texture analysis. I. General outline, *J. Appl. Cryst.*, 22 (1989), 439-447.

42. C. S. Barrett, T. B. Massalski, *Structure of Metals*, (McGraw Hill Book Company, 1966).

43. www.ebsd.com (accessed on 01/10/2009).

44. Stuart I. Wright, Jun-Wu Zhao, Brent L. Adams, Automated determination of lattice orientation from electron backscattered kikuchi diffraction patterns, *Textures and Microstructures*, 13 (1991), 123-131

45. Valerie Randle, Olaf Engler, *Introduction to Texture Analysis: Macrotexture, Microtexture and Orientation Mapping*, (Gordon and Breach Science Publishers, 2000)

46. H. G. Bunge, Advantages of neutron diffraction in texture analysis, *Textures and Microstructures*, 10 (1989), 265-307.

47. H. P. Lee, H. J. Bunge, C. Esling, Determination of the complete orientation distribution function by the zero range method, *Texture and Microstructures*, 6 (1986), 289-313.

48. R. W. K. Honeycombe, *The Plastic Deformation of Metals*, (Edward Arnold, 1975).

49. M. Sindel, G. D. Köhlhoff, K. Lücke, and B. J. Duggan, Development of cube texture in coarse grained copper, *Textures and microstructures*, 12 (1990), 37-46.

50. T. J. Headly, J. A. Brooks, A new bcc-fcc orientation relationship observed between ferrite and austenite in solidification structures of steels, *Met. and Mat. Trans. A*, 33A (2002), 5-15.

51. G Bouche, J. L. Bechade, M. H. Mathon, L. Allais, A. F. Gourgues, L. Naze, Texture of welded joints of 316L stainless steel, multi-scale orientation analysis of a weld metal deposit, *Journal of nuclear materials*, 277 (2000), 91-98.

52. M. R. Daymond, M. A. M. Bourke, R. B. Von Dreele, B. Clausen, T. Lorentzen, Use of Rietveld refinement for elastic micro-strain determination and for evaluation for plastic strain history from diffraction spectra, *J Appl. Phys.* 82 (1987), 1554-1562.

53. T. M. Holden, J. H. Root, R. A. Holt, M. Hayashi, Neutron diffraction measurements of stress, *Physica B*, 213-214 (1995), 793-796.

54. P. J. Withers, A. P. Clarke, A neutron diffraction study of load partitioning in continuous Ti/SiC composites, *Acta Mater.*, 46 (1998), 6585-6598.

55. W. F. Hosford, *The mechanics of crystals and textured polycrystals*, (Oxford University Press, 1993), p. 18.

56. J. F. Nye, Elastic behaviour of single crystals: anisotropy, *Encyclopaedia of Materials: Science & Technology*, 1-11 (2008), 2415-2422.

57. G. I. Taylor, Plastic strain in metals, *Journal of Inst of Metals*, 62 (1938), 307.

58. S. E. Schoenfeld, S. Ahzi, R. J. Asaro, Elastic-plastic crystal mechanics for low symmetry crystals, *J. Mech. Phys. of Solids*, 43 (1995), 415-446.

59. M. T. Hutchings, P .J. Withers, *Introduction to characterization of residual stresses by neutron diffraction*, (CRC Press, 2003).

60. T. Lorentzen, Anisotropy of lattice strain response, in *Analysis of residual stress by diffraction using neutron and synchrotron radiation* Ed. by M. E. Fitzpatrick and A. Lodini, (Taylor and Francis, 2003), pp 114-130.

61. C. N. Tome, Elastic behaviour of polycrystals, *Encyclopaedia of Materials: Science & Technology*, 1-11 (2008), 2409-2415.

62. D. I. Bolef, J. De Klerk, Anomalies in the elastic constants and thermal expansion of chromium single crystals, *Physical Review*, 129 (1963), 1063-1067.

63. G. A. Alers, Elastic moduli of vanadium, *Phys. Rev.*, 119 (1960), 1532-1535.

64. F. H. Featherston, J. R. Neighbours, Elastic constants of tantalum, tungsten and molybdenum, *Phys. Rev.*, 130 (1963), 1324-1333.

65. J. A. Rayne, B. S. Chandrasekhar, Elastic constants of iron from 4.2 to 300 K, *Phys. Rev.*, 122 (1961), 1714-1716.

66. P. M. Sutton, The variation of the elastic constants of crystalline aluminium with temperature between 63 K and 773 K, *Phys. Rev.*, 91 (1953), 816-821.

67. M. Yamamoto, Elastic constants of nickel crystals, *The 634th report of the Research Institute for Iron, Steel and other metals*, (1951), 308-320.

68. J. R. Neighbours, G. A. Alers, The elastic constants of silver and gold, *Phys. Rev.*, 111 (1958), 707-712.

69. W. C. Overton Jr., J. Gaffney, Temperature variation of the elastic constants of the cubic elements. I.Copper, *Phys. Rev.*, 98 (1955), 969-977.

70. H. M. Ledbetter, Monocrystal-Polycrystal elastic constants of a stainless steel, *Phys. Stat. Sol.*, 85 (1984), 89-96.

71. I. H. Swift, E. P. T. Tyndall, Elasticity and creep of lead single crystals, *Phys. Rev.*, 61 (1942), 359-364.

72. R. Hill, The elastic behaviour of a crystalline aggregate, *Proc. Phys. Soc. A*, A65 (1952), 349-354.

73. Z Hashin, S Shtrikman, A variational approach to the theory of the elastic behaviour of polycrystals, *J Mech Phys of solids*, 10 (1962), 343-352.

74. U. F. Kocks, The relation between polycrystal deformation and single-crystal deformation, *Metallurgical Trans.*, 1 (1970) 1121-1143.

75. J. D. Eshelby, The determination of the elastic field of an ellipsoidal inclusion, *Proc. of the Royal Soc. A*, 241 (1957), 376-396.

76. A. Molinari, S. Ahzi, R. Kouddane, On the self-consistent modelling of elastic-plastic behaviour of polycrystals, *Mechanics of Materials*, 26 (1997), 43-62.

77. J. W. Hutchinson, Elastic-plastic behaviour of polycrystalline metals and composites, *Proc. of the Royal Soc. London A*, 319 (1970), 247-272.

78. A. Baczmanski, C Braham, Elasto-plastic properties of duplex steel determined using neutron diffraction and self-consistent model, *Acta Mater.*, 52 (2004), 1133-1142.

79. P. A. Turner, C. N. Tome, A study of residual stresses in Zircaloy-2 with rod texture, *Acta Metall. Mater.*, 42 (1994), 4143-4153.

80. B. Clausen, T. Lorentzen, T. Leffers, Self-consistent modelling of the plastic deformation of FCC polycrystals and its implications for diffraction measurements of internal stresses, *Acta. Materialia*, 46 (1998), 3087-3098.

81. M. R. Daymond, H. G. Priesmeyer, Elastoplastic deformation of ferritic steel and cementite studied by neutron and self-consistent modelling, *Acta Materialia*, 50 (2002), 1613-1626.

82. H. M. Ledbetter, Monocrystal elastic constants in the ultrasonic study of welds, *Ultrasonics*, 23 (1985) 9-13.

83. C Austin, S. K. Bate, J. P. Hayes, G. Knowles, A constitutive model for single bead and multi–pass type 316 austenitic weld metal, (Serco Assurance Report: PC/GNSR/5087)

84. A. J. Wilby, The manufacture of austenitic stainless steel welded specimens for the IMC/TRAINSS project, (British Energy Generation Ltd., 1999).

85. P. J. Bouchard, Residual Stresses near repairs in a 19.6 mm thick, 412 mm diameter stainless steel pipe girth weld (TRAINSS Project Final Report).

86. P. J. Bouchard, R.A.W Bradford, Validated axial residual stress profiles for fracture assessments of austenitic stainless steel pipe girth welds, *Proceedings of ASME PVP Conference, vol. 423, Fracture and Fitness,* (2001) 93-99.

87. M. Turski, P. J. Withers, J. A. Francis, Determination of residual stress at weld interruptions by neutron diffraction, *Z. Kristallogr.* Suppl. 27 (2008), 231-243.

88. L M Gourd, *Principles of Welding Technology*, 3rd edn. (Butterworth-Heinemann Ltd., 1995).

89. N. Suutala, T. Takalo, T. Moisio, The relationship between solidification and microstructure in austenitic and austenitic-ferritic stainless steel welds, *Metallurgical Trans. A*, 10A (1979), 512-514.

90. John C. Lippold, *Welding Metallurgy and Weldability of Stainless Steels*, (Wiley Blackwell, 1995).

91. T. Takalo, N. Suutala, T. Moisio, Austenitic solidification mode in austenitic stainless steel welds, *Metallurgical Trans. A*, 10A (1979), 1173-1181.

92. N. Suutala, T. Takalo, T. Moisio, Ferritic-austenitic solidification mode in austenitic stainless steel welds, *Metallurgical Trans. A*, 11A (1979), 717-725.

93. T. Takalo, N. Suutala, T. Moisio, Single phase ferritic solidification mode in austenitic-ferritic stainless steel welds, *Metallurgical Trans. A*, 10A (1979), 1183-1190.

94. http://www.isis.rl.ac.uk/OpenGENIE (accessed on September 2006).

95. http://www.ncnr.nist.gov/programs/crystallography/software/gsas.html (accessed on September 2006).

96. X. Shan, Thermo-mechanical modelling of a single-bead-on-plate weld using the finite element method, *International J. of Pressure vessel and piping*, 86 (2009), 110-121.

97. X. Ficquet, D.J. Smith, C.E. Truman', E.J. Kingston and R.J. Dennis Measurement and prediction of residual stress in a bead-on-plate weld benchmark specimen, *International Journal of Pressure Vessels and Piping*, 86 (2009), 20-30.

98. C. E. Truman, M. C. Smith, The NeT residual stress measurement and modelling round robin on a single weld bead-on-plate specimen, *Int. J. of Pressure Vessel and Piping*, 86 (2009), 1-2.

99. Dean Deng, Hidekazu Murakawa, Numerical simulation of temperature field and residual stress in multi-pass welds in stainless steel pipe and comparison with experimental measurements, *Computational Materials Science*, 37 (2006), 269-277.

100. T. B. Brown, T.A. Dauda, C.E. Truman, D.J. Smith, D. Memhard and W. Pfeiffer Predictions and measurements of residual stress in repair welds in plates, *International J. of Pressure vessel and piping*, 83 (2006), 809-818.

101. D. S. Kupperman, K. J. Reimann, Ultrasonic wave propagation and anisotropy in stainless steel weld metal, *IEEE Trans. on Sonics and Ultrasonics*, SU-27 (1980), 7-15.

Appendix – A

Mitsui Babcock

Welding Services Department
P.O. Box 8, Birmingham New Road,
Tipton, DY4 8YY
Tel 0121 530 5000 Fax 0121 530 5103

Table of Recorded Parameters for the Weld Pad

BE Groove Welds			Job No.	46981
Electrode Type	**Batch No.**	**Electrode Dia.**		**Weld Length**
Babcock 'S'	P0911	5 mm		150 mm
Welder No.	**Welder Name**	**Preheat**		
324	T. Flavell	10°C		

Layer No.	Run No.	Amps (A)	Volts (V)	Heat Input (J/mm)	Time (sec)	Interpass Temp (°C)
1	3	23.1	158	2026	83.4	125
1	4	22.8	156	1873	79.1	124
1	7	22.7	160	2086	86.4	219
1	11	22.5	160	2140	88.9	85
2	15	22.5	161	2040	84.7	244
2	18	22.7	161	2006	82.6	278
2	19	23.1	160	2166	88.2	103
2	21	23.4	161	2166	86.4	245
3	32	23.3	158	2133	87.0	111
3	33	23.5	158	2060	84.3	190
3	35	23.0	161	2146	87.1	279
4	47	23.6	158	2153	86.7	285
4	52	23.2	159	2206	90.0	180
5	66	25.1	157	2373	90.4	210
5	69	25.0	158	2226	84.7	320
6	78	23.9	158	2133	84.8	269
6	82	24.5	158	2073	80.4	272
6	85	25.1	157	1960	74.8	266
7	98	23.5	157	1813	73.8	271
7	100	22.9	157	2120	88.5	329
7	103	22.5	158	2160	91.2	328
8	115	22.9	159	2126	87.1	126
8	119	23.3	158	2413	98.4	242
9	133	22.4	159	1993	84.1	158
9	134	22.7	157	2013	84.9	219
9	135	22.9	159	2100	86.1	259
10	147	22.4	158	2206	93.7	77
10	148	22.7	157	2060	86.8	183
11	157	22.7	157	2100	88.7	260
11	158	23.0	157	2020	84.2	297
11	159	23.2	159	2226	90.8	299

Mitsui Babcock

Welding Services Department
P.O. Box 8, Birmingham New Road,
Tipton, DY4 8YY
Tel. 0121 530 5000 Fax. 0121 530 5103

Table of Recorded Parameters for the Weld Pad continued...

BE Groove Welds			Job No.	46981
Electrode Type	**Batch No.**	**Electrode Dia.**		**Weld Length**
Babcock 'S'	P0911	5 mm		150 mm
Welder No.	**Welder Name**		**Preheat**	
324	T. Flavell		10°C	

Layer No.	Run No.	Amps (A)	Volts (V)	Heat Input (J/mm)	Time (sec)	Interpass Temp (°C)
12	168	23.2	160	2380	96.2	74
12	169	22.9	158	2213	92.0	152
13	180	23.1	158	2033	83.8	233
13	181	22.8	157	2106	88.5	250
13	182	23.5	160	2180	87.1	271
14	193	23.0	157	1986	82.6	184
14	194	23.1	159	1980	80.9	188
15	210	24.4	159	2413	93.6	18
15	211	26.7	157	2660	95.0	107
15	212	23.5	158	2120	85.8	194
16	223	23.2	157	2066	85.3	111
16	224	23.2	159	2093	85.4	143
17	236	24.0	157	2240	89.2	141
17	237	23.7	159	2100	83.8	224

Appendix - B

Mitsui Babcock

Welding Services Department
P.O. Box 8, Birmingham New Road,
Tipton, DY4 8YY
Tel. 0121 530 5000 Fax. 0121 530 5103

Table of Recorded Parameters for Single-Bead Welds

BE Groove Welds			Job No.	46981		
Electrode Type	**Batch No.**	**Electrode Dia.**		**Weld Length**		
Babcock 'S'	P0911	5 mm		100 mm		
Welder No.	**Welder Name**		**Preheat**			
324	T. Flavell		10°C			

Run No.	Amps (A)	Volts (V)	Time (sec)	Heat Input (J/mm)	Min. Bead Height (mm)	Interpass Temp (°C)
3	151	23.3	99.6	3500	6.90	30
4	149	23.2	92.4	3190	6.17	27
5	150	23.2	81.4	2830	5.17	24
6	149	23.5	85.8	3000	5.75	60
7	150	23.4	83.8	2940	5.27	45
8	150	23.2	83.9	2910	5.00	99
9	150	23.4	88.6	3100	5.19	80
10	150	23.8	81.7	2910	5.10	56
11	168	23.8	54.2	2160	4.28	17
12	180	24.1	47.2	2040	4.28	20
13	166	23.7	62.3	2450	4.23	28
14	160	25.4	72.2	2930	4.62	28
15	178	23.7	48.0	2020	3.61	25
16	167	23.2	76.6	2960	5.43	23
17	166	23.4	59.9	2320	4.65	47
18	166	23.7	68.4	2690	5.25	39
19	168	23.4	68.9	2700	4.57	60
20	166	23.2	64.2	2470	4.76	56
21	165	23.3	65.4	2510	4.99	99
22	168	22.6	70.7	2680	5.83	98
23	163	23.2	73.8	2780	5.49	21
24	165	23.0	76.9	2910	4.03	20
25	166	23.1	71.5	2740	4.08	18
26	164	23.0	67.4	2540	4.81	68
27	164	22.9	73.1	2740	4.79	63
28	161	22.7	65.8	2400	5.43	82
29	161	22.6	77.9	2830	5.94	98
30	161	22.6	64.0	2320	5.36	94
31	161	22.5	71.0	2570	5.52	120
32	164	23.1	78.9	2900	4.86	138
33	160	21.9	76.4	2760	6.27	31
34	160	22.5	74.4	2670	5.56	37
35	161	22.3	77.6	2780	5.64	27
36	159	22.4	76.7	2730	5.74	80
37	159	22.4	72.0	2590	5.14	75

Heat Input too high	
Grooves for 3-bead weld	

*** Run Numbers 1 and 2 were trial runs carried out on flat plate**